

# **Ice-contact volcanism in the Vífilsfell Region, southwest Iceland**

Christopher W. Hamilton

Department of Earth Sciences  
Dalhousie University  
Halifax, Nova Scotia

April 2004

Submitted in partial fulfillment of the requirements  
for the degree of Honours Bachelor of Science

© Copyright by Christopher W. Hamilton, 2004

## *Fire and Ice*

*Some say the world will end in fire;  
Some say in ice.  
From what I've tasted of desire  
I hold with those who favor fire.  
But if it had to perish twice,  
I think I know enough of hate  
To know that for destruction ice  
Is also great  
And would suffice.*

—Robert Frost (1929)



**DALHOUSIE**  
*University*

Department of Earth Sciences  
Life Sciences Centre, Room 3006  
Halifax, Nova Scotia  
CANADA B3H 4J1

Tel: (902) 494-2358

Fax: (902) 494-6889

E-mail: [earth.sciences@dal.ca](mailto:earth.sciences@dal.ca)

WWW: <http://meguma.earthsciences.dal.ca>

Date: April 30, 2004

**Author:** Christopher W. Hamilton

**Title:** Ice-contact volcanism in the Vífilsfell Region, southwest Iceland

Degree: B.Sc.

Convocation: May 25, 2004

Permission is herewith granted to Dalhousie University to circulate and to have copied for non-commercial purposes, at its discretion, the above title upon the request of individuals or institutions.

---

Christopher W. Hamilton

Signature of Author

---

Dr. D. Barrie Clarke

Signature of Advisor

The author reserves other publication rights, and neither the thesis nor extensive abstracts from it may be printed or otherwise reproduced without the author's written permission.

The author attests that permission has been obtained for the use of any copyrighted material appearing in this thesis (other than brief excerpts requiring only proper acknowledgement in scholarly writing) and that all such use is clearly acknowledged.

# Table of Contents

Acknowledgements.....	1
Abstract.....	2
Chapter 1 Introduction	
1.1 Location and Purpose.....	3
1.2 Scope and Claim .....	4
1.3 Significance .....	5
1.4 Previous Interpretation.....	6
1.5 Organization.....	7
Chapter 2 Ice-contact volcanism	
2.1 Introduction.....	9
2.2 Varieties of ice-contact volcanism.....	10
2.3 Criteria for identifying sub-ice volcanoes .....	14
2.4 The passage zone .....	15
2.5 Ice-contact lithofacies and structural relationships.....	18
2.6 Thick and thin ice cases for sub-ice volcano evolution .....	22
2.7 Gjálp, Iceland.....	24
2.8 Brown Bluff, Antarctica .....	30
2.9 Paleo-environmental reconstructions using ice-contact volcanoes .....	33
2.10 Summary.....	35
Chapter 3 Phreatomagmatic fragmentation	
3.1 Introduction.....	37
3.2 Mechanisms of explosive phreatomagmatic interactions .....	37
3.3 Molten Fuel-Coolant Interaction .....	38
3.4 Timeline for experimental Molten Fuel-Coolant Interactions.....	40
3.5 The efficiency of phreatomagmatic interactions .....	41
3.6 Water vapour films .....	46
3.7 Rayleigh-Taylor instability .....	47
3.8 Kelvin-Helmholtz instability .....	50
3.9 Superheating and spontaneous nucleation .....	51
3.10 Thermal detonation.....	52
3.11 Phreatomagmatic pyroclasts .....	53
3.12 Characteristics of phreatomagmatic deposits .....	57
3.13 Summary.....	60
Chapter 4 Methods	
4.1 Remote sensing.....	62
4.1.1 Unsupervised classifications.....	62
4.1.2 Supervised classifications .....	63
4.1.3 Remote sensing analysis of the Vífilsfell Region.....	65
4.1.4 Procedure .....	66
4.2 Field survey.....	68

4.3	Geochemical analysis .....	69
4.3.1	CIPW norm calculations .....	69
4.3.2	Normalized basalt tetrahedra .....	70
4.3.3	Procedure .....	73
Chapter 5 Observations and Results		
5.1	Remote sensing .....	75
5.2	Field Observations .....	83
5.3	Petrography and Geochemistry .....	92
5.3.1	Petrographic analysis .....	92
5.3.2	Geochemical analysis .....	95
Chapter 6 Discussion and Interpretation		
6.1	Introduction.....	99
6.2	Remote sensing .....	99
6.3	Lithostratigraphic relationships .....	103
6.3.1	Northern Bláfjöll.....	104
6.3.2	Vífilsfell.....	106
6.3.3	Arnarþúfur .....	108
6.4	Petrographic and Geochemical analysis .....	111
6.5	Schematic model of ice-contact volcanism in the Vífilsfell Region .....	115
6.6	Summary.....	125
Chapter 7 Summary of Conclusions		
7.1	Ice-contact volcanism in the Vífilsfell Region .....	128
References.....		131
Appendices		
Appendix A Remote sensing.....		136
A.1	Cartographic Model 1 (Principal Components Analysis).....	137
A.2	Cartographic Model 2 (24-bit band composite).....	139
A.3	Cartographic Model 3 (24-bit composite) .....	140
A.4	Cartographic Model 4 (8-bit band composite).....	141
A.5	Cartographic Model 5 (8-bit composite images) .....	142
A.6	Cartographic Model 6 (band composite classification) .....	143
A.7	Cartographic Model 7 (component composite classification) .....	147
Appendix B Field Observations.....		149
B.1	Field Observations .....	150
Appendix C Geochemistry.....		161
C.1	Electron Microprobe Data (original oxide weight percentages).....	162
C.2	Electron Microprobe Data (normalized oxide weight percentages) .....	169
C.3	CIPW norm calculation .....	176
C.4	Hypersthene conversion.....	187

# Table of Figures

Chapter 1	Introduction	
Figure 1.1	Location map I.....	3
Figure 1.2	Location map II .....	4
Figure 1.3	Geological map of the Vífilsfell Region .....	7
Chapter 2	Ice-contact volcanism	
Figure 2.1	Hyaloclastite flow deposits.....	12
Figure 2.2	The passage zone .....	16
Figure 2.3	Changes in passage zone elevation.....	17
Figure 2.4	Schematic model of sub-ice volcano formation .....	22
Figure 2.5	Thin ice case .....	23
Figure 2.6	Thick ice case.....	24
Figure 2.7	Gjálp location map.....	25
Figure 2.8	Photographs of the 1996 Gjálp eruption.....	27
Figure 2.9	Brown Bluff location map .....	31
Figure 2.10	Brown Bluff, Antarctica .....	32
Figure 2.11	Reconstruction of Pleistocene ice thickness in northern Iceland.....	34
Chapter 3	Phreatomagmatic Fragmentation	
Figure 3.1	Thermal Explosion Experiment II (TEE II).....	41
Figure 3.2	Timeline for experimental MFCI.....	41
Figure 3.3	Water-to-melt mass ratio .....	44
Figure 3.4	Water-to-melt volume ratio .....	45
Figure 3.5	Differential flow speeds.....	45
Figure 3.6	Boundary-layer instabilities.....	47
Figure 3.7	Rayleigh-Taylor instabilities.....	48
Figure 3.8	Cycles of boundary-layer instability and melt detachment .....	48
Figure 3.9	Vortex instability .....	51
Figure 3.10	Formation of Kelvin-Helmholz instabilities .....	51
Figure 3.11	Thermal detonation.....	53
Figure 3.12	Phreatomagmatic pyroclast morphologies.....	54
Figure 3.13	Synthetic phreatomagmatic pyroclasts .....	54
Figure 3.14	Principal phreatomagmatic pyroclast types .....	55
Figure 3.15	Phreatomagmatic deposits .....	58
Chapter 4	Methods	
Figure 4.1	Principal Component Analysis .....	67
Figure 4.2	Fundamental basalt tetrahedron.....	71
Figure 4.3	General basalt tetrahedron .....	72
Chapter 5	Observations and Results	
Figure 5.1	Band composite image of the Vífilsfell Region.....	76
Figure 5.2	Component composite of the Vífilsfell Region .....	77
Figure 5.3	Band composite cluster classification.....	78
Figure 5.4	Frequency distribution histograms of the band classification.....	78

Figure 5.5	Component composite cluster classification.....	79
Figure 5.6	Frequency distribution histograms of the component classification.....	79
Figure 5.7	Band composite classiciation with cluster threshold .....	81
Figure 5.8	Component composite classification with cluster threashold .....	82
Figure 5.9	Field observation zones .....	84
Figure 5.10	Northern Bláfjöll, Vífilfell, and Arnabúfur .....	85
Figure 5.11	Basal pillow lavas (Northern Bláfjöll).....	86
Figure 5.12	Passage zone (Northern Bláfjöll).....	86
Figure 5.13	Contact between Northern Bláfjöll and Vífilfell.....	87
Figure 5.14	Peripheral slump deposits (Vífilfell).....	87
Figure 5.15	Volcanic bombs (Vífilfell) .....	88
Figure 5.16	Vent Region (Vífilfell) .....	88
Figure 5.17	Arnabúfur viewed from the northwest.....	89
Figure 5.18	Arnabúfur viewed from the zouttheast .....	89
Figure 5.19	Rythmic bedding (Arnabúfur) .....	90
Figure 5.20	Armoured lapilli (Arnabúfur) .....	90
Figure 5.21	Flutes (Arnabúfur) .....	91
Figure 5.22	Climbing ripples (Arnabúfur) .....	91
Figure 5.23	Steeply inclied beds (Arnabúfur).....	92
Figure 5.24	Distal palagonite mounds (Arnabúfur) .....	92
Figure 5.25	Photomicrograph of Northern Bláfjöll sample Wpt094 .....	93
Figure 5.25	Photomicrograph of Vífilfell sample Wpt107.....	93
Figure 5.26	Photomicrograph of Arnabúfur sample Wpt043 .....	94
Figure 5.27	Photomicrograph of Arnabúfur sample Wpt059 .....	94
Figure 5.28	High-magnification BSE image of Arnabúfur sample Wpt043 I .....	95
Figure 5.29	High-magnification BSE of Arnabúfur sample Wpt043 II.....	95
Figure 5.30	K <sub>2</sub> O versus SiO <sub>2</sub> .....	96
Figure 5.31	CaO versus MgO + FeO .....	97
 Chapter 6 Discussion and Interpretation		
Figure 6.1	Band composite cluster interpretation.....	100
Figure 6.2	Component composite cluster interpretaion .....	102
Figure 6.3	Sample classification using the normative basalt tetrahedron.....	113
Figure 6.4	Location and orientation of the schematic cross-section .....	115
Figure 6.5	Schematic cross-section .....	116
Figure 6.6	Cross-sectional view of Northern Bláfjöll, Vífilfell, and Arnabúfur .....	124
Figure 6.7	Plan-view of Northern Bláfjöll and Vífilfell, and Arnabúfur .....	125

# Acknowledgements

I wish to acknowledge the University of Iceland and International Student and Exchange Services at Dalhousie University for providing me with the opportunity to study in Iceland; the Dalhousie International Study/Work International Fund for providing financial support for my studies abroad; and the Geodetic Survey of Iceland (Lanmælingar Íslands) for generous donation of multispectral satellite imagery of the Vífilfell Region. I am grateful for the technical assistance I received from Gordon Brown, Patricia Stoffyn, Joyia Chakungal, and Sarah Carruzzo during petrographic and geochemical phases of my thesis research. I also wish to thank the many wonderful professors that I have had the privilege to work with while studying in the Earth Sciences Department at Dalhousie University, and specifically acknowledge the contributions made by Gunter Muecke, Marcos Zentilli, Martin Gibling, and Lawrence Plug. I would also like to acknowledge Magnus Tumi Guðmundon for numerous insightful discussions relating to ice-contact volcanism and Jóhann Helgason for introducing me to the Vífilfell Region and for providing valuable scientific reviews. Additionally, I would like to thank Barrie Clarke for many helpful scientific discussions and for his thorough reviews, both of which greatly improved the quality of this thesis. Finally, I wish to thank my family for their tremendous encouragement and enduring support.



## Abstract

Ice-contact volcanism, and specifically subglacial volcanism, can provide information about paleo-environments such as the extent and thickness of former glaciers and ice sheets. In southwest Iceland, approximately 30 km southeast of Reykjavík on the Reykjanes Peninsula, the regions of Northern Bláfjöll, Vífilfell, and Arnarþúfur contain structures associated with Pleistocene ice-contact volcanism. This study combines remote sensing classification of multispectral satellite imagery, field observations, and geochemical analysis to determine the relationship between these features. Remote sensing classification of SPOT 5 imagery using Geographic Information Systems (GIS) generates 16 significant spectral clusters.

Determination of significant clusters and their spatial distribution facilitates subsequent field investigations. Ground-truthing of Northern Bláfjöll reveals a flat-topped volcano with steep sides that consists of basal pillow lavas, pillow-breccia, altered hyaloclastite (palagonite), flow-foot breccia, welded scoria, and superincumbent subaerial lava flows. Vífilfell directly overlies Northern Bláfjöll and encompasses a conical mound of palagonite with isolated welded scoria, volcanic bombs, dykes with pillowed surfaces, and peripheral slump deposits. Arnarþúfur comprises a series of linearly oriented discrete mounds with rhythmically layered fine-grained palagonite and clast supported beds that include varying proportions of armoured lapilli. Beds typically contain flow indicators such as climbing ripples, cross-beds, and flutes. Electron microprobe analysis of major element concentrations in volcanic glass reveals that Northern Bláfjöll, Vífilfell, and Arnarþúfur have indistinguishable olivine-normative tholeiite compositions. Northern Bláfjöll is a tuya that emerged from a deep englacial meltwater lake with a surrounding ice thickness exceeding 400 m, according to the passage zone elevation above the surrounding plain. Vífilfell is a subglacial mound that formed beneath thin-ice conditions with episodic meltwater drainage during its emplacement. Arnarþúfur is an ice-confined hyaloclastite mass-flow deposit that combines characteristics of pyroclastic density currents, turbidites, and eskers. Stratigraphic relationships suggest that Arnarþúfur formed in association with the Vífilfell eruption as a result of gravity-controlled mobilization of unconsolidated volcanoclastic material into an ice-confined meltwater drainage system. The chemical homogeneity of Northern Bláfjöll, Vífilfell, and Arnarþúfur suggest a common magma source and rapid emplacement of the volcanic deposits relative to the evolution of the melt.

**Key words:** volcanism, ice-contact, subglacial, hyaloclastite, geochemistry, remote sensing, Iceland

# Chapter 1 Introduction

## 1.1 Location and Purpose

The Vífilfell Region in southwest Iceland, approximately 30 km southeast of Reykjavík, contains a variety of volcanic deposits within the regions of Northern Bláfjöll, Vífilfell, and Arnarþúfur. Figure 1.1 illustrates the location of the study region and Figure 1.2 depicts the spatial relationship between Northern Bláfjöll, Vífilfell, and Arnarþúfur. The purpose of this thesis is to determine paleo-environmental conditions affecting the emplacement of volcanic lithofacies in the Vífilfell Region.

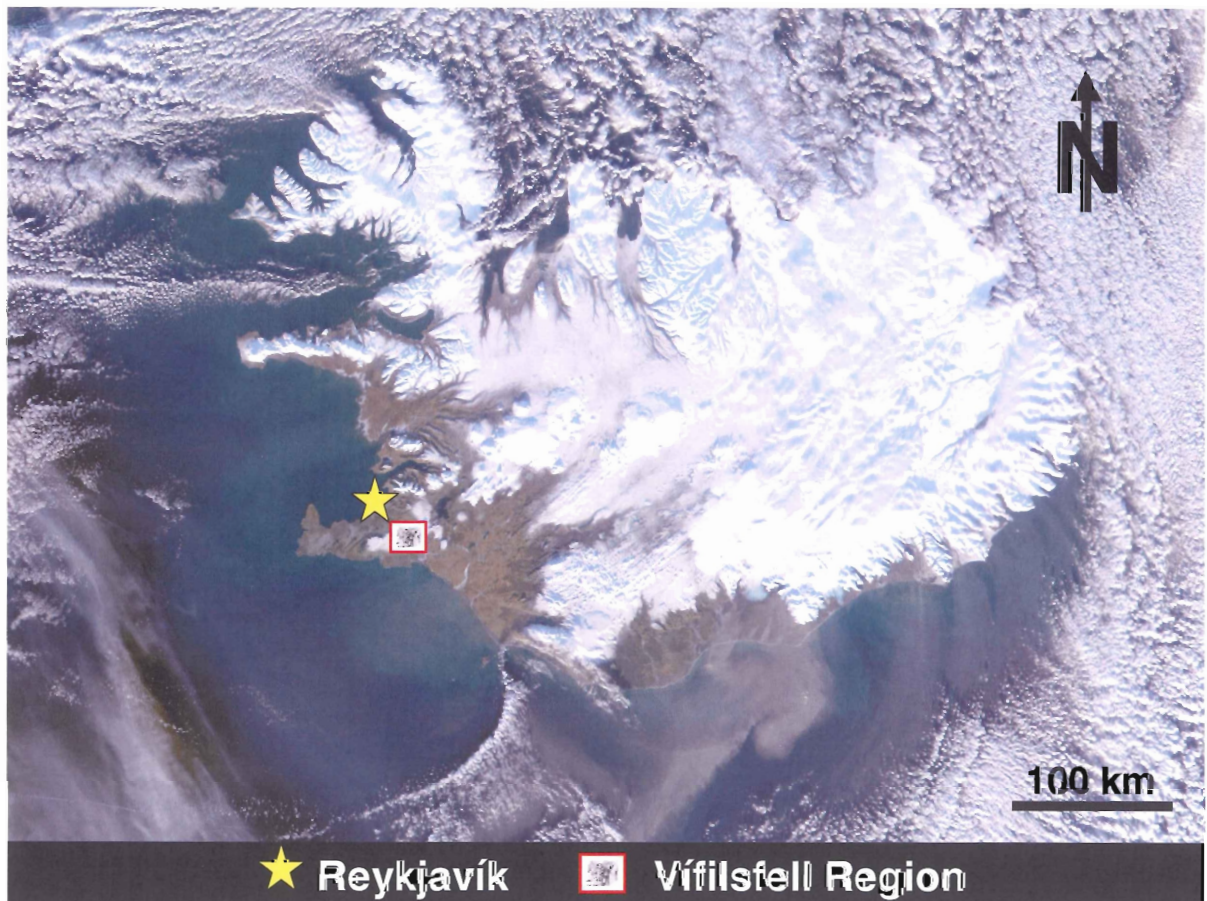


Figure 1.1: Location map I. The Vífilfell Region is located ~30 km southeast of Reykjavík on the Reykjanes Peninsula of Iceland. Moderate Resolution Imaging Spectroradiometer (MODIS) satellite image acquired January 28, 2002 (Descloitres 2002).

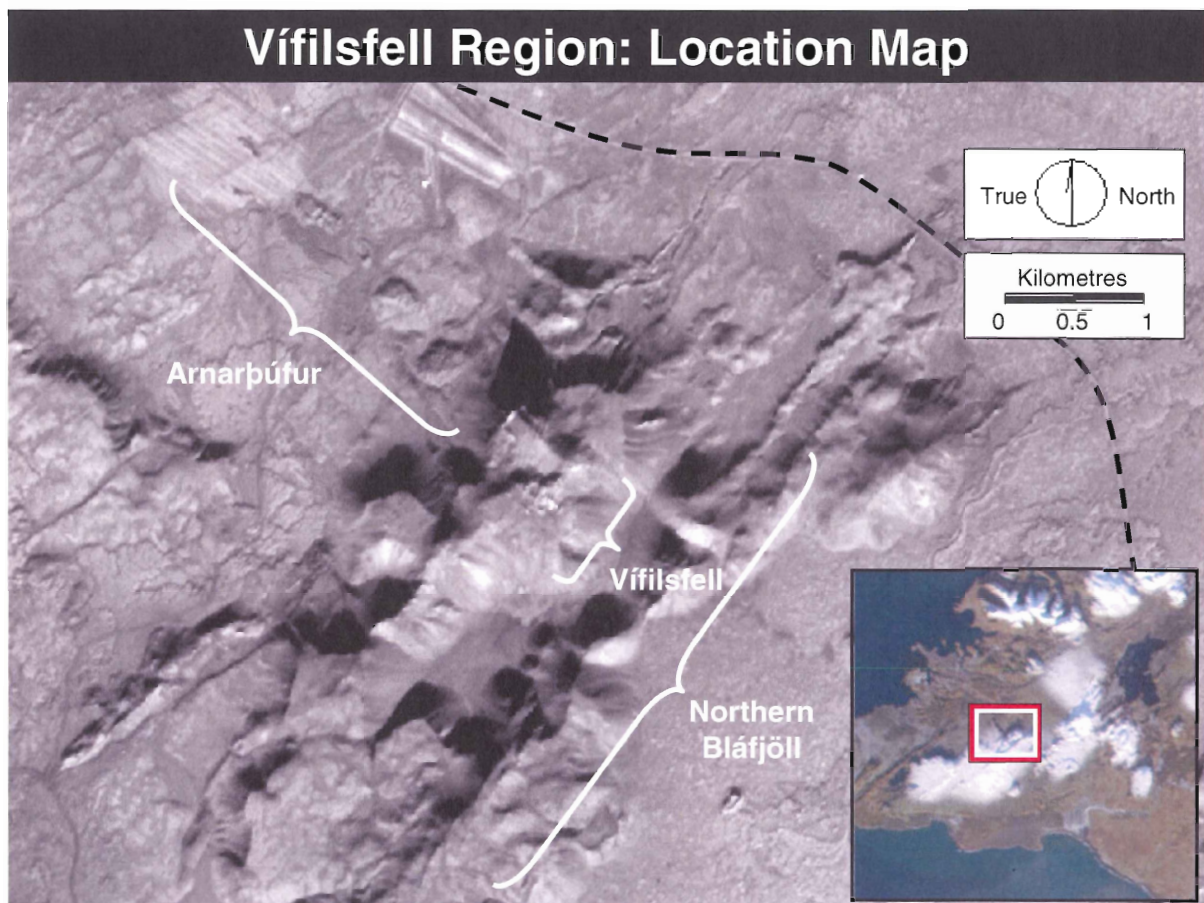


Figure 1.2: Location map II. Study area with the locations of principal ice-contact volcanic landforms indicated. The dashed line identifies the position of Highway 1.

## 1.2 Scope and Claim

The focus of this thesis is on ice-contact volcanic deposits in the Vífilsfell Region with emphasis on Northern Bláfjöll, Vífilsfell, and Arnarþúfur. Detailed examination of interglacial lavas in the Vífilsfell Region is outside the scope of this project. To determine the spatial distribution, lithostratigraphy, and chemical composition of Northern Bláfjöll, Vífilsfell, and Arnarþúfur deposits, I have used three primary research methods: multispectral satellite image classification, field surveys, and geochemical analysis. The spatial distribution of principal land-cover classes is determined using remote sensing prior to conducting field work. Preliminary field surveys focus on regions with interpreted hyaloclastite land-cover. Subsequent field work focuses on determining the lithostratigraphic relationships between

ice-contact volcanic deposits. Samples collected in the field survey are analyzed petrographically and geochemically to determine the compositional relationship between Northern Bláfjöll, Vífilfell, and Arnarþúfur deposits. The evidence shows that the Northern Bláfjöll is a tuya, Vífilfell is a subglacial mound, and Arnarþúfur is an ice-contact hyaloclastite mass-flow deposit.

### **1.3 Significance**

Hyaloclastite flow deposits are rarely preserved *in situ* and are rarely considered within schematic models of ice-contact volcanism. A better understanding of hyaloclastite mobilization and emplacement in subglacial environments is important for developing better models of subglacial volcano emplacement, interpreting paleo-environmental conditions and former ice thicknesses, and assessing the hazards facing communities near ice-covered volcanoes. For instance, on November 13, 1985, a small volcanic eruption issuing from an ice-covered volcano in the Columbian Andes, Nevado del Ruiz, generated a large volume of meltwater. The meltwater travelled downslope and developed into a catastrophic mud flow that inundated the town of Armero, killing over 23 000 people. Subglacial eruptions in Iceland can generate similar meltwater floods, termed jökulhlaups. Recent examples of subglacial volcanic eruptions in Iceland include the 1996 and 1998 eruptions of Gjálp. Furthermore, terrestrial subglacial volcanism may provide an analogue for some volcanic processes on Mars, such as hyaloclastite production, and the formation of aureoles and escarpments associated with Olympus Mons and Arsia Mons (Helgason 1999). Ice-contact volcanism involving lava flows and underlying permafrost can cause localized phreatomagmatic explosions that may be responsible for generating volcanic rootless cones

on Mars (Fagents *et al.* 2002; Lanagan *et al.* 2001). Investigation of terrestrial ice-contact volcanism can facilitate interpretation of surface features on Mars.

## 1.4 Previous Interpretation

Jónson (1978) explored the geology of the Vífilfell Region and interpreted Northern Bláfjöll as a *stapi* (Icelandic for tuya) and considered it probable that Bláfjöll, of which Northern Bláfjöll is a part, accumulated in many subglacial eruptions. Jónson (1978) identified a series of low palagonite mounds (Arnarpúfur) that extend northwest from Vífilfell. Jónson (1978) interpreted Vífilfell as the southern end of a fissure eruption that also formed Arnarpúfur. A complete translation of the original description by Jónson (1978) is included below and Figure 1.3 presents the accompanying geological map of the Vífilfell Region.

As a unit the Bláfjöll Mountains (55-685 m, map sheet 17) are constructed as a *stapi* (tablemountain) and within them are found very thick layers of pillow basalts as can be seen in the southern part of Jósepsdalur valley. Some of this pillow basalt is very feldspar porphyritic, but it is not known whether that is more typical of the formation as a whole or is more local. Clearly, the pillow basalt in the southwest part of the mountains, like for instance in Hákollur, is very phyrlic and this is the case widely in the western mountains. On top of the mountain is a lava cover that extends over considerable width and large craters from which these lavas have undoubtedly come. These basalt lavas (grey stage lavas, *gragryti*) are fresh and youthful. It contains considerable amount of olivine. Phenocrysts are not prominent and seem normally to consist of crystal groups rather than individual crystals. Picotite (spinel) occurs commonly in the olivine, but not elsewhere. The Bláfjöll grey lava consists of the following primary constituents:

Plagioclase	42.0%
Pyroxene	34.9%
Olivine	16.2%
Opaques	6.8%
Phenocrysts: Plagioclase	2.4%
Olivine	6.8%
Number of counted points:	452

Dykes are seen in a few places in Bláfjöll, including one just south of the craters at the very top of the mountain. Phenocrysts can be observed with the naked eye, these are mainly groups of plagioclase, pyroxene, and olivine crystals, but in addition the rock has an unusually high content of opaques. The olivine phenocrysts are built up of many, sometimes 7-8, crystals and in this case the intervening space is rich in opaques as well as in the olivine themselves. Some of these opaques are undoubtedly spinel, but clear identification is mostly difficult due to oxidation. The olivine crystals are often 1-1.5 mm in diameter. The composition of the rock in the dyke turned out to be as follows:

Plagioclase	44.0%
Pyroxene	36.2%
Olivine	11.9%
Opagues	7.8%
Phenocrysts: Olivine	2.1%
Number of counted points:	472

It is probable that the Bláfjöll Mountains accumulated in many subglacial eruptions. It is interesting that a row of low palagonite (móberg) hills/peaks, Arnarþúfur, striking northwest-southeast extends away from Vífilfell (655 m), which is the northernmost peak/corner of Bláfjöll and here it is considered that this represents a fissure. The top of Vífilfell could thus be the southern end of the fissure and perhaps a function by another fissure striking northeast-southwest. Many things related to this are poorly investigated, but this formation first made onto a map in 1958 (Trggvason and Jónsson 1958).

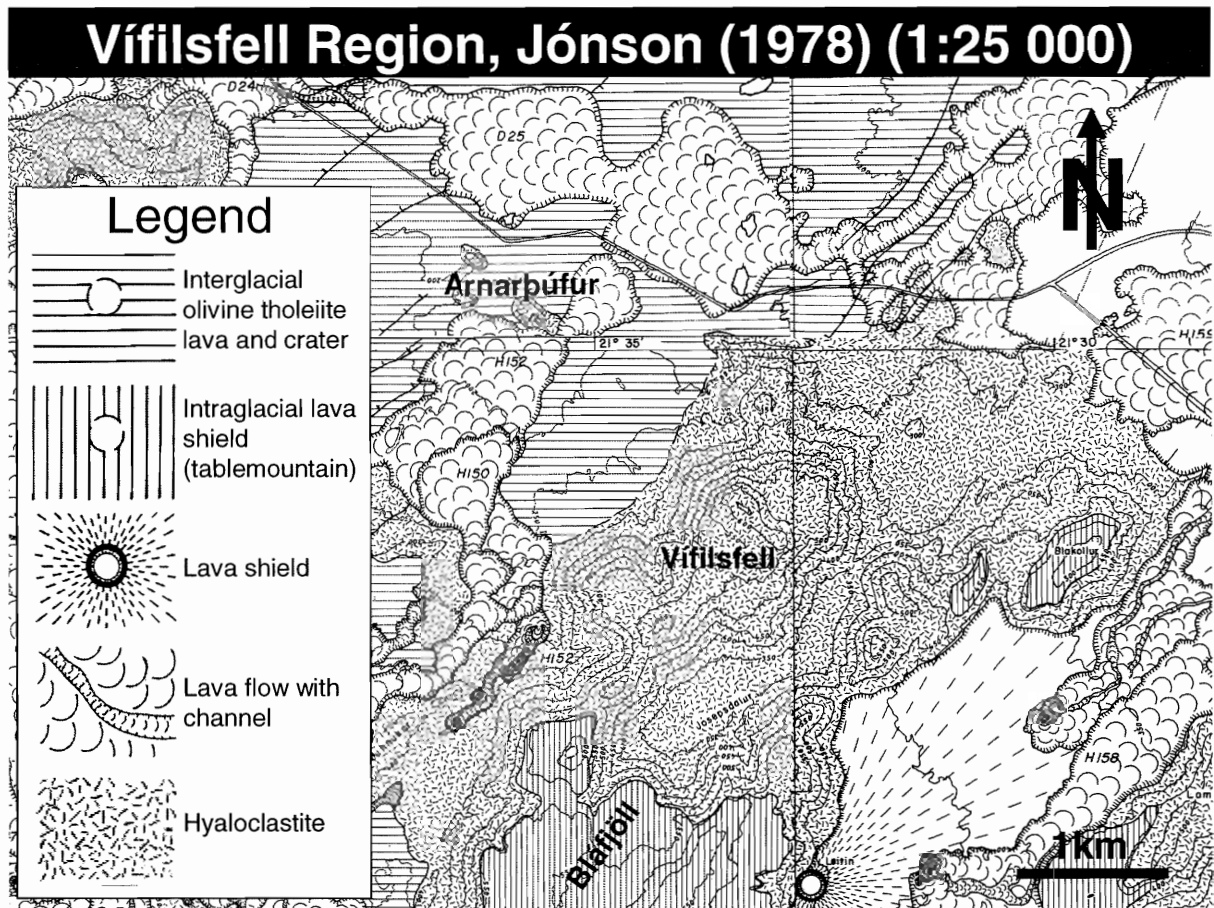


Figure 1.3: Geological map of the Vífilfell Region. Composite of map sheets 16, 17, 19, and 20 (Jónsson 1978) depicting the geology of Northern Bláfjöll, Vífilfell, and Arnarþúfur deposits.

## 1.5 Organization

Chapters 2 and 3 provide background information relating to ice-contact volcanism and phreatomagmatic interactions. This information is a prerequisite for exploring ice-contact

volcano formation, hyaloclastite flow emplacement, and paleo-environmental reconstructions. In addition, Chapter 2 presents the principal varieties of ice-contact volcanism, schematic models for ice-contact volcano formation, and case studies that explore the phases of ice-contact volcano emplacement, subglacial volcano lithostratigraphy, and regional paleo-environmental reconstructions based on ice-contact volcano morphology. Chapter 3 discusses the mechanisms of heat transfer between magma and external water, and describes the lithological products of phreatomagmatic fragmentation. Phreatomagmatic fragmentation results from Molten Fuel-Coolant Interaction (MFCI) and produces a variety of lithological products depending on the efficiency of heat transfer within the melt-water system. Chapter 3 presents a summary of thermodynamic processes associated with MFCI, compares results from contrasting MFCI experiments, and explores the characteristics of phreatomagmatic pyroclasts in relation to MFCI efficiency.

Chapter 4 introduces the methods used to analyze ice-contact volcanic deposits in the Vífilfell Region, including remote sensing techniques, field observations, and geochemistry. The first section describes the method of the remote sensing investigation, which uses Geographic Information Systems (GIS) to classify discrete spectral clusters with multispectral satellite data (SPOT 5 imagery). The second section presents a summary of field survey methods. The final section provides a description of the methods used during the geochemical analysis, including sample selection, thin-section preparation, microprobe analysis, and post-processing of the data.

Chapter 5 summarizes the observations and results obtained from each of the three principal methods of investigation: remote sensing, field surveys, and geochemical analysis. Chapter 6 presents a discussion and interpretation of these observations. Chapter 7 provides a summary of conclusions.

# Chapter 2 Ice-contact volcanism

## 2.1 Introduction

Sub-ice volcanism provides information about the local thickness of former glaciers and ice-sheets. Paleo-environmental reconstructions based on sub-ice volcanism require detailed structural investigations of volcanic complexes to identify distinctive lithofacies and structural relationships that are diagnostic of ice-volcano interaction. The following parameters strongly influence the sequence of ice-contact volcano lithofacies: magma composition; thermal and rheological properties of the magma; effusion rates; duration and number of eruptive phases; ice thickness and rheology; bedrock topography; water drainage systems; and the availability of external water within the system. Depending on the interaction among these parameters, six basic ice-contact structures may result: tuyas, tindars, subglacial mounds (SGMs), hyaloclastite flows, some stratovolcano deposits, and volcanic rootless cones (pseudocraters).

The purpose of this chapter is to determine the applicability of ice-contact volcano lithostratigraphy for paleo-environmental reconstructions of former ice thickness and extent. The following review introduces various forms of ice-contact volcanism, their principal lithofacies and structural expression, and models of volcano formation beneath thin and thick ice. A theoretical understanding of ice-contact volcanism makes possible the exploration of natural examples and an evaluation of reconstructions of ice thickness based on the ice-contact volcanoes characteristics. Although melt composition strongly affects the morphology of ice-contact volcanoes, this review examines only terrestrial ice-contact volcanism involving basaltic melts.



## 2.2 Varieties of ice-contact volcanism

Six principal structures result from ice-contact volcanism: 1) tuyas, 2) tindar, 3) subglacial mounds, 4) hyaloclastite flows, 5) some stratovolcano deposits, and 6) pseudocraters. This section describes the formation and principal lithofacies of each of these structures.

1) Tuyas (*stapi* in Icelandic) are flat-topped, steep-sided volcanoes that form in ice-contact environments. Tuya and *stapar* are singular forms of tuyas and *stapi*, respectively. Tuyas contain basal pillow lavas and pillow joint-block breccia units with mantling vitriclastic deposits (hyalotuff and hyaloclastite), flow-foot breccia (mixed hyaloclastite and lava breccia), and superincumbent subaerial sheet lava flows. In 1941, Lindal recorded in his diary the first description of *stapi* and proposed their sub-ice origin (Thorarinsson, personal communication to Mathews, 1969 cited in Hickson 2000). In 1943, Kjartansson made the first published account of *stapi*; however, his book, *Árnesinga Saga*, remains generally inaccessible to the global scientific community because the Icelandic text has not been translated. In 1947, following visits to Iceland and discussions with Kjartansson, Mathews published the first English description of *stapi*, which he termed tuyas. The term tablemountain, which is commonly used as a synonym for tuya, is misleading and should be avoided because many tablemountains are not associated with ice-contact volcanism. Tuyas are typically considered the sub-ice expression of subaerial shield volcanoes, however, tuyas can also result from subglacial fissure eruptions if the volcanic pile emerges from an englacial lake and subaerial lava flows are emplaced above the passage zone.

2) Tindar are linear ridges that consist of pillow lava, pillow joint-block breccia, and/or vitriclastic deposits. Tindar result from sub-ice fissure eruptions and do not have capping subaerial sheet lava flows.

3) Subglacial mounds (SGMs) are conical structures consisting of pillow lava, pillow joint-block breccia, and/or hyalotuff and hyaloclastite (Hickson 2000). Subglacial mounds are the sub-ice expression of subaerial cinder cones and are lithologically identical to tindar. The term tindar commonly refers to both sub-ice fissure ridges and SGMs; however, their morphological variation warrants a nomenclatural distinction.

One or more sub-ice volcanoes may be termed M6berg ridges, M6berg formations, or M6berg mountains; however, the term M6berg is ambiguous because submarine volcanoes can also be termed M6berg mountains (Walker 1965). To avoid confusion, local formation names should replace the general M6berg term (Hickson 2000).

4) Hyaloclastite flows are a rare type of volcanic deposit that can form as voluminous basalt flows travel downslope in shallow marine (Bergh and Sigvaldason 1991) or subglacial environments (Walker and Blake 1966). Bergh and Sigvaldason (1991) used the term “flow” to describe a stratigraphic unit that contains a complex internal structure with strong evidence for flowage, striking uniformity between widely spaced outcrops, and unrelated deposits above and below. Berge and Sigvaldason (1991) used the term “hyaloclastite flow” to describe flow deposits consisting of a dense core of crystalline basalt with an autobrecciated carapace that contains abundant hyaloclastite. Berge and Sigvaldason (1991) distinguished hyaloclastite flows from pyroclastic flows because of their dense basaltic component, and from debris flows because they contain abundant evidence to support high temperature deposition.

The Standard Depositional Unit for hyaloclastite flows includes basal columnar-jointed basalt (C) overlain by cube-jointed basalt (K) and/or pillow lavas (P) and isolated pillow lavas (IBP) with a mantle of hyaloclastite breccia (Bergh and Sigvaldason 1991). Hyaloclastite breccias include four major types: 1) lobate basalt hyaloclastite breccia (LO);

2) isolated and broken pillow hyaloclastite breccia (BPH); 3) sideromelane shard hyaloclastite (SSH); and 4) bedded hyaloclastite (BH). Figure 2.1 summarizes the field characteristics and inferred flow mechanisms for the facies within the Standard Depositional Unit for hyaloclastite flows.

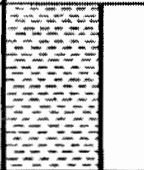
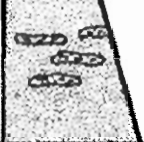




FACIES	COLUMN	FIELD CHARACTERISTICS	FLOW MECHANISM
BH		<ul style="list-style-type: none"> <li>- multiple normal graded beds</li> <li>- small- and large-scale crossbedding</li> <li>- relatively well sorted</li> <li>- alignment bedding</li> </ul>	Low-concentration turbulent suspension flow (turbidite)
SSH		<ul style="list-style-type: none"> <li>- high matrix-and shard content</li> <li>- extensive zeolitization (light color)</li> <li>- local basalt-segregations and fragmental flow layers</li> <li>- vesicular, concave-convex shaped particles</li> </ul>	High-concentration subaqueous granular mass flow
IBPH / LO		<ul style="list-style-type: none"> <li>- poorly sorted</li> <li>- internally structureless</li> <li>- matrix more than 20%</li> <li>- large basalt bodies (lobes) resting unsupported in the matrix</li> <li>- aligned and flow-folded basalt-injections</li> <li>- infill topographic depressions</li> <li>- rectilinear clast shapes</li> </ul>	
IPB / P		<ul style="list-style-type: none"> <li>- isolated pillows with less than 20% matrix</li> <li>- close-packed pillows and pillow tubes</li> <li>- circular and ellipsoid shapes</li> <li>- textural zoning</li> </ul>	
K		<ul style="list-style-type: none"> <li>- irregular jointing</li> <li>- compact lobes/rotated basalt slivers</li> <li>- fanning /rosette-shaped columns</li> </ul>	Coherent lava flow
C		<ul style="list-style-type: none"> <li>- regular columns</li> <li>- extensive</li> </ul>	

Figure 2.1: Hyaloclastite flow deposits. Summary of field characteristics and flow mechanisms for the facies within Standard Depositional Unit of hyaloclastite flow deposits (Bergh and Sigvaldason 1991).

Arnarþúfur deposits are similar to the bedded hyaloclastites (BH) of the Standard Depositional Unit for hyaloclastite flows. More in-depth discussion of bedded hyaloclastite flows is, therefore, warranted. Bedded hyaloclastite flows occur at the top of the Standard

Depositional Unit and contain prominent layering that includes alternating coarse- to fine-grained lapilli and tuff that form beds 0.1-2.0 m in thickness. Beds are normal- to reverse-graded and are laterally continuous for several hundred meters. Bedded hyaloclastite deposits commonly contain lower and upper divisions. Lower divisions include massive normal-graded hyaloclastite deposits with overlying deposits of laminated lapilli tuff that are 1 cm in thickness. Upper divisions include fine-grained hyaloclastite, small-scale ripples, and low-angle cross-beds that range from planar-tabular to undulatory. Bergh and Sigvaldason (1991) proposed two mechanisms for bedded hyaloclastite emplacement: 1) low-density turbulent flows moved downslope and deposited hyaloclastite from suspension after the main body of the deposit came to rest; and 2) a series of phreatomagmatic explosion pulses involving distal regions of the flow generated turbulent suspensions that deposited hyaloclastite.

In subglacial, environments hyaloclastite flows can travel great distances. For instance, Walker (1966) described a hyaloclastite flow, which he termed palagonite breccia mass, that travelled 22-35 km beneath a valley glacier in southeast Iceland. Walker (1966) proposed that jökulhlaups (glacier floods) may facilitate the passage of the lava beneath ice by creating subglacial channels prior to the emplacement of hyaloclastite flows.

5) Stratovolcanoes are complex structures that include lava flows and pyroclastic deposits. Although ice-contact volcanism may occur near the crater or on the flanks of stratovolcanoes, ice-contact deposits do not tend to dominate their morphological form (Smellie 2000; Lescinsky and Fink 2000).

6) Pseudocraters, also termed volcanic rootless cones, result from interactions between lava and near-surface water, including water-saturated sediments and ground-ice. Heat transfer from lava flows to underlying water can generate phreatomagmatic explosions that excavate lava and underlying sediments to form conical accumulations of ejecta on the

surface of the lava flow (Cas and Wright 1988; Lanagan *et al.* 2001; Geeley and Fagents 2001; Fagents *et al.* 2002). Pseudocrater deposits consist primarily of layered pyroclasts, spatter, lava fragments, and excavated sediments. In some instances, cone forming phreatomagmatic interactions involve water derived from underlying ice and, therefore, some pseudocraters represent a form of ice-contact volcanism. In contrast to the previously described forms of ice-contact volcanism, pseudocraters result from supra-ice volcanism rather than sub-ice volcanism.

### **2.3 Criteria for identifying sub-ice volcanoes**

Subglacial volcanoes initiate rapid melting of overlying ice and cause an englacial vault to form. Depending on the initial ice thickness and eruption duration, the englacial vault can develop into a lake. During subglacial eruptions, the bulk of volcanic material is emplaced within water. Smellie (2000) outlined the following criteria for distinguishing volcanoes that form in ice-contact settings from volcanoes that form in non-glacial environments, such as stable lakes, rivers, and marine environments: 1) the region in which a suspected sub-ice volcano is located must have a history of glaciation; 2) paleotopographic evidence must demonstrate that no barriers were capable of ponding water other than glacial ice during the time of the eruption; 3) *in situ* macrofossils and organic-rich soil horizons are absent within sub-ice volcano formations; 4) in the volcanic sequence itself, subaerially erupted lava and tephra draping subaqueous deposits from the same eruption is typically indicative of water-emergent volcanism, however, transition from a subaqueous to subaerial deposits within a volcanic succession does not necessarily imply ice-contact; 5) outcrop-wide erosion surfaces formed by wave action are absent; and 6) sedimentary structures indicative of fluvial or shallow water environments, such as well-rounded clasts, ripple marks, imbrication,

hummocky cross-stratification, etc., are typically absent within protected environments such as englacial vaults or lakes. The presence of fluvial sedimentary structures, however, does not exclude the possibility of ice-contact volcanism because water draining beneath a glacier or ice sheet may produce rounded clasts and flow deposits. Additionally, Smellie (2000) stated that during subglacial eruptions, ice-retaining walls confine volcanoclastic sediments and cause beds to dip toward the vent. Volcanoes with steep-sloped sides and vent-dipping beds are characteristic of ice-confinement during emplacement.

## **2.4 The passage zone**

In water-emergent volcanoes, the boundary between subaqueously deposited flow-foot breccia (mixed hyaloclastite and flow-foot breccia) and subaerial sheet lavas, termed the passage zone, corresponds to the water-level surrounding a volcanic pile at the time of emplacement (Jones 1969). The elevation of the passage zone can change throughout an eruption depending on the relative motion between the volcanic pile and surrounding water (Jones and Nelson 1970). Dramatic or erratic changes in passage zone elevation are diagnostic of a volcano emplacement within an englacial lake because rapid water-level fluctuations are not possible within marine or stable lake environments. Erosion, mantling by scree slopes, and possible overprinting by successive eruptions issuing from a particular volcanic center can, however, obscure changes in passage zone elevation and complicate interpretations of water-level fluctuations.

The structural expression of the water-air interface within volcanic successions merits further discussion because of its potential for distinguishing ice-contact volcanoes from volcanoes formed in marine and stable lake environments. When a volcano emerges from a water body, the volcanic conduit and vent soon become disconnected from the surrounding

water. A restricted water supply lowers the water-to-melt ratio and causes the style of eruption to change from Surtseyan to Strombolian or Hawaiian. A change from hyalotuff production to lava effusion accompanies this change in eruption style.

When a subaerial lava flow encounters water, the surface of the lava quenches into fine-grained glass fragments, termed hyaloclastite. Continued effusion of lava into water may cause pillow lavas to form. Rapid cooling of the pillows causes them to fragment into joint-block breccia that mixes with the hyaloclastite to form flow-foot breccia. Flow-foot breccia at the front of the advancing lava flow is prone to gravitational instability and forms a prograding delta with a surface slope of 30-40° (Jones 1969; Jones and Nelson 1970). The passage zone, between the upper surface of the flow-foot breccia delta and base of the subaerial sheet lavas, corresponds to the water level at the time of lava flow emplacement (Jones 1969; Figure 2.2).

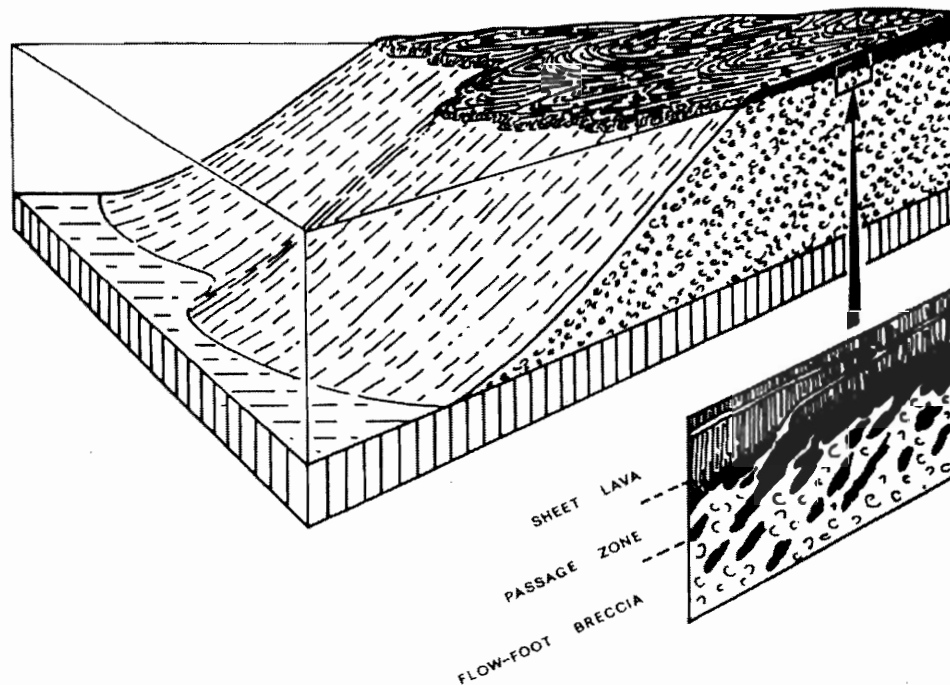


Figure 2.2: The passage zone. When a basalt lava flow enters water, it fragments to form mixed hyaloclastite and breccia deposits, termed flow-foot breccia. The water level at the time of lava flow emplacement corresponds to the passage zone, a narrow region between the flow-foot breccia and subaerial sheet lavas (Jones 1969; Jones and Nelson 1970).

Changes in the elevation of the passage zone result from either vertical movements of the surrounding water or the volcanic pile (Figure 2.3). For instance, drainage of a meltwater lake can lower the lake level, whereas increased melting rates or a decrease in meltwater flux through the subglacial drainage system can raise the lake level. Subsidence or inflation of the volcano can similarly affect the elevation of the passage zone.

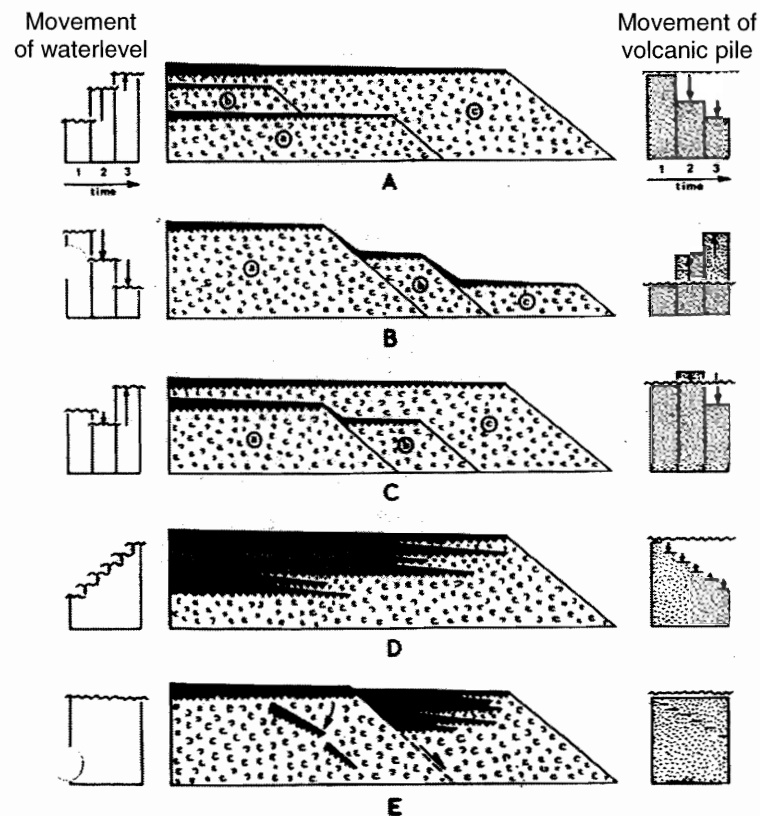


Figure 2.2: Changes in passage zone elevation. Schematic diagrams illustrating the structural relationships formed by successive lava flows entering water where vertical motions of the water level relative to the volcanic pile have occurred. Solid black represents subaerial sheet lava. Lunate ornament represents flow-foot breccia (Jones and Nelson 1970).

Although lake and marine levels are typically constant over the duration of a single eruption, tides can have an effect on the height of the passage zone in marine environments. In ice-dammed lakes, rapid water level fluctuations of several hundred meters are possible (Paterson 1994; Skilling 1994) and are consistent with observed displacements of passage



zones elevations within water-emergent ice-contact volcanoes (Jones and Nelson 1970, Skilling 1994; Smellie and Skilling 1994; Smellie 2000). Repeated changes in water level relating to drainage and subsequent refilling of unstable englacial lakes can produce complex structural relationships that are diagnostic of volcano emplacement within an ice-dammed lake. The difference between the maximum passage zone level and surrounding bedrock elevation provides a minimum estimate of the local ice thickness during volcano emplacement; however, the maximum thickness of the surrounding glacier cannot be determined using this method.

## **2.5 Ice-contact lithofacies and structural relationships**

Sub-ice volcanic lithofacies include vitriclastic sediments and crystalline lavas. To understand the processes involved in the formation of ice-contact volcanoes requires detailed examination of these lithofacies and their structural expression.

Phreatomagmatic interactions typically produce large quantities of sideromelane, a reddish to brown glass, which occurs in two principal forms: hyaloclastite and hyalotuff. Hyaloclastite and hyalotuff differ in size and shape and represent two distinct forms of phreatomagmatic interaction. Hyaloclastite forms by non-explosive cooling-contraction granulation, whereas hyalotuff forms by explosive Molten Fuel-Coolant Interactions (Chapter 3). Hyaloclastite is typically coarser grained than hyalotuff and has angular to blocky grains with low vesicle content (<25% by volume) and convex grain perimeters greater than 20% (Skilling 1994). Hyalotuff consists of vesicular shards (>25% vesicles by volume) with broken vesicle margins with convex perimeters less than 20% (Skilling 1994). In the field, discrimination between hyaloclastite and hyalotuff is nearly impossible, and many researchers have abandoned the distinction in favour of using hyaloclastite in a more

descriptive sense to represent both grain morphologies. Hyaloclastite forms primarily by spalling of glass fragments from the quenched lava surfaces. Hyaloclastite includes blocky, fusiform, moss-like, platy, spherical, and drop-like fragment varieties (Wholetz 1983; Cas and Wright 1988; Morrissey *et al* 2000). Sideromelane readily weathers by hydration and oxidation to yellowish-brown to reddish-brown palagonite (Allen *et al.* 1981; Cas and Wright 1988), which imparts a characteristic brown colour to most ice-contact volcanoes.

The following summary describes volcano lithofacies identified within two sub-ice volcanoes in Antarctica: Mount Pinafore on Alexander Island, and Brown Bluff in Graham Land (Smellie and Skilling 1994; Skilling 1994). This classification is generally consistent with the lithofacies identified in other locations in Antarctica (Smellie 2000), Iceland (Walker 1965; Jones 1969, 1969, 1970; Jones and Nelson 1970; Furnes *et al.* 1980; Allen *et al.* 1981, 1982; Bourgeois *et al.* 1998; Werner and Schmincke 1999; Smellie 2000; Skilling 2002; Guðmundsson 2001; Guðmundsson *et al.* 1997, 2002), northern British Columbia (Mathews 1947; Allen *et al.* 1982; Hickson 2000), and in the state of Washington (Lescinsky and Fink 2000). Skilling (1994) identified the following ice-contact lithofacies: 1) pillow lava; 2) cobble, gravelly, and sandy varieties of hyaloclastite; 3) hyalotuff; 4) sandstone; 5) conglomerate; 6) pillow-joint block breccia; and 7) subaerial lava.

1) Pillow lava units consist of complete pillow lavas with interpillow tuff, internal cavities, and massive beds <1 m to 30 m thick. Pillow lavas form by intrusion into open water, water-saturated sediments, and earlier pillow lavas (Skilling 1994).

2) Cobble hyaloclastite units have indistinct planar stratification with dips of 15-30°, medium sand to gravel matrix comprising 10-30% of the deposit and polymictic gravel to cobble clasts that may include fragmented pillow lava. Cobble hyaloclastite units are poorly sorted, and range in thickness from <1 m to 20 m. Cobble hyaloclastite deposits can result

from density-modified grain flow on the slopes of hyaloclastite deltas or by post-depositional slumping of unconsolidated hyaloclastite deltas. Cobble hyaloclastite tends to form when the lava extrusion rate or volume is high. Gravelly hyaloclastite units contain monomictic grains ranging in size from sand to gravel. Gravelly hyaloclastite deposits form <1 cm to 1.5 m thick beds that are generally ungraded and poorly to moderately sorted. Gravelly hyaloclastite deposits result from density-modified grain flow on delta foresets when lava extrusion rates or volumes are low. Sandy hyaloclastite units are located down dip from conglomerate and gravelly hyaloclastite deposits. Sandy hyaloclastite deposits are generally <1 m thick, consist of silt to medium or coarse sand grains that are monomictic, well sorted, and ungraded to normally graded. Sandy hyaloclastite deposits may contain indistinct planar laminated drapes or ripple structures, cross beds, and water escape structures. Sandy hyaloclastite deposits form by gravitational collapse of hyaloclastite deltas and, in some instances, are associated with low-density turbidity currents.

3) Hyalotuff is generally similar in appearance to hyaloclastite and is difficult to distinguish in the field. Hyalotuff units, however, form by explosive subaqueous eruption and subsequent sedimentation. Depositional mechanisms for hyalotuff units include subaqueous fall, density-modified grain flow, and turbidity currents, all of which may contain subaqueously erupted sideromelane fragments and/or subaerial pyroclasts.

4) Sandstone units include two types: subaqueous fall deposits and turbidites. Subaqueous fall deposits drape the underlying topography in <0.75 m thick beds that may exhibit indistinct planar laminated layers with well-sorted silt to coarse sand-sized grains. Turbidite deposits contain planar and ripple cross-laminated beds that are <1 m thick and exhibit normal grading. The grains are generally monomictic and range in size from silt to

medium sand. The first type of sandstone forms by suspension and sedimentation of airfall tephra, whereas the second type forms in association with low-density turbidity currents.

5) Sandy conglomerate is prevalent within ice-contact deposits. Conglomerate deposits are either matrix- or clast-supported and are typically massive, poorly-sorted, and hydrothermally altered. Conglomerate deposits form by gravitational collapse of lithified vent proximal facies. Conglomerate deposits commonly occur as irregular bodies on the foreset slopes of hyaloclastite deltas. Conglomerate units are generally <1 m-15 m thick.

6) Pillow joint-block breccia units have blocky to hackly jointing with areas of curved entablature, incipient marginal pillowing, and form beds <1 m-10 m thick. Pillow joint-block breccias are water-cooled lava flows that typically form at the brink of hyaloclastite deltas.

7) Subaerial lavas are typically compound pahoehoe flows with reddened surfaces that form units <1 m to 10 m thick. Subaerial lava flows overlie flow-foot breccia deposits that consist of hyaloclastite and crystalline lava fragments.

The ice-contact lithofacies listed above represent four evolutionary phases: 1) initial ice melting and basal pillow lava emplacement, 2) explosive melt-water interaction and hyalotuff cone formation, 3) episodic slope failure, and 4) hyaloclastite delta formation and subaerial lava emplacement (Skilling 1994). Tuyas represent complete sub-ice volcano sequences, whereas tindar and SGMs represent incomplete sequences that fail to emerge from the surrounding meltwater and do not develop subaerial lava flows (Figure 2.4). A given ice-contact structure may, or may not, have a basal pillow lava unit depending on the confining ice thickness and hydrostatic pressure at the time of formation. Cycles of meltwater drainage and accumulation may cause repetition of evolutionary phases and slope failure can rework deposits and produce complex stratigraphic relationships within the volcanic structure.

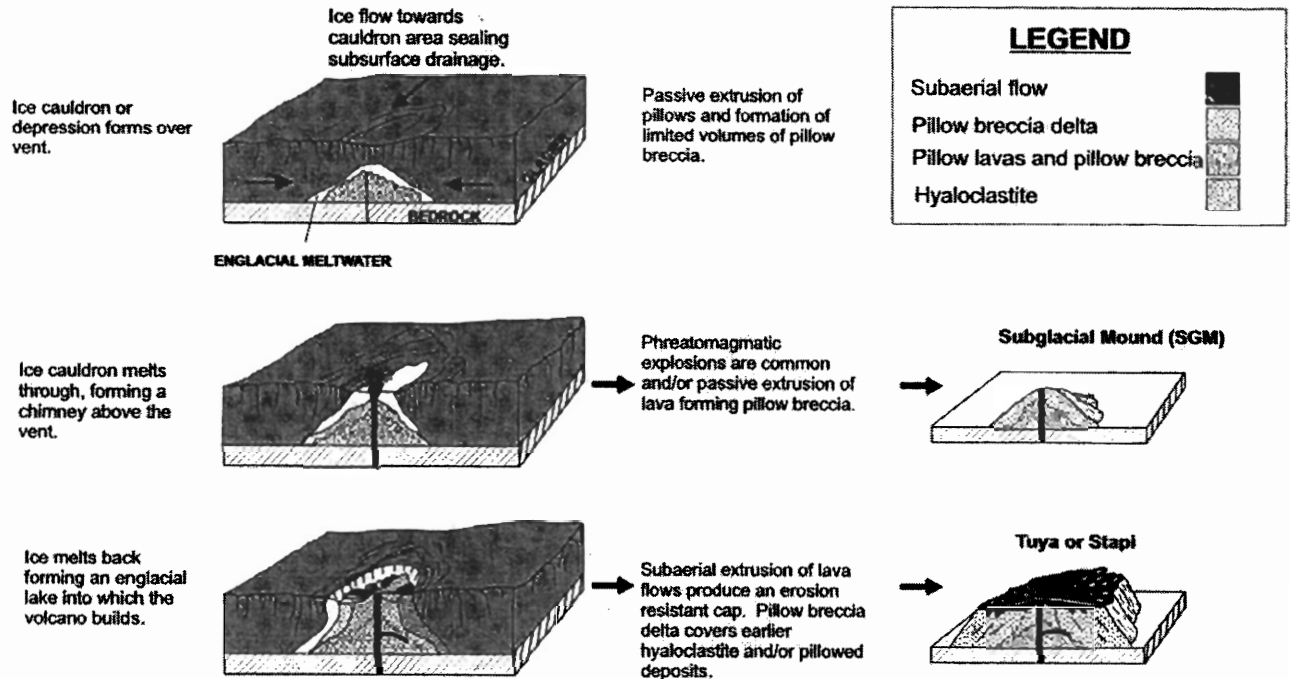


Figure 2.4: Schematic model of sub-ice volcano formation. Schematic diagram illustrating the stages in the development of subglacial mounds (analogous to tindar formation) and monogenetic tuya (Hickson 2000 adapted from Jones 1969, 1970). Top: initial ice melting and basal pillow lava emplacement. Middle: explosive melt-water interaction and hyalotuff cone formation. Bottom: hyaloclastite delta formation and subaerial lava emplacement. Phases of episodic slope failure are not shown.

## 2.6 Thick and thin ice cases for sub-ice volcano evolution

The general progression from basal pillow lava formation through the explosive hyalotuff stage and into the hyaloclastite delta and subaerial phases depends on the availability of magma and environmental conditions such as ice thickness, bedrock topography, and water drainage. The two basic evolutionary models for sub-ice volcanoes are the thin ice and thick ice scenarios. Volcanic eruptions on the steep flanks of stratovolcanoes differ substantially from eruptions beneath ice caps and ice sheets and frequently result in pyroclastic surges or flows (Guðmundsson 2001; Lescinsky and Fink 2000). Detailed discussion of sub-ice eruptions associated with stratovolcanoes is beyond the scope of this review.

Thin ice refers to ice less than 200 m in thickness. In the thin ice case, ice is dominantly in the brittle regime and ice deformation rates are low (Guðmundsson 2001). In the thin ice case, ductile ice flow cannot balance ice-melt. Penetration of the ice causes rapid loss of thermal energy to the atmosphere. When volcanic eruptions occur beneath thin ice, melting is largely confined to the vent area and the total volume of meltwater is smaller than for equivalent eruptions beneath thick ice (Figure 2.5). Vitriclastic sediments dominate volcanic deposits formed under thin ice conditions and pillow lavas are typically absent (Guðmundsson 2001). Examples of volcanic eruptions beneath thin-ice include all 20<sup>th</sup> Century eruptions at Grímsvötn, Iceland (Guðmundsson and Björnsson 1991; Guðmundsson 2001).

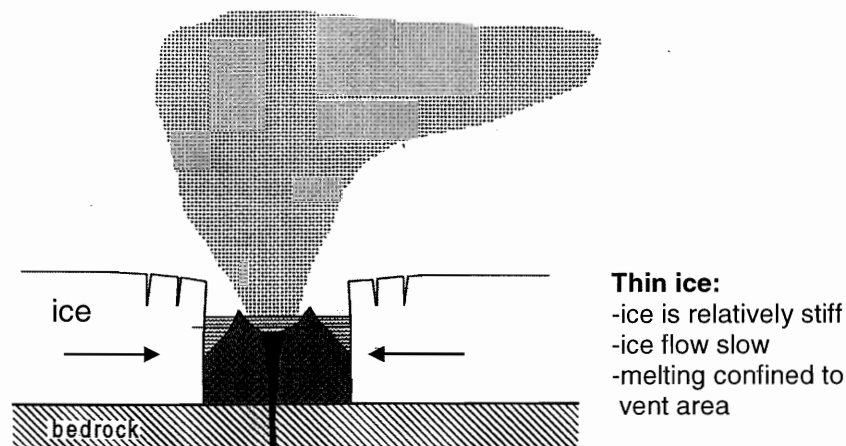


Figure 2.5: Thin ice case. Schematic diagram illustrating the characteristics of a volcanic eruption beneath ice that is less than 200 m in thickness (Guðmundsson 2001).

In the thick-ice case, volcanic eruptions occur beneath several hundred meters of ice and removal of ice from the bottom of the glacier by melting and subsequent drainage generates large stresses and high deformation rates in the overlying ice (Guðmundsson 2001). Ductile ice flow largely compensates for the loss of ice volume near the volcanic vent and delays penetration of the ice (Guðmundsson 2001). Ductile ice flow enhances ice melting by continuously transporting new ice to the melt region. Replenishment of melted ice confines

the erupted material and affects the morphology of the volcano (Figure 2.6). Volcanic eruptions beneath thick ice generally produce steep-sided deposits with well-developed basal pillow lava units that grade into pillow joint-block breccia and vitriclastic deposits (Guðmundsson 2001). The 1996 and 1998 Gjálp eruptions beneath Vatnajökull are examples of volcanism under thick-ice conditions (Björnsson *et al.* 2001; Guðmundsson *et al.* 1997, 2002).

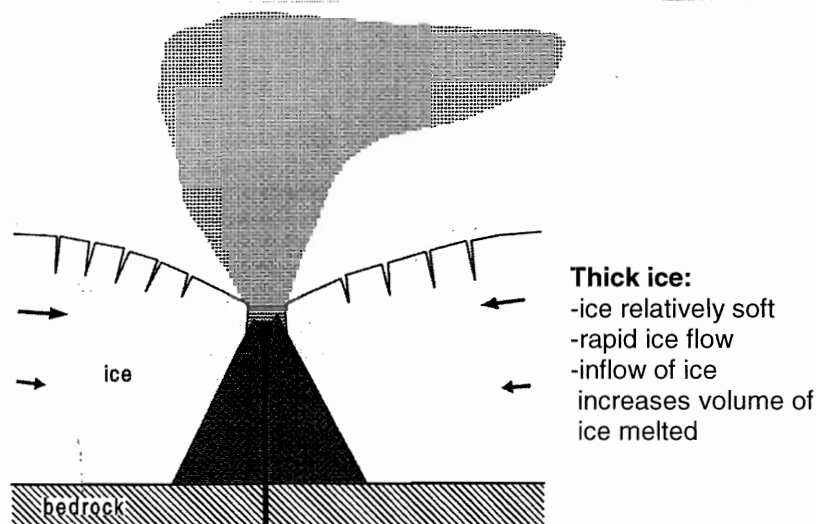


Figure 2.6: Thick ice case. Schematic diagram of a volcanic eruption beneath ice that is much greater than 200 m in thickness (Guðmundsson 2001).

## 2.7 Gjálp, Iceland

Subglacial eruptions occur when magma extrudes from a volcanic vent beneath a valley glacier or ice sheet (Smellie, 2000). Subglacial eruptions typically generate large volumes meltwater, and can either be explosive or non-explosive depending upon the confining pressure exerted by the overlying ice. Subglacial eruptions produce some structures that are nearly indistinguishable from nonglacial subaqueous eruptions; however, subglacial edifices have a diagnostic sequence of volcanic structures. The sequence of volcanic structures largely depends upon the thickness of the overlying ice and the volume of magma extruded.

The 1996 Gjálp eruption is a well-documented example of a modern subglacial eruption originating beneath thick ice. The 1996 Gjálp eruption, named after a Giantess in

Nordic mythology, provides information about ice melting rates during a subglacial eruption, drainage of meltwater from eruption sites, formation and morphology of hyaloclastite ridges, and mechanisms that preserve subglacial volcanic deposits.

The 1996 Gjalp eruption occurred near the central region of the temperate ice cap Vatnajökull, southeast Iceland (Figure 2.7). The eruption site was located between the central volcanoes of Grímsvötn and Bárðarbunga. A minor subglacial eruption may have also taken place on the southeast corner of Bárðarbunga at the same time as the Gjalp eruption because two shallow depressions formed in the ice surface there (Guðmundsson *et al.* 2002). The pre-eruption ice thickness was 550-750 m.

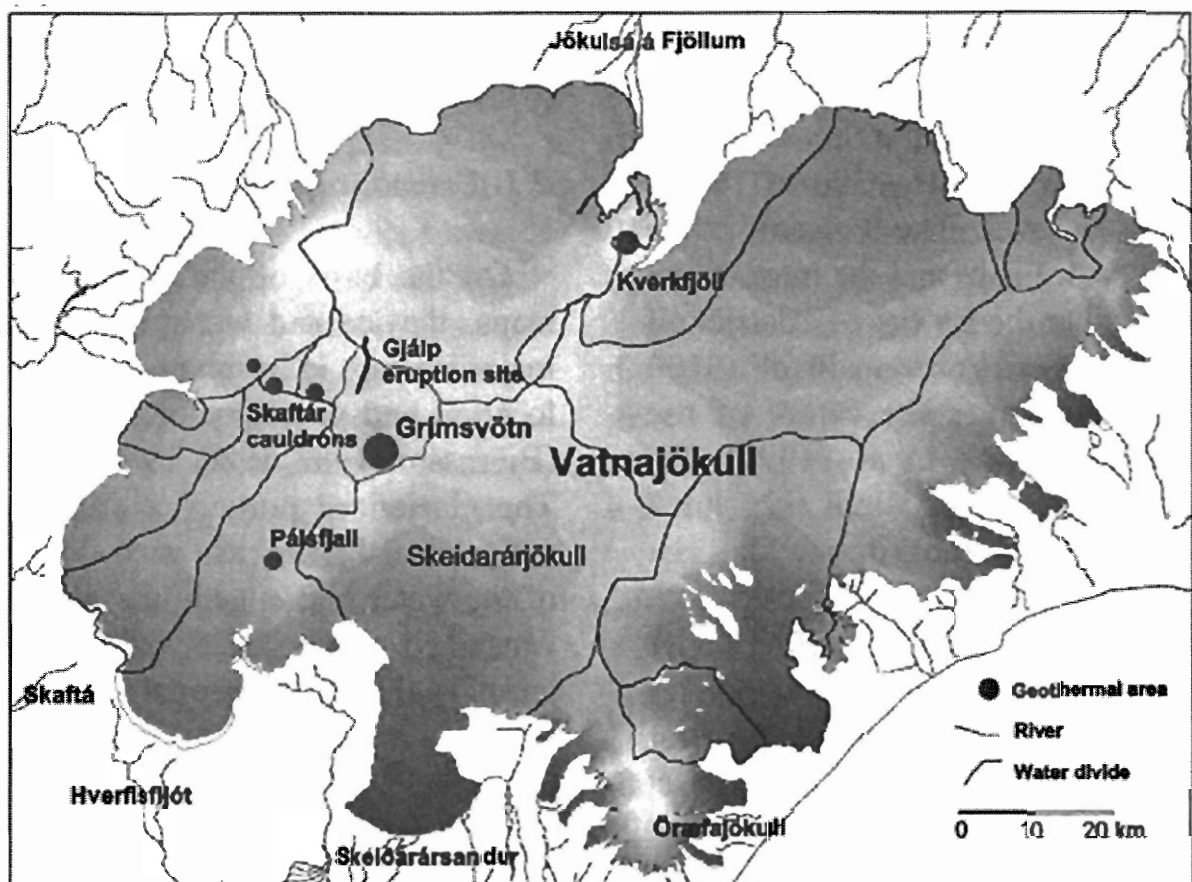


Figure 2.7: Gjalp location map. The 1996 Gjalp occurred near the central region of Vatnajökull, southeast Iceland. Meltwater from the eruption initially flowed south to Grímsvötn (Björnsson 2002).



On September 29, 1996, a 5.4 magnitude earthquake occurred at Bárðarbunga. The start of the eruption was marked by the onset of continuous tremors at approximately 22 hours GMT on September 30, 1996. The following morning two depressions in the ice surface, known as cauldrons, were observed from the air and, after 16 hours of eruption, the cauldrons were ~2 km wide and ~100 m deep (Guðmundsson 1997). The ice cauldrons enlarged as the meltwater drained along the glacial bed and into the subglacial Grímsvötn caldera (Figure 5.9), which contains a subglacial lake sustained by geothermal activity (Guðmundsson 1997). Pressure exerted on Gjálp meltwater by overlying ice forced the water over the rim of the Grímsvötn caldera. A shallow linear depression on the ice surface between the Gjálp eruption site and the Grímsvötn lake corresponded to the underlying meltwater flow path.

After 31 hours, the eruption broke through the ice surface and became a Surtseyan type with characteristic subaerial explosive phreatomagmatic activity. The elevation of the eruption column was typically 4-5 km; however, on October 3 the eruption column reached a maximum height of 9 km (Guðmundsson 1997). The onset of Surtseyan volcanic activity coincided with the collapse of an ice block 200-300 m in diameter into the underlying eruptive vent and the formation of a 50-100 m high chimney through the ice. For twelve days, the duration of the subaerial phase, no significant widening of the chimney took place because the rate of ice inflow balanced the rate of ice melting. During the second day of the eruption, a new cauldron developed to the north of the first one, suggesting that the eruptive fissure had lengthened to 6 km. The intensity of the eruption diminished after the first four days and ended on October 13.

During the first four days the average melting rate during was  $5000 \text{ m}^3 \cdot \text{s}^{-1}$  and by the end of the eruption  $3 \text{ km}^3$  of ice had melted (Guðmundsson *et al.* 2002). The meltwater

accumulated in the Grímsvötn caldera, and on November 5, three weeks after the end of the eruption, the water suddenly drained from Grímsvötn in a glacial outburst flood, termed a jökulhlaup. The temperature of the meltwater was 15-20 °C, and it caused considerable ice melting as it flowed south and enlarged the existing subglacial tunnel system. The jökulhlaup drained 3.6 km<sup>3</sup> of water to Skeiðarásandur and had a peak discharge of  $40\text{-}50 \times 10^3 \text{ m}^3 \cdot \text{s}^{-1}$  at midnight on November 5. The first flood wave drained into Skeiðará, but within a few hours water flowed from numerous outlets along the entire southern perimeter of Skeiðarájökull (Figure 2.8).

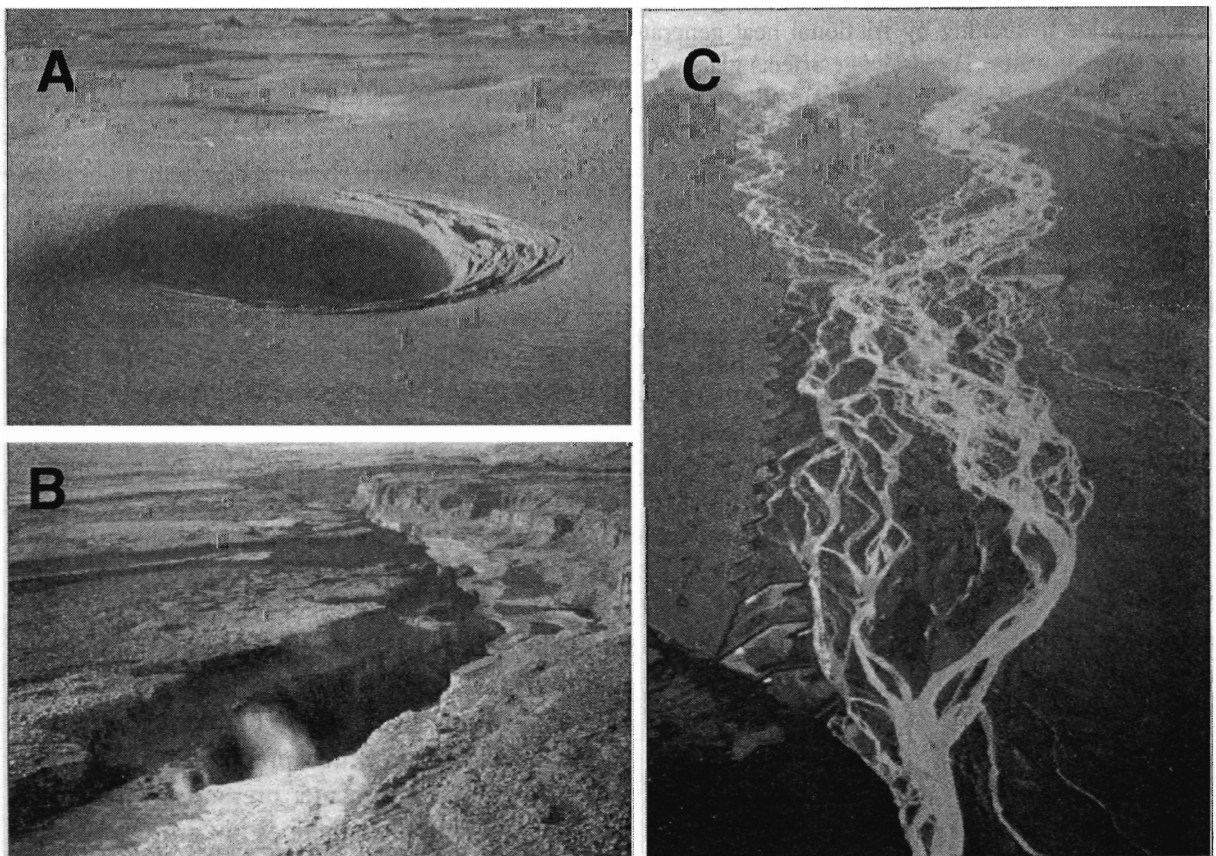


Figure 2.8: Photographs of the 1996 Gjalp eruption. A: ice-cauldrons above Gjalp during the early phases of the eruption. B: meltwater draining south Gjalp flowed in an open channel before entering a subglacial tunnel system *en route* to Grímsvötn. C: A jökulhlaup from meltwater dammed in Grímsvötn drains onto the Skeiðarásandur (Björnsson 2002).

The jökulhlaup travelled  $\sim 10 \text{ km} \cdot \text{hour}^{-1}$  and caused intense erosion and sedimentation. Jökulhlaup sediments consisted exclusively of materials eroded downstream from Grímsvötn. Volcaniclastic sediments from Gjálp must, therefore, have been deposited *en route* to and within the Grímsvötn caldera. During the year following the 1996 Gjálp eruption, extensive fields of kettle holes formed in jökulhlaup deposits where partially buried ice blocks, some of which were up to 2000 tonnes, melted.

A crevassed subsidence structure at the eruption site widened from 4 to 7 km in the three months after the eruption and reached a maximum width of 8 km in June 1997. Otherwise the surface of Vatnajökull remained intact, suggesting that the effects of eruptions within temperate glaciers are localized and do not trigger widespread basal sliding.

The pre-eruption topography of the Gjálp eruption site included mounds and short ridges with a relief of 100-200 m, rising from a plateau 950-1100 m above sea level. (Guðmundsson *et al.* 2002). The pre-eruption ice-thickness was 550-750 m. The Gjálp ridge is 6 km long and has a volume of  $0.70 \text{ km}^3 \pm 0.15 \text{ km}^3$ . The ridge is highly porous with a density ranging from 1500 to 2300  $\text{kg} \cdot \text{m}^{-3}$  (Guðmundsson *et al.* 2002). The magma erupted was basaltic andesite with an eruption temperature of  $1090 \pm 50 \text{ }^\circ\text{C}$  and density of  $2700 \text{ kg} \cdot \text{m}^{-3}$ . During the eruption and the following six weeks,  $\sim 4.0 \text{ km}^3$  of ice melted, requiring the extrusion of  $\sim 0.4 \text{ km}^3$  of magma (Guðmundsson *et al.* 1997).

During the Gjálp eruption, volcanic deposits piled against confining ice walls to produce a steep-sloped hyaloclastite ridge with lateral dimensions that are truncated relative to structures of a similar volume that form in unconfined aqueous environments. The southern and central parts the ridge are steep with slopes of  $30\text{-}35^\circ$  (Guðmundsson *et al.* 2002). The relief in the southern part is of 200-250 m and rises steeply to 400-450 m in the central part (1500-1550 m above sea level). The width in the southern section is  $\sim 500$  m and

in the central section, the width of the deposit is ~1000 m. In the northern section, the height of the deposit is 1150-1200 m and the width is ~2 km. The edifice extends 1.5 km west of the fissure, resulting in a distinct asymmetry in the northern part of the ridge with respect to the fissure axis. Variations in basal water pressure may explain differences in edifice form along the fissure. Partial floating of the overlying ice in the northern part is likely to have resulted from high basal water pressures. As the ice was lifted, confining pressures would have been reduced, thereby allowing lateral spreading of the volcanic deposits (Guðmundsson *et al.* 2002).

The volume of the volcanic pile increased from approximately 0 to 0.4 km<sup>3</sup> in the first three days, and then from 0.4 to 0.7 km<sup>3</sup> in the next ten days (Guðmundsson *et al.* 1997). Aerially dispersed tephra amounted to ~0.01 km<sup>3</sup> and accounts for 1-2% of the total volume erupted material. The existence of sediments accumulated in Grímsvötn is based on geophysical surveying before and after the eruption (Guðmundsson 2001). The volume of sediments is ~0.07 km<sup>3</sup>, which is equivalent to ~10% of the total volume erupted. The total volume of erupted material is, therefore, ~0.78 km<sup>3</sup>.

Gravity profiling conducted in 1997, 1998, and 2000 revealed considerable variations in density along the ridge (Guðmundsson *et al.* 2002). The low density of the southern and central deposits, 1900 km<sup>3</sup> · m<sup>-3</sup> and 1500-1600 km<sup>3</sup> · m<sup>-3</sup>, respectively, implies that pillow lavas are not the dominant rock type within the deposit because pillow lavas typically have a density of 2300-2400 km<sup>3</sup> · m<sup>-3</sup>. Basal pillow lavas could, however, account for up to 10% of the total volume in the southern and central portions of the Gjálp ridge. In the northern part of the ridge, the mean density is 1900 km<sup>3</sup> · m<sup>-3</sup>, consistent with a structure containing a large proportion of pillow lavas. The minimum estimate is, therefore, that no pillows exist within the Gjálp ridge and the maximum estimate is that the structure is ~33% pillow lavas.

Cooling of pillow lavas alone cannot explain the high heat transfer rates associated with the 1996 Gjálp eruption ( $3 \times 10^5 \text{ W} \cdot \text{m}^{-2}$ ) because the time required for pillows to solidify is at least one order of magnitude too great to account for the observed energy flux (Guðmundsson *et al.* 1997). The observed energy flux can be explained by the quenching and fragmentation of magma into glass combined with highly turbulent convection of meltwater mixed with quenched glass and ash. The majority of the ridge must, therefore, be composed of hyaloclastite rather than crystalline rocks.

The 1996 Gjálp consists primarily of unconsolidated volcanic glass fragments and tephra that are easily affected by subglacial erosion. Alteration of unconsolidated hyaloclastite into palagonite, and the uniform convergence of ice into the ice cauldron that overlies the volcanic pile, helps to preserve the Gjálp hyaloclastite ridge (Guðmundsson *et al.* 2002). The rate of hyaloclastite alteration in the subglacial environment is unknown; however, under subaerial conditions in Surtsey (1963-67), basaltic tephra was palagonitized into dense tuff within 1-2 years when subjected to mild hydrothermal activity at 80-100 °C. At Gjálp, subglacial melting continued from the onset of the eruption on September 29, 1996 into 1999, indicating that high temperatures in at least parts of the edifice could have contributed rapid rates of palagonitization. Shielding from regional ice flow for several years during the infilling of englacial vault and overlying depressions in the ice may be an important factor in preserving many subglacial formations.

## **2.8 Brown Bluff, Antarctica**

Brown Bluff is a water-emergent volcano that is a part of the James Ross Island Volcanic Group (JRIVG), located on the Tabarin Peninsula, Antarctica (Figure 2.9). The southern half of Brown Bluff is ice-covered, whereas the northern half is well-exposed and outcrops in five

corries (cirques) with a total exposed thickness of 400 m and an area of 4 km<sup>2</sup> (Skilling 1994). Brown Bluff is 1 Ma in age and was erupted in a back-arc setting associated with subduction along the western margin of the Antarctic Peninsula (Skilling 1994). Baker *et al.* (1973) proposed a submarine origin for hyaloclastite deposits within the JRIVG based on a general sequence progressing from deep-water hyaloclastite and palagonite tuffs to shallow-water pyroclastic rocks, followed by subaerial lava flows and scoria, all of which were subsequently uplifted by >400 m since the end of the Pliocene. González-Ferrán (1982) supported the model proposed by Baker *et al.* (1973), and suggested that the present scattered outcrops of the JRIVG represent relics of an extensive basaltic plateau.

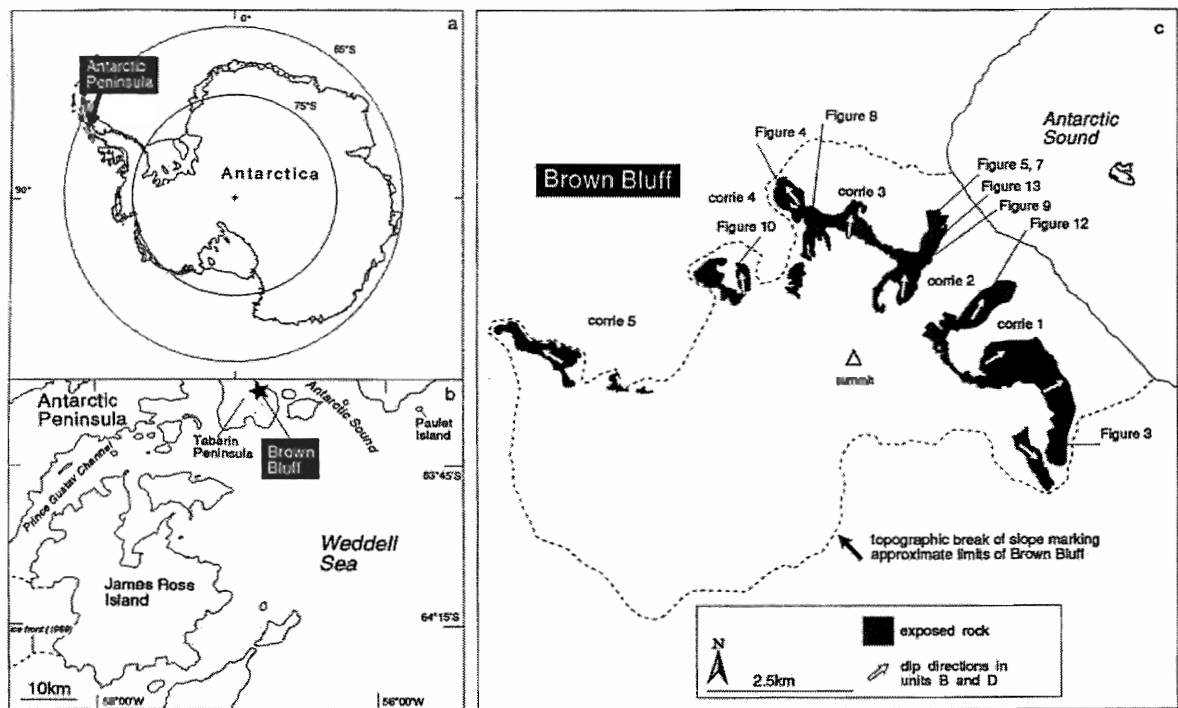


Figure 2.9: Brown Bluff location map. Regional setting of Brown Bluff with corrie locations (Skilling 1994).

Smellie and Skilling (1994) presented an alternative view stating that the late Cenozoic scattered volcanic sequences on the Antarctic Peninsula are subglacially erupted,

and that Brown Bluff is a water-emergent volcano of subglacial origin formed during the Pleistocene in an englacial meltwater lake enclosed by >400 m thickness of ice. The basis of their interpretation consists of detailed structural investigations of Brown Bluff and Mount Pinafore, Alexander Island, and comparison of these structures with other subglacial volcanoes in Iceland, Canada, and Antarctica. Skilling (1994) identified seventeen distinct lithofacies comprising five structural units (A-E; Figure 2.10). Skilling (1994) divided the evolution of Brown Bluff into the following chronological stages: pillow volcano (Unit A), hyalotuff cone (Units B and D), slope failure (Unit C), and hyaloclastite delta formation with superincumbent subaerial lava flows (Unit E).

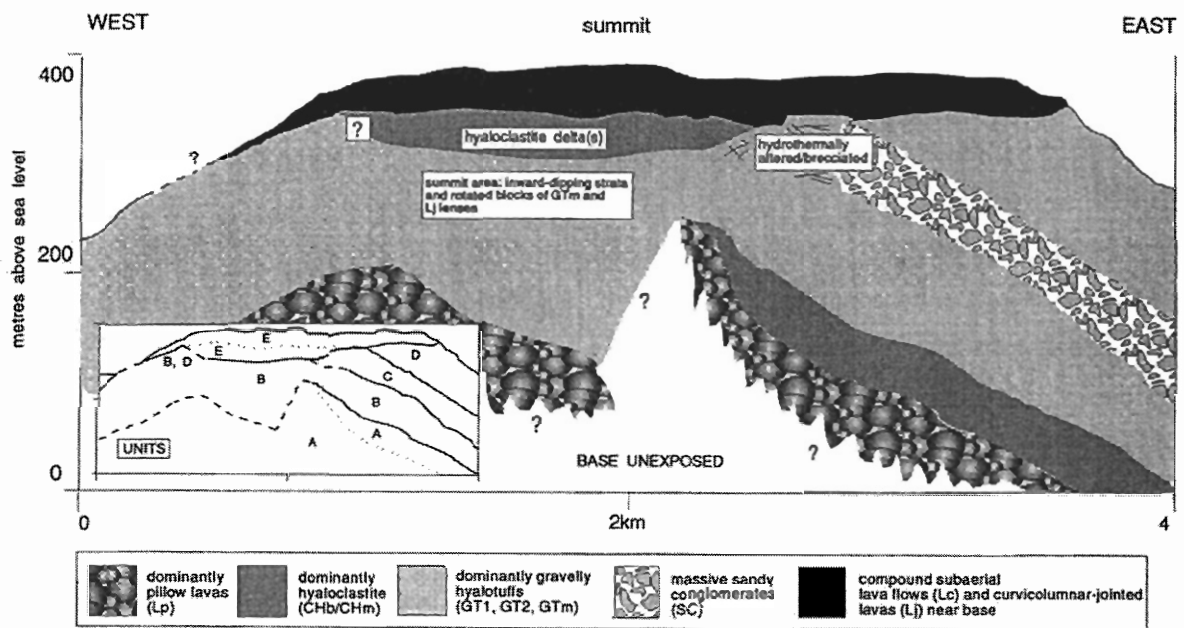


Figure 2.10: Brown Bluff, Antarctica. Simplified composite cross-section of Brown Bluff illustrating the relative positions of principal lithofacies (Skilling 1994).

Smellie and Skilling (1994) offered four lines of evidence to support subglacial origin of Brown Bluff. Debris avalanche deposits in Unit C juxtaposed with subaerial lavas and hyalotuffs in corrie 4 imply at least two episodes of drainage, with a minimum drawdown of

100 m in each case. Water fluctuations of this magnitude could not occur in an ocean or non-glacial lake, over the time scale of emplacement. The presence of interbedded water-cooled lavas and subaqueous tuffs in Unit D similarly represents rapid water level fluctuations. Paleo-topography that could confine a former non-glacial lake is absent. The structural sequence of Brown Bluff is similar to subglacial volcanic edifices in other parts of the world. Seismic stratigraphy of continental shelf sediments provides evidence that large-scale ice-sheet fluctuations affected the JRIVG region during the last 6 Ma.

The proposed subglacial origin for Brown Bluff (Smellie and Skilling 1994; Skilling 1994) challenges pre-existing theories of volcanic emplacement within the JRIVG, and provides valuable information about paleo-environmental conditions on the Antarctic Peninsula during the Cenozoic. This example highlights the importance of thorough lithostratigraphic analysis of volcanic landforms to ensure accurate paleo-environmental interpretation.

## **2.9 Paleo-environmental reconstructions using ice-contact volcanoes**

An understanding of ice-contact lithofacies, structural relationships, and models of sub-ice volcano formation makes possible an examination of the applicability of ice-contact volcanism for paleo-environmental reconstructions. Walker (1965) considered the distribution and heights of Móberg formations in the Neovolcanic Zone of northern Iceland and noticed a general increase in the height of these structures towards the present Vatnajökull ice cap. He believed that the elevation of these mountains correlated with the thickness of the Pleistocene ice sheet, and asserted that the former ice thickness was approximately equal to the summit of the Móberg formations (Figure 2.11).



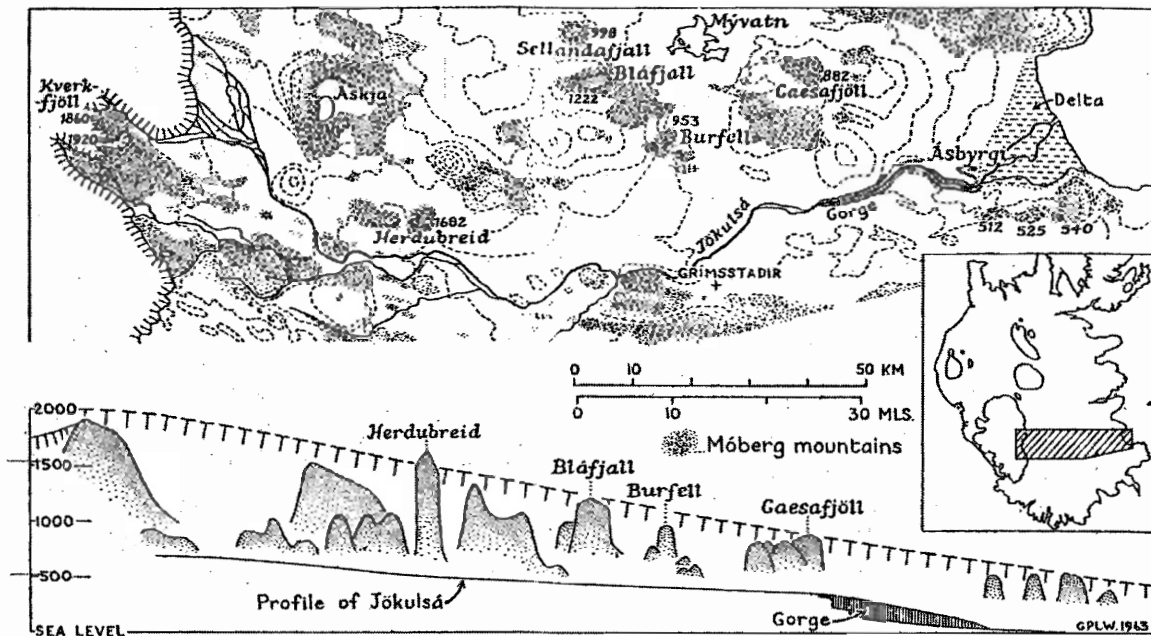


Figure 2.11: Reconstruction of Pleistocene ice thickness in northern Iceland. Palagonite tuff-breccia mountains (Móberg Formations) in part of northern Iceland exhibit a systematic decrease in their elevation from the south to north and may be related to the profile of the Pleistocene ice sheet (Walker 1965).

Walker's (1965) paleo-ice thickness reconstruction raises an intriguing possibility that groups of ice-contact volcanoes can be used to infer regional ice thickness and patterns of glaciation. Walker (1965) emphasized the importance of distinguishing between Móberg formations that form in englacial and marine environments and assumed that the thickness of the Pleistocene ice sheet was approximately equivalent to the peaks of the highest Móberg formations. Extrapolation of ice-contact relationships from local to regional scales can, however, be problematic. Nevertheless, with sufficient lithostratigraphic and chronological data, it may be possible to infer the characteristics of former ice-sheets and glaciers using the structural properties of ice-contact volcanoes.

To improve Walker's (1965) paleo-ice thickness reconstruction, passage zone elevations should be used to infer ice thickness rather than peak heights of Móberg formations because glacial erosion can significantly reduce the maximum elevation of

subglacial volcanoes (Bourgeois *et al.* 1998). Paleo-ice thickness reconstructions based on the summits of Móberg formations may substantially underestimate former ice thicknesses and, therefore, a more reliable approach would be to correlate the minimum thickness of the ice sheet with passage zones, the elevations of which are unaffected by erosion. Additionally, absolute age dating of the ice-contact volcanoes in the Northern Neovolcanic Zone of Iceland would improve Walker's (1965) paleo-ice thickness reconstruction by establishing the when the subglacial volcanoes were emplaced. If the volcanoes were emplaced at different times, they may have been emplaced under different ice thicknesses or even under different glaciers. In northern Iceland, ice thickness changes can occur rapidly. For instance, Stötter *et al.* (1999) identified seven periods of glacial advance in northern Iceland within the past 5000 years alone. The assumption that the Móberg formations identified by Walker (1965) were emplaced beneath a single ice sheet of constant thickness may be unrealistic.

## **2.10 Summary**

Ice-contact volcano types include tuyas (*stapar*), tindars, subglacial mounds (SGMs), hyaloclastite flows, some stratovolcano deposits, and pseudocraters. The standard sequence for tuya emplacement progresses from deep-water basal pillow lava formation to an explosive phreatomagmatic phase characterized by vitriclastic tephra deposits, and finally a shallow-water-emergent phase with subaerial lava flows overlying hyaloclastite deltas. Tindars and SGMs are lithologically similar to tuyas; however, they represent incomplete tuya sequences because they do not have subaerial lava caps.

The products of sub-ice volcanism include varieties of pillow lava, pillow breccia, hyalotuff, hyaloclastite, conglomerates, sandstone flow-foot breccia, and subaerial lava. Variations in ice thickness, episodic drainage of the englacial meltwater lake, and multiple

eruptive episodes can alter the standard sequence of sub-ice volcano emplacement.

Fortunately, the presence of hyalotuff and hyaloclastite, pillow lava vesicles, and elevation of the passage zone can provide useful indicators of paleo-environmental conditions, such as water depth and ice thickness, at the time of emplacement. Vitriclastic deposits include hyalotuff and hyaloclastite, both of which are representative of two contrasting eruptive environments. Hyalotuffs typically form by explosive Molten Fuel-Coolant Interaction and volatile disintegration, whereas hyaloclastite forms in comparatively passive environments by cooling-contraction granulation. Discrimination between hyalotuff and hyaloclastite can, however, be difficult in the field and requires petrographic analysis of grain morphologies to be conclusive. Explosive processes are characteristic of vent-proximal shallow-water phreatomagmatic interactions, whereas passive lava-water interactions generally occur on pillow lava surfaces or where subaerial lava flows enter water.

The passage zone is a narrow transition region between subaerial sheet lavas and underlying flow-foot breccia that defines the air-water interface of former englacial meltwater lakes. As lava enters water, it fragments into lithic blocks and hyaloclastite that forms a prograding delta on which successive subaerial lava flows can advance. The varying position of the passage zone records changes in water level and, therefore, in ice-confined lakes, the passage zone elevation above bedrock provides a minimum ice thickness for the surrounding glacier or ice-sheet.

Systematic investigation of contemporaneously emplaced sub-ice volcano distribution and passage zone elevations in volcanically active regions, such as the Northern Neovolcanic Zone in Iceland, would provide a means of reconstructing former ice thickness and extent; however, a thorough attempt to reconstruct regional glacial morphology using this method has never been made.

# Chapter 3 Phreatomagmatic fragmentation

## 3.1 Introduction

Phreatomagmatism refers to volcanic processes involving the interaction between magma and external water. Forms of external water include marine, littoral, lacustrine, fluvial, meteoric, phreatic (groundwater), hydrothermal, and ice meltwater (Morrissey *et al.* 2000). On Earth, phreatomagmatic interactions are common occurrences because of the prevalence of the external water in volcanically active zones. Explosive phreatomagmatic fragmentation results from Molten Fuel-Coolant Interactions (MFCIs) involving magma and external water. Phreatomagmatic activity ranges from passive quenching and cooling-contraction granulation of magma to large-scale thermohydraulic explosions (Morrissey *et al.* 2000). The study of volcanic structures and deposits resulting from phreatomagmatic interaction requires detailed consideration of the processes and physical controls affecting phreatomagmatic fragmentation.

This chapter first introduces Molten Fuel-Coolant Interactions (MFCIs) as the dominant process by which explosive phreatomagmatic fragmentation occurs and then proceeds to explore vapour films and boundary-layer instabilities in greater detail. The final sections examine the lithological products of melt-water interaction and the characteristics of phreatomagmatic deposits.

## 3.2 Mechanisms of explosive phreatomagmatic interactions

Proposed mechanisms for explosive melt-water interaction include: 1) vaporization of external water drawn into the melt conduit by the Venturi effect as ascending magma decreases the pressure at the conduit walls (Jones 1970); 2) admixture of unconsolidated

water-saturated sediments and magma as rising magma encounters a wet sediment slurry in the vent (Kokelaar 1983); and 3) Molten Fuel-Coolant Interactions involving hydrodynamic premixing, triggering, melt fragmentation, and explosive vaporization of water (Colgate and Sigurgeirsson 1973; Wohletz 1983, 1986; Sheridan and Wohletz 1983; Zimanowski 1998; Morrissey *et al.* 2000). Molten Fuel-Coolant Interaction (MFCI) is the most plausible mechanism for generating explosive phreatomagmatic activity. Molten Fuel-Coolant Interaction is analogous to Fuel-Coolant Interaction, which is a well-documented phenomenon in foundries and thermo-nuclear reactors. Fuel-Coolant Interactions involves rapid heat transfer between a hot fuel, such as molten lead, and a coolant, such as water. Fuel-Coolant Interactions are responsible for some of the most devastating industrial explosions in history (Wohletz 1983; Morrissey *et al.* 2000).

### **3.3 Molten Fuel-Coolant Interaction**

Molten Fuel-Coolant Interactions have four principal stages: 1) hydrodynamic premixing; 2) triggering; 3) fine-fragmentation; and 4) vaporization and expansion (Zimanowski 1998). Stage 1 involves initial contact and coarse premixing of fuel (magma/lava) and coolant (water) under stable vapour-film boiling conditions (Morrissey *et al.* 2000). High thermal flux causes encapsulating vapour films to develop and pressurize vapour films around portions of the melt that prevent efficient heat transfer from melt to water (Leidenfrost phenomenon). Hydraulic fracturing, stress corrosion, capillarity, vapour-film collapse, water jetting, boundary-layer instabilities, and molecular diffusion increase the surface area of the melt-water contact during the hydrodynamic premixing phase (Morrissey *et al.* 2000). Premixing occurs within seconds to minutes (Zimanowski 1998) over distance scales ranging from submicrometers to meters (Morrissey *et al.* 2000).

Stage 2 begins when vapour films collapse with sufficient energy to trigger fine fragmentation of the melt. Heat transfer and pressurization of vapour films during the premixing phase causes water vapour to become a metastable superheated fluid (Morrissey *et al.* 2000). Thermal expansion of water vapour increases the density contrast between magma and surrounding vapour films. If vapour films continue to heat and expand without disruption, undercooling of the water vapour causes vapour film condensation and collapse (Morrissey *et al.* 2000). Vapour films may require several cycles of expansion and collapse to obtain sufficient energy to overcome the surface tension of the melt (Wohletz 1983). Triggering of melt fragmentation typically occurs when vapour films reach their spontaneous nucleation temperature ( $T_{SN}$ ) and collapse resulting from rapid condensation (water hammer) or when a pressure pulse of external origin, such as a seismic wave, passes through the system and disrupts the stability of superheated vapour films (Morrissey *et al.* 2000). In either case, collapse of vapour films leads to disintegration of the melt surface into smaller particles, increases the total area of the heat transfer surface, and causes thermal and mechanical coupling of the magma (fuel) and water (coolant). In the absence of insulating vapour-film layers, heat transfers rapidly from the melt to the water. High heat transfer rates cause thermal expansion and pressurization of the surrounding water (Morrissey *et al.* 2000). The duration of the trigger phase is typically a few microseconds (Zimanowski 1998).

Stage 3 begins when the thermal expansion of water increases the load stress on the melt beyond its yield strength and initiates brittle fracturing and fine-fragmentation of the melt. Morrissey *et al.* (2000) envision that the local temperature of the melt is near its solidus and that brittle fractures develop in response to thermal contraction or tensional stress waves associated with vapour-film collapse. Stress waves typically propagate faster than thermal waves and, therefore, thermal contraction likely affects only melt surfaces, whereas

mechanical stresses affect the bulk of the melt (Morrissey *et al.* 2000). In MFCIs, the melt behaves like an elastic-plastic material, and undergoes brittle fracturing because the strain rate induced by the rapid thermal expansion of water is high and the melt does not have time to respond by ductile deformation (van der Pluijm and Marshak 1997). The fine fragmentation occurs within less than one millisecond (Morrissey *et al.* 2000) to a few milliseconds (Zimanowski 1998).

Stage 4 involves water vaporization and explosive expansion of the melt-water system. Melt fragmentation and fine-scale mixing cause rapid thermal equilibration and transform superheated water into superheated steam. The water-steam phase transition causes volumetric expansion of the melt-water mixture and mechanical and thermal decoupling of the fuel-coolant system as new vapour films form around the remaining melt (Morrissey *et al.* 2000). Steam generation requires a few milliseconds and vapour expansion occurs within seconds to minutes (Zimanowski 1998). Explosive phreatomagmatic eruptions may involve numerous cycles of premixing, triggering, fine-fragmentation, and explosive steam generation, whereas non-explosive fuel-coolant interactions terminate at the hydrodynamic mixing or trigger phase (Morrissey *et al.* 2000).

### **3.4 Timeline for experimental Molten Fuel-Coolant Interactions**

Direct observation of volcanic MFCIs are not possible and, therefore, to study the processes and timescales involved requires scaled laboratory experiments. Zimanowski (1998) presented a timeline for MFCIs based on the Thermal Explosion Experiment II (TEE II). The experiment uses remelted olivine-melilitite heated to 1653 K with a melt mass of 0.4 kg, density of  $2880 \text{ kg} \cdot \text{m}^{-3}$ , and viscosity of  $1.3 \text{ Pa} \cdot \text{s}$  (Zimanowski 1998). Figure 3.1 illustrates

the setup and entrapment configuration of the TEE II. Figure 3.2 summarizes the stages of MFCI.

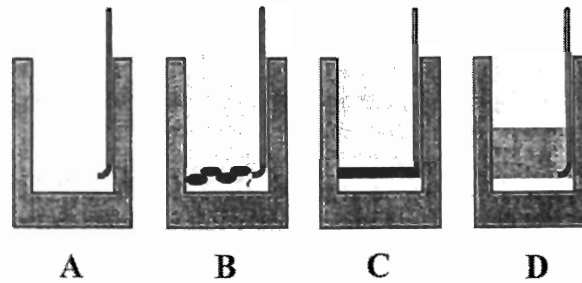


Figure 3.1: Thermal Explosion Experiment II (TEE II) setup. Schematic cross-section illustrating the stages of melt-water interaction within the crucible. A) A thin-walled steel tube inserted into the melt. B) Water injected into the melt to establish a local water-melt premix. C) Thermohydraulic expansion in the premixed zone occurs after initiation of the trigger phase. D) Superheated steam expands adiabatically to ambient pressure and propels the overlying melt out of the crucible (Morrissey *et al.* 2000).

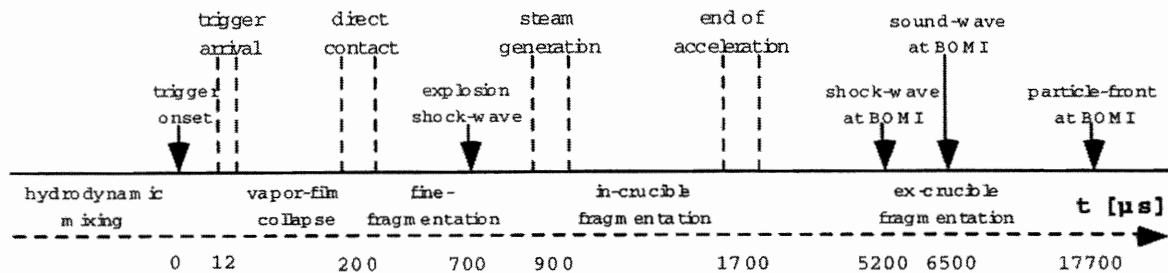


Figure 3.2: Timeline for experimental MFCI (Zimanowski 1998). Following initial hydrodynamic premixing, a projectile makes contact with the melt surface and triggers a shock wave at  $t=0 \mu\text{s}$ . At  $t=12 \pm 2 \mu\text{s}$  the trigger pulse passes through the premixed layer. At  $t=700 \pm 2 \mu\text{s}$  a force transducer detects the maximum shock wave envelope. At  $t=5200 \mu\text{s}$  a seismometer mounted on the top of the containment records the explosion shock wave. The time range marked “steam generation” represents the repulsion force signal recorded by the force transducer and the initiation of expansion detected by high-speed optical recording. “end of acceleration” corresponds with the time range for complete melt ejection. “sound wave at BOMI” and “particle front at BOMI” respectively represent the passage of the expansion sound wave and impact of the first major particle front onto the top plate of the containment, as measured by the seismometer.

### 3.5 The efficiency of phreatomagmatic interactions

All phreatomagmatic mechanisms result from enhanced thermal flux from magma to water relative to dry (magmatic) eruptions. Volcanic eruptions involve the conversion of thermal energy into mechanical energy, including seismic and acoustic energy, fragmentation energy, and kinetic energy of fragment motion (Morrissey *et al.* 2000). In nearly all cases,



phreatomagmatic interactions release more kinetic energy and have more highly fragmented deposits than otherwise equivalent magmatic eruptions (Zimanowski 1998). The size distribution of juvenile fragments and mode of fragment dispersal corresponds to the efficiency of the phreatomagmatic interaction. With increasing efficiency, more thermal energy converts to mechanical energy, which increases fragmentation and dispersal (Morrissey et al. 2000). The efficiency of a phreatomagmatic interaction is termed the conversion ratio (CR). The efficiency of a phreatomagmatic interaction is the work of the system,  $W_{sys}$ , divided by the thermal energy of the magma (Wohletz 1986):

$$Efficiency = CR = \frac{W_{sys}}{m_m C_m (T_m - T_{ref})} = \frac{\Delta KE + \Delta PE + p_0 \Delta V_{sys}}{m_m C_m (T_m - T_{ref})} \quad [3.1]$$

where  $m_m$  is the mass of the magma,  $C_m$  is the specific heat of the melt,  $T_m$  is the absolute temperature of the melt,  $T_{ref}$  is the reference temperature (298 K),  $\Delta KE$  is the change in kinetic energy,  $\Delta PE$  is change in potential energy,  $p_0$  is the initial pressure, and  $\Delta V_{sys}$  is the change in the volume of the system.

To achieve the most efficient reactions, complete thermal equilibrium is necessary and requires uniform melt fragments with a diameter of approximately one micrometer (Wohletz 1986). In nature, poorly sorted phreatomagmatic deposits with juvenile grain sizes ranging from ash to lapilli (4-32 mm) indicate that the efficiency of phreatomagmatic interaction is well below the theoretical limit (Wohletz 1986). The efficiency of natural phreatomagmatic explosions is generally 10% or less (Wohletz 1986); however, the proportions of water and melt largely determine the final thermodynamic state of water within the system and the degree of melt fragmentation (Morrissey et al. 2000).

Various laboratory experiments yield contrasting results for the optimum proportions of water and melt. The range of values demonstrates that initial conditions strongly affect the optimum water-to-melt ratio and the efficiency of MFCIs. The following section compares experimental results obtained from the Los Alamos National Laboratory and the Thermal Explosion Experiment II (TEE II).

Sheridan and Wohletz (1983) presented results from MFCI experiments conducted at the Los Alamos National Laboratory using Fe-Al thermite reactions. Thermite melt is similar to basaltic melt with respect to viscosity, density, and crystallization behaviour; however, its enthalpy is approximately three times greater. Sheridan and Wohletz (1983) used the excess enthalpy in their experiments to produce a silicate melt by mixing quartz sand with the thermite (magnetite plus aluminium) in the explosion device. For these experiments, the maximum conversion of thermal to mechanical energy occurs when water-to-melt ratios are of 0.3 to 0.7 owing to the high enthalpy of thermite reactions, Sheridan and Wohletz (1983) scaled these values to 0.1 and 0.3 to represent basaltic magmas. The most efficient conversion of thermal to mechanical energy occurs near the transition between steam expansion in its superheated and saturated states, corresponding to a water-to-magma mass ratio near 0.3 (Wohletz 1983, 1986). Figure 3.6 shows a plot of phreatomagmatic efficiency versus water-to-melt mass ratio.

When the water-to-melt mass ratio is below 0.3 to 0.4, depending on melt composition, steam is dominantly in its superheated state, whereas higher water-to-mass ratios produce saturated steam (Wohletz 1986). For water-to-melt mass ratios below approximately 0.1 and above 3.0, conversion of thermal to mechanical energy becomes inefficient and explosive activity is weak or entirely suppressed (Wohletz 1983; Fagents *et*

al. 2002). Figure 3.3 illustrates the relationship between water-to-melt mass ratio, explosive energy, eruption style, and various types of volcanic deposits.

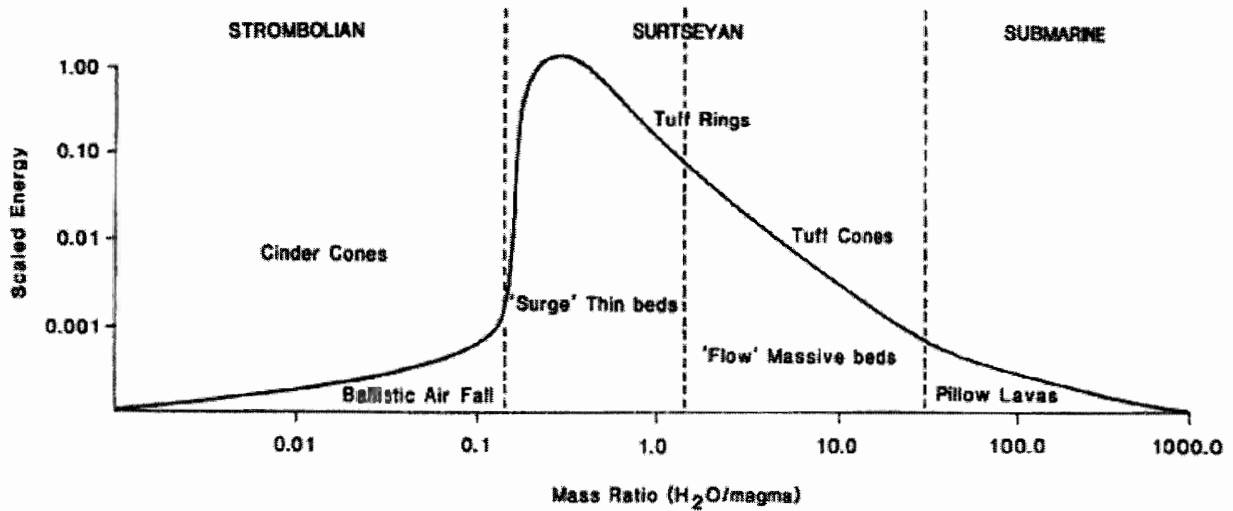


Figure 3.3: Water-to-melt mass ratios. Inter-relationship between water-to-melt mass ratio and mechanical energy with superimposed styles of volcanism and deposit types (Kokelaar 1986 based on Wohletz 1983).

Zimanowski (1998) presented an alternative value for the optimum water-to-melt ratio based on results from the Thermal Explosion Experiment II (TEE II). These experiments, which use low viscosity ( $1 \text{ Pa} \cdot \text{s}$ ) remelted olivine-melilitite with an initial temperature of  $1350 \text{ }^\circ\text{C}$ , reveal that the optimum conditions for generating high intensity phreatomagmatic explosions involve melt-water mixtures with a water-to-melt volume ratio of approximately 0.11, which is equivalent to a water-to-melt mass ratio of 0.03 to 0.04, and a differential flow speed of  $4.2 \pm 0.2 \text{ m} \cdot \text{s}^{-1}$  (Zimanowski 1998; Morrissey et al. 2000). Figures 3.4 and 3.5 graphically summarize the results of the TEE II experiments.

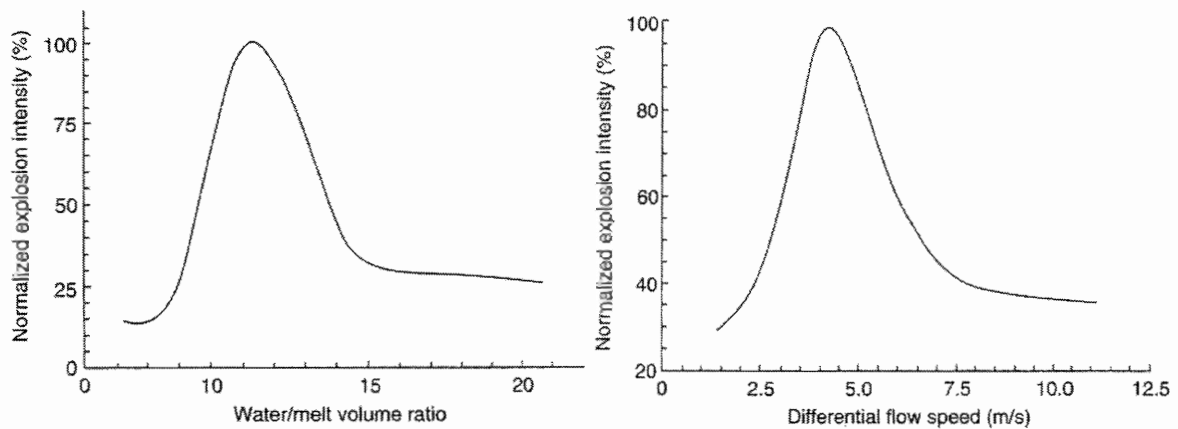


Figure 3.4 (Left): Water-to-melt volume ratio. Water-to-melt volume ratios (%) versus normalized explosion intensity (%) obtained from the Thermal Explosion Experiment II (TEE II) using a constant differential flow speed of  $4.5 \pm 0.2 \text{ m} \cdot \text{s}^{-1}$ . The optimum water-to-melt volume ratio is approximately 11% (Morrissey et al. 2000).

Figure 3.5 (Right): Differential flow speeds. Differential flow speeds of mixing at a constant water-to-melt volume ratio of 0.11 (11%) versus normalized explosion intensity (%) based on results from the TEE II. The optimum differential flow speed is  $4.2 \pm 0.2 \text{ m} \cdot \text{s}^{-1}$  (Morrissey et al. 2000).

The optimum water-to-melt mass ratio for generating highly efficient phreatomagmatic interactions vary by an order of magnitude in different experiments. The optimum water-to-melt mass ratio obtained using Fe-Al thermite melt at the Los Alamos National Laboratory is approximately 0.3 (Sheridan and Wohletz 1983, Wohletz 1983, 1986), whereas the optimum water-to-melt mass ratio derived from the TEE II using remelted olivine-melilitite is 0.03 to 0.04 (Zimanowski 1992). An adequate explanation for the discrepancy between these experimental results does not currently exist; however, chemical and physical differences between the melts used at the Los Alamos National Laboratory and for the TEE II may contribute to the observed variability in the optimum water-to-melt ratio.

Additional experiments show that under otherwise identical conditions, the efficiency of MFCIs increases with decreasing confining pressure (Morrissey et. al 2000), lower melt viscosity (Zimanowski 1998), and increasing melt temperature (Colgate and Sigurgeirsson 1973; Zimanowski 1998). Non-condensable gas bubbles within the melt also affect explosive

phreatomagmatic interactions. For instance, Zimanowski (1998) demonstrates that the presence of non-condensable gas bubbles reduces the efficiency of MFCIs and that concentrations of non-condensable gas above 15% by volume prevent explosive interactions entirely.

### **3.6 Water vapour films**

Rapid heat transfer from magma to surrounding water causes the liquid water at the contact to vaporize and coalesce into thin vapour films within a few nanoseconds (Zimanowski 1998). Vapour films at the melt-water interface insulate the remaining water from the magma (Leidenfrost phenomenon) and allow coarse mixing and gradual fragmentation of the melt without explosive heat transfer. In the absence of triggering effects, such as spontaneous nucleation or thermal detonation, continued heat transfer causes the vapour films to expand until they reach a critical thickness, at which point undercooling initiates and the vapour films collapse by condensation (Morrissey *et al.* 2000). Vapour films oscillate in thickness on microsecond to millisecond timescales and cause acceleration of water vapour relative to the melt (Wohletz 1986). Acceleration of water vapour normal to the melt surface causes Rayleigh-Taylor instabilities to develop, whereas acceleration of the vapour-film parallel to the vapour-melt interface causes shearing and generates Kelvin-Helmholtz instabilities. If the collapse of vapour films produces sufficient acceleration to overcome surface tension forces, water jets penetrate the melt and can become partially or completely entrapped beneath the melt surface. Subsequent heat transfer causes the trapped water to expand and can result in additional fragmentation of the melt (Morrissey *et al.* 2000). Boundary-layer instabilities and water jetting can cause fine-scale mixing of magma and water by distorting and fragmenting

the melt surface. As the melt-water interface becomes more convoluted, its surface area increases and promotes rapid heat transfer from melt to water.

Explosive phreatomagmatic interactions generally occur when magma or lava encounters water with a hydrostatic pressure below the critical pressure for water. The critical pressure for water is 21.74 MPa and represents the limit for the water/steam phase transition (Zimanowski 1998). Insulating vapour films, which allow premixing and subsequent phreatomagmatic explosions to occur, can only develop at significantly lower pressures. A decrease in the hydrostatic pressure accompanying progressive growth of a volcanic structure, or the sudden drainage of ice-dammed water, may cause non-explosive melt-water interactions to become explosive.

### 3.7 Rayleigh-Taylor instability

Rayleigh-Taylor instabilities form at the interface between two immiscible fluids, such as water vapour and magma (Figure 3.6). Instability waves can develop and grow from the surface of the liquid body depending on the density contrast between the two fluids, surface tension, viscosity, and acceleration of the gas towards the liquid (Equation 3.2).

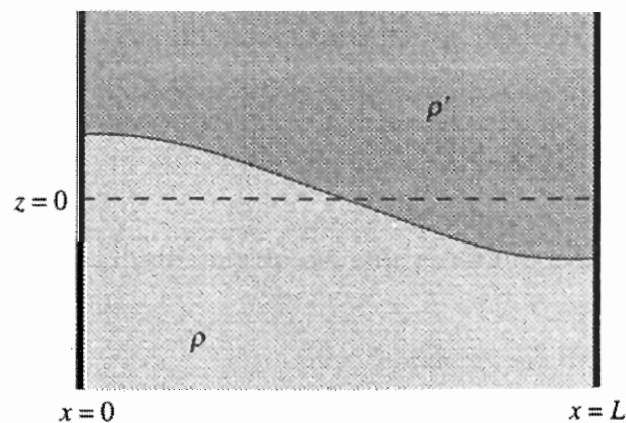


Figure 3.6: Boundary-layer instability. Cross-section in the plane  $z = 0$  in a container of width  $L$  containing a fluid layer beneath a denser fluid. When Equation 2 (below) is satisfied, surface tension prevents perturbation of the fluid interface. If Equation 2 is not satisfied, relative motion between the two fluids begins (Faber 1995).

$$L < \pi \sqrt{\frac{\sigma}{(\rho' - \rho)g}} \quad [3.2]$$

where  $L$  is width of the container,  $\sigma$  is the interfacial surface tension,  $\rho'$  is the density of the denser fluid,  $\rho$  is the density of the less dense fluid, and  $g$  is gravitational acceleration. With time, the amplitude of the stimulated waves increases until reaching a threshold, at which point globules of liquid will detach from the interface (Figures 3.7 and 3.8).

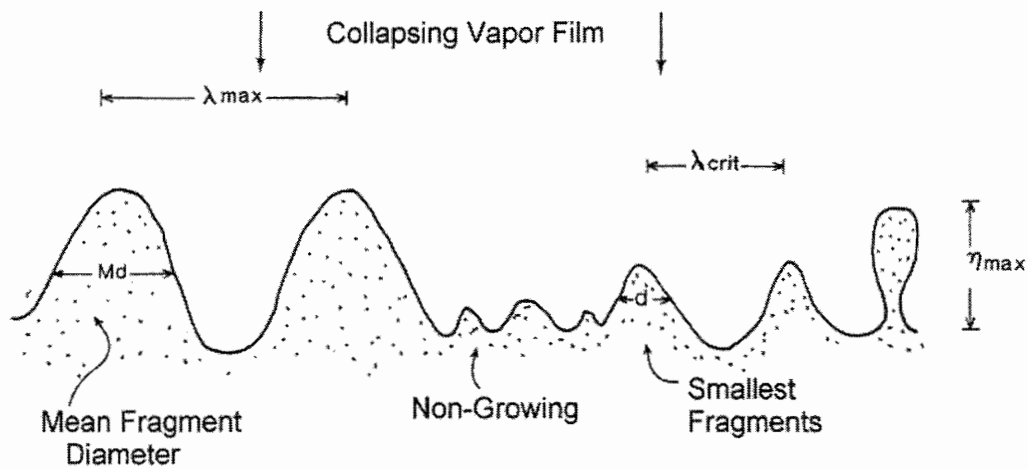


Figure 3.7: Rayleigh-Taylor instabilities. Illustration of a planar Taylor (Rayleigh-Taylor) instability at the interface between magma and a collapsing water-vapour film (Wohletz 1986).

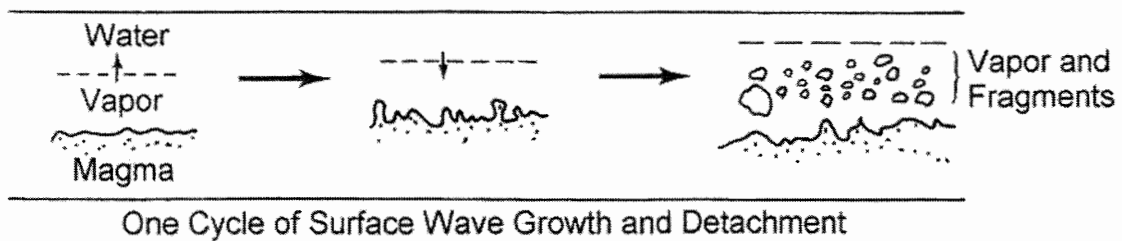


Figure 3.8: Cycles of boundary-layer instability and melt detachment. A complete cycle of instability growth demonstrating how oscillation of the vapour-film thickness transmits sufficient momentum to the magma to distort its surface into waves that grow until they detach from the melt surface to form small fragments (Wohletz 1986).

If the surface tension of the liquid is high, and the cooling rate and viscosity is low, the globules will have a spherical shape, whereas if the viscosity or cooling rate is high, the globules will develop into sub-rounded or elongated forms (Zimanowski 1998). Wohletz

(1986) uses the following equation to calculate the amplitude of Rayleigh-Taylor instabilities,  $\eta$ :

$$\eta = \left[ \frac{a(\rho_m - \rho_w)k}{\rho_m + \rho_w} - \frac{\sigma k^3}{\rho_m + \rho_w} \right]^{1/2} \quad [3.3]$$

where  $a$  is the acceleration of a nearly incompressible water vapour-film towards the melt surface during phases of film collapse,  $\rho_m$  and  $\rho_w$  are the respective densities of the melt and water,  $k$  is the instability wave number ( $2\pi/\lambda$ ), and  $\sigma$  is the melt surface tension. For the amplitude of an initial surface instability to grow without dampening, the wavelength must exceed a critical value,  $\lambda_{crit}$  (Wohletz 1986):

$$\lambda_{crit} = \frac{2\pi}{k_{crit}} = 2\pi \left[ \frac{\sigma}{a(\rho_m - \rho_w)} \right]^{1/2} \quad [3.4]$$

The maximum wavelength,  $\lambda_{max}$ , is the most abundant wavelength for Rayleigh-Taylor instabilities because it is the fastest growing wavelength. Wohletz (1986) calculated  $\lambda_{max}$  using:

$$\lambda_{max} = \frac{2\pi}{k_{max}} = 2\pi \left[ \frac{3\sigma}{a(\rho_m - \rho_w)} \right]^{1/2} = 3^{1/2} \lambda_{crit} \quad [3.5]$$

The median diameter of juvenile fragments produced from explosive MFCIs is approximately  $\lambda_{max}/2$  (Wohletz 1986). Wohletz (1986) further demonstrated that the average speed that instability driven mixing can propagate from the initial melt-water interface towards the interior of the molten body is  $\lambda_{max}/t$ , where  $t$  is inverse of the maximum amplitude of the Rayleigh-Taylor instability:



$$t = \frac{1}{\eta_{\max}} = \left[ \frac{3(3\sigma)^{1/2}(\rho_m - \rho_w)}{[a(\rho_m - \rho_w)]^{3/2}} \right]^{1/2} \quad [3.6]$$

The timescale of vapour-film oscillation limits the growth of instabilities and, therefore, the growth time and growth rate of Rayleigh-Taylor instabilities in relation to vapour-film oscillations must be considered. For thermite-water interactions, instability growth occurs in less than several milliseconds and is consistent with the microsecond to millisecond timescales of vapour-film oscillation (Wohletz 1986). Colgate and Sigurgeirsson (1973) showed that the growth rate,  $\omega$ , of a perturbation of wave number  $k = \pi/\lambda$  is:

$$\omega = \left[ \frac{(\rho_m - \rho_w)}{(\rho_m + \rho_w)a \cdot k} \right]^{1/2} \quad [3.7]$$

### 3.8 Kelvin-Helmholtz instability

Kelvin-Helmholtz instabilities are waves that develop at the boundary between two layers of fluid with slightly different densities as they move relative to one another in a direction parallel to their interface (Faber 1995). Waves that develop on the surface of a pond or lake when the wind speed exceeds a critical value are an example of Kelvin-Helmholtz instabilities. Under otherwise identical conditions, the most pronounced Kelvin-Helmholtz instabilities develop when the density contrast between the two fluids is low. Melt fragmentation resulting from Kelvin-Helmholtz instability is, therefore, most effective when melt is highly vesiculated. Figure 3.9 illustrates an infinite array of parallel vortex lines in an otherwise stationary fluid that become unstable when infinitesimally displaced. Figure 3.10 shows a stage in the development of Kelvin-Helmholtz instability that occurs when pairs of vortex lines encircle one another. Kelvin-Helmholtz instabilities increase boundary surface

area, promote fine-scale mixing, and increase the rate of heat transfer rates from melt to water.

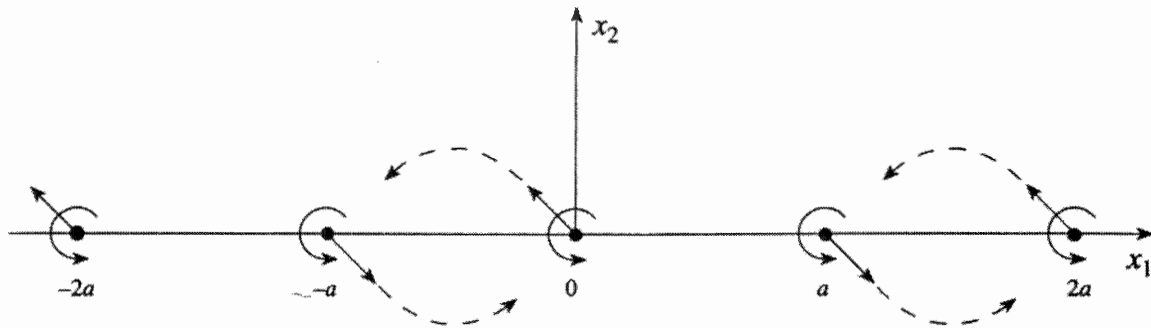


Figure 3.9: Vortex instability. Cross-section through part of an infinite array of parallel vortex lines all of strength  $K$ , situated on the line  $x_1 = na$  ( $n = 0, \pm 1, \pm 2$ , etc.). The vortex lines are unstable and move with small displacements (inclined arrows). The continuation of these arrows implies that the vortex lines may circle around one another in pairs (Faber 1995).

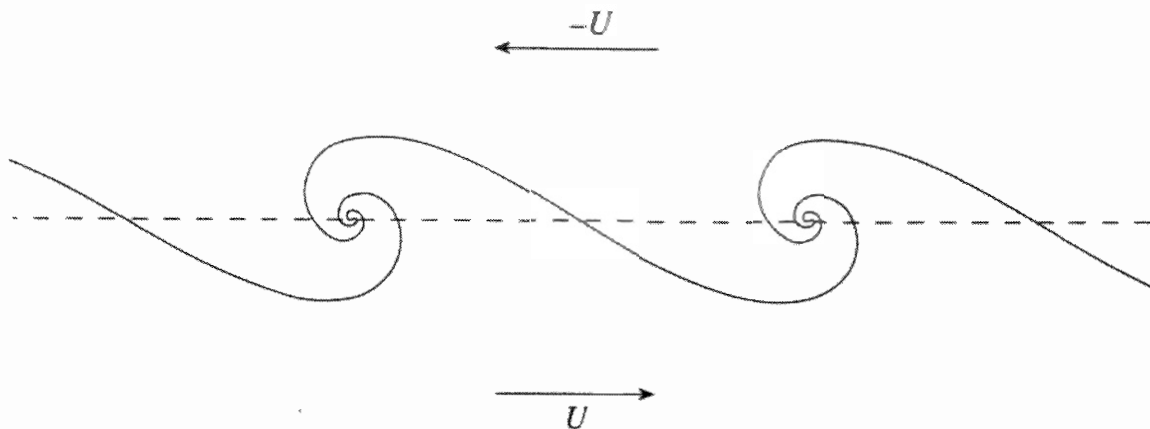


Figure 3.10: Formation of Kelvin-Helmholtz instabilities. A stage in the development of the Kelvin-Helmholtz instability (Faber 1995).

### 3.9 Superheating and spontaneous nucleation

Superheating is a metastable thermodynamic state in which a substance remains in its liquid state above its boiling temperature for any given pressure. In this condition, physical and chemical disturbances can cause the liquid to vaporize (Wohletz 1986). For instance, a moderate-to-high frequency seismic wave can cause local entropy changes in superheated water and initiate a nucleate-boiling front that propagates as a vaporization wave (thermal detonation). Even in the absence of disturbances, superheating can only progress to a

maximum temperature,  $T_{SN}$ , before spontaneous nucleation occurs by homogeneous boiling. The limiting case for vapour explosion resulting from homogeneous boiling occurs when the interface contact temperature,  $T_i$ , exceeds  $T_{SN}$  (Morrissey et al. 2000; Wohletz 1986). For the instantaneous heating case (Morrissey et al. 2000; Wohletz 1986), the temperature of the melt-water interface,  $T_i$ , is:

$$T_i = \frac{T_m(\alpha_m / \sqrt{\kappa_m}) + T_w(\alpha_w / \sqrt{\kappa_w})}{(\alpha_m / \sqrt{\kappa_m}) + (\alpha_w / \sqrt{\kappa_w})} \quad [3.8]$$

where  $T$  is temperature,  $\alpha$  is thermal conductivity, and  $\kappa$  is thermal diffusivity for water,  $w$ , and melt,  $m$ , respectively. In nature, particles and dissolved compounds in the water may act as sites for nucleation lower the value of  $T_{SN}$  (Fagents *et. al* 2002). The pressure limit for spontaneous nucleation is 1.3 MPa (Kokelaar 1986).

### 3.10 Thermal detonation

Thermal detonation involves the rapid vaporization of a liquid behind a propagating shockwave. Shock waves propagating through a magma-water mixture can promote mixing and thermal detonation if the differential acceleration of melt particles relative to the water is sufficient to fragment the melt into smaller pieces (Wohletz 1986). Rapid heat transfer from small melt fragments to the water behind the shock wave causes rapid vapour expansion. If vapour expansion produces particle velocities that satisfy the Chapman-Jouguet condition, a self-sustained shockwave will ensue (Wohletz 1986). To fulfill the Chapman-Jouguet condition, the melt breakup time must be shorter than the time required for the melt particles and water to achieve the same velocity (velocity equilibration). Increasing the initial confining pressure of the melt-water system increases the likelihood of thermal detonation;

however, thermal detonation is not likely to occur above an initial pressure of 50 MPa (Wohletz 1986). This model for thermal detonation assumes that melt fragmentation and magma mixing result from rapidly changing pressure-volume conditions across the shock wave front rather than spontaneous nucleation of water vapour (Wohletz 1986). Figure 3.11 illustrates the stages of thermal detonation and the conditions that exist across the shock wave.

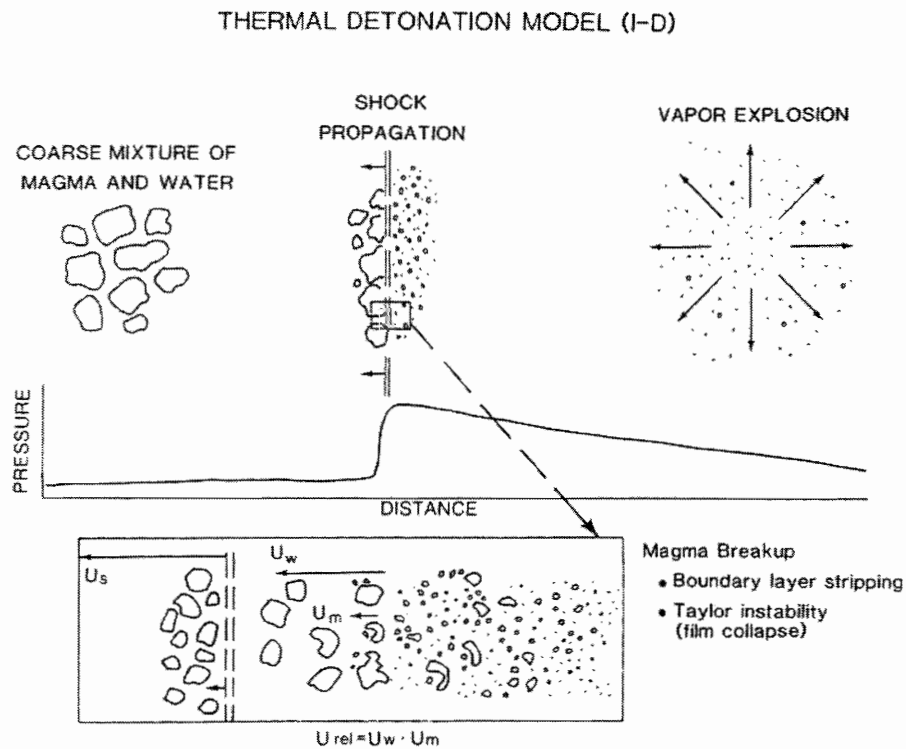


Figure 3.11: Thermal detonation. Propagation of a shock wave initiates thermal detonation of a magma-water mixture. The inset box shows an expanded view of the conditions across the shock wave where  $u_s$  is the velocity of the shock wave,  $u_w$  is the water velocity,  $u_m$  is the magma velocity. Where  $u_{rel} = u_s - u_m$  reaches a critical value, processes such as boundary-layer stripping and Taylor instability fragment the melt and increase heat transfer rates (Wohletz 1986).

### 3.11 Phreatomagmatic pyroclasts

Phreatomagmatic interactions generate a diverse assortment of grain morphologies that include juvenile pyroclasts and secondary products. Wohletz (1983) divided

phreatomagmatic pyroclasts into five dominant shape-types: 1) blocky and equant; 2) vesicular and irregular with smooth surfaces; 3) moss-like and convoluted; 4) spherical or drop-like; and 5) plate-like. Transport processes and alteration, however, complicate identification of grain types because roundness and fragmentation of pyroclasts tend to increase with transport distance, and strong alteration may completely obscure primary grain morphology (Wohletz 1983). Figures 3.12 and 3.13 illustrate examples of natural and synthetic phreatomagmatic grains. Figure 3.14 shows examples of Wohletz's five principal morphological types.

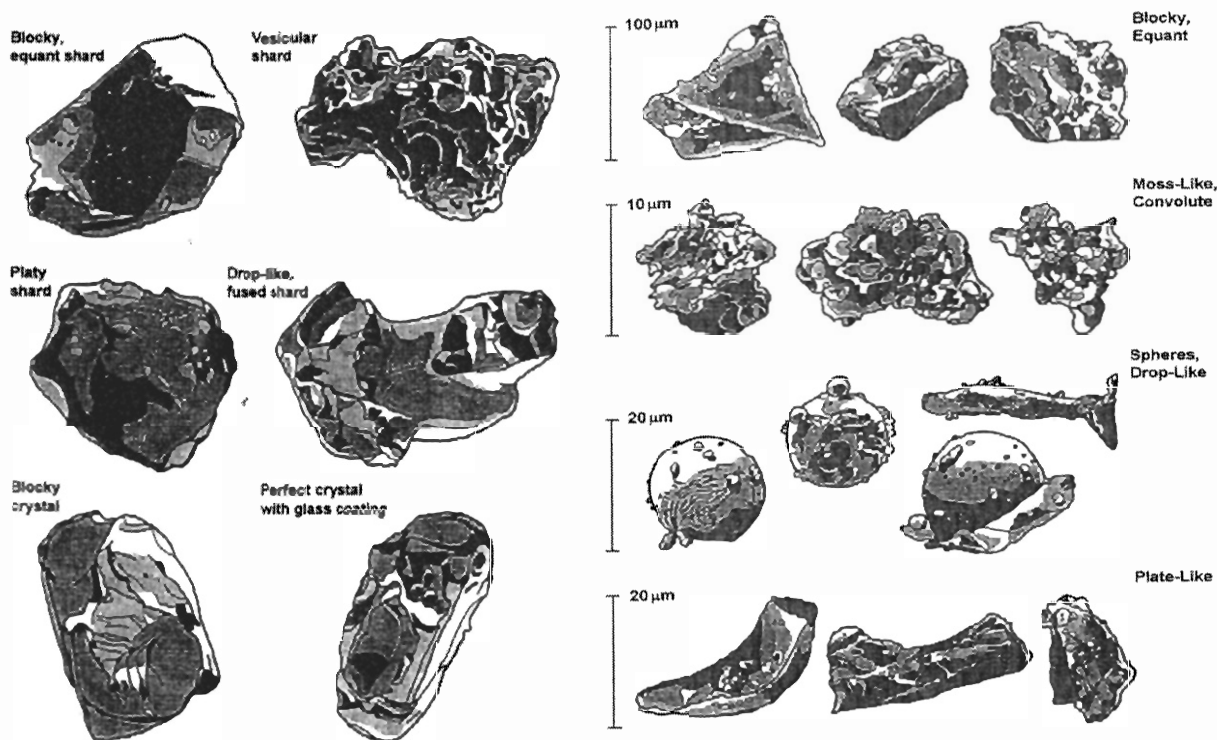


Figure 3.12 (Left): Phreatomagmatic pyroclast morphologies. Clast shapes characteristic of phreatomagmatic fragmentation (Morrissey *et al.* 2000).

Figure 3.13 (Right): Synthetic phreatomagmatic pyroclasts. Scale drawings of clast types synthetically produced by thermite-water experiments at the Los Alamos National Laboratory (Morrissey *et al.* 2000).

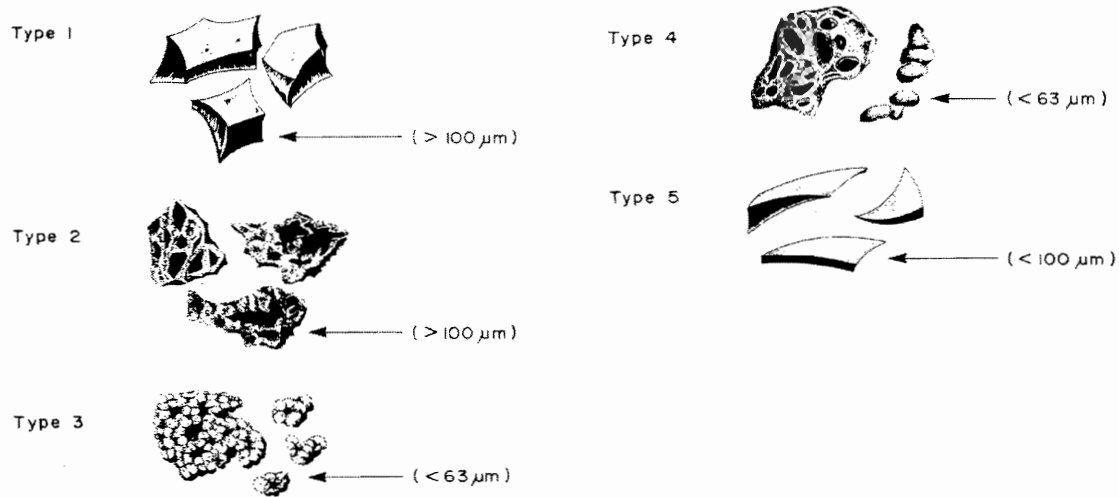


Figure 3.14: Principal phreatomagmatic pyroclast types. Examples of Wholetz's five principal phreatomagmatic pyroclast types with typical grain diameters in parentheses. Type 1: blocky and equant; Type 2: vesicular and irregular; Type 3: moss-like; Type 4: spherical or drop-like; and Type 5: plate-like (Cas and Wright 1988).

Type 1 pyroclasts are the most common variety of coarse grained tephra (diameter  $>63 \mu\text{m}$ ) within phreatomagmatic deposits. These glassy fragments typically have blocky to equant shapes with smooth, vesicle-free surfaces; however, Type 1 pyroclasts also include pyramidal shapes, pointed chips, and splinters (Wohletz 1983). If surface irregularities are present, they result from abrasion, alteration, and/or exposure of internal vesicles. Quenching of the melt produces fractures at angles of less than  $45^\circ$  to the melt surface, which results in the formation of blocky clasts with planar to curvilinear surfaces (Morrissey *et al.* 2000). Type 1 pyroclasts may form from melt compositions ranging from basaltic to rhyolitic.

Type 2 pyroclasts include vesicular and irregular grains with smooth surfaces that are greater than  $63 \mu\text{m}$  in diameter. The grain surfaces between vesicles may be smooth, rounded, or lumpy with a fused or fluid-formed appearance (Wohletz 1983). Vesicle edges are typically smooth and rounded. Type 2 pyroclasts suggest significant vesiculation of the magma prior to explosive interaction with external water. Elongate grains may result from

low quenching rates that allow pyroclasts to deform after fragmentation. These pyroclasts form only from basaltic melts.

Type 3 pyroclasts are moss-like grains that are found only in the fine fraction (diameter  $<63 \mu\text{m}$ ) of basaltic phreatomagmatic deposits. These grains bear a resemblance to moss in that they have a delicate appearance with interconnected structures and high surface area. Moss-like grains have convoluted shapes with highly irregular surfaces that consist of numerous globular masses attached together and may show fluid-form connections between larger masses (Wohletz 1983). Moss-like grains result from vapour-film oscillations that produce turbulence and rapidly expose unquenched melt to the surrounding water by spalling quench fragments from the surface of the molten body. Type 3 pyroclasts may exhibit fluidal surface textures if portions of the melt fragment prior to quenching (Morrissey *et al.* 2000). Moss-like grains form when boundary layer instabilities or rapid formation of vapor films cause viscous deformation of melt surfaces under tensional stress conditions (Morrissey *et al.* 2000).

Type 4 pyroclasts include spherical and drop-like grains with smooth curved surfaces. Spherical and drop-like grains rarely exist as independent particles and generally attach to larger blocky grains or agglutinate to form botryoidal surface encrustations (Wohletz 1983). Broken drop-like fragments may have exposed vesicular interiors. Spherical or drop-like grains are present within the fine fraction (diameter  $<63 \mu\text{m}$ ) of basaltic phreatomagmatic deposits. Spherical and drop-like grains develop when boundary layer instabilities cause spherical or ribbon-like structures to grow and detach from the melt surface (Morrissey *et al.* 2000).

Type 5 pyroclasts are plate-like grains with irregular or smoothly curved surfaces. Irregular grains form when the melt contains abundant microlites. Plate-like grains include

crescent shapes, chips, and splinters that show at least one curved surface that represents the vesicle wall of a bubble with a diameter greater than that of the grain. Plate-like grains are less than 63  $\mu\text{m}$  in diameter. Morrissey *et al.* (2000) interpreted platy grains as pieces of quenched melt that are stepped from the melt body by vapour film oscillations, thermal detonation, and Kelvin-Helmholtz instabilities.

Phreatomagmatic deposits also tend to include accretionary and armoured lapilli, which form within eruption columns and associated pyroclastic flows. Accretionary lapilli are lapilli-sized (4-64 mm) pellets that typically exhibit a concentric internal structure. They form by accretion of ash around a nucleus, which may be either a water droplet or solid particle, and are most commonly associated with phreatomagmatic or phreatic eruptions (Cas and Wright 1988). Accretionary lapilli may occur within pyroclastic falls, base-surges, or flow deposits (Francis 2001). Armoured or cored lapilli have a recognizable lithic core and a thick (<2 cm) shell of unstructured ash. Armoured lapilli are common within basaltic base-surge deposits and may form when fragments within base-surge clouds accumulate a coating of sticky wet ash (Cas and Wright 1988).

### **3.12 Characteristics of phreatomagmatic deposits**

Phreatomagmatic interactions produce a wide range of volcanic structures (Figure 3.15). Explosive phreatomagmatic interactions contribute directly to the formation of tuff cones, tuff rings, maars, diatremes, pseudocraters (rootless cones), hornitos, littoral cones, subglacial mounds (SGM), tindars, tuyas, and some stratovolcano deposits (Wohletz 1986; Kokelaar 1986; Guðmundsson *et al.* 1997; Hickson 2000; Morrissey *et al.* 2000; Lescinsky and Fink 2000; Geeley and Fagents 2001; Fagents *et. al* 2002). Non-explosive water-melt interactions are responsible for the formation of pillow lavas when water-to-melt ratios



and/or confining pressures are high. When water-to-melt ratios are very low, Strombolian and possibly Hawaiian eruptions form cinder cones. Additionally, Surtseyan, Phreatoplinian, and many Vulcanian eruptions result from interactions between melt and external water and, therefore, are associated with phreatomagmatic activity (Cas and Wright 1988; Francis 2001). Pyroclastic flow deposits, including base-surge deposits and some ignimbrites, result from gravitational instability in eruption columns of phreatomagmatic origin (Cas and Wright 1988; Francis 2001). In a broad sense, phreatomagmatic interactions affect the majority of all terrestrial volcanoes because of prevalence of external water on or near the Earth's surface (Zimanowski 1998).

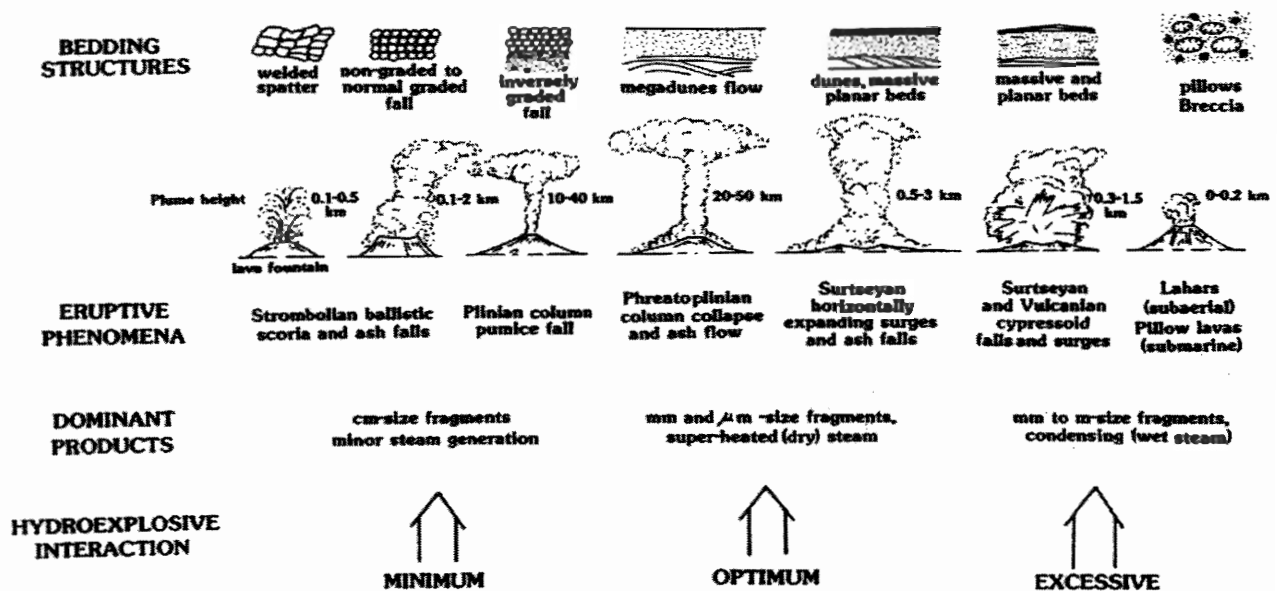


Figure 3.15: Phreatomagmatic deposits. Relationship between various forms of phreatomagmatic interaction and their geological products. The type of hydroexplosive interaction depends on the prevalence of water within the system. When the water-to-melt ratio decreases below (minimum) or increases above (excessive) the optimum ratio, the efficiency of the phreatomagmatic interaction decreases. Dominant products refer to clast size (degree of fragmentation) and steam conditions. Eruptive conditions describe the style of volcanism and depositional mechanisms. Eruption column height is greatest when the water-to-melt is optimum. Bedding structures vary widely depending on the initial form of phreatomagmatic interaction (Sheridan and Wohletz 1983).

Zimanowski (1998) specified the following criteria for identifying explosive phreatomagmatic deposits. Juvenile clasts derived from explosive phreatomagmatic interactions are typically intensely fragmented, poorly-sorted, vesicle-poor to vesicle-free, and inclusion-rich. The proportion of country-rock in explosive phreatomagmatic deposits can be high, in excess of 90%. Grain sizes typically range from ash to lapilli; however, explosive phreatomagmatic deposits also include large blocks of country rock up to several meters in diameter that commonly concentrate in layers without impact sags. The absence of impact sags indicates horizontal transportation within pyroclastic flows. Explosive phreatomagmatic deposits generally exhibit signs of soft-sediment deformation and plastering of wet ash layers onto obstacles and particles (i.e., armored lapilli). Flow textures are common and include dunes, antidunes, imbrication, chute-and-pool textures, and all types of surge textures. Explosive phreatomagmatic eruptions tend to form craters that are much larger than craters formed during dry (magmatic) eruptions involving equivalent magma volumes (Zimanowski 1998). High thermal equilibration rates resulting from melt-water interaction generate phreatomagmatic eruption columns that are colder, denser, and less gravitationally stable than otherwise equivalent magmatic eruption columns. Collapse of phreatomagmatic eruption columns containing abundant water frequently results in the generation of lahars and the deposition of non-welded pyroclastic flow deposits.

Phreatomagmatic deposits generally include fine-grained sideromelane, which is a tan to brown glass that readily alters by hydration and oxidation to form yellowish-brown to reddish-brown palagonite (Cas and Wright 1988). Sideromelane may be present in the form of either hyaloclastite or hyalotuff (Skilling 1994; Smellie and Skilling 1994). Hyaloclastite forms by non-explosive quenching of basaltic melt and subsequent cooling-contraction granulation, whereas hyalotuff results from explosive fragmentation of glass (Wohletz 1983).

Hyaloclastite is typically associated with pillow lavas and includes angular to blocky grains with low vesicle content (<25% vesicles by volume) and convex grain perimeters greater than 20% (Skilling 1994). Hyalotuff consists of vesicular shards (>25% vesicles by volume) with broken vesicle margins and convex perimeters less than 20% (Skilling 1994). In the field, discrimination between hyaloclastite and hyalotuff is exceptionally difficult and many researchers have abandoned the distinction at the outcrop scale in favour of using hyaloclastite in a more descriptive sense to represent both grain morphologies (Werner and Schmincke 1998).

### **3.13 Summary**

Explosive phreatomagmatic fragmentation occurs when Molten Fuel-Coolant Interactions (MFCIs) take place between melt and external water. Molten Fuel-Coolant Interactions involve four stages: 1) premixing; 2) triggering; 3) fine-fragmentation; and 4) vaporization and expansion. Initial contact between melt (magma or lava) and water generates insulating water vapour films around portions of the melt that allow coarse premixing to occur. The trigger phase initiates when spontaneous nucleation or thermal detonation causes vapour films to collapse with sufficient energy to fragment the melt. Fine-fragmentation and coupling (thermal and mechanical) of melt and water leads to rapid thermal equilibration of the system. Increased heat transfer rates transform superheated water into superheated steam, which causes volumetric expansion of the fuel-coolant mixture and decoupling of the remaining melt and water as new vapour-film layers develop.

Oscillating vapour-film thickness and vapour-film collapse produce acceleration of water vapour relative to the melt and may generate surface instabilities (Rayleigh-Taylor and

Kelvin-Helmholtz instabilities) and water jets. Surface instabilities and water jetting promote mixing and increase the rate of heat transfer from the melt to the surrounding water.

The efficiency of the conversion between thermal and mechanical energy depends primarily on the physical and chemical properties of the melt, the water-to-melt ratio, the degree of mixing prior to water vaporization, and hydrostatic pressure. Experiments involving Fe-Al thermite-water mixtures indicate that the optimum water-to-melt mass ratio is approximately 0.3 (Sheridan and Wohletz 1983, Wohletz 1983, 1986), whereas the optimum water-to-melt mass for experiments using remelted olivine- melilitite ranges from 0.03 to 0.04 (Zimanowski 1998; Morrissey et al. 2000). The discrepancy between these results illustrates that the optimum water-to-melt ratio for generating efficient phreatomagmatic interactions is not constant. Differences in melt composition may contribute to the observed range of values; however, a comprehensive explanation has not been proposed and the topic remains the subject of active research.

Volcanic deposits resulting from phreatomagmatic interaction are widespread. Grain size distribution, textures, and structural relationships within these deposits provide valuable information about the physical conditions of the eruption. Additionally, phreatomagmatic deposits provide a means of determining the presence of near surface water and reconstructing paleoenvironments. Understanding explosive phreatomagmatic interactions and associated phenomena such as pyroclastic flows are also important for assessing the dangers that face communities living near active volcanoes.

# Chapter 4 Methods

## 4.1 Remote sensing

Remote sensing is a means of acquiring information about an object without coming in direct physical contact with the subject under investigation (Campbell 2002). In the context of this paper, remote sensing refers to analysis of multispectral satellite imagery and involves classification of materials into groups based on their spectral reflectance and emittance properties. The objective of image classification is to automatically categorize all pixels in an image into land-cover classes or themes. The two primary methods of image classification include unsupervised and supervised classification techniques (Lillesand and Kiefer 2000; Sabins 2000; Campbell 2002). Unsupervised classifications do not assume prior knowledge of ground-cover types and their spatial distribution within the classification region, whereas supervised classifications do. Supervised classifications require extensive prior knowledge to define training sites that represent all major ground-cover types (Lillesand and Kiefer 2000). The purpose of performing a remote sensing classification of the Vífilsfell Region is to identify the distribution of major ground cover-types to make subsequent field surveys more efficient. In this instance, only an unsupervised classification is appropriate because ground-cover identities were unknown in the region prior to ground-truthing.

### 4.1.1 Unsupervised classifications

Unsupervised classifications identify natural groupings or clusters within the spectral data; however, the information identity of each of these clusters is unknown and the analyst must use external reference data to determine the relationship between spectral clusters and ground-cover types (Lillesand and Kiefer 2000). Unsupervised classification algorithms require no prior knowledge of the imaged region; detailed human decision-making is not

required, and the clusters identified within the image represent distinct spectral classes in the image data that might not be apparent if applying a supervised classifier (Campbell 2002). The disadvantages and limitations of unsupervised classifications include: reliance upon natural groupings in the data and matching these groups with information categories; generation of erroneous classes; lack of control over which classes are included in the classification; and variations in the spectral properties of imaged materials over time. Spectral variability makes unsupervised classifications unsuitable for change analysis because cluster divisions and their information identities do not remain constant (Campbell 2002). Unsupervised classifications are ideal for identifying the natural spectral classes that exist in the data set as a basis for determining what ground-cover classes can be reliably extracted during subsequent supervised classifications (Lillesand and Keiffer 2000).

#### **4.1.2 Supervised classifications**

In supervised classifications, an analyst identifies information categories and examines their spectral separability, whereas in unsupervised classifications an algorithm automatically identifies spectrally separable classes with unknown information identities. Supervised classifications use sample regions of known identity, termed training sites, to classify pixels of unknown identity. The selection of good training data is imperative in an accurate classification. To define training sites, the analyst digitizes polygons around areas that represent a homogeneous ground-cover class. These regions are carefully selected to avoid mixed pixels on the boundaries of land-cover types. To obtain an accurate classification, the training sites must represent all spectral classes constituting each information category (Sabins 2000). Some information categories, such as water and vegetation, have high spectral variability and require numerous training sites to obtain an accurate classification. If an

information category has high spectral variability, discrete spectral clusters within the information category must each have a corresponding training site. Subsequent amalgamation of spectral discrete classes into general information categories produces a meaningful classification result.

Supervised classifications are more suitable for time series analysis than unsupervised classifications because: the analyst defines which information classes are included in the classification; training sites and spectral clusters have known information identity; and serious errors are detectable by comparing classification results with the original training sites, which are regions of known identity. The disadvantages and limitations of supervised classifications include: the necessity to manually define training sites for all significant classes within the image; an analyst-imposed classification structure upon the data; and incompatibility between operator-defined classes and natural classes. To improve classification accuracy, an unsupervised classifier should be used to determine the natural spectral classes within the image prior to performing a supervised classification (Lillesand and Kiefer 2000; Campbell 2002).

In practice, pixels rarely contain one homogeneous land-cover type and, therefore, mixed pixels with composite signatures typically exist wherever multiple land-cover types converge, such as along boundaries of linear features and land parcels. Classification errors resulting from mixed pixels can be minimized using a probability based classification algorithm, such as a Bayer's classifier, which assumes that pixels contain mixed land-cover. Bayer's classifications assign a probability of class membership to each pixel using an operator-defined membership function (Campbell 2002).

### 4.1.3 Remote sensing analysis of the Vífilfell Region

High-resolution multispectral satellite imagery enables rapid and efficient mapping of numerous land-cover types. Remote sensing classification of the Vífilfell Region, combined with subsequent ground-truthing, enables identification of principal volcanic lithofacies and determination of the physical characteristics of geological materials contributing to the observed spectral signatures. The remote sensing analysis has three phases: 1) application of preliminary unsupervised classifications (cluster analysis) to identify the spatial distribution of significant spectral classes within the Vífilfell Region; 2) ground-truthing and sampling of representative sites within the study region that correspond to dominant spectral classes; and 3) evaluation of unsupervised classification techniques with respect to the identification of ice-contact volcano lithofacies.

Lanmælingar Íslands (Geodetic Survey of Iceland) donated the satellite imagery used in this analysis. The data set consists of four enhanced multispectral Systeme Pour L'observation de la Terre (SPOT) 5 bands. The SPOT 5 imagery (Image Frame: 709\_218, ID # 57092180209061318002J) was captured on September 6, 2002 at 13:18:00. The data were acquired using the High Resolution Geometric (HRG) instrument in colour mode with an incident angle of  $5.277137^\circ$ . The data are in raster format (geotiff) and consist of three bands with 10 m spatial resolution (Band 1: 0.50 - 0.59  $\mu\text{m}$ ; Band 2: 0.61 - 0.68  $\mu\text{m}$ ; Band 3: 0.78 - 0.89  $\mu\text{m}$ ), and one short-wave infrared band with 20 m resolution (Band 4: 1.58 - 1.75  $\mu\text{m}$ ), all of which are combined with panchromatic data (0.48 - 0.71  $\mu\text{m}$ ) to produce four enhanced bands, each with a resolution of 2.5 m. The image contains partial cloud cover with associated shadows in the southwest quadrant and shadows on western slopes.



#### 4.1.4 Procedure

The first step of the remote sensing analysis involves the acquisition of satellite imagery and relevant reference materials, such as aerial photographs, oblique photographs, geological maps, and descriptions of the Vífilfell Region. Materials collected during this phase include SPOT 5 satellite imagery, vertical and oblique aerial photographs, regional geological and tectonic maps, and published descriptions of the Vífilfell Region (Jónson 1978).

The second step involves importation of the satellite imagery into IDRISI 32 version 2 and transformation of the data into UTM projection with WGS 84 datum. Landmarks in the study region are correlated with observable features in aerial photographs and map sheets to establish a qualitative assessment of the image quality and limit of detection.

In the third step, the variance in each band is determined using Principal Component Analysis (PCA). Similar reflectance and emittance properties of materials at different wavelengths can produce extensive interband correlation in multispectral imagery (Lillesand and Kiefer 2000). Principal Component Analysis compares the variance in each band and generates new component images from the linear combinations of the original values (Lillesand and Kiefer 2000). For multispectral data, the linear contributions from the original bands to pixels within the composite image are in the form (Campbell 2002):

$$A = C_1X_1 + C_2X_2 + \dots + C_nX_n \quad [4.1]$$

where A is the new pixel value in the component image;  $X_1$ ,  $X_2$ , and  $X_n$  are the pixel values in the original spectral bands; and  $C_1$ ,  $C_2$ , and  $C_n$  are coefficients applied to the pixel values in each respective band. The values of the coefficients are calculated to ensure that the new pixel value, A, contains the maximum information content that a single band can convey

(Campbell 2002). In the first principal component image, every pixel has a value corresponding to the variance at that location in each of the bands. The principal components

transformation represents a change in coordinate system from the measurement axes of the original bands to a new set of axes that are rotated with respect to the originals. The origin of the new coordinate axes corresponds to the mean value of the original data (Figure 4.1). The orientation of the first axis is chosen to maximize the variance in the original data and the orientation of each successive axis is orthogonal to all others to ensure that the data represented by each axis is uncorrelated (Lillesand and Kiefer 2000). The first axis corresponds to the first principal components image, the second axis to the second principal components image, and so on. The pixel values in each principal components image are calculated using Equation 4.1 with new set of coefficients.

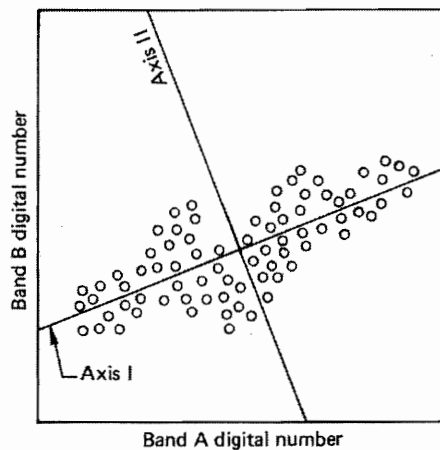


Figure 4.1: Principal Component Analysis (PCA). PCA involves the transformation of pixel values from original coordinate axes (Band A and Band B) to a new set of axes (Axis I and Axis II). The origin of the new axes corresponds to the mean of the data distribution, and the orientation of each axis maximizes the variance within the data set while remaining orthogonal to all other axes. Axis I corresponds to the first principal component and Axis II to the second principal component (Lillesand and Kiefer 2000).

Principal Component Analysis reveals that bands 1, 3, and 4 have the largest variance, and that principal components 1, 2, and 3 cumulatively contain 99.83% of the total variance with the data set (Component 1: 85.85%; Component 2: 9.47%, Component 3: 4.15%; and Component 4: 0.17%). Combination of components 1, 2, and 3 into a three-

channel composite image, therefore, results in a loss of only 0.17% of the total information content present within all four of the original bands. Cartographic Model 1 (Appendix A.1.1) details the procedure for performing PCA in IDRISI 32 version 2 and Appendix A.1.2 contains a summary the PCA results.

In the fourth step, the original bands with the largest variance are combined into 24-bit and 8-bit composite images. The 24-bit image is used for visualization and qualitative analysis, whereas the 8-bit composite image is used in subsequent unsupervised classifications as a seed image. Cartographic Models 2-5 (Appendix A.2-A.5) depict the method for generating composite images.

The fifth step employs the 8-bit composite images produced in step four to seed two unsupervised classifications. The first classification uses the 8-bit band composite (Blue: Band 1, Green: Band 3, and Red: Band 4), and the second cluster analysis uses the 8-bit component composite image (Blue: Component 1, Green: Component 2, and Red: Component 3). After testing a variety of classification parameters, a fine generalization level combined with an operator-defined maximum number of clusters to retain was determined to generate the most meaningful results. Cartographic Models 6 and 7 (Appendix A.6 and A.7) summarize the procedure for classifying the band composite and component composite images.

## **4.2 Field survey**

The Vífilsfell Region is snow covered throughout most of the year and is assessable for field work from approximately the beginning of May to the end of October. Field surveys were conducted during two periods in 2003. The first field survey was completed during the second half of May and the second phase of field work was completed during a two-week

period in mid-August. The Vífilfell Region is located approximately 30 km southeast of Reykjavík and accessible on foot from auxiliary roads extending south from Highway 1. Field equipment included geological hammer, compass, hand-lens, altimeter, magnetic flux gauge, and Global Positioning System receiver (Garmin GPS V).

Field surveys concentrated in regions that were presumed to contain abundant hyaloclastite deposits, identified during the preliminary remote sensing analysis. Field observations were focused on ice-contact volcanic deposits. Investigation of interglacial subaerial lava flows in the Vífilfell Region was outside the scope of the field surveys.

### **4.3 Geochemical analysis**

Geochemical analysis using an electron microprobe enables quantitative comparison of volcanic glass samples from the Vífilfell Region. The purpose of this comparison is to determine the compositional relationships among Northern Bláfjöll, Vífilfell, and Arnarþúfur deposits.

The proportion of glass relative to crystals in a sample depends on the amount of crystallization prior to eruption and the degree of undercooling after eruption. Samples from Northern Bláfjöll, Vífilfell, and Arnarþúfur range from holohyaline to holocrystalline rocks and, thus, represent a broad spectrum of cooling histories. Glass samples provide a good basis for geochemical comparison because of the high glass-to-crystal ratio within deposits in the Vífilfell Region.

#### **4.3.1 CIPW norm calculations**

The CIPW norm calculation is a formula that synthesizes sample mineralogy from geochemical data, assuming that complete crystallization were to occur at low pressure under

of critically silica-undersaturated rocks towards nepheline from silica-undersaturated and silica-saturated rocks towards quartz. The plane of silica saturation (En-Di-Ab) divides the region of silica-undersaturated rocks towards the critical plane of silica undersaturation from the silica-saturated rocks near quartz. The generalized form of the basalt tetrahedron is derived by substituting of plagioclase, olivine, augite, and hypersthene for the pure end members albite, forsterite, diopside, and enstatite, respectively (Figure 4.3). The generalized form of the basalt tetrahedron is useful for summarizing the geochemical characteristics of basalts (Morse 1980).

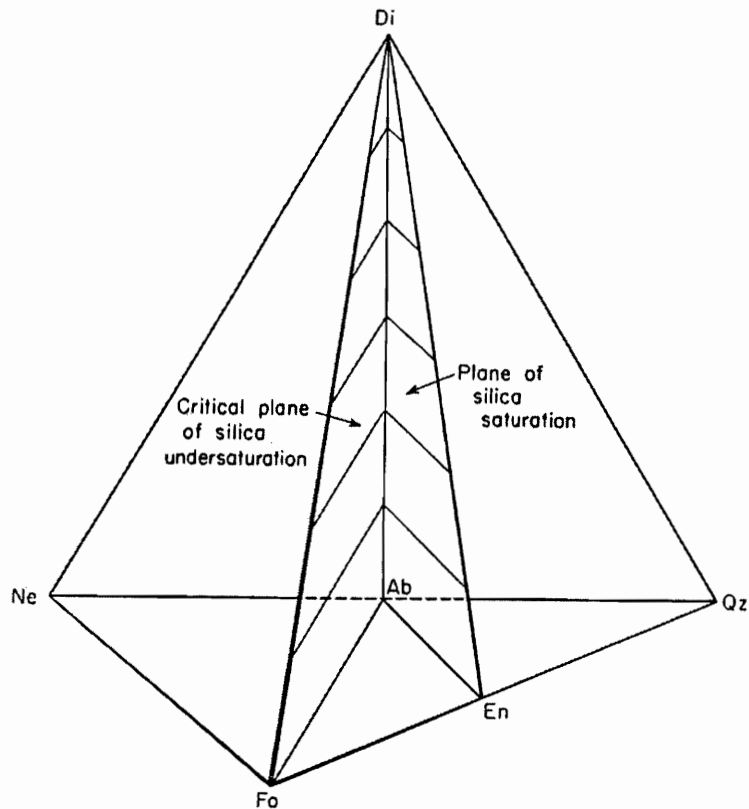


Figure 4.2: Fundamental basalt tetrahedron. This quaternary system includes forsterite (Fo), diopside (Di), nepheline (Ne), and quartz (Qz) apices with albite (Ab) and enstatite (En) respectively plotted on the Ne-Qz and Fo-Qz line segments. The Di-Fo-Ab plane is the critical plane of silica undersaturation and the Di-En-Ab is the plane of silica saturation.

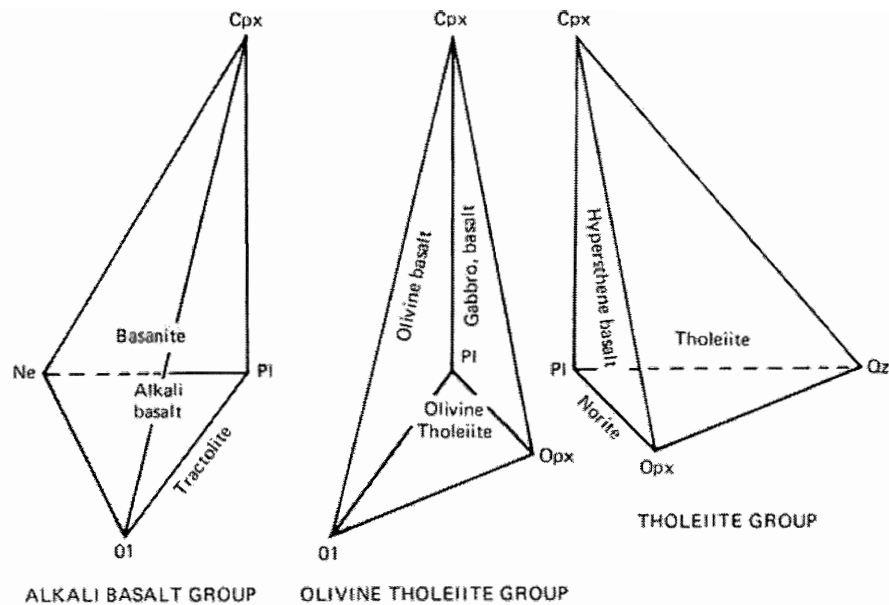


Figure 4.3: General basalt tetrahedron. In the general form of the fundamental basalt tetrahedron, olivine (Ol), clinopyroxene (Cpx), plagioclase (Pl), and orthopyroxene (Opx) replace the pure end members Fo, Di, Ab, and En, respectively. The planes of critical silica undersaturation and silica saturation divide the tetrahedron into three volumes. Basanites plot to the Ne side of the plane of critical silica undersaturation, olivine tholeiites between the planes of critical silica undersaturation and silica saturation, and quartz tholeiites on the quartz side of the plane of critical silica saturation.

The planes of critical silica undersaturation and silica saturation divide the basalt tetrahedron into three groups: 1) alkali basalt, 2) olivine tholeiite and 3) tholeiite (Morse 1980). Alkali basalts are silica-undersaturated, plot to the nepheline side of the plane of critical silica undersaturation, and include normative olivine and nepheline. Olivine basalts lie on the plane of critical undersaturation, and contain normative olivine, but no hypersthene. Olivine tholeiites are silica-undersaturated, plot between the planes of silica saturation and critical silica undersaturation and include normative hypersthene and olivine. Hypersthene basalts are silica-saturated, plot on the plane of silica saturation, and contain hypersthene, but no free quartz. Quartz normative tholeiites are silica-oversaturated, plot to quartz side of the plane of silica saturation, and contain normative quartz and hypersthene.

### 4.3.3 Procedure

A subset of samples was selected from hand specimens collected from Northern Bláfjöll, Vífilsfell, and Arnarþúfur. All samples contain glass in the form of hyaloclastite and glassy chilled margins of lava flows. Polished thin-sections were prepared from the hand samples and were examined using a petrographic microscope to identify homogeneous grains free of microlites and alteration. Petrographic examination reveals that eighty-three grains within eleven samples were suitable for microprobe analysis. The eleven samples include one from Northern Bláfjöll (Wpt094), three from Vífilsfell (Wpt091, Wpt092, Wpt107), and seven from Arnarþúfur (Wpt042, Wpt043, Wpt051, Wpt059 (×2), Wpt060, Wpt070). The polished thin-sections were carbon coated and analyzed for major element compositions (Si, Ti, Cr, Fe, Mn, Mg, Ca, Na, K, and P) using the JEOL 8200 Electron Microprobe at Dalhousie University. Major element compositions were obtained using wavelength spectrometry with an accelerating voltage of 15 kV, current of 20 nA, and a defocused spot size of 20 μm. The electron microprobe was calibrated using the following standards: MnO<sub>2</sub> for MnO; sanidine for K<sub>2</sub>O, Al<sub>2</sub>O<sub>3</sub>, and SiO<sub>2</sub>; jadeite for Na<sub>2</sub>O; Cr metal for Cr<sub>2</sub>O<sub>3</sub>; garnet for FeO; Kakanui kaersutite for CaO, MgO, and TiO<sub>2</sub>; and fluorapatite for P<sub>2</sub>O<sub>5</sub>.

Two sites were typically analyzed within each glass clast; however, some grains were analyzed at one to five sites depending on their size, homogeneity, and degree of alteration. Sample Wpt042 yields anomalous total weight percentages ranging from 90.02 to 101.74% and was discarded from the data set. The weight percentages for the remaining samples were normalized to 100% and their CIPW norms calculated using a spreadsheet-based CIPW norm calculation (Hollocher 2003).

To plot the CIPW norm data within the basalt tetrahedron, the weight percentage of the normative hypersthene is recalculated into constituent quartz and olivine. Multiplication

of the weight percent of normative hypersthene obtained for each sample by the ratio between molecular weights of quartz (60.09) and hypersthene (variable depending on the Fe/Mg ratio of the sample), yields the quartz contribution of hypersthene. The olivine contribution from hypersthene was obtained by subtracting the quartz contribution from hypersthene from the original weight percent of normative hypersthene for the sample. The quartz and olivine contributions from hypersthene are subsequently added to the original weight percentages of normative quartz and olivine, respectively, to obtain new normative values that are compatible with the axes of the basalt tetrahedron.



# Chapter 5 Observations and Results

## 5.1 Remote sensing

Remote sensing analysis of SPOT 5 data of the Vífilsfell Region involves: 1) Principal Component Analysis (PCA) of the original data; 2) recombination of bands and component into composite images; 3) classification of composite images into discrete spectral clusters; and 4) interpretation of cluster identities. This section presents the results of the first three phases, and Chapter 6 contains an interpretation of cluster identities.

Principal Component Analysis (PCA) determines variability within each of the original bands and generates a new set of component images. Two sets of four components are generated from the original SPOT 5 bands using PCA. The first set of four components uses unstandardized variables for the PCA transformation, and generates images with the following variance percentages: Component 1: 85.85%; Component 2: 9.47%; Component 3: 4.51%; and Component 4: 0.17%. Unstandardized variables are used during PCA transformations to assign bands with high variance, typically infrared bands, greater weight. If standardized variables are used, all bands have an equal weight. Principal Component Analysis of the SPOT 5 data using standardized variables generates components with the following percentage variance: Component 1: 81.76%; Component 2: 13.47%; Component 3: 4.30%; and Component 4: 0.47%. Overall, use of unstandardized rather than standardized variables accounts for a modest increase in the total variance within first three components from 99.53% to 99.83% and, therefore, components generated using unstandardized variables are preferable for combining into a 3-band composite image.

Cartographic Model 1 (Appendix A.1.1) summarizes the procedure for performing PCA using unstandardized variables and Appendix A.1.2 contains the PCA results in tabular

form. Principal Component Analysis reveals that bands 1, 3, and 4 contain the most variance, and therefore, include more information than any original band combination. Bands 1, 3, and 4 are combined into a 24-bit composite for visualization purposes and an 8-bit composite for use during subsequent cluster classifications. Similarly, 24-bit and 8-bit composite images are generated from components 1, 2, and 3. Cartographic Models 2-5 (Appendix A.2-A.5) summarize the procedure for creating 24-bit and 8-bit composites. Figures 5.1 and 5.2 present the 24-bit band and component composite images.

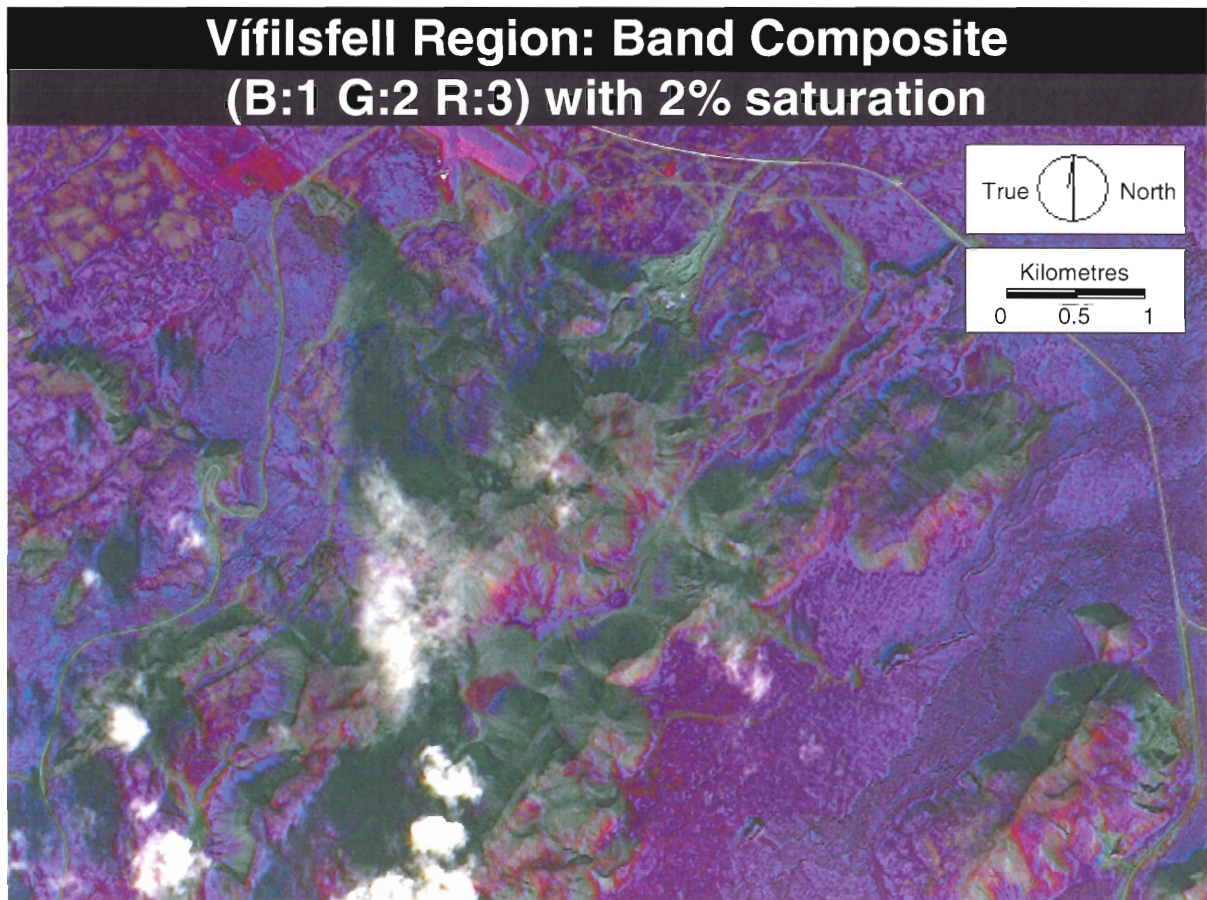


Figure 5.1: Band Composite image of the Vífilfell Region. SPOT 5 bands 1, 3, and 4 are combined into a 24-bit false colour image with 2% saturation and linear scaling. Band 1 (0.50 - 0.59  $\mu\text{m}$ ) is assigned to blue (B), Band 3 (0.78 - 0.89  $\mu\text{m}$ ) is assigned to green (G), and Band 4 (B4: 1.58 - 1.75  $\mu\text{m}$ ) is assigned to red (R).

## Vífilsfell Region: Component Composite (B:1 G:2 R:3) with 1% saturation

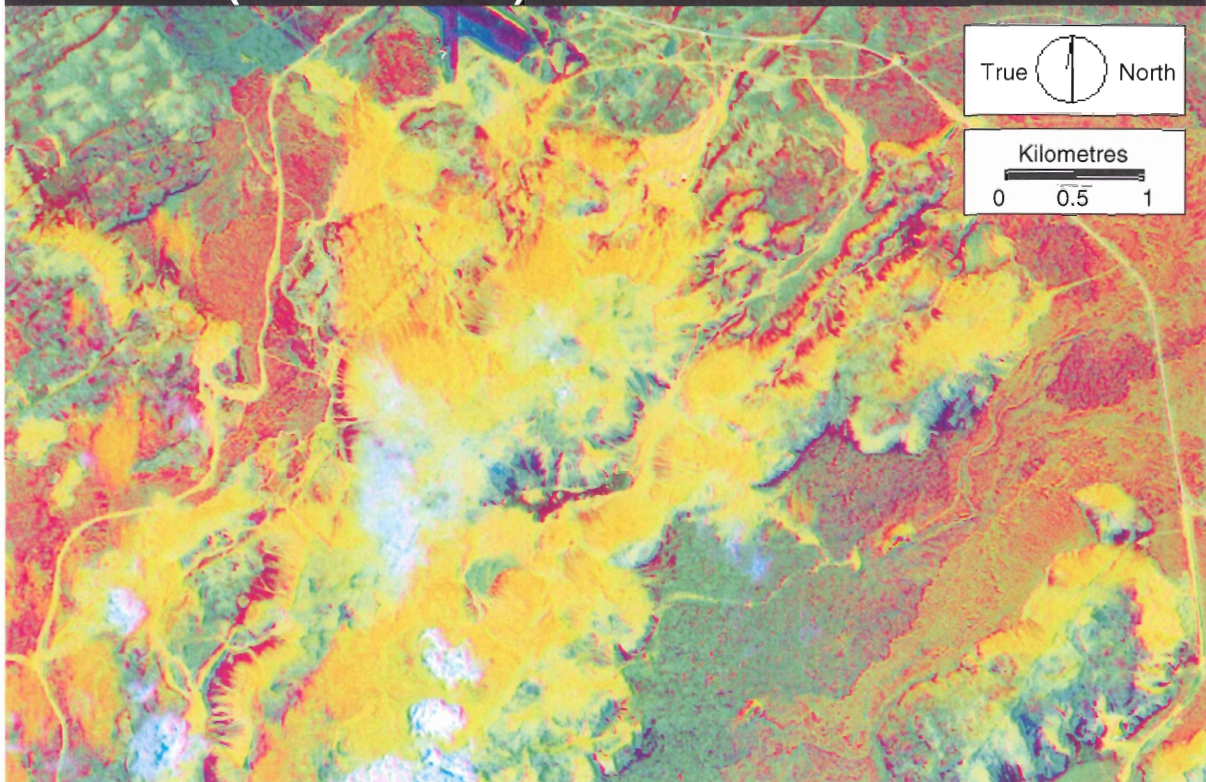


Figure 5.2: Component Composite image of the Vífilsfell Region. The first three components derived from Principal Components transformations of the original SPOT 5 data set are combined into a 24-bit false colour image. Component 1 is assigned to blue (B), Component 2 is assigned to green (G), and Component 3 is assigned to red (R).

Classification of 8-bit band and component composite images into discrete spectral clusters involves three stages: 1) first 8-bit composites are inputted into the cluster classifier with all clusters retained; 2) frequency distribution histograms and visual inspection are used to identify the maximum number of significant clusters; and 3) 8-bit composites are reclassified with a specified maximum number of clusters. Cartographic Models 6 (Appendix A.6.1) and 7 (Appendix A.7.1) review the procedure for classifying 8-bit band and component composite images. Figures 5.3-5.6 present the unsupervised classification results with all clusters retained and accompanying frequency distribution histograms. Appendix A (A.6.2 and A.7.2) portray the frequency distribution histograms numerically.

# Vífilsfell Region: B:1 G:3 R:4 Band Composite Cluster Classification (All Classes)

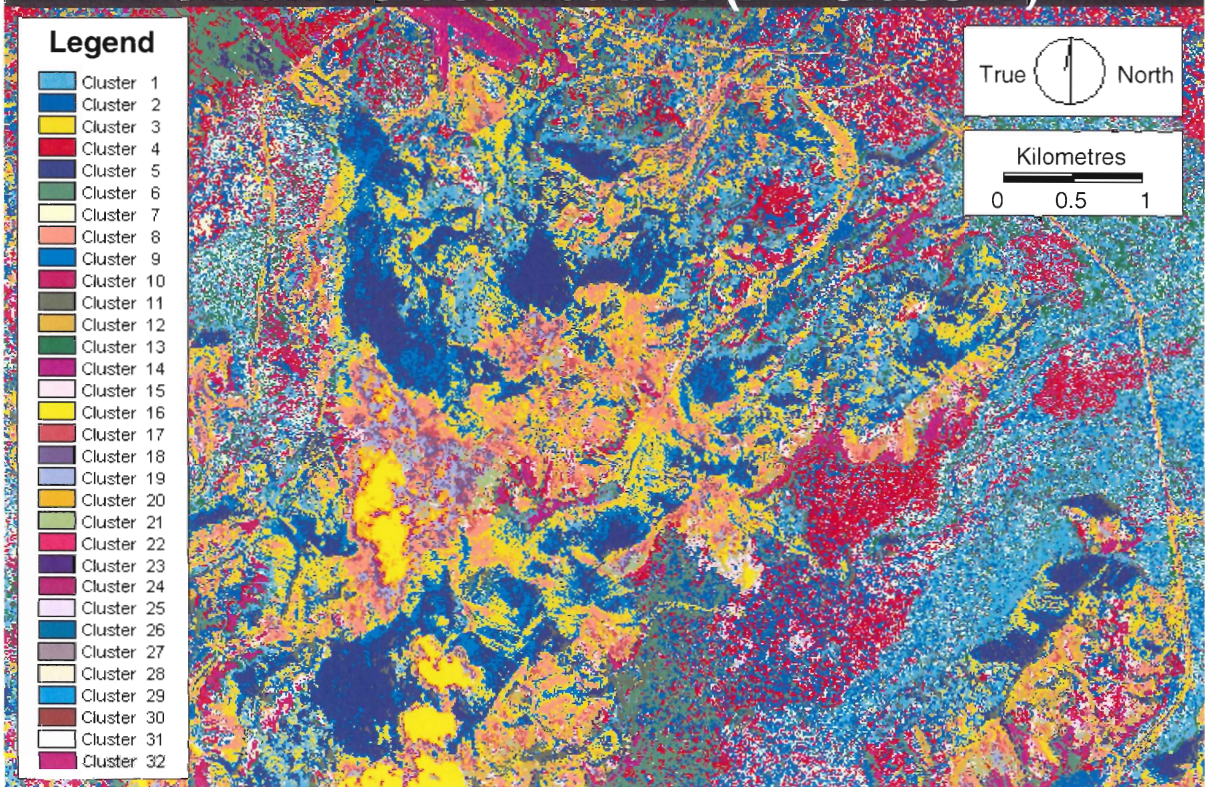


Figure 5.3: Band Composite Cluster Classification. The B1-B3-B4 8-bit band composite image is classified into spectral clusters. The classification generates 32 discrete clusters, all of which are retained in this image.

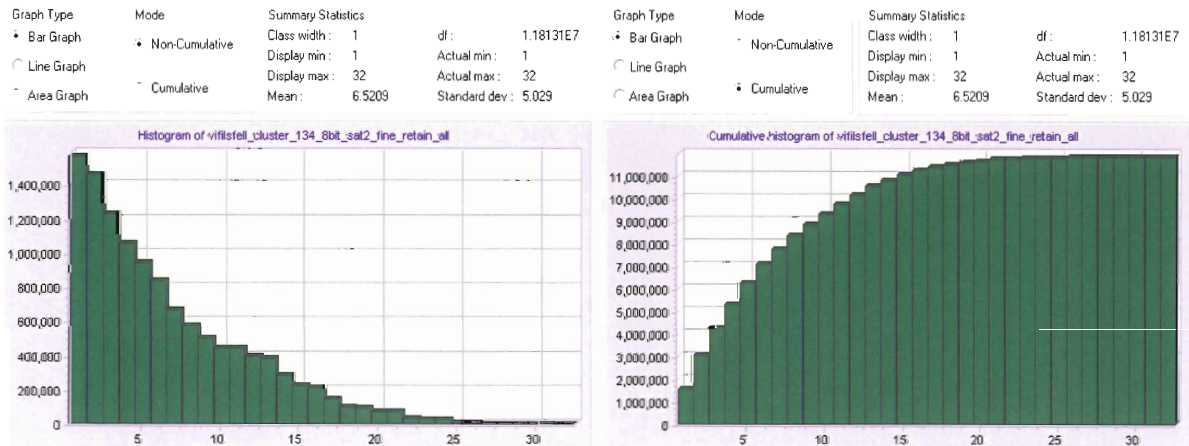


Figure 5.4: Frequency distribution histograms of the Band Composite Classification. Left: Non-cumulative frequency distribution histogram. Right: Cumulative frequency histogram. Clusters greater than 16 have less than 1% of the total pixel frequency each and do not contribute significantly to the image classification.

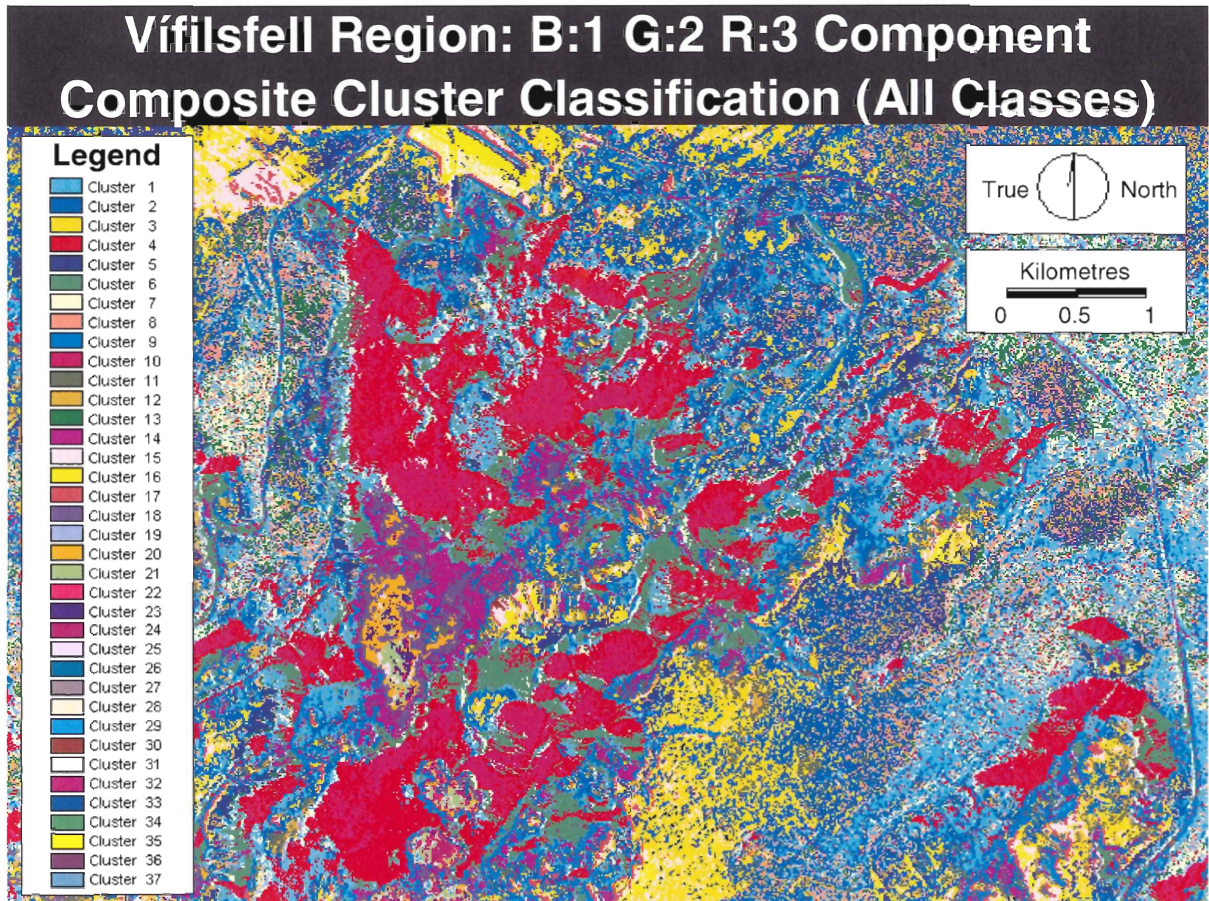


Figure 5.5: Component Composite Cluster Classification. The C1-C2-C3 8-bit component composite image is classified into spectral clusters. The classification generates 37 discrete clusters, all of which are retained in this image.

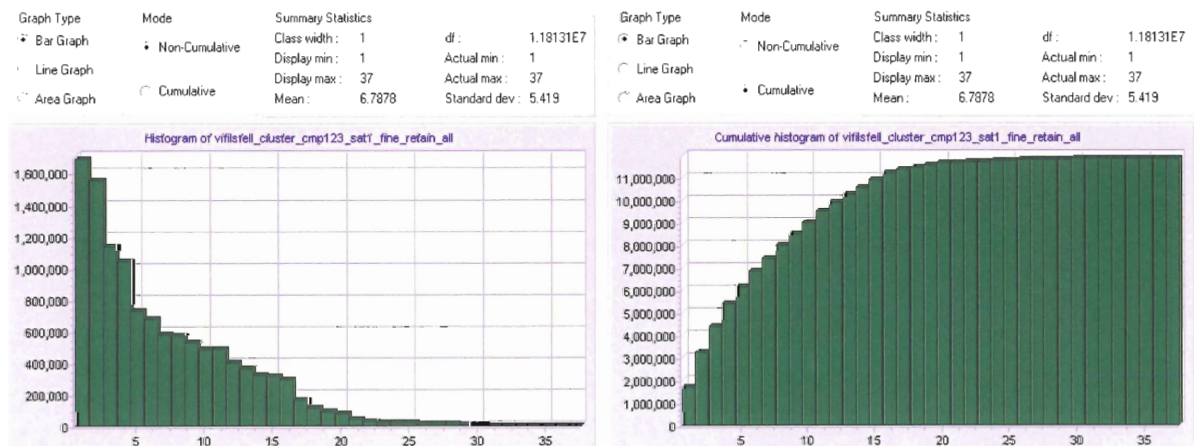


Figure 5.6: Frequency distribution histogram of the Component Composite Classification. Left: Non-cumulative frequency histogram. Right: Cumulative frequency distribution histograms. Clusters greater than 16 have less than 1% of the total pixel frequency each and do not contribute significantly to the image classification.

The band composite classification generates 32 clusters, of which the first 16 clusters have a cumulative proportion of 96.34%. All clusters greater than cluster 16 have frequency proportions less than 1%. The classification result for the component composite image is similar to the band composite classification. The component composite classification includes 37 discrete clusters with clusters 1 to 16 having a cumulative proportion of 94.47%. Clusters from 17 to 37 each have frequency proportions less than 1%. Clusters with frequency proportions less than or equal to 1% are deemed insignificant and, therefore, in both the band composite and component composite classifications the maximum number of significant clusters is 16. To verify that clusters greater than 16 are truly insignificant, the distribution of pixels within each cluster is examined individually to search for patterns of spatial organization.

Examination of the spatial distribution of low frequency clusters in the band composite classification reveals that 10 of the 16 low frequency clusters belong to two information classes with high spectral severability: cloud cover and vegetation. Clusters 18, 19, 20, 21, 24, and 26 correspond to concentric zones within clouds in the southwest quadrant of the image. The spectral signature of a cloud of water droplets depends largely on cloud density and thickness, both of which affect scattering and absorption of incident sunlight. A single cloud with variable density and thickness can, therefore, include a large number of discrete clusters, all of which have similar, but differentiable, spectral signatures. Clusters 22, 23, 25, and 26 are in close proximity to one another and define different sections of the grass-covered air strip in the northwest quadrant of the image. Clusters 17, 28, 29, 30, 31, and 32 show no evident spatial groupings and do not clearly correspond to a particular information class.

In the component composite classification, 9 of the 21 low frequency clusters correspond to cloud cover (clusters 18, 20, 21, 22, 23, 24, 25, 26, and 29) and two additional clusters represent air strip vegetation (clusters 28 and 31). Clusters 17, 19, 27, 30, 32, 33, 34, 35, 36, and 37 do not exhibit clearly defined spatial groupings.

To develop the final band and component composite classifications, the 8-bit composite images (B1-B3-B4 and C1-C2-C3) are reclassified with a maximum number of clusters set to 16. Cartographic Models 6 (Appendix A.6.1) and 7 (Appendix A.7.1) detail the procedure for generating the second set of cluster classifications. Figures 5.7 and 5.8 present the results of new cluster classifications.

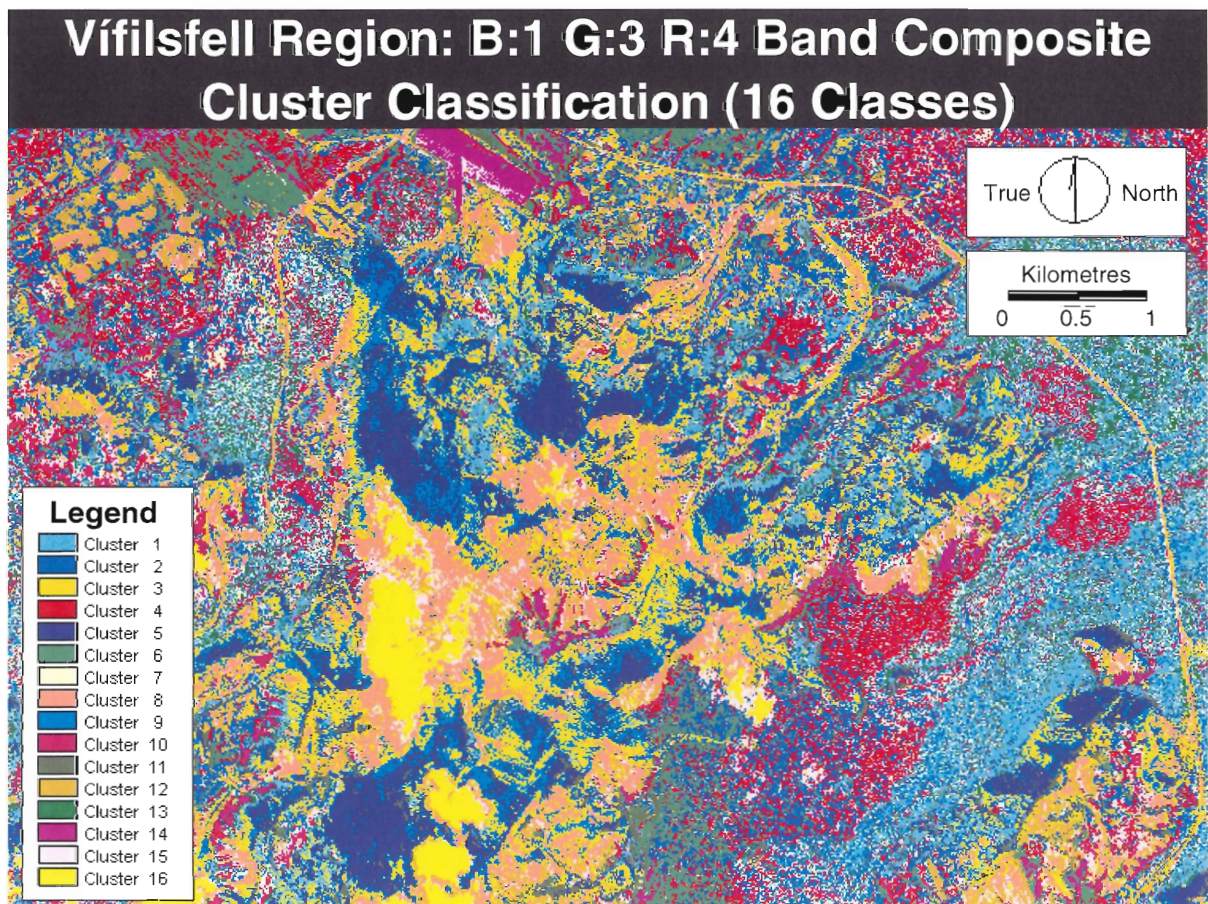


Figure 5.7: Band Composite classification with cluster threshold. The 8-bit band composite image (B1-B3-B4) is reclassified with a maximum number of clusters set to 16. The imposed cluster threshold forces low frequency clusters into higher frequency clusters with the most similar spectral signatures.

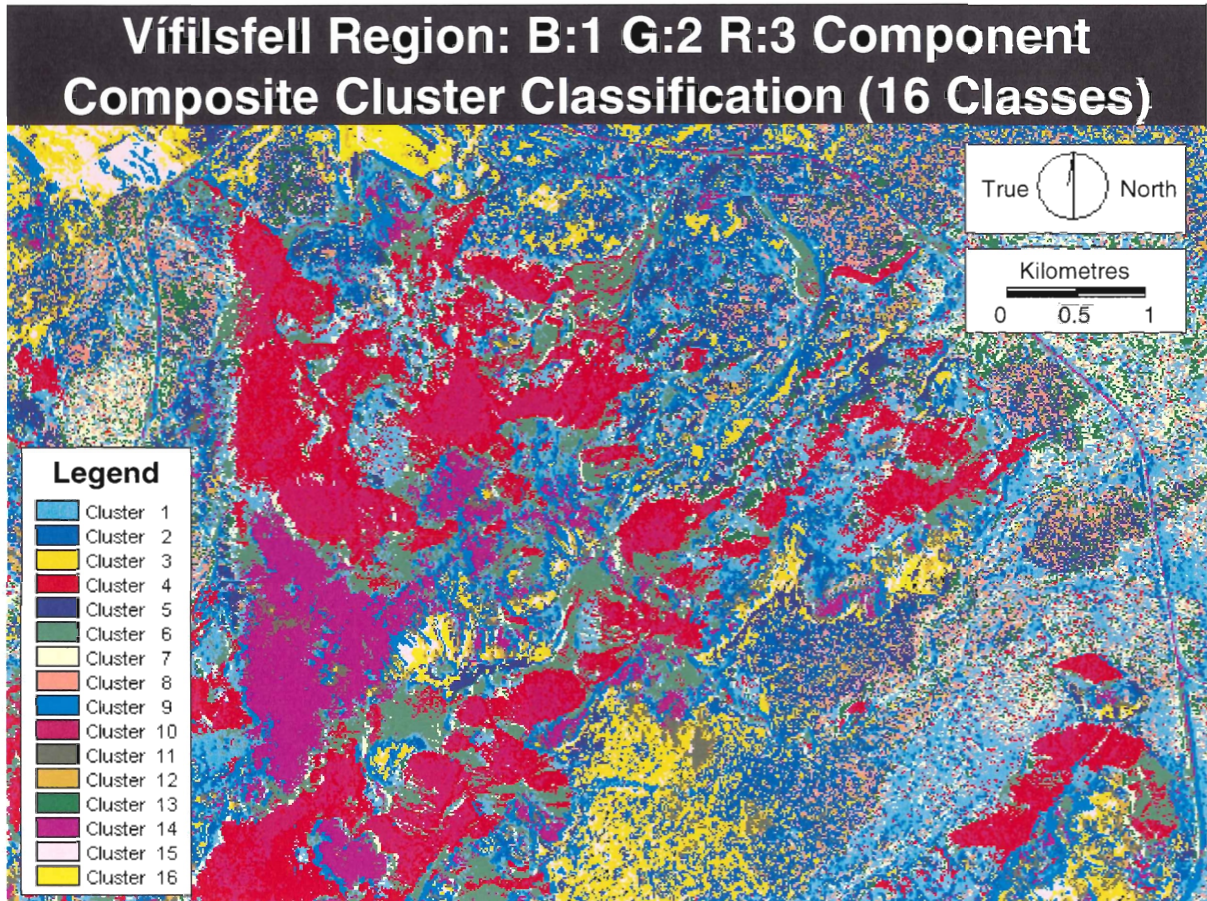


Figure 5.8: Component Composite classification with cluster threshold. The 8-bit component-composite image (C1-C2-C3) is reclassified with a maximum number of clusters set to 16.

Within the new cluster classifications, low frequency clusters present in the original classifications are forced into clusters with the most similar spectral signatures. Low frequency clusters that represent information classes with high spectral variability, such as cloud cover and vegetation, are consequently amalgamated into high frequency clusters with similar spectral characteristics and, presumably, common informational identity.

Chapter 6 presents an interpretation of ground cover types for each significant cluster within the band and component composite classifications. Chapter 6 contains a discussion of the accuracy of the remote sensing classification based on field observations within the study region.



## 5.2 Field Observations

The Bláfjöll mountains, located in the eastern section of the Reykjanes Peninsula, span a distance of approximately 12 km, trending southwest-northeast. Northern Bláfjöll represents the northernmost region within the Bláfjöll mountain chain. Northern Bláfjöll rises from a gently sloping plain with an elevation of approximately 120 m above sealevel (asl). Northern Bláfjöll is a steep-sided volcano with a plateau located approximately 530 m asl. Vífilfell directly overlies Northern Bláfjöll plateau and has peak elevation of 655 m asl. Arnarþúfur deposits extend from the base of Northern Bláfjöll towards the northwest.

Field observations provide a basis for interpreting lithostratigraphic relationships between ice-contact lithofacies in the Vífilfell Region, and for determining which ground-cover types contribute to the spectral clusters identified during the remote sensing analysis. During the field survey, 83 observation sites were established, of which 75 are precisely defined with GPS coordinates. The field observation sites group into 13 general zones (Figure 5.9). Zone 1 is an active gravel quarry that exposes basal pillow lavas from Northern Bláfjöll. Zones 2 and 3 are cliff exposures that include deposits from the upper section of Northern Bláfjöll and the contact between Northern Bláfjöll and Vífilfell. Zone 4 consists of peripheral Vífilfell deposits. Zone 5 corresponds to the outer crater region of Vífilfell, and Zone 6 to the Vífilfell vent region. Zone 7 is a channel with Vífilfell deposits that extends away from the vent region. Zone 8 defines the peak of Vífilfell. Zones 9, 10, and 11 respectively represent the proximal, central, and distal regions of Arnarþúfur. Zone 12 corresponds to a section of lava flow that underlies Arnarþúfur and Zone 13 includes an isolated deposit of aeolian sediment that appears derived from hyaloclastite.

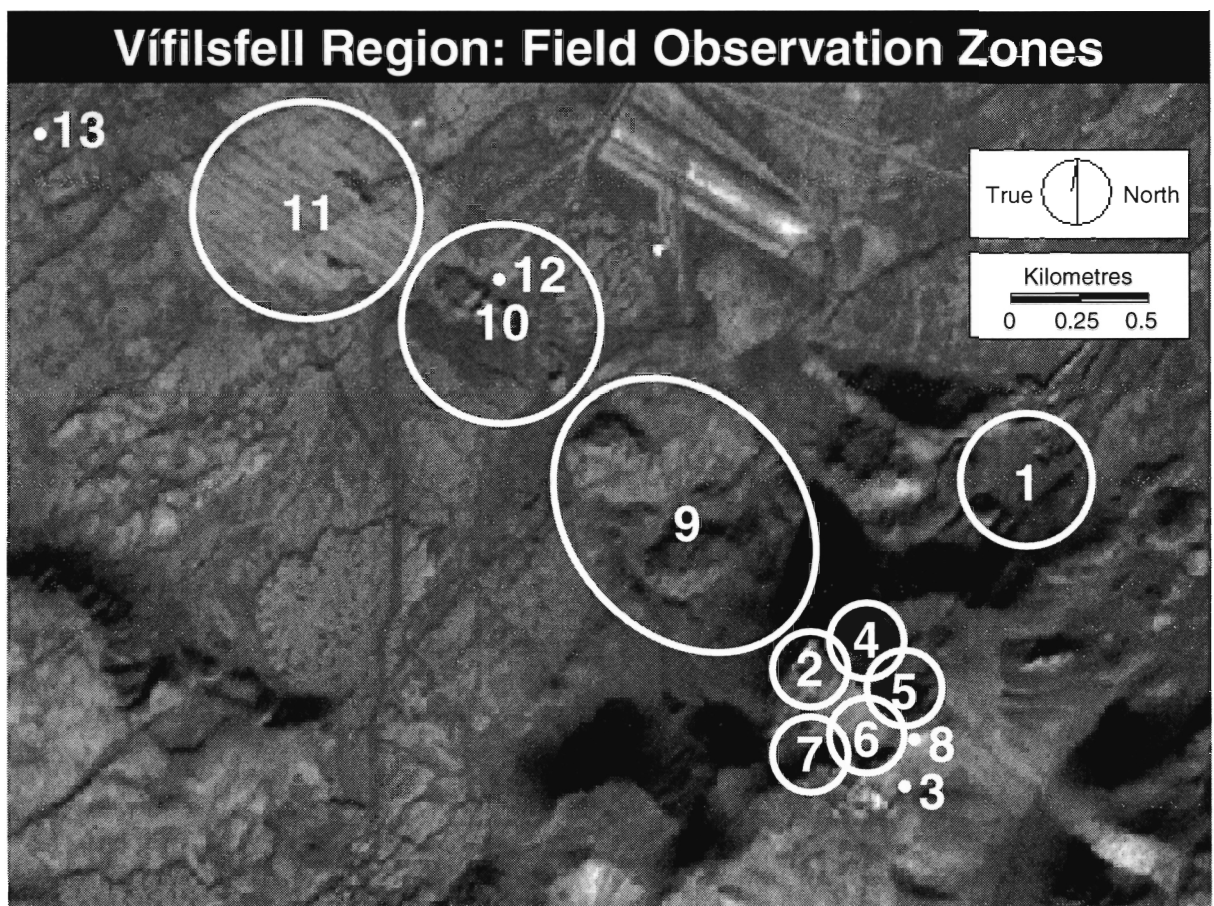


Figure 5.9: Field observation zones. Zone 1 contains pillow deposits from Northern Bláfjöll. Zones 2 and 3 include both Northern Bláfjöll and Vífilfell deposits. Zones 4-8 correspond to Vífilfell deposits, which dominantly include hyaloclastite. Zones 9-11 represent Arnarþúfur hyaloclastite deposits. Zone 12 includes an outcrop of subaerial lava that underlies Arnarþúfur and Zone 13 corresponds to an isolated deposit of aeolian sediment.

Appendix B.1 provides outcrop descriptions for each of the 83 observation sites with reference to the zones described above. The summary below provides synthesis of the observation table presented in Appendix B.1. To facilitate subsequent discussion of deposits within the Vífilfell Region, Northern Bláfjöll deposits are represented with blue (light blue for unconsolidated detritus and dark blue for *in situ* material), Vífilfell deposits are depicted with red, and Arnarþúfur deposits are coded yellow (Figure 5.10).

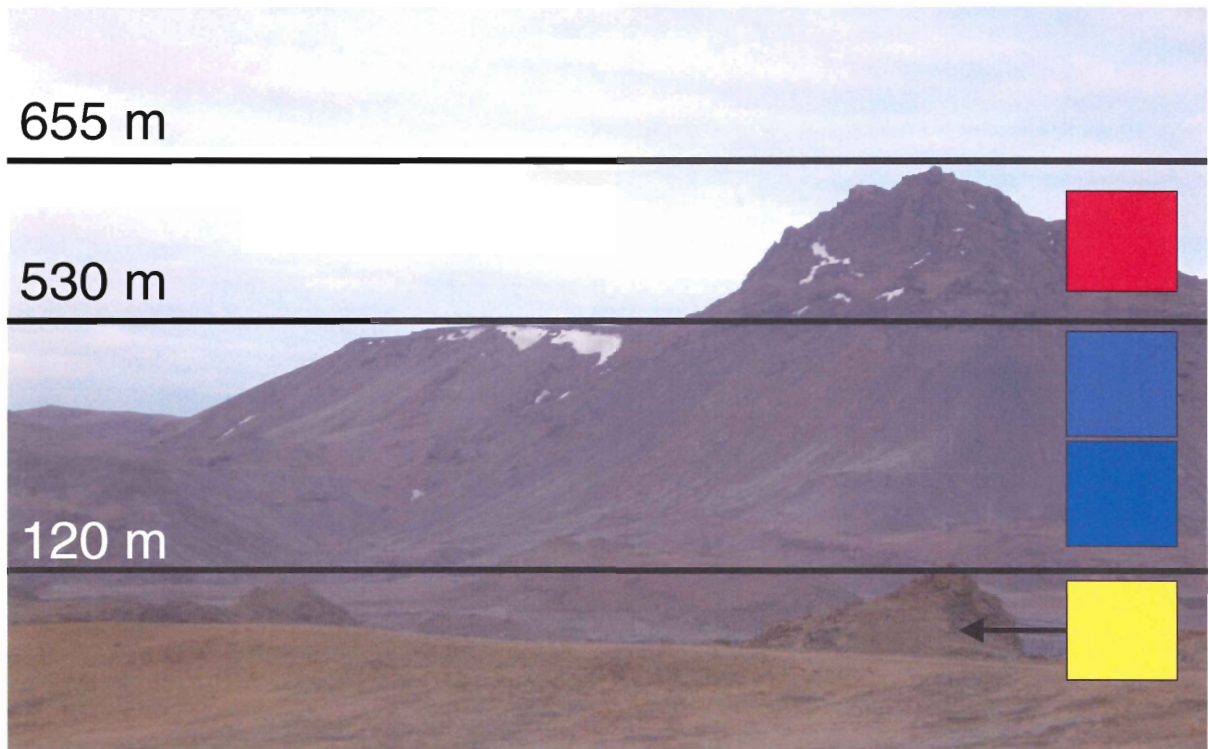


Figure 5.10: Northern Bláfjöll, Vífilfell, and Arnarþúfur viewed from the northwest. The plain surrounding Bláfjöll is 120 m above sea level (asl), the upper surface of the Northern Bláfjöll lava plateau is 530 m asl, and the peak of Vífilfell is 655 m asl. Arnarþúfur deposits are represented with yellow, Northern Bláfjöll deposits with blue (light blue for scree and dark blue for *in situ* material), and Vífilfell deposits colour coded red.

Northern Bláfjöll includes basal pillow lava deposits that are well-exposed in a gravel quarry to the north (Figure 5.11). Mantling of the lower flanks of Northern Bláfjöll beneath scree deposits obscures exposures of *in situ* material. In the upper regions of Northern Bláfjöll, slopes become increasingly steep, and well-exposed cliff outcrops are common. On the northwest side of Northern Bláfjöll, a lithofacies transition occurs within the upper cliff section between approximately 492 and 499 m asl. The lithofacies transition corresponds to a change from subaqueous to subaerial deposits. The transition begins where a thick accumulation of mixed hyaloclastite, scoria, and breccia (flow-foot breccia) forms a sharp contact with an overlying scoria unit that is 0.5 m thick. The thickness of the flow-foot breccia unit is unknown because the base of the deposit is not exposed. The scoria unit

contains undulating beds and forms a sharp contact with superincumbent intermediate lava that is 1 m thick. A 0.4 m thick lava flow with undulose contacts above and below overlies the intermediate lava unit. The 0.4 m thick lava flow supports a 1.7 m thick sheet lava unit, which is overlain by a 0.5 m thick scoria deposit with an undulose basal contact. A sharp planar contact at 499 m asl separates the scoria unit from a 6 m thick sheet lava flow (Figure 5.12). The planar contact corresponds to the upper surface of a passage zone and delimits the maximum water level elevation during the period of lava flow emplacement. The transition from subaqueously deposited flow-foot breccia to subaerial lava flows through a succession of transitional scoria and lava units is consistent with the model proposed by Jones and Nelson (1970) that considers relative motion of the volcanic pile and surrounding water level. Northern Bláfjöll deposits above the planar contact are exclusively composed of subaerial lava.

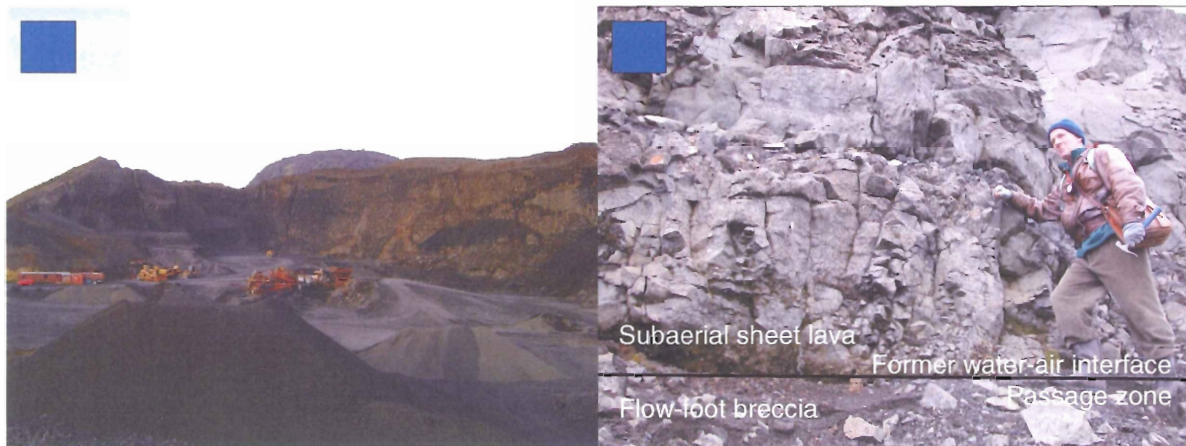


Figure 5.11 (left): Basal pillow lavas (Northern Bláfjöll). A gravel quarry to the north of Bláfjöll exposes basal pillow lavas.

Figure 5.12 (right): Passage zone (Northern Bláfjöll). An abrupt transition from mixed hyaloclastite and breccia (flow-foot breccia) to subaerial sheet lava corresponds to the passage zone that defines the water-air interface during lava flow emplacement. The elevation of the passage zone is approximately 500 m above mean sealevel.

Lava flow successions extend from the maximum passage zone elevation to the upper surface of the lava plateau at approximately 526 m asl. The upper lava surface has a well

preserved glassy selvage and contains parallel lineations that trend southeast-northwest (Figure 5.13). A sharp contact separates the Northern Bláfjöll lava plateau from Vífilfell deposits. Basal deposits from Vífilfell dominantly consist of palagonitized hyaloclastite, but also include angular lithic fragments near the contact. Pillow lavas are not present within the basal deposits of Vífilfell. On the southeast side of Vífilfell, bedded hyaloclastite deposits exhibit intense deformation (Figure 5.14). Deformed deposits conform to the underlying topography, and appear to have flowed down slope as a partially consolidated mass that warped and folded *en route*.



Figure 5.13 (left): Contact between Northern Bláfjöll and Vífilfell. A sharp contact divides Northern Bláfjöll lavas from overlying palagonitized hyaloclastite deposits that are part of Vífilfell. Parallel lineations on the upper surface of the Northern Bláfjöll lava plateau trend SE-NW and may represent glacial striae.

Figure 5.14 (right): Peripheral slump deposit (Vífilfell). Bedded hyaloclastite along the eastern margin of Vífilfell exhibits deformation.

Deposits of palagonitized hyaloclastite in the northern regions of Vífilfell contain rare dykes with pillowed surfaces. In the crater region of Vífilfell, volcanic bombs are prevalent (Figure 5.15). In contrast to the majority of Vífilfell deposits, the volcanic bombs are typically crystalline and, therefore, must have been excavated from underlying country rock. Within the crater region are localized zones where hyaloclastite has been zeolitized by hydrothermal alteration and low grade metamorphism. In the southeast section of the crater

region, approximately 554 m asl, is an anomalous scoria deposit. A 20 cm thick unit of massive hyaloclastite grades upwards into a 3 m thick scoria deposit that forms a sharp contact with an agglutinated scoria unit. The agglutinated scoria unit grades into a 1-3 m thick welded scoria deposit with an overlying agglutinated scoria unit that is 0.5 m thick. A deeply eroded hyaloclastite deposit overlies the scoria sequence. In the vent region, steeply inclined beds with undulating surfaces dip towards a single focus that corresponds to the location of the central vent (Figure 5.16). The vent-proximal deposits form a horseshoe-shaped mound within the crater that opens into a channel to the southwest. The channel curves northwest with distance from the vent and abruptly terminates at the edge of a cliff that has a vertical drop of several hundred meters. The cliff edge corresponds to the western margin of the Northern Bláfjöll plateau.



Figure 5.15 (left): Volcanic bombs (Vífilsfell). The crater region contains abundant volcanic bombs that are dominantly composed of crystalline material.

Figure 5.16 (right): Vent region (Vífilsfell). Thin beds with undulating surfaces dip towards a common center.

Arnarþúfur deposits include a series of discrete mounds of palagonitized hyaloclastite that extend approximately 2 km northwest from the base of Northern Bláfjöll (Figure 5.17).

With distance from Northern Bláfjöll, the mounds decrease in size and fan out from the central axis of the deposit (Figure 5.18).

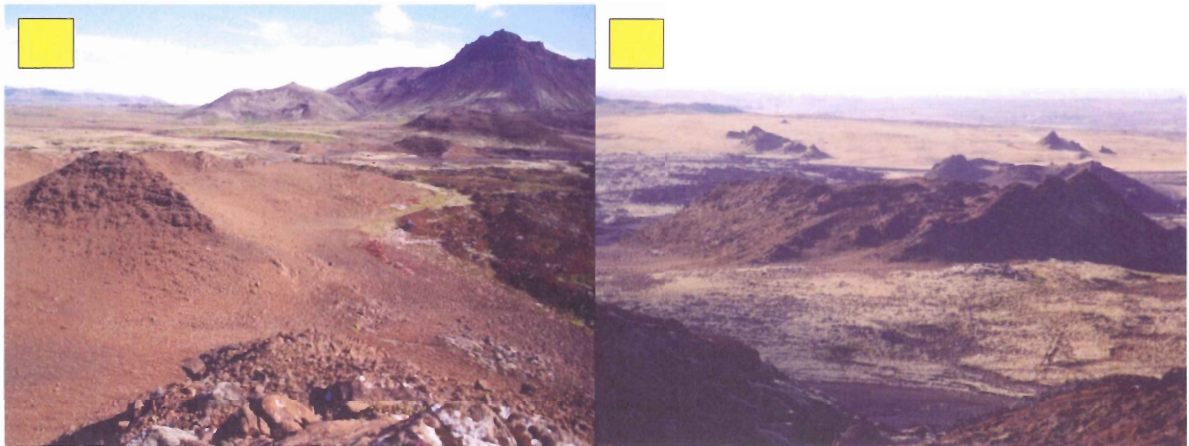


Figure 5.17 (right): Arnarþúfur viewed from the northwest. Palagonite outcrops form a discontinuous deposit that extends to the slopes of Northern Bláfjöll.

Figure 5.18 (left): Arnarþúfur viewed from the southeast. Arnarþúfur deposits viewed from Northern Bláfjöll appear as a series of discrete mounds that decrease in size towards the northwest. Overall, Arnarþúfur deposits have a lobate form that widens horizontally and thins vertically with distance from Bláfjöll.

In close proximity to Northern Bláfjöll, Arnarþúfur outcrops include well-bedded and massive deposits that contain angular to subangular clasts with diameters of <math><1-20\text{ mm}</math>, (modal diameter 4-5 mm). Rhythmic layering within outcrops is common and beds range from matrix supported to clast supported, with some beds containing up to 70% clasts. Clast-rich beds are more resistant to erosion than clast-poor beds. Differing rates of erosion accentuated the rhythmic bedding of layered outcrops (Figure 5.19). The proportion of armoured lapilli varies within beds, ranging from rare to abundant (Figure 5.20). Beds near the middle of the proximal deposits are concave down and dip away from the southeast-northwest trending central axis of Arnarþúfur. Near the margins of the deposit, bedding varies from planar to curvilinear.

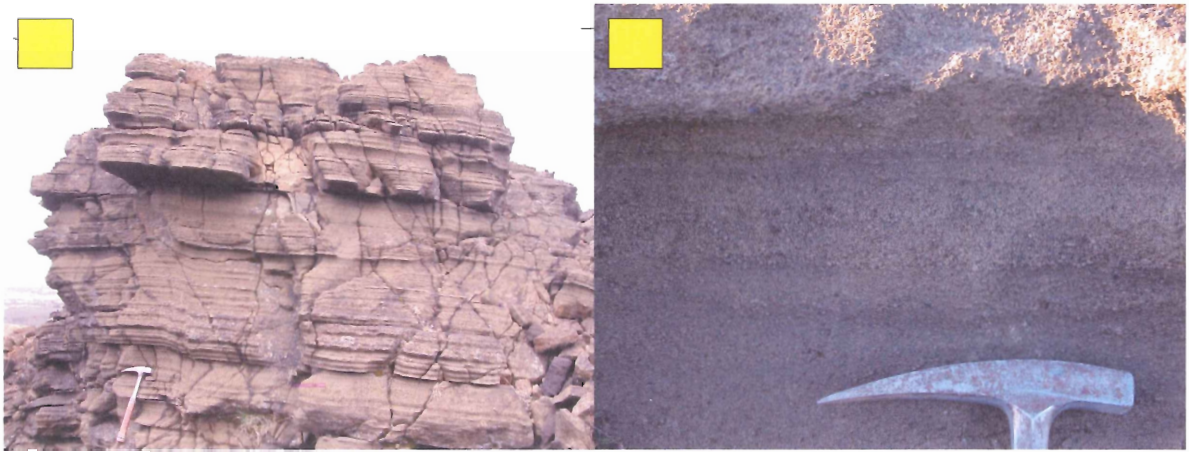


Figure 5.19 (left): Rhythmic bedding (Arnarþúfur). Bedded palagonite exhibits rhythmic layering between erosion-resistant coarse-grained beds and more deeply eroded fine-grained beds.

Figure 5.20 (right): Armoured lapilli (Arnarþúfur). Some beds with Arnarþúfur deposits are dominantly composed of armoured lapilli with glass clast cores.

Central Arnarþúfur deposits contain medium-grained subangular clasts and abundant armoured lapilli. Beds vary from planar to curvilinear with inclinations ranging from horizontal to vertical. Central deposits typically have well-defined rhythmic bedding, and some outcrops have beds dipping towards a central southeast-northwest trending axis with ripple marks on bedding surfaces that are indicative of down-dip flow. Flutes indicate a north-westerly flow direction (Figure 5.21) and climbing ripples, characteristic of unidirectional currents and high sedimentation rates, are common in central Arnarþúfur deposits (Figure 5.22). Bedding orientations vary substantially and commonly dip in opposite directions within individual outcrops (Figure 5.23). Beds range from matrix-supported to clast-supported with some beds having in excess of 80% glass clasts. Clasts typically range from 2-25 mm in diameter; however, in some beds clasts diameters may exceed 50 mm. Clasts are generally angular to subangular, and armoured lapilli are common.



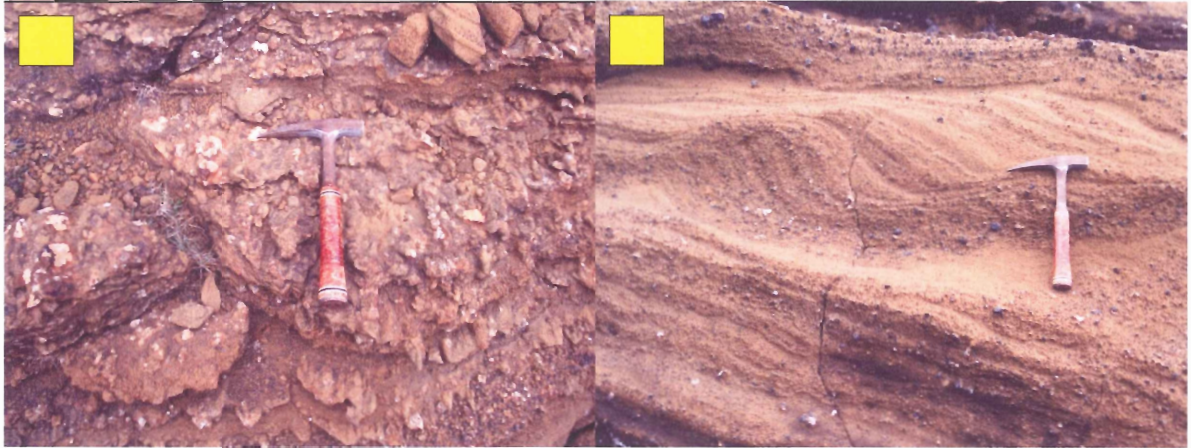


Figure 5.21 (left): Flutes (Arnarþúfur). Successive bedding surfaces exhibit prevalent flutes with southeast-northwest orientation.

Figure 5.22 (right): Climbing ripples (Arnarþúfur). Climbing ripples, indicative of high sedimentation rates from fluid flows, are common within central Arnarþúfur deposits.

Some beds within central Arnarþúfur contain a series of small strike-slip faults that are several meters in length and have displacements of 4-27 cm. Fault motions vary from sinistral to dextral. Small fractures extend perpendicular to the fault plane. The fault planes are nearly vertical and extend southeast-northwest. The orientation of these small faults is perpendicular to the direction of large southwest-northeast trending tectonic faults in the local region. Lava flows adjacent to Arnarþúfur deposits exhibit well-defined glacial striations that trend southeast-northwest.

In distal regions of Arnarþúfur, deposits consist of small isolated mounds of palagonitized hyaloclastite that diminish in size to meter-scale outcrops farthest from Northern Bláfjöll (Figure 5.24). Outcrops range from well bedded to massive. Bedding, where present, is planar. Clasts are generally fine-grained and subangular. Armoured lapilli are rare to absent. Northwest of the most distal Arnarþúfur deposits are thick (0.3-1 m) accumulations of very-fine grained aeolian sediments within local depressions. The aeolian sediments are rust to light brown in colour and appear derived from hyaloclastite; however, their source region is unknown.

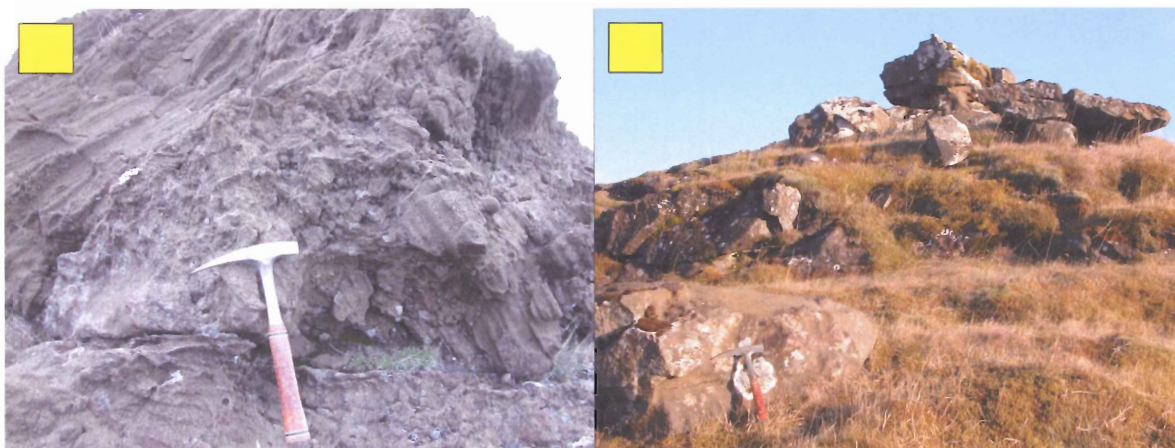


Figure 5.23 (left): Steeply inclined beds (Arnarþúfur). In the central region of Arnarþúfur, some outcrops contain steeply inclined beds with dips varying by  $180^\circ$ .

Figure 5.24 (right): Distal palagonite mounds (Arnarþúfur). The distal region of Arnarþúfur includes numerous meter-scale palagonite mounds.

### 5.3 Petrography and Geochemistry

Geochemical analysis of Vifilsfell Region involves three stages: 1) preliminary petrographic examination of thin sections to identify homogeneous and unaltered glass clasts; 2) electron microprobe analysis of suitable glass clasts to determine major element compositions; and 3) post-processing of the geochemical data to determine sample compositions and chemical trends.

#### 5.3.1 Petrographic Analysis

Thin sections prepared from hand specimens were examined using a petrographic microscope to identify glass clasts suitable for geochemical analysis. Within ideal glass clasts, microlites, inclusions, vesicles, and alteration are absent.

Of the nineteen thin sections from the Vifilsfell Region that were examined petrographically, eleven samples appear to contain homogeneous and unaltered glass. The eleven hyaloclastite samples include one from Northern Bláfjöll (Wpt094), three from

Vífilsfell (Wpt091, Wpt092, Wpt107) and seven from Arnarþúfur (Wpt042, Wpt043, Wpt051, Wpt059 (×2), Wpt060, Wpt070).

The fine-grained glass matrix within the sample from Northern Bláfjöll (Wpt094) exhibits intense palagonitization (Figure 5.25). Olivine and plagioclase microlites are present within the matrix and olivine phenocrysts are common. Seven glass clasts were selected for chemical analysis. The selected samples include two types: 1) homogeneous and unaltered glass clasts with diameters ranging from 0.2-0.4 mm, and 2) larger vesiculated clasts, 1-2 mm diameter, that contain minor microlitic inclusions of olivine and plagioclase in addition to homogenous and unaltered regions, 0.1-0.3 mm in diameter, which are suitable for sampling using the electron microprobe.

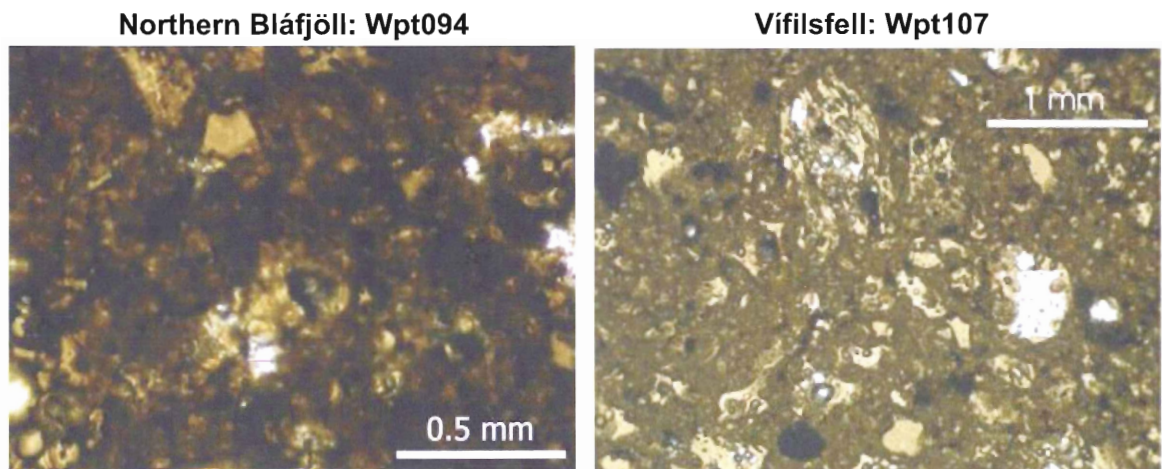


Figure 5.25 (Left): Photomicrograph of Northern Bláfjöll sample Wpt094. Plane polarized light. The dark-coloured matrix results from intense palagonitization of sideromelane glass (hyaloclastite).

Figure 5.26 (Right): Photomicrograph of Vífilsfell sample Wpt107. Plane polarized light. The skeletal olivine phenocryst (top-center) is indicative of rapid cooling within quenched melt.

Hyaloclastite samples from Vífilsfell (Wpt070, Wpt091, Wpt092, Wpt107) contain fine-grained matrix that is less altered than the sample from Northern Bláfjöll (Wpt094). The abundance of glass clasts ranges from rare (Wpt092) to common (Wpt091 and Wpt107).

Samples contain abundant olivine phenocrysts and opaques. Olivine phenocrysts commonly

exhibit skeletal growth (Figure 5.26). Glass clasts are vesicular and irregular, Type 2, to spherical and drop like, Type 4 (Wohletz 1983). In total, 30 homogenous and unaltered grains were selected from within the Vífilfell samples.

Arnarpúfur samples (Wpt042, Wpt043, Wpt051, Wpt059 (×2), Wpt060, Wpt070) contain palagonitized hyaloclastite matrix, however, the matrix is less altered than in samples from either Northern Bláfjöll or Vífilfell. Opaques and microlites of plagioclase and olivine are common within the fine-grained glass matrix (Figure 5.27). Olivine phenocrysts are abundant and are typically coated within ~0.1 mm thick glass shells (Figure 5.28). Glass clasts are abundant and include two principal varieties: blocky and equant grains, Type 1; and vesiculated and irregular pyroclasts, Type 2 (Wohletz 1983). Forty-nine homogenous and unaltered glass clasts were selected from the Arnarpúfur samples for subsequent geochemical analysis.

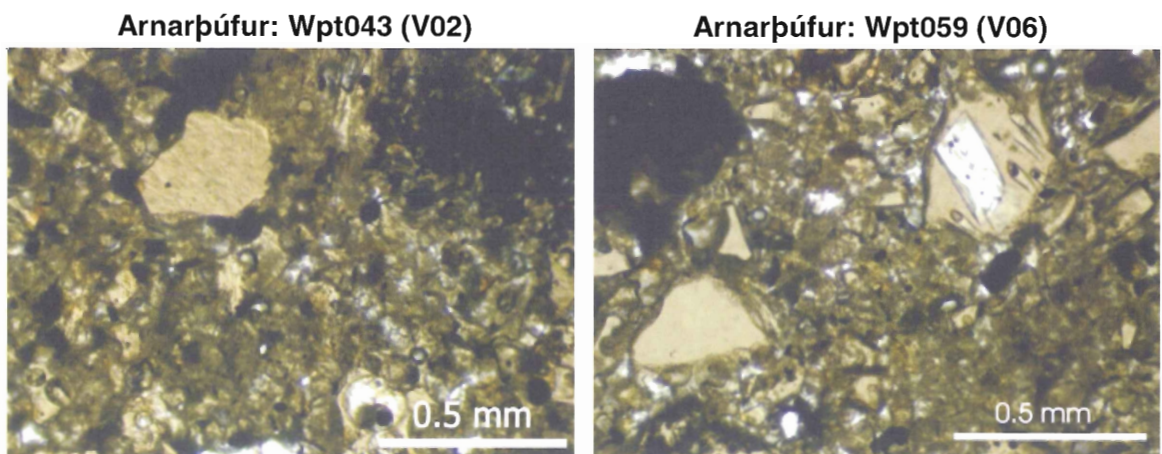


Figure 5.27 (Left): Photomicrograph of Arnarpúfur sample Wpt043. Plane polarized light. The blocky and equant (Type 1) pyroclast in the top-left of the image is typical example of the homogenous, unaltered, and microlite free glass clasts that were analyzed for major element compositions. The matrix contains fine-grained glass and opaques in addition to abundant olivine and plagioclase microlites.

Figure 5.28 (Right): Photomicrograph of Arnarpúfur sample Wpt059. Plane polarized light. The glass clast in the lower-left of the image exhibits a narrow hydration rim, and the glass clast in the top-right of the photomicrograph contains an olivine microphenocryst.

High magnification photomicrographs ( $\times 180$ -500) illustrate the clastic texture of hyaloclastite samples from Arnarþúfur (Figures 5.29 and 5.30). Figure 5.29 portrays an example of Type 2 phreatomagmatic pyroclasts with smooth vesicular embayments (Wohletz 1983). Figure 5.23 depicts hyaloclastite grains with 1-5  $\mu\text{m}$  thick hydration rims.

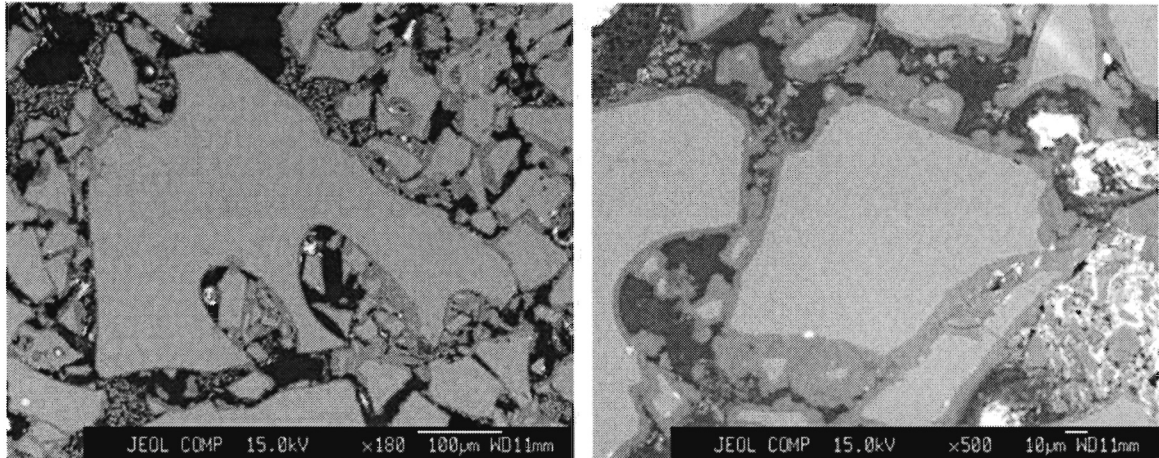


Figure 5.29 (Left): High-Magnification backscattered electron image of Arnarþúfur sample Wpt043 I. The sample exhibits a clastic texture with very fine glass fragments of the matrix nested within the vesicle embayments of Type 2 pyroclast.

Figure 5.30 (Right): High-Magnification backscattered electron image of Arnarþúfur sample Wpt043 II. Fine-grained glass fragments have a high surface to volume ratio are completely hydrated (altered to palagonite), whereas larger glass fragments have hydration rims surrounding unaltered glass cores.

### 5.3.2 Geochemical Analysis

Of the 98 glass clasts selected for geochemical analysis, 83 grains proved to be homogenous and unaltered under high magnification; the 15 heterogeneous grains were not analysed using the electron microprobe. Appendices C.1 and C.2 contain the major element compositions of glass samples. Appendix C.1 includes the original oxide weight percentages, whereas Appendix C.2 contains the original data normalized to 100%. Sample Wpt042 generated anomalous total weight percentages that range from 90.02 to 101.74% and, consequently, this sample was discarded from the data set. Figure 5.31 depicts an example of a Harker diagram ( $\text{K}_2\text{O}$  versus  $\text{SiO}_2$ ) and Figure 5.32 displays a plot of  $\text{CaO}$  versus  $\text{MgO} + \text{FeO}$ .

## Electron Microprobe Data: normalized oxide weight %

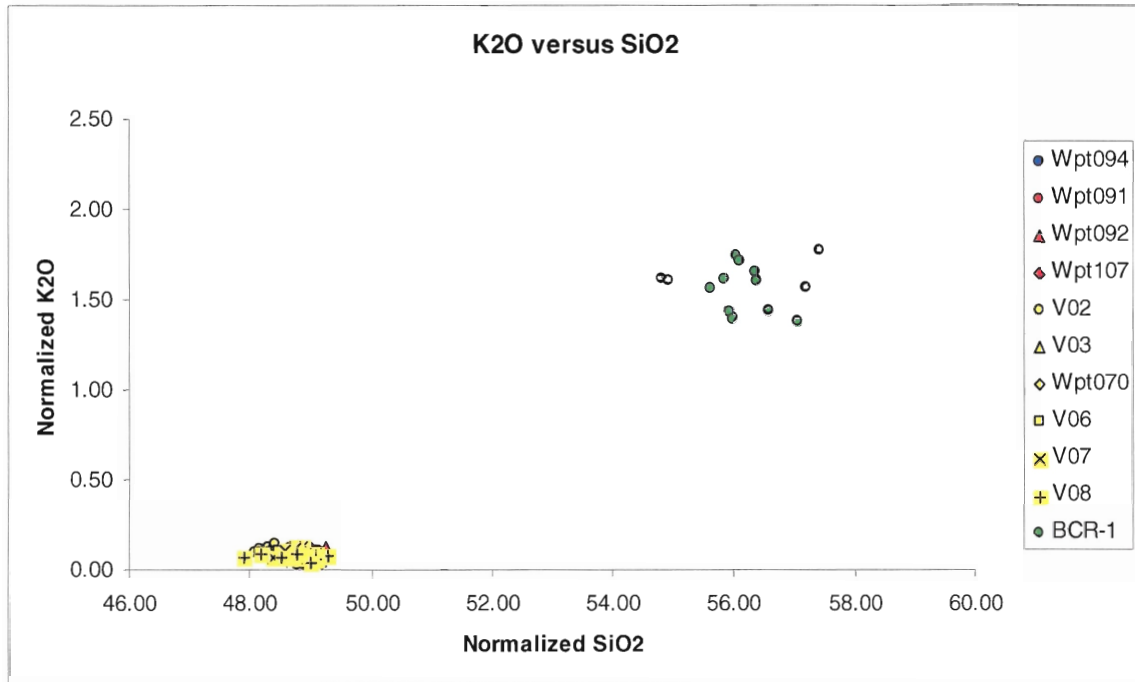


Figure 5.31.1: K<sub>2</sub>O versus SiO<sub>2</sub> with reference sample BCR-1.

## Geochemical analysis: normalized oxide weight %

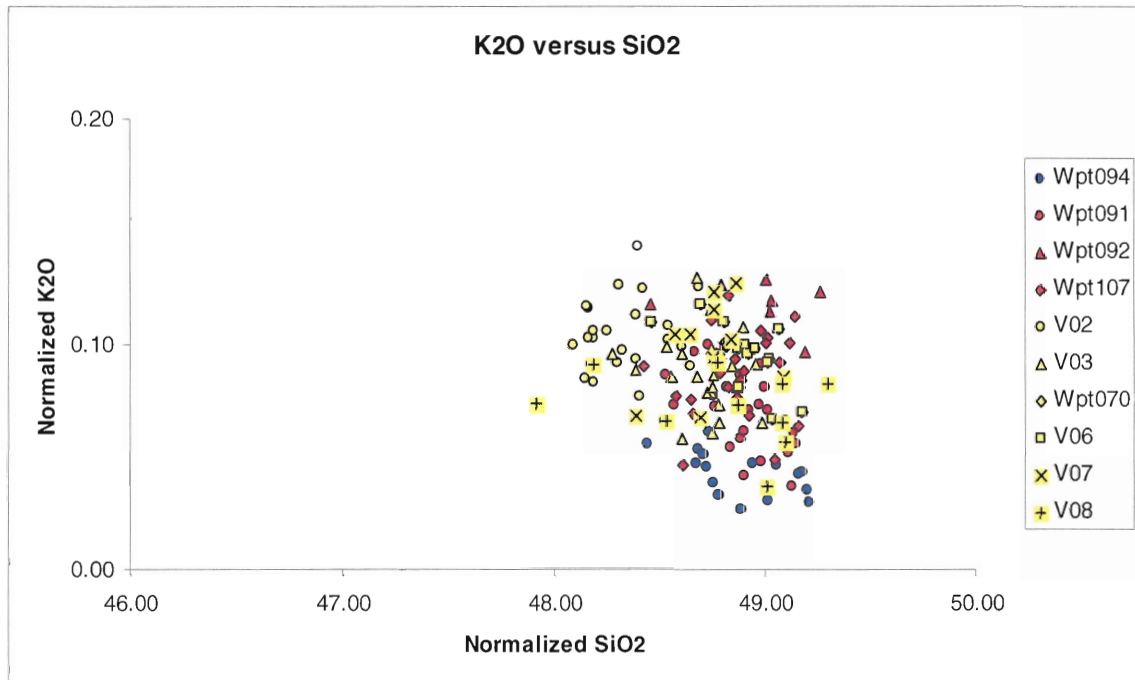


Figure 5.31.2: K<sub>2</sub>O versus SiO<sub>2</sub>. Enlarged view of Figure 5.26.1 illustrating the distribution of major element compositions of samples from the Vífilfell Region

## Electron Microprobe Data: normalized oxide weight %

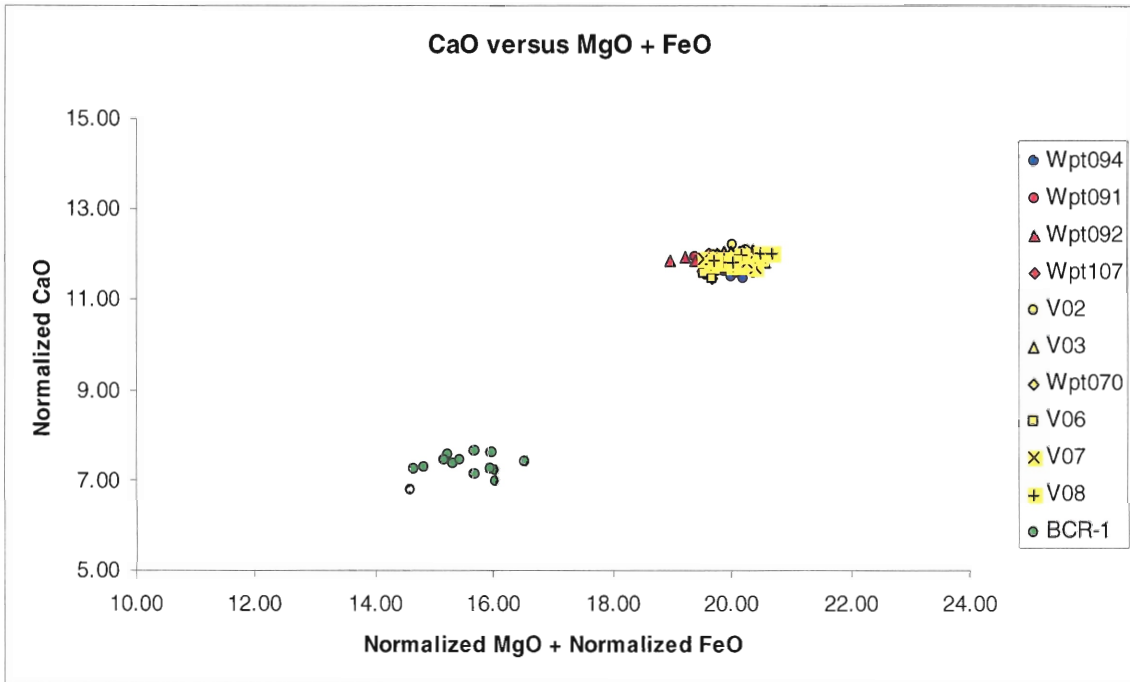


Figure 5.32.1: CaO versus MgO + FeO with reference sample BCR-1.

## Electron Microprobe Data: normalized oxide weight %

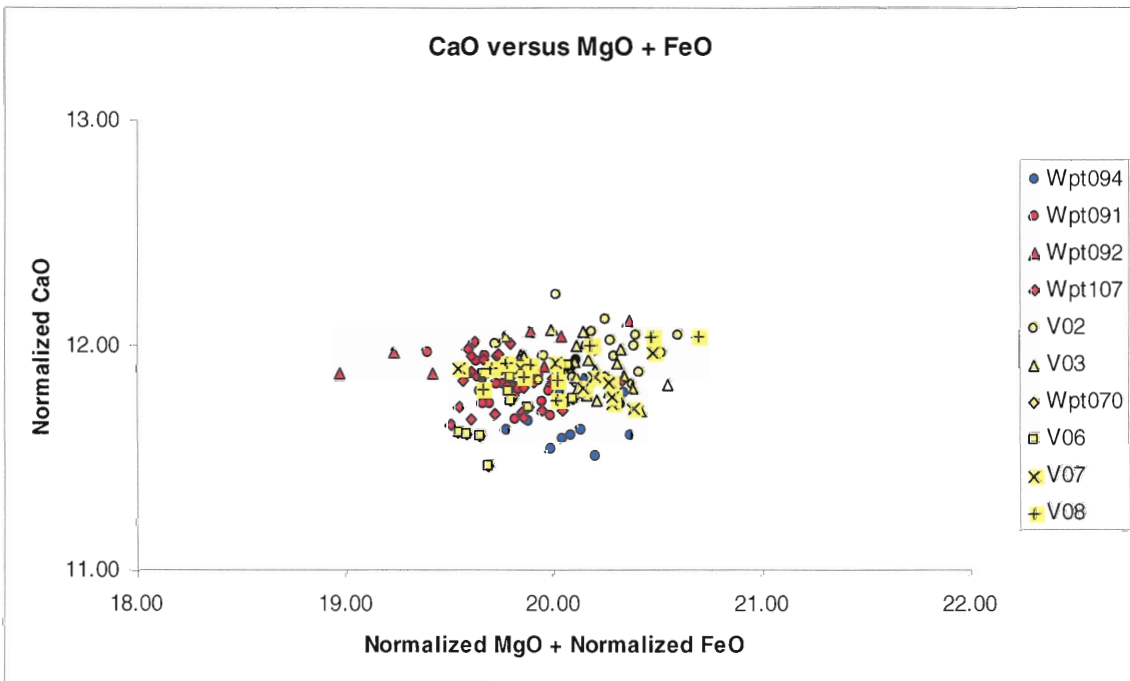


Figure 5.32.2: CaO versus MgO + FeO. Enlarged view of the Figure 5.27.1 illustrating the clustering of major element compositions of samples from the Vífilfell Region

The major element compositions of samples from the Vífilsfell Region plot in compact clusters with all graphs and show no evident fractionation trends. Appendix A.3 presents the CIPW normative mineralogy calculated from the normalized oxide weight percentages of each sample from the Vífilsfell Region, excluding Wpt042, and the reference sample BCR-1. Appendix A.4 contains hypersthene corrections for the CIPW normative data. In Chapter 6, the generalized basalt tetrahedron is used to plot the CIPW normative data and classify the sample compositions.



# Chapter 6 Discussion and Interpretation

## 6.1 Introduction

The investigation of ice-contact volcanism in the Vífilfell Region uses a combination of techniques that include: remote sensing, field observations, and geochemical analysis.

Classification of multispectral imagery provides an overview of the study region, and permits more efficient investigation of lithostratigraphy in the field by identifying specific regions of interest prior to conducting field surveys. Establishment of ground-control points enables assessment of the preliminary remote sensing classification and provides detailed lithostratigraphic information that is essential for interpreting the depositional history of ice-contact lithofacies in the study region. Subsequent geochemical analysis of samples collected in the field establishes the genetic relationship between the Northern Bláfjöll, Vífilfell, and Arnarþúfur, all of which are the principal ice-contact volcanic landforms within the study region.

## 6.2 Remote sensing

Unsupervised classification of the blue (B): Band 1, green (G), Band 3, and red (R): Band 4 (B1-B3-B4) band composite image, yields 32 clusters, of which 16 are significant (cumulative proportion 95.09%). The cluster analysis of the B: Component 1; G: Component 2; R: Component 3 (C1-C2-C3) component composite image generates 37 clusters, of which 16 are significant (cumulative proportion 94.67%). Patterns of pixel distribution are used to assign provisional land-cover types (information identities) to significant clusters. Figures 6.1 and 6.2 summarize the interpreted information identities of the band composite and component composite classifications. In the legends accompanying Figures 6.1 and 6.2, land-cover classes are ordered in descending pixel frequency (area). To facilitate comparison,

discrete spectral classes constituting a single information category (land-cover type) have not been amalgamated into one information class; instead, clusters with similar identity are assigned similar colours (i.e., the two discrete spectral classes that correspond to hyaloclastite in the band composite classification are assigned different shades of yellow).

## Interpreted Band Composite Classification

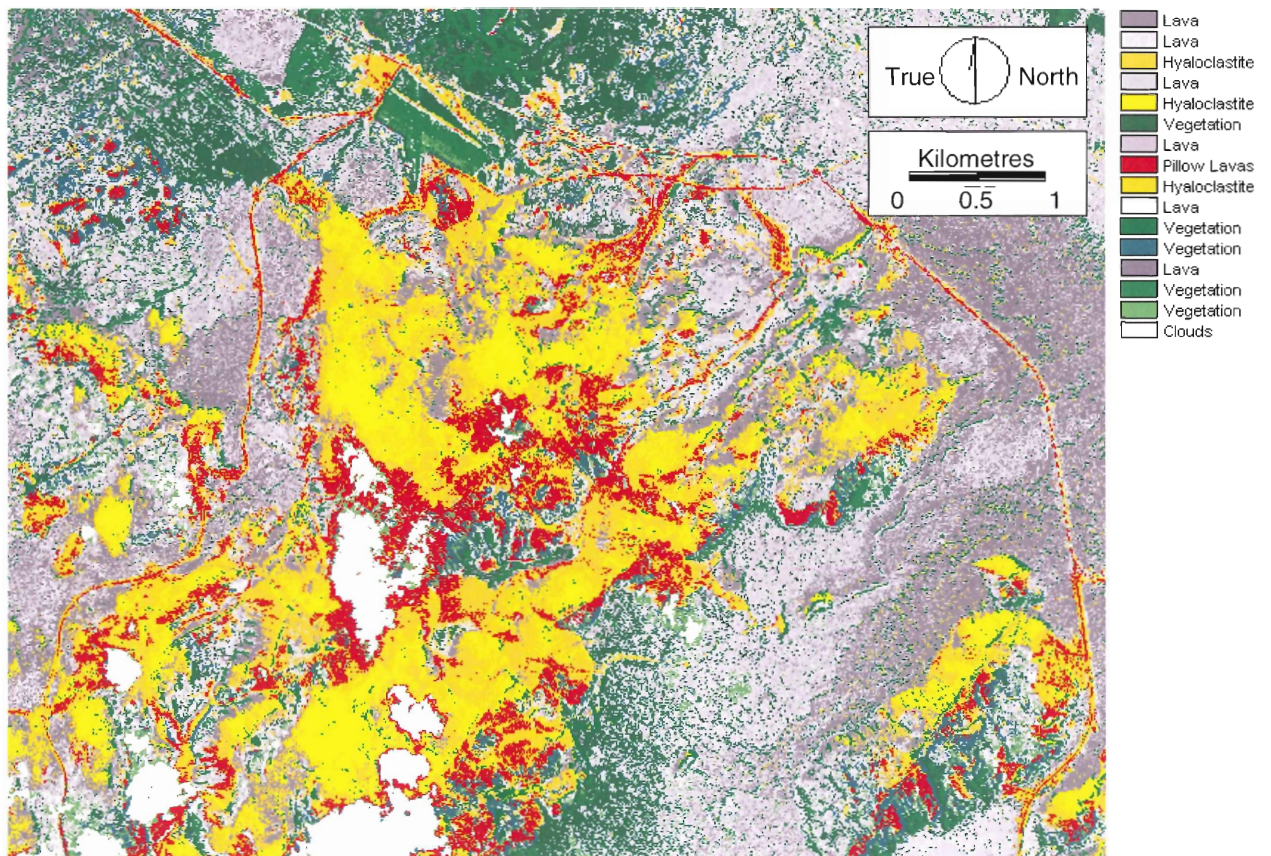


Figure 6.1: Band composite cluster interpretation. The band composite image includes five information categories: subaerial lava, pillow lavas, hyaloclastite, vegetation, and clouds.

The band composite includes 16 significant spectral clusters representing five distinct information classes: lava (grey), hyaloclastite (yellow), pillow lava (red), vegetation (green), and clouds (white). The dominant land-cover type in the study region is lava (grey), which includes six contributing spectral classes (clusters 1, 2, 4, 10, and 13). In the study area, the lava class includes two end-member types: rough lava, which casts intense shadows within

the flow field, and smoother lava with few associated shadows. Although lava types are highly variable, rough lava is tentatively assumed to correspond with a'a, whereas smooth lava represents pahoehoe. Flow fronts are discernible in the image, particularly in the southwest quadrant.

The hyaloclastite information category (yellow) includes three contributing spectral classes that have a close spatial association (clusters 3, 5, and 9). Hyaloclastite deposits concentrate in the center of the image along the surface and margin of the central massif, Northern Bláfjöll. A hyaloclastite-covered region, Arnarþúfur, extends northwest from Northern Bláfjöll across the surrounding plain. A sharp north-south termination of the hyaloclastite class coincides with the edge of the shadow cast by the large cloud in the southwest. The effect of shadowing, both from Northern Bláfjöll and from clouds, compromises the accuracy of the land-cover classification. In the southeast quadrant of the image, a second large hyaloclastite deposit is well exposed; however, the hyaloclastite class abruptly ends to the southeast of this exposure. The abrupt termination of this hyaloclastite class in the southwest presumably results from a combination of shadowing on northwest slope of the hyaloclastite ridge and mantling by vegetation on the southeastern slope.

The pillow lavas (red) outcrop in a gravel quarry to the north, along roads, and on the Northern Bláfjöll plateau. The pillow lava class has one contributing spectral cluster (cluster 8). Interpretation of cluster 8 as pillow lavas is based on its exposure within the quarry. The quarry extracts pillow lavas for road metal, hence the association of this class with roads and highways.

The vegetation information class (green) includes five spectral classes (clusters 6, 11, 12, 14, and 15). Clusters 14 and 15 cover a rectilinear region in the northeastern quadrant of the image. The rectilinear region corresponds to a grass-covered airstrip. Clusters 14 and 15

are, therefore, likely to represent grass, or similar vegetative-cover, in other regions of the image. Cluster 12 concentrates on southeastern slopes of high-relief features and within lava flows. Considering the association of cluster 12 with bare rock surfaces and steep slopes, this this vegetation class probably corresponds with mossy land-cover.

The interpreted component composite and band composite classifications contain equivalent information categories: lava, hyaloclastite, pillow lava, vegetation, and clouds. The information classes within the interpreted component composite image exhibit similar patterns of spatial distribution. The component composite classification, however, contains two additional lava classes and fewer classes of vegetation and hyaloclastite (Figure 6.2).

### Interpreted Cluster Composite Classification

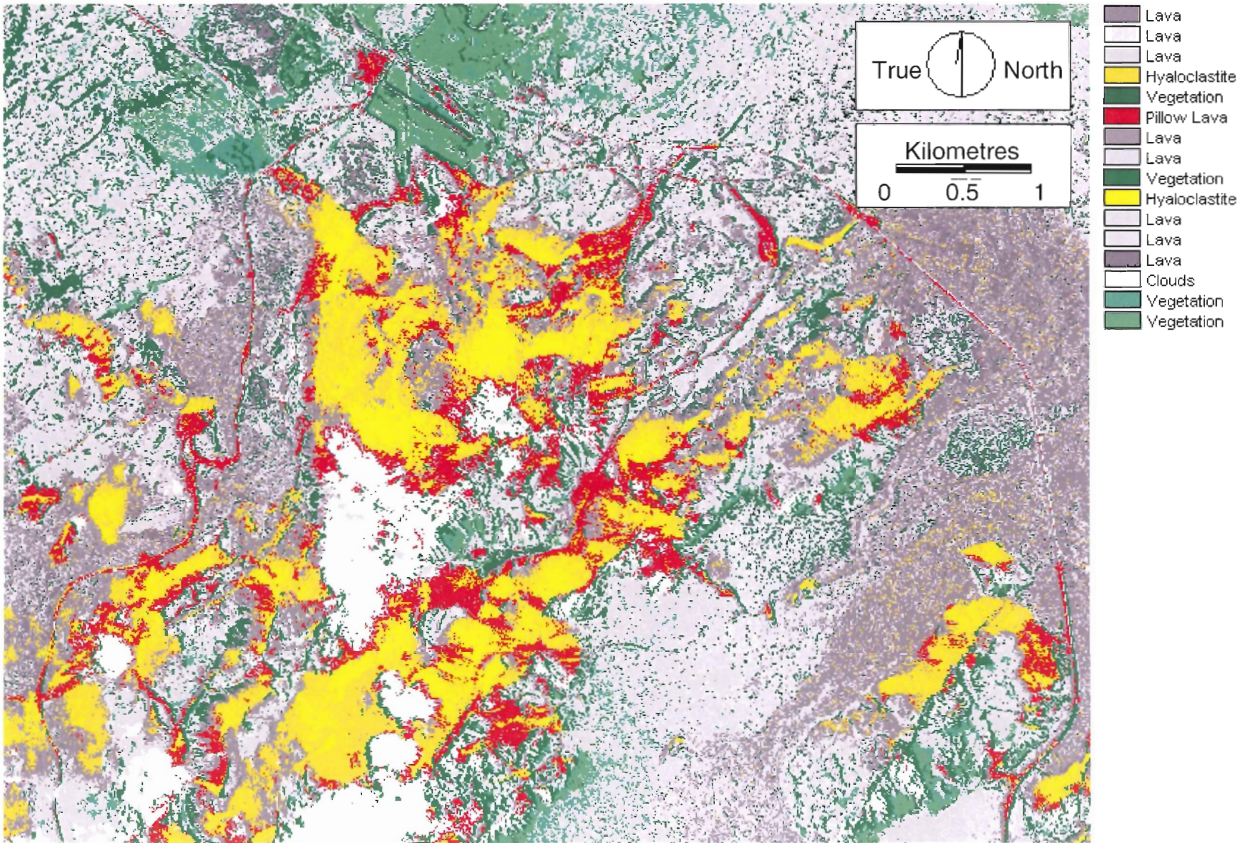


Figure 6.2: Component composite cluster interpretation. The component composite classification includes five information categories: subaerial lava, pillow lavas, hyaloclastite, vegetation, and clouds. The spatial distribution of pixels belonging to each information category is similar within the band and component composite classifications.

The band composite and component composite classifications generate similar results and typically contain multiple spectral clusters for a given information class. Amalgamation of land-cover types (clusters) into broader information categories produces generalized classifications that are useful for planning field surveys. The classifications provide an overview of the spatial distribution of materials within the study region; however, shadowing and mantling compromise the accuracy of the classification. Unsupervised classification of multispectral satellite imagery is, therefore, suitable for preliminary site investigation, but unsuitable for generating high quality geological maps.

### **6.3 Lithostratigraphic relationships**

Within the Vífilfell Region are three regions associated with Pleistocene ice-contact volcanism: Northern Bláfjöll, Vífilfell, and Arnarpúfur. These regions include high relief volcanic landforms containing abundant hyaloclastite deposits and minor exposures of pillow lava, scoria, flow-foot breccia, and subaerial lava. In the cluster interpretation, ice-contact lithofacies in the Vífilfell Region correspond to hyaloclastite and the mixed class associated with the hyaloclastite ridge. Field observations focus on regions where ice-contact lithofacies are the most prevalent in the remote sensing interpretation. Field surveys in Vífilfell Region enable detailed examination of lithostratigraphic relationships and provide a basis for evaluating the accuracy of the remote sensing land-cover interpretation. Description of the ice-contact landforms in the Vífilfell Region progresses from the oldest (Northern Bláfjöll) to youngest (Vífilfell and Arnarpúfur). Discussion of interglacial lavas in the Vífilfell Region is outside the scope of this section.

### 6.3.1 Northern Bláfjöll

Northern Bláfjöll is a flat-topped volcano with steep sides that contains basal pillow lavas, pillow-block breccia, altered hyaloclastite (palagonite), flow-foot breccia, welded scoria, and superincumbent subaerial lavas. Basal deposits of subaqueous crystalline lavas (pillow lavas and pillow-block breccia) indicate initial extrusion of magma beneath ice much greater than 200 m in thickness (Guðmundsson 2001). The progression from pillow lavas and pillow-block breccia to hyaloclastite represents a change in eruption style from passive effusion to explosive phreatomagmatic activity. The change in eruption style corresponds with a reduction in hydrostatic pressure that results from thinning of ice overlying the vent by melting. In approximately the uppermost 15 m of Northern Bláfjöll, deposits change from hyaloclastite to hyaloclastite and scoria deposits. The change in lithofacies represents a decrease in the efficiency of phreatomagmatic activity. Phreatomagmatic efficiency depends primarily on the availability of external water (Chapter 3). Variation in water availability could result from restriction of external water from the volcanic vent by accumulation of volcanoclastic sediments in the vent region, from water level fluctuations in response to sudden water drainage of the englacial lake, or from gradual changes in the ice-melt rate relative to meltwater drainage.

Continued construction of the Northern Bláfjöll causes emergence of the volcanic pile from the surrounding englacial meltwater lake. Subaerial lava effusion begins when the rate of water recharge into the vent system falls below the threshold for explosive phreatomagmatic activity. Lava spreading from the volcanic vent encounters water along the margins of the volcanic pile and, in the presence of water, lava surfaces cool rapidly and fragment into hyaloclastite. Enhanced cooling rates cause the lava flow to fracture internally and brecciate. Flow-foot breccia, consisting of hyaloclastite and lava blocks, cascades from

the flow front through the water to form a prograding delta upon which subsequent subaerial lava flows advance. The passage zone between the flow-foot breccia and overlying subaerial lavas represents the elevation of the englacial lake at the time of emplacement and provides a minimum estimate of the surrounding ice thickness (Jones 1969, 1970; Jones and Nelson 1970). The maximum passage zone elevation within Northern Bláfjöll is approximately 400 m above the surrounding plain and, therefore, the ice thickness during the emplacement of Northern Bláfjöll was greater than 400 m. Continued subaerial lava effusion and delta formation broadened the plateau of Northern Bláfjöll. Northern Bláfjöll is elongated along a north-south trending axis, suggesting that the structure results from a prolonged fissure eruption that did not concentrate on a single vent during its early stages.

Volcanic tremors and oversteepening of the prograding delta likely generated series of gravity flows and mass wasting events, the remains of which have not been preserved. The uppermost surface of the Northern Bláfjöll is well preserved with intact glass rinds covering lava surfaces. The upper surfaces of the subaerial lavas contain possible evidence of glacial striations with southeast-northwest orientations that indicate that Northern Bláfjöll was ice-covered prior to the onset of the Vífilfell eruption.

Stratigraphically, Northern Bláfjöll exhibits a standard tuya sequence (Mathews 1947). Jónson (1978) was correct in his interpretation that Northern Bláfjöll is a *stapi* (Icelandic for tuya); however, he also refers to Northern Bláfjöll as an intraglacial shield volcano and tablemountain. The terms intraglacial shield volcano and tablemountain are misleading for the following reasons: 1) tuyas do not exhibit shield morphology, and 2) all tablemountains are not of volcanic, let alone subglacial, origin. To avoid ambiguity, Northern Bláfjöll should be formally designated a tuya. Interpretation of an ice-contact origin for Northern Bláfjöll is reasonable considering the lithostratigraphy of the volcano, evidence of

glaciation in southwest Iceland (Thordarson and Hoskuldsson 2002; Geirsdóttir *et al* 2000), and the absence of paleotopography capable of damming a 400 m deep lake.

### **6.3.2 Vífilfell**

Vífilfell overlies Northern Bláfjöll and encompasses a conical mound of palagonite with isolated welded scoria, volcanic bombs, dykes with pillowed surfaces, and peripheral slump deposits. Vífilfell deposits rest directly on the surface of the Northern Bláfjöll lava plateau, and are separated from it by a sharp contact with no intervening till layers or soil horizons. The basal deposits of Vífilfell consist predominantly of hyaloclastite and do not include pillow lavas. The prevalence of hyaloclastite and absence of crystalline lava indicates that the initial phase of the Vífilfell eruption was explosively phreatomagmatic and, therefore, the thickness of the overlying ice was initially less than 200 m.

Bedding orientations clearly define a single vent that has a horse-shoe shape opening to southwest that curves northwest with distance. In vent-proximal beds, the prevalence of fine-grained hyaloclastite with small waveforms implies cycles of extrusion, fragmentation, and collapse of volcanoclastic material into the vent. In natural environments, such as the Vífilfell region, where repeated cycles of volcanoclastic extrusion and fragmentation modified primary grain sizes, reliable estimates of melt-water ratios and Molten Fuel-Coolant Interaction efficiency using grain-size analysis are not possible.

Volcanic bombs lacking well-defined impact sags illustrate that competent blocks of country rock, presumably derived from Northern Bláfjöll, underwent minimal lateral transport following ejection. Along the northwest and eastern margins of Vífilfell, peripheral slump deposits consist of palagonite with deformed bedding and are well preserved, whereas



to the west, palagonite deposits are steep-sided and terminate in sheer cliff faces at the edge of the Northern Bláfjöll plateau.

Welded scoria beds, approximately 475 m above the surrounding plain, have hyaloclastite deposits above and below. Alternation of hyaloclastite and welded scoria deposits provide evidence of significant water-level fluctuation during the Vífilfell eruption. The peak of Vífilfell is 655 m above mean sea-level and approximately 535 m above the surrounding plain. The peak of Vífilfell is composed of palagonitized hyaloclastite and does not include crystalline lavas.

Vífilfell is a subglacial mound constructed within an unstable meltwater lake following an initial subglacial eruption phase beneath thin ice. Volcaniclastic material generated during the Vífilfell eruption phase was deposited stably on the plateau of Northern Bláfjöll until the slopes of the conical mound exceeded their angle of repose and the material began to flow. To the east, mobilized volcaniclastic material abutted against ice, whereas to the west, material flowed into available accommodation space. The regional ice flow direction may account for the initial asymmetry in available accommodation space. Southeast-northwest trending glacial striations are consistent with the interpretation that the paleo-ice flow direction was towards the northwest. Water within glaciers follows a path that is approximately perpendicular to the equipotential surface of a glacier (Paterson 1994) and, therefore, meltwater associated with the Vífilfell eruption would have been forced to the northwest. Interaction between the southeasterly flowing ice and Northern Bláfjöll could have enhanced the initial asymmetry of the subglacial drainage system. The regional ice flow direction would produce a local compressive regime on the southeast side of Northern Bláfjöll where the ice encountered an immovable barrier, whereas on the opposite side of Northern Bláfjöll, a local extensional regime would result as ice flow velocities increased to

the northwest from a minimum near the northwest slope. The increase in pressure on the southeast side of Northern Bláfjöll would cause the ice to press directly against the slope. On the northwest side of Northern Bláfjöll, the extensional regime could have caused crevasses or moulins to develop in the ice.

A cavity may also have formed near the northwest slope of Northern Bláfjöll, where heat transfer from crystalline lavas melted the surrounding ice and ice-flow velocities were too slow to balance the rate of ice melting. Warm meltwater would rapidly expand an existing subglacial tunnel system, and could generate the accommodation space required to host volcanoclastic sediments generated during the Vífilfell eruption. The prevalence of abundant meltwater would, however, rapidly remove heat from the Northern Bláfjöll lavas and a cavity on the northwest slope would be ephemeral. The cavity could only have provided accommodation space for Vífilfell deposits if the Northern Bláfjöll and Vífilfell eruptions occurred in close succession.

Glacial striations on the upper surface of Northern Bláfjöll, in addition to the clear lithostratigraphic break between the Northern Bláfjöll plateau and the base of Vífilfell, indicate that ice mantled Northern Bláfjöll prior to the emplacement of Vífilfell. Infilling of ice into the englacial lake associated with the Northern Bláfjöll eruption enabled a second lake to form during the Vífilfell eruption that was stable at a higher elevation and capable of supplying sufficient water to sustain explosive phreatomagmatic activity.

### **6.3.3 Arnarpúfur**

During the Vífilfell eruption, subaqueous accumulations of hyaloclastite filled the available accommodation space on the Northern Bláfjöll lava plateau and began to destabilize where hyaloclastite slopes exceeded their angle of repose. Unstable hyaloclastite deposits mobilized

into gravity-modified hyaloclastite flows that descended into a subglacial water drainage system to the northwest. Arnarþúfur consists of a southeast-northwest trending series of discrete palagonite mounds that appear to be remnants of a once continuous deposit. Sedimentary structures and grain morphology within Arnarþúfur deposits vary systematically with distance from Northern Bláfjöll and Vífilfell. Arnarþúfur deposits subdivide into proximal, central, and distal facies based on their position with respect to Northern Bláfjöll and Vífilfell.

Near the base of Northern Bláfjöll, Arnarþúfur deposits form thick, rhythmically layered, concave-down beds that dip away from a central axis. The central axis of the deposits extends from Northern Bláfjöll to the northwest and corresponds to the center of the principal subglacial tunnel that existed during the Vífilfell eruption. Hyaloclastite deposition from hyaloclastite flows progressively infilled the tunnel system. Melting of the ice surrounding the hyaloclastite deposits created additional accommodation space for subsequent hyaloclastite flows. Proximal deposits have palgonitized hyaloclastite matrix containing coarse-grained clasts with angular to subangular morphologies that are representative of short lateral transport distances. Armoured lapilli with glass clast cores are common in some beds. Abundant armoured lapilli, which form when ash plasters onto grain surfaces in water-saturated eruption columns (Cas and Wright 1988; Chumacher and Schmincke 1991), indicate that some material erupted from Vífilfell entered into subaerial plume phase prior to being incorporated into the ice-confined hyaloclastite flows.

Large hyaloclastite mass-flows could have formed when triggers, such as seismicity or eruption column collapse, mobilized voluminous deposits in the Vífilfell region. Intense phreatomagmatic explosions generated large volumes of fine-grained ash within a water-saturated eruption plume that rapidly coated larger glass clasts and made the eruption column

gravitationally unstable. Collapse of the eruption column would have introduced large volumes of armoured lapilli into the englacial meltwater lake and triggered large hyaloclastite flows with abundant armoured lapilli entrained within them. Large mass-flows developed into turbidites, each of which could have a coarse-grained basal layer decoupled from a turbulent upper layer that contains fine-grained hyaloclastite in suspension. Sediment deposition from turbidity currents may account for the bed pairs within rhythmically bedded Arnarþúfur deposits. Large hyaloclastite flows could also have generated flute marks on the surfaces of underlying beds and climbing ripples where sedimentation rates are high. Hyaloclastite deposition from low density currents that continuously flush material from the Vífilfell vent region-produced beds containing ungraded sediment between successive turbidite deposits. Ice-confined hyaloclastite flows moving through the subglacial drainage system rapidly deposited sediment along tunnel margins where friction reduced sediment velocity and allowed grains to settle from the current. Oversteepening of inward-dipping beds along the tunnel margins caused minor sediment mobilization and generated small ripple marks as material flowed towards of the center of the channel.

In distal regions of Arnarþúfur, deposits contain fine-grained subangular clasts and rare armoured lapilli. Deposits lack rhythmic layering and bedding is poorly defined. In the distal region, current density and sedimentation deposition rates were low. Following the Vífilfell eruption, ice-flow velocities in distal region would have been greater than in proximal regions where shielding by Northern Bláfjöll and Vífilfell would have had the greatest affect. High ice flow velocities would accelerate the rate of subglacial erosion in distal regions of Arnarþúfur relative to proximal regions. Estimation of the original volume of Arnarþúfur in relation to Vífilfell is not possible given the unknown extent of erosion affecting Arnarþúfur and uncertainties concerning tephra deposition onto the surrounding ice.

Arnarþúfur is an ice-confined hyaloclastite mass-flow deposit that was emplaced contemporaneously with Vífilfell. The characteristics of Arnarþúfur differ from previously described hyaloclastite flow deposits, which contain crystalline lava cores. Arnarþúfur deposits, however, are similar to the bedded hyaloclastites (BH) that occur at the top of the Standard Depositional Unit of hyaloclastite flow deposits of the Fljotshverfi Group (Berge and Sigvaldason 1991).

Jónson (1978) proposed Vífilfell and Arnarþúfur to be products of a subglacial fissure eruption; however, lithological and structural evidence does not support the interpretation that Arnarþúfur is a primary structure. To the contrary, Arnarþúfur contains abundant evidence to support hyaloclastite deposition from northwest moving mass-flow. The previously proposed origin of Vífilfell and Arnarþúfur must, therefore, be reconsidered.

#### **6.4 Petrographic and Geochemical analysis**

Hyaloclastite samples from Northern Bláfjöll contain Type 1 pyroclasts and samples from Vífilfell and Arnarþúfur include pyroclasts Types 1, 2, and 4. Type 1 pyroclasts are blocky and equant, and they form when melt surfaces quench and develop fractures of less than 45° relative to the melt surface. Type 2 pyroclasts include vesicular and irregular grains that suggest vesiculation of the melt prior to fragmentation. Type 2 pyroclasts quench more slowly than Type 1 pyroclasts, and may deform into elongate shapes after fragmentation. The presence of abundant skeletal olivine and Type 2 pyroclasts within individual samples, such as Wpt107 from Vífilfell, provides additional evidence that quenching rates were high during some phases of the Vífilfell eruption. Type 4 pyroclasts are spherical to drop-like and result from boundary layer instabilities that occur during melt-water interactions. The

abundance of highly fragmented pyroclasts within Vífilfell and Arnarþúfur supports the conclusion that these deposits are products of explosive phreatomagmatic interactions.

Electron microprobe analyses of major element compositions (Si, Ti, Cr, Fe, Mn, Mg, Ca, Na, K, and P) within glass samples obtained from Northern Bláfjöll, Vífilfell, and Arnarþúfur reveals that materials from the three regions have indistinguishable olivine-normative tholeiite compositions (Figure 6.3). The glass compositions plot close to the plane of silica saturation on the cotectic line between plagioclase and olivine. The geochemical data do not contain obvious fractionation trends.

The chemical homogeneity of the samples suggests a common magma source and an emplacement time for the volcanic complex less than the time required for discernible magma evolution. Minimal magma evolution, in combination with field observations that indicate a period of ice coverage over Northern Bláfjöll prior to emplacement of Vífilfell, can be reconciled if the period between eruption phases was brief, perhaps on the order of  $1-10^2$  years. This short period would allow sufficient time for infilling of the ice-cauldron by ductile ice deformation and restriction or closure of the subglacial drainage system associated with Northern Bláfjöll eruption, in addition to limiting the time available for significant magma evolution.

An alternative explanation for the chemical homogeneity of samples from the Vífilfell Region involves steady-state element concentrations within an open-system magma chamber. O'Hara (1977) proposed the idea of steady-state magma chambers to account for the chemical homogeneity of Mid-Ocean Ridge Basalts (MORBs). The Reykjanes Volcanic Belt, associated with an active rift zone, includes the Vífilfell Region and, therefore, steady state magmatism is worthy of consideration as a mechanism to restrict variation in the magma composition.

Within a refilled, tapped, and fractionated (RTF) magma chamber, all elements can reach steady-state concentrations when the rate of element supply from new magma inputs perfectly balances the rate of material loss by crystallization and eruption (White 2003). For the system to reach steady state, however, the RTF magma chamber must undergo many cycles of refilling, eruption, and fractional crystallization (White 2003). If a steady state RTF magma chamber fed the Northern Bláfjöll and Vífilfell eruptions, the chemical composition of the magma would have remained constant.

The steady state RTF model is applicable to open-system magma chambers where magma input and volcanic activity is frequent, such as Kilauea and mid-oceanic ridge systems (White 2003). In the Vífilfell Region, however, volcanic activity is less frequent (Thordarson and Hoskuldsson 2002) and, therefore, steady state conditions may, or may not, have been reached in the magma chamber that fed the Northern Bláfjöll and Vífilfell eruptions.

The genetic relationship between Northern Bláfjöll and Vífilfell suggests that these two features are members of the same volcanic formation and have a closer genetic association than a purely stratigraphic analysis would suggest. Mantling of the Northern Bláfjöll lava plateau beneath ice, however, suggests that a prolonged hiatus in volcanic activity occurred between the emplacement of Northern Bláfjöll and Vífilfell. Evidence of a hiatus in volcanic activity precludes the possibility that Northern Bláfjöll and Vífilfell are products of a single eruptive phase.

## 6.5 Schematic model of ice-contact volcanism in the Vífilfell Region

The following schematic model summarizes the stages in the formation of Northern Bláfjöll, Vífilfell, and Arnarþúfur (Figure 6.6.1-6.6.13). The cross-section of the schematic illustrations extends from A to B, spanning a distance of approximately 4 km (Figure 6.4). The cross-section is viewed from the northeast looking towards the southwest. Features within the schematic illustrations are not drawn to scale.

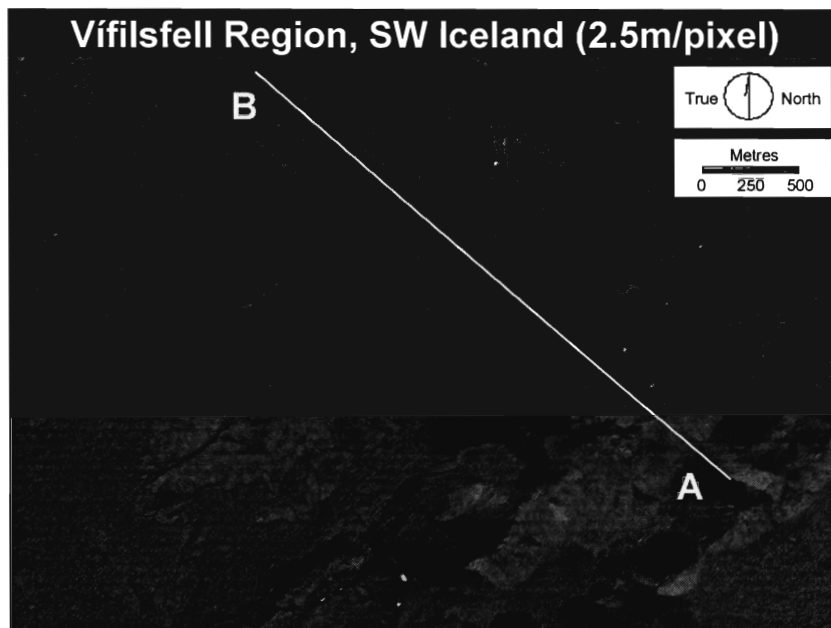


Figure 6.4: Location and orientation of the schematic cross-section. The cross-section spans a distance of approximately 4 km.

Prior to the emplacement of Northern Bláfjöll, the ice flow direction in the In the Vífilfell Region was from the southeast to the northwest (Figure 6.6.1). Assuming planar bedrock topography, equipotential surfaces are perpendicular to the maximum slope of the glacier surface. The thickness of the glacier in the Vífilfell Region decreases to the northwest and, therefore, equipotential surfaces trend southwest-northeast (perpendicular to the plane of the cross section in Figure 6.6.1). Water within glacier moves perpendicular to



equipotential surfaces and, therefore, flows to the northwest in the Vífilfell Region. The asymmetry of Arnarþúfur with respect to the axis of Bláfjöll results from initial asymmetry in ice flow direction.

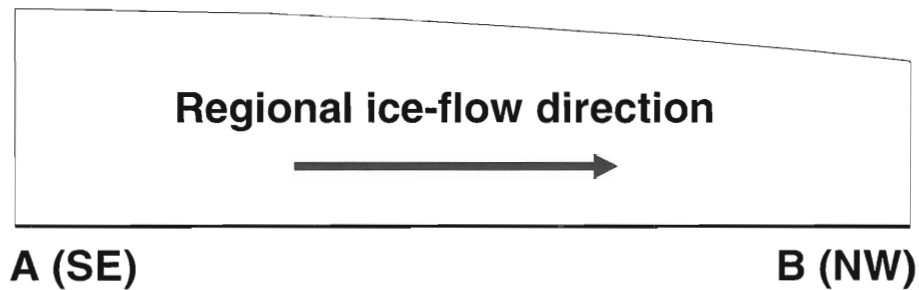


Figure 6.6.1: Regional ice-flow direction in the Vífilfell Region prior to the emplacement of Northern Bláfjöll. The thick black line at the base of the cross-section represents the bedrock surface. Pale blue represents glacial ice.

The Northern Bláfjöll eruption begins beneath ice much greater than 200 m in thickness. The large confining pressure suppresses explosive phreatomagmatic interactions and causes extruded material to form pillow lavas within the meltwater filled englacial vault (Figure 6.6.2). Ductile deformation of ice overlying the volcanic vent delays penetration of glacier and causes a depression (ice cauldron) to form in the ice surface.

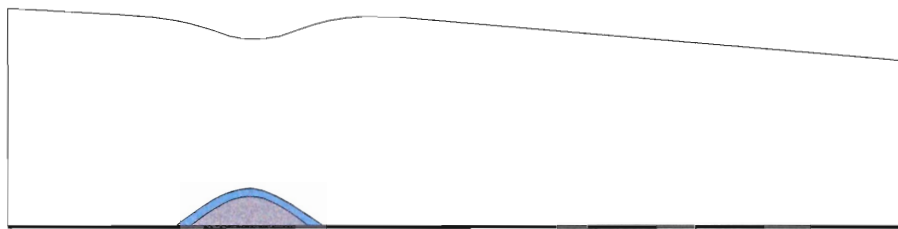


Figure 6.6.2: The initial phase of the Northern Bláfjöll eruption. Dark grey represents pillow lavas and dark blue corresponds to liquid water.

Continued pillow lava emplacement and ice melting causes the ice to thin and fracture. Concentric ring fractures develop and the ice cauldron begins to collapse into the

englacial vault (Figure 6.6.3). Meltwater descends the equipotential gradient towards the northwest and thermal erosion expands the subglacial meltwater drainage system.

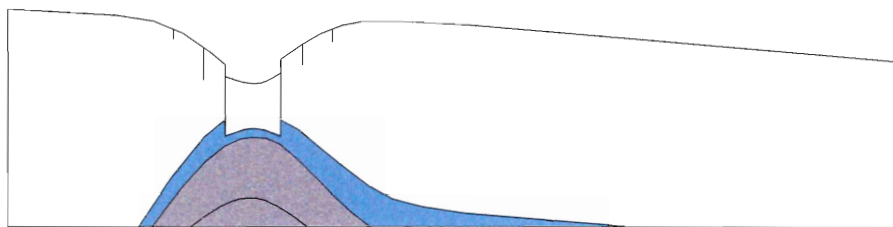


Figure 6.6.3: Formation of an ice cauldron above Northern Bláfjöll.

Penetration of the ice causes rapid reduction in confining pressure, enabling explosive phreatomagmatic activity to begin (Figure 6.6.4). The change in eruption style corresponds to a lithofacies change from pillow lavas to mixed pillow-block breccia and hyaloclastite. Ice melting continues to expand the subglacial drainage system and deposits begin to develop a structural asymmetry.

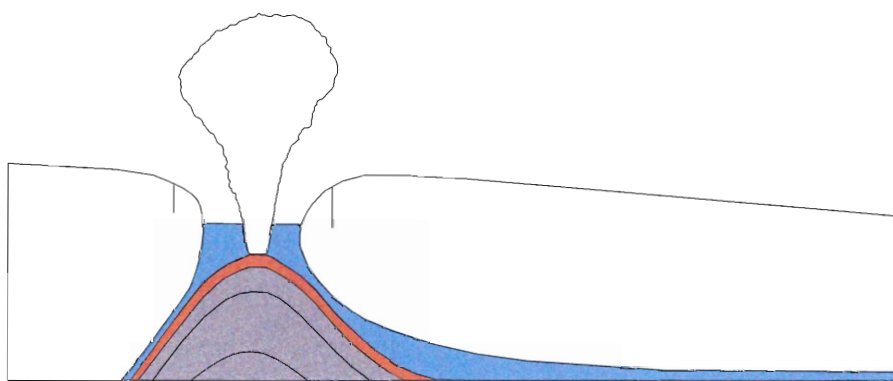


Figure 6.6.4: Onset of a subaerial plume phase during the Northern Bláfjöll eruption. Dark brown corresponds to mixed hyaloclastite and scoria. Light grey represents the subaerial eruption plume.

As the volcanic pile builds upwards through the meltwater lake, further reduction in hydrostatic pressure causes pillow-block breccia formation to cease while hyaloclastite production continues (Figure 6.6.5). Once the volcanic pile nears the air-water interface, restriction of water from the vent region lowers the water-to-melt ratio and reduces the

efficiency of phreatomagmatic activity. Reduction in phreatomagmatic efficiency coincides with scoria emplacement. Subaerial lava effusion begins when the volcano emerges from the englacial lake and the rate of water recharge reduces below the threshold for explosive phreatomagmatic activity. When lava flows encounter the surrounding water, lava surfaces quench and fragment into hyaloclastite. Enhanced cooling rates cause the lava to fracture internally and brecciate. Deposits of hyaloclastite and breccia mix to form a prograding delta consisting of flow-foot breccia that supports subsequent subaerial lava flows. The passage zone, between the flow-foot breccia deposits and subaerial lava flows, corresponds to the water level of the englacial during the Northern Bláfjöll eruption.

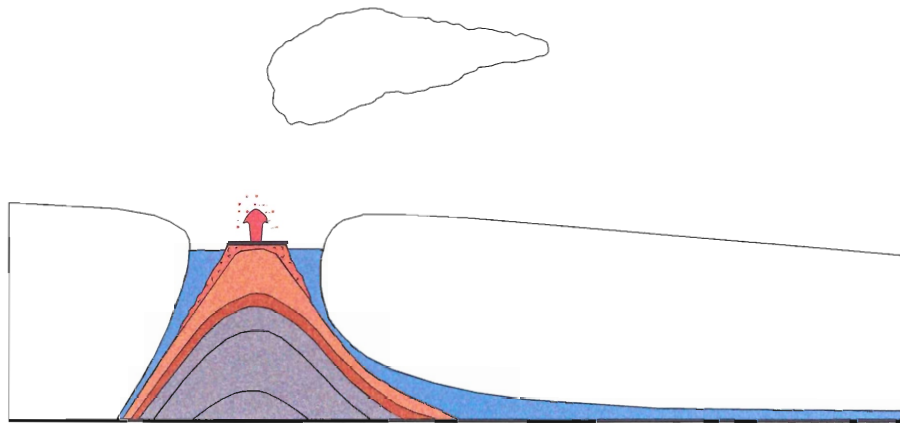


Figure 6.6.5: Emergence of Northern Bláfjöll from the surrounding englacial lake. Light brown signifies hyaloclastite, orange zones with lunate markings correspond to flow-foot breccia, and the black line overlying flow-foot breccia deposits represents the extent of subaerial lava flows. Red corresponds to vent region from which lava is extruded either passively or from fire fountains depending on the volatile content of the magma. The zone beneath the subaerial lava flow corresponds to the location of the passage zone, which defines the elevation of the water-air interface during the Northern Bláfjöll eruption.

Continued advance of subaerial lava over the prograding delta of flow-foot breccia enables Northern Bláfjöll to develop a broad plateau (Figure 6.6.6). The boundary between flow-foot breccia and subaerial lavas is 400 m above the surrounding plain and corresponds to the minimum ice thickness during the eruption.

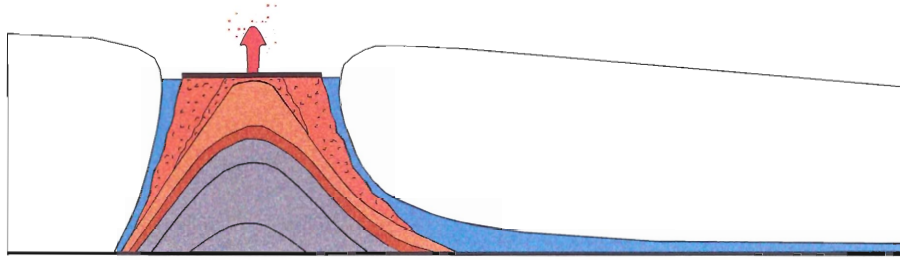


Figure 6.6.6: Development of the Northern Bláfjöll lava plateau.

Following termination of the Northern Bláfjöll eruption, ice infills the former meltwater lake by ductile deformation (Figure 6.6.7). Oversteepened margins of Northern Bláfjöll are gravitationally unstable and collapse in mass-wasting events. Convection of water through the volcanic pile transfers heat from the basal pillow lavas to the overlying material and promotes hyaloclastite palagonitization. Advancing ice from the southwest erodes poorly consolidated volcanoclastic sediments, plucks lava blocks from the southwest margin of Northern Bláfjöll, and creates southeast-northwest trending glacial striations on upper lava surfaces.

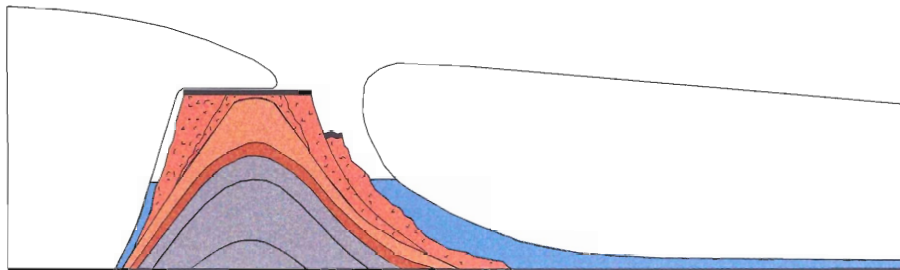


Figure 6.6.7: Advance of glacial ice over Northern Bláfjöll.

The southwest-northeast orientation of Northern Bláfjöll is perpendicular to the regional ice flow direction, acts as flow barrier, and establishes a local ice divide in the glacier. Ice flow towards the northwest creates a local compressive regime near the southeast flank of Northern Bláfjöll that presses ice directly against the slope. On the northwest side of

Northern Bláfjöll a local extensional regime develops where ice flow velocities increase from a minimum on the northwest slope. Heat transfer from crystalline lava melts the ice surrounding Northern Bláfjöll. Ice inflow rates balance the rate of ice melting to the southeast; however, to the northwest ice flow rates are too low to balance the melting and a cavity in the ice develops along the northwest slope of Northern Bláfjöll. If the strain in the ice is sufficiently great near the northwest margin of Northern Bláfjöll, tension fractures could develop that could grow into either crevasses or moulins. Following a period of dormancy, a second eruption commences (Figure 6.6.8). The second eruption occurs beneath thin ice, less than 200 m in thickness, and rapidly melts the overlying ice, which is insufficiently thick to flow by ductile deformation into the englacial vault below. Low confining pressure enables explosive phreatomagmatic activity to develop from the onset of the eruption.

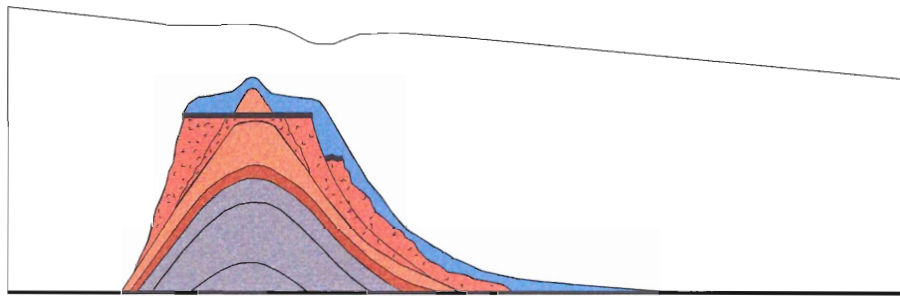


Figure 6.6.8: Onset of the Vífilfell eruption.

The Vífilfell eruption quickly penetrates the overlying ice and develops a subaerial plume (Figure 6.6.9). Explosive phreatomagmatic activity generates hyaloclastite that constructs a mound around the vent and mantles the underlying Northern Bláfjöll lava plateau. Intense phreatomagmatic explosions excavate lithic blocks from Northern Bláfjöll

and deposit them as volcanic bombs in the vent region. Meltwater preferentially flows towards the northwest and expands subglacial drainage conduits by thermal erosion.

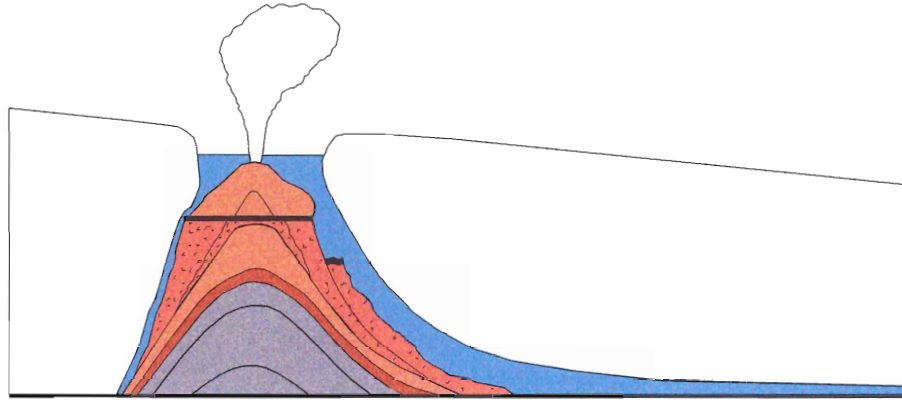


Figure 6.6.9: Subaerial plume phase of the Vífilsfell eruption.

Plastering of ash onto the surface of hyaloclastite grains entrained within the wet (water saturated) eruption plume produces armoured lapilli. Once armoured lapilli gain sufficient mass they decouple from the plume and fall into the englacial lake and onto the surrounding ice surface (Figure 6.6.10). The armoured lapilli settle through the water column onto the surface of the hyaloclastite deposits. Oversteepening of the hyaloclastite mound causes the material to flow towards the periphery of the deposit. Flows abut against ice to the southeast where accommodation space is unavailable. Towards the northwest, the hyaloclastite flows pour over the side of the Northern Bláfjöll plateau and into the meltwater drainage system. Armoured lapilli entrained with the hyaloclastite flows are transported from the vent region. Seismicity and periodic collapse of the eruption column destabilize peripheral hyaloclastite deposits and trigger large hyaloclastite flows that separate into a coarse-grained base surge and an upper turbulent current with fine-grained sediments in suspension. Periodic sediment deposition from hyaloclastite flows generates rhythmic bedding sequences in Arnarþúfur deposits.

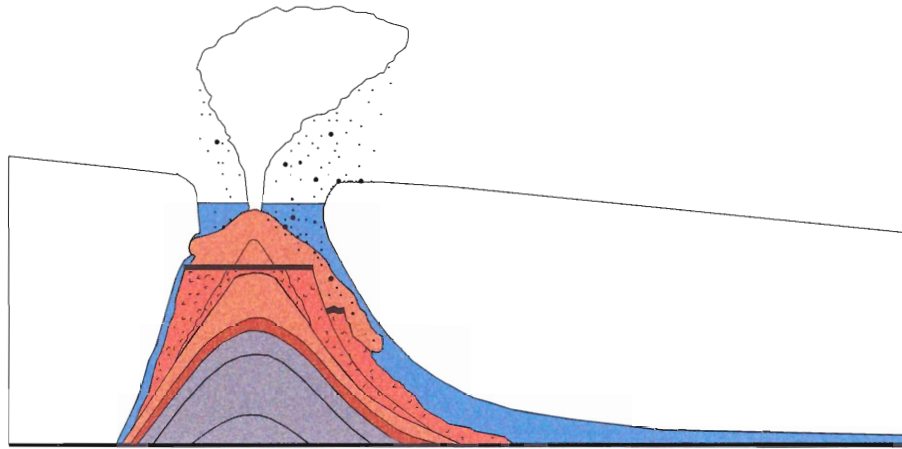


Figure 6.6.10: Production of armoured lapilli and hyaloclastite mobilization during the Vífilfell eruption.

Gravitational potential energy changes to kinetic energy as the hyaloclastite flows descend from the Northern Bláfjöll plateau towards the surrounding plain. Most of the material accumulates near the base of Northern Bláfjöll, but some volcanoclastic sediments travel over 2 km northwest through the subglacial tunnel system. The hyaloclastite flow deposits exhibit characteristics of pyroclastic flow deposits, turbidites, and eskers (Figure 6.6.11). Ice-confinement produces beds that dip towards the axis of the subglacial tunnel system. As the flows stack one above the other they melt overlying ice and create additional accommodation space for subsequent flows. With distance from Northern Bláfjöll, the flow deposits thin vertically and widen laterally. Arnarþúfur deposits exhibit an overall lobate morphology with constituent beds containing variable concentrations of armoured lapilli. Within the Arnarþúfur deposits, grain sizes decrease and clast roundness increases with distance.

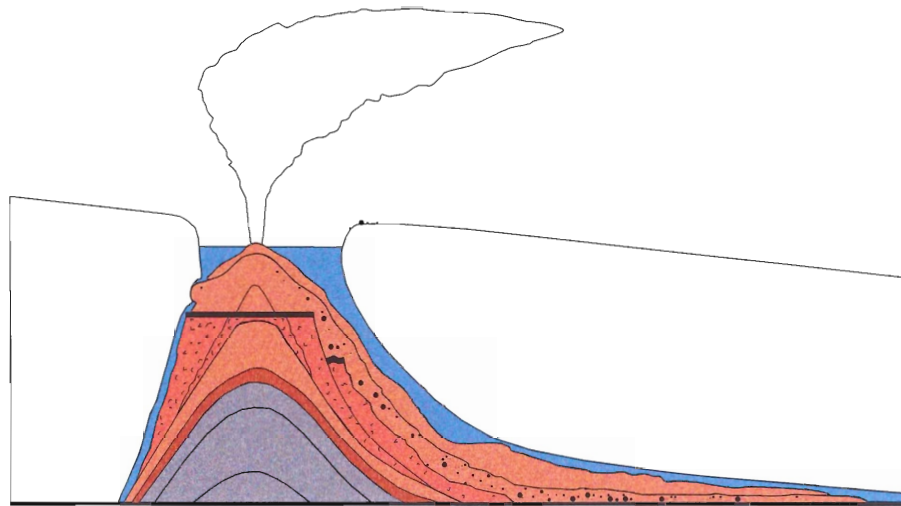


Figure 6.6.11: Emplacement of ice-contained hyaloclastite flow deposits during the Vífilfell eruption.

Following the Vífilfell eruption, drainage of the englacial lake reduces the hydrostatic pressure in the connected drainage system and the tunnel system rapidly infills by ductile ice deformation (Figure 6.6.12). Overlying ice exerts pressure on the unconsolidated hyaloclastite flow deposits and causes them to deform. Ice flow from the southeast to the northwest reestablishes a compressive regime on the southeast flank of Northern Bláfjöll and an extensional regime near the northwest slope. Slow ice flow velocities to the northwest of Northern Bláfjöll contribute to a low rate of subglacial erosion that provides Arnarþúfur deposits with sufficient time to palagonitize.

Petrographic analysis of samples from the Vífilfell Region reveals that hyaloclastite from Northern Bláfjöll is more intensely palagonitized than hyaloclastite from either Vífilfell or Arnarþúfur, and that Arnarþúfur deposits are the least palagonitized. These observations are consistent with the proposed model of hyaloclastite flow emplacement, because the rate of palagonitization depends largely on the availability of heat. The dense pillow lava core of Northern Bláfjöll would supply heat to drive hydrothermal circulation and rapid palagonitization, whereas Arnarþúfur deposits lack a crystalline core and, therefore, in the absence of a heat source, palagonitization rates would be low.



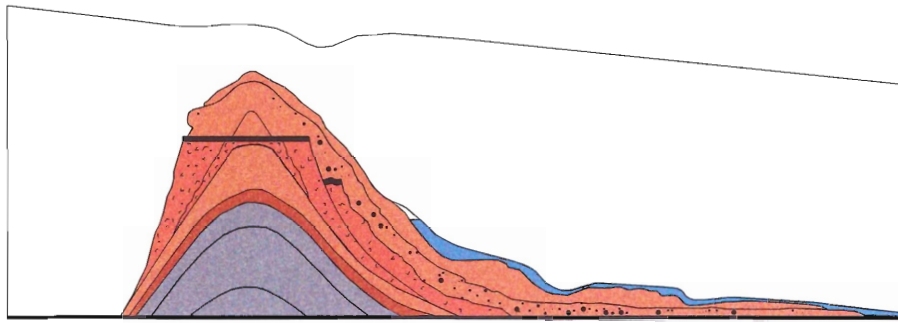


Figure 6.6.12: Advance of glacial ice over Northern Bláfjöll and Vífilfell.

Glacial and subaerial erosion of Arnarpúfur deposits produces a series of discrete mounds (Figure 6.6.13). Figures 6.7 and 6.8 depict the stratigraphic relationship between Northern Bláfjöll (blue), Vífilfell (red), and Arnarpúfur (yellow). Light blue corresponds to mass wasting deposits and scree slopes, whereas dark blue represents *in situ* Northern Bláfjöll deposits.

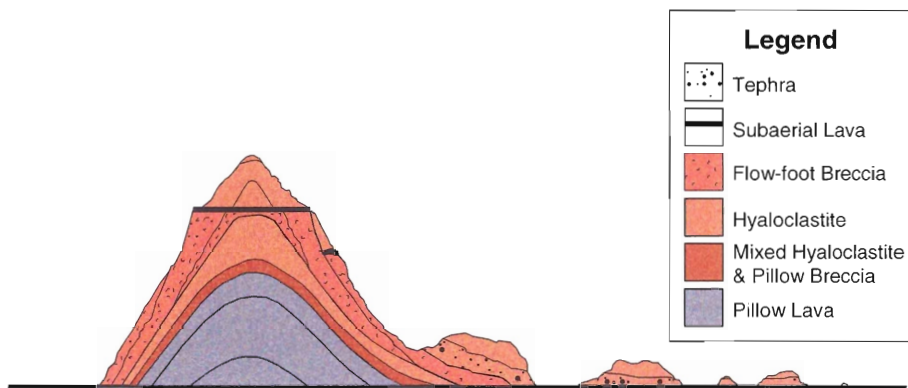


Figure 6.6.13: Current morphology of ice-contact deposits in the Vífilfell region.

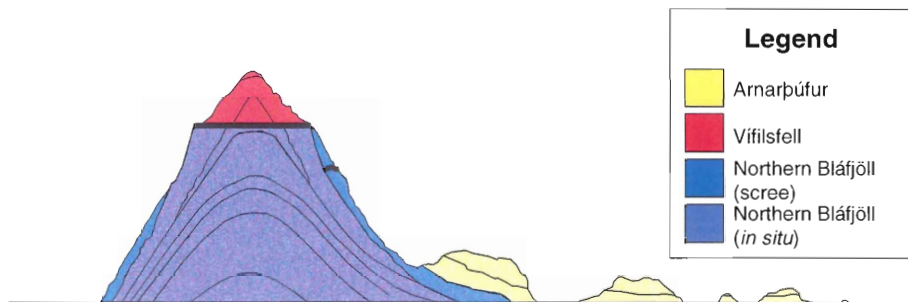


Figure 6.7.1: Cross-sectional view of the lithostratigraphic relationship between Northern Bláfjöll (blue), Vífilfell (red), and Arnarpúfur (yellow). Dark blue represents *in situ* deposits light blue symbolizes unconsolidated material from Northern Bláfjöll.

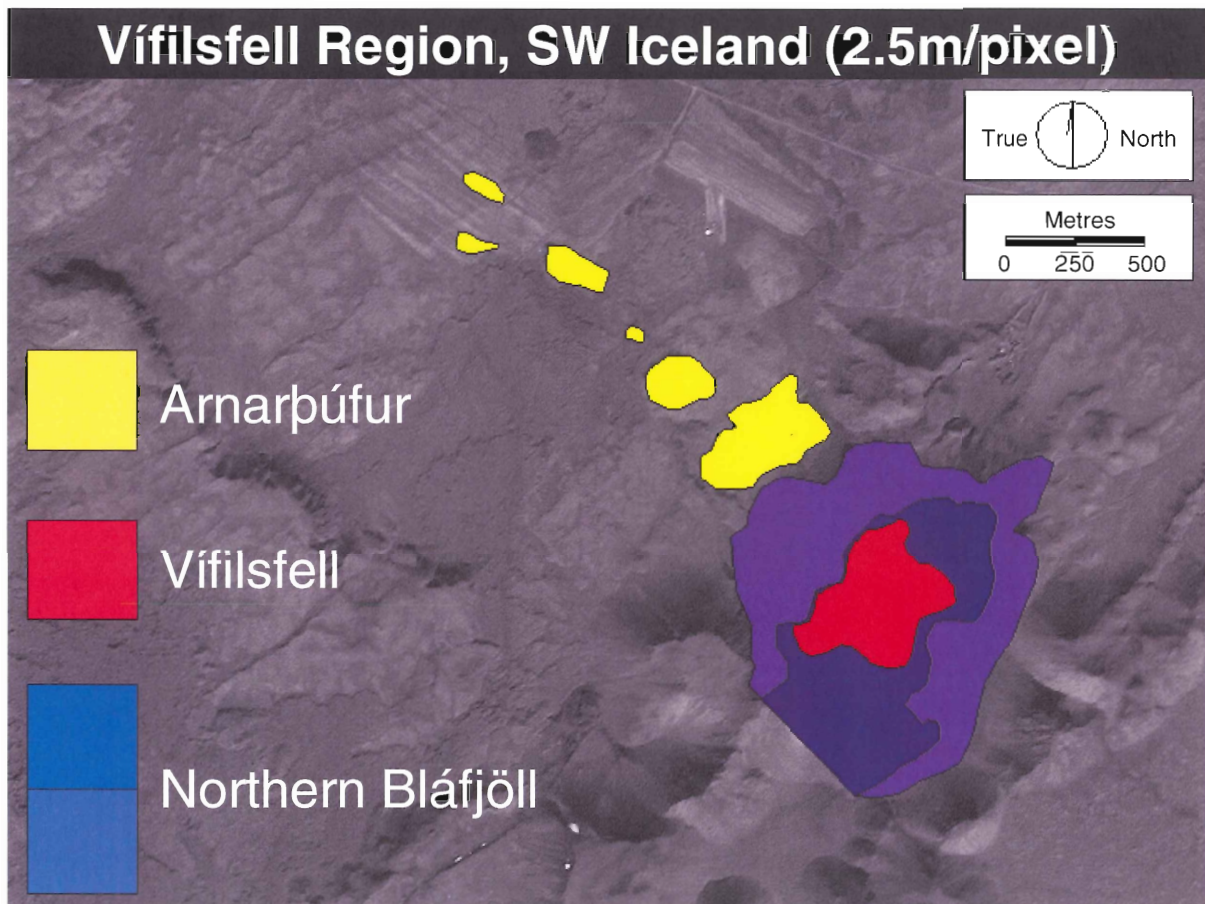


Figure 6.7.1: Plan-view of Northern Bláfjöll, Vífilfell, and Arnarþúfur.

## 6.6 Summary

Remote sensing interpretation of cluster classifications provides an excellent indication of the spatial distribution of general information categories such as lava and hyaloclastite; however, specific lithofacies are difficult to distinguish. For example, pillow lavas are not reliably discernible from subaerial lavas, transitional lithofacies with mixed spectral signatures such as flow-foot breccia do not correspond to a unique spectral cluster, and lithofacies such as scoria and welded spatter are not present within the classifications. Remote sensing analysis of ice-contact lithofacies is suitable for preliminary site investigation, but not for determining specific lithostratigraphic relationships.

Field observations indicate that Northern Bláfjöll, Vífilfell, and Arnarþúfur are products of ice-contact volcanism. Northern Bláfjöll is a tuya, Vífilfell is a subglacial mound, and Arnarþúfur is an ice-confined hyaloclastite flow that combines characteristics of pyroclastic flow deposits, turbidites, and eskers, but differs substantially from previously described hyaloclastite flow deposits in Iceland. Emplacement of Northern Bláfjöll occurred within a glacier greater than 400 m in thickness, based on the elevation of the passage zone above the surrounding plain. At the onset of the Vífilfell eruption ice thickness above the Northern Bláfjöll lava plateau was less than approximately 200 m, as evidenced by explosive phreatomagmatic deposits at the base of Vífilfell. Arnarþúfur formed during the Vífilfell eruption as hyaloclastite flows deposited volcaniclastic sediments within a subglacial tunnel system that extended from Vífilfell to the northwest.

Geochemical data indicate that Northern Bláfjöll, Vífilfell, and Arnarþúfur have indistinguishable olivine-normative tholeiite compositions, suggesting a common magma source and a minimal magma evolution. For no discernible magma differentiation to have occurred, the period between the Northern Bláfjöll and Vífilfell eruptions must have been brief. Assuming that Northern Bláfjöll and Vífilfell formed during the same glacial period and that the ice thickness outside the region of volcanic activity remained approximately constant during the interval between the Northern Bláfjöll and Vífilfell eruptions, surrounding ice thickness would, therefore, have been 400-600 m based on the passage zone elevation of Northern Bláfjöll and pressure constraints during the Vífilfell eruption. Abrupt transition from hyaloclastite to welded scoria in Vífilfell deposits can further constrain paleo-ice thickness if one assumes that the contact corresponds to a former lake level. The base of the welded scoria unit has an elevation of approximately 600 m (480 m above the

surrounding plain) and, therefore, the glacier surrounding the englacial lake must have been at least 480 m thick and consequently the paleo-ice thickness was 480-600 m.

Despite apparent morphological and lithostratigraphic differences among ice-contact deposits in the Vífilfell Region, the compositional similarity of Northern Bláfjöll, Vífilfell, and Arnarþúfur indicates a genetic relationship. The Northern Bláfjöll and Vífilfell eruptions either issued from a non-steady-state or steady-state magma chamber. If the Northern Bláfjöll and Vífilfell eruptions originated from a non-steady state magma chamber, the interval between eruptions must have been brief, perhaps on the order of years, to account for the chemical homogeneity of glass samples. If Northern Bláfjöll, Vífilfell, and Arnarþúfur are products of a refilled, tapped, and fractionated (RTF) magma chamber that is in steady-state, the time interval between Northern Bláfjöll and Vífilfell eruptions could have been much longer and still be consistent with all of the data.

# Chapter 7 Summary of Conclusions

## 7.1 Ice-contact volcanism in the Vífilfell Region

Northern Bláfjöll consists of basal pillow lavas, intermediate palagonitized hyaloclastite, scoria, and flow-foot breccia (mixed hyaloclastite and lava breccia) deposits with superincumbent subaerial lava flows. Northern Bláfjöll is a steep-sided volcanic edifice with a planar lava plateau. Northern Bláfjöll exhibits the characteristics of subglacial volcano that emerged from a deep (~400 m) englacial lake. Lithostratigraphic and morphological evidence supports the interpretation that Northern Bláfjöll is a tuya.

Vífilfell directly overlies Northern Bláfjöll and consists primarily of palagonitized hyaloclastite with minor proportions of zeolitized hyaloclastite, welded-scoria, rare dykes and wall-rock lithics derived from underlying volcanic deposits. The prevalence of hyaloclastite and the absence of basal pillow lavas suggests that Vífilfell was emplaced under thin ice conditions with an overlying glacier thickness less than 200 m. Vífilfell matches the criteria of a subglacial mound (SGM).

Arnarþúfur includes a series of discrete palagonitized hyaloclastite outcrops, trending southeast-northwest. With distance from Northern Bláfjöll and Vífilfell, the size of the outcrops generally decreases. Proximal deposits, with respect to Bláfjöll, are massive to well-bedded and contain abundant armoured lapilli within some beds. Glass clasts are common and range from angular to subangular with grain sizes ranging from fine to coarse. Central Arnarþúfur deposits are typically well-bedded and commonly contain flow structures, such as climbing ripples and flutes. These flow structures indicate high sedimentation rates from unidirectional flows moving southeast to northwest. Armoured lapilli are abundant within some beds in the central region, and clasts are typically angular to subangular with

grain sizes ranging from fine to coarse. Distal Arnarþúfur deposits are massive to well-bedded and contain rare flow structures. Armoured lapilli are present in distal regions, but they are less common than within central and proximal deposits. Glass clasts are rounded to subangular and grain sizes are fine to medium. Vent-proximal lithologies such as dykes or volcanic bombs are absent within all sections of Arnarþúfur.

Although compositions of Arnarþúfur deposits are geochemically indistinguishable from Northern Bláfjöll and Vífilfell, lithostratigraphic evidence suggests Arnarþúfur contains material generated during the Vífilfell eruption. The following is a possible interpretation of the emplacement scenario for Arnarþúfur deposits. The Vífilfell eruption commenced beneath a thin ice-cover and rapidly melted through the overlying glacier. Low confining pressure and abundant external water enabled explosive phreatomagmatic activity and hyaloclastite production to occur. Hyaloclastite from the vent region mixed with meltwater and was transported to the western margin of the Northern Bláfjöll. Accumulations of hyaloclastite destabilized and descended as mass-flows from the edge of the lava plateau into a subglacial tunnel system extending northwest from Bláfjöll. Decoupling of each mass-flow into a dense lower layer and a turbulent upper layer produced rhythmically bedded deposits within the tunnel system. Some of the material from the Vífilfell eruption entered into a subaerial plume phase and became coated in thin layers of ash to form armoured lapilli. Armoured lapilli decoupled from the subaerial plume and settled within the ephemeral englacial lake surrounding Vífilfell. Mass-flows containing entrained armoured lapilli produced armoured lapilli-rich beds within Arnarþúfur deposits. Episodic collapse of the eruption column may have contributed to the destabilization of hyaloclastite deposits perched on the margins of the Northern Bláfjöll.

Arnarþúfur exhibits structural characteristics of subaqueous pyroclastic flows, such as pyroturbidites (Cas and Wright 1988); however, the linear distribution of Arnarþúfur deposits suggests that the volcanoclastic sediments were confined during emplacement. Considering the evidence that supports an ice-contact origin for Northern Bláfjöll and Vífilfell, ice confinement is a reasonable mechanism to restrict the lateral distribution of Arnarþúfur deposits. Arnarþúfur deposits are similar to the bedded hyaloclastites of the Standard Depositional Unit for hyaloclastite flows (Bergh and Sigvaldason 1991); however, no evidence exists to support the presence of a crystalline basalt core. Classification of Arnarþúfur deposits is, therefore, challenging because their characteristics are unique relative to previously described volcanoclastic deposits. I propose that Arnarþúfur is an ice-confined hyaloclastite mass-flow deposit; not a subglacial fissure eruption deposit as Jónson (1978) claimed.

Lithostratigraphic relationships within Northern Bláfjöll and Vífilfell deposits provide a means of estimating the thickness of the surrounding glacier during the time of volcano emplacement. Northern Bláfjöll has a maximum passage zone elevation of 400 m above the surrounding plain and, therefore, the minimum ice-thickness during volcano emplacement was 400 m. Vífilfell deposits contain no basal pillow lavas and appear to have been emplaced under thin ice conditions and, consequently, the inferred maximum ice-thickness above the base of Vífilfell during the onset of this eruption phase was 200 m. Vífilfell directly overlies the Northern Bláfjöll lava plateau and, therefore, a conservative estimate of ice-thickness during the emplacement of Vífilfell is 400-600 m.

## References

- Allen, C. C., Gooding, J. L., Jercinovic, M., and Keil Klaus. (1981) Altered basalt glass: a terrestrial analog to the soil of Mars. *Icarus*, **45**: 347-369.
- Allen, C. C., Jercinovic, M. J., and Allen, J. S. B. (1982) Subglacial volcanism in north-central British Columbia and Iceland. *Journal of Geology*, **90**: 699-715.
- Baker, P. E., González-Ferrán, O., and Vergara, M. (1973) Paulet Island and the James Ross Island Volcanic Group. *British Antarctic Survey Bulletin*, **32**: 89-95.
- Batiza, R. and White, J. D. L. (2000) Submarine lavas and hyaloclastite. *In*: Sigurdsson H. (ed.), *Encyclopedia of Volcanoes*. Toronto: Academic Press, 361-381.
- Bergh, S. and Sigvaldason, G. E. (1991) Pleistocene mass-flow deposits of basaltic hyaloclastite on a shallow submarine shelf, South Iceland. *Bulletin of Volcanology*, **53**: 597-611.
- Björnsson, H. (2002) Subglacial lakes and jökulhlaups in Iceland. *Global and Planetary Change*, **35**: 255-271.
- Björnsson, H., Rott, H., Gudmundsson, S., Fischer, A., Siegel, A., and Gudmundsson, M. T. (2001) Glacier-volcano interactions deduced by SAR interferometry. *Journal of Glaciology*, **47**(156): 58-70.
- Bourgeois, O., Dauteuil, O., and Van Vliet-Lanoë, B. (1998) Pleistocene subglacial volcanism in Iceland: tectonic implications. *Earth and Planetary Science Letters*, **164**: 165-178.
- Büttner, R., Pierfancesco, D., and Zimanowski, B. (1999) Identifying magma-water interaction from surface features of ash deposits. *Nature*, **40**: 688-690.
- Campbell, J. B. (2002) *Introduction to remote sensing*, 3<sup>rd</sup> ed. New York: Guilford Press, 621.
- Cas, R. A. F., and Wright, J. W. (1988) *Volcanic Successions: modern and ancient*. 2<sup>nd</sup> ed. Boston: Unwin Hyman, 528 pp.
- Chumacher, R. and Schmincke H.-U. (1991) Internal structure and occurrence of accretionary lapilli – a case study at Laacher See Volcano. *Bulletin of Volcanology*, **53**: 612-634.
- Colgate, S. A. and Sigurgeirsson, T. (1973) Dynamic mixing of water and lava. *Nature*, **244**: 552-555.



- Descloitres, J. and the MODIS Land Rapid Response Team, NASA/GSFC (2002) *MODIS satellite image* (VE Record ID# 11567). Retrieved March 22, 2004, from <http://visibleearth.nasa.gov/cgi-bin/viewrecord?11567>
- Faber, T. E. (1995) *Fluid Dynamics for Physicists*. New York: Cambridge University Press, 440 pp.
- Fagents, S. A., Lanagan, P., and Greeley, R. (2002) Rootless cones on Mars: a consequence of lava-ground ice interaction. In: Smellie, J. L., and Chapman, M. G. (eds.) *Volcano-Ice Interaction on Earth and Mars*. Geological Society, London, Special Publications, **202**, 295-317.
- Francis, P. (2001) *Volcanoes: a planetary perspective*. 2<sup>nd</sup> ed. Toronto: Clarendon Press, 443 pp.
- Furnes, H., Fridleifsson, I. B., and Atkins, F. B. (1980) Subglacial volcanics – on the formation of acid hyaloclastites. *Journal of Volcanology and Geothermal Research*, **8**: 95-110.
- Geirsdóttir, Á., Hardardóttir, J., Sveinbjörnsdóttir, Á. E. (2000) Glacial extent and catastrophic meltwater events during the deglaciation of Southern Iceland. *Quaternary Science Reviews*, **19**: 1749-1761.
- Greeley, R. and Fagents, S. A. (2001) Icelandic pseudocraters as analogs to some volcanic cones on Mars. *Journal of Geophysical Research*, **106**(E9): 20,527-20,546.
- González-Ferrán, O. (1982) The Antarctic Cenozoic Volcanic Provinces and their implication in Plate Tectonic Processes. In: Craddock, C. (ed.) *Antarctic Geoscience*. Madison, Wisconsin: The University of Wisconsin Press, 687-694.
- Guðmundsson, M. T., Pálsson, F., Björnsson H., and Högnadóttir Þ. (2002) The hyaloclastite ridge formed in the subglacial 1996 eruption in Gjálp, Vatnajökull, Iceland: present day shape and future preservation. In: Smellie, J. L. and Chapman, M. G., (eds.), *Ice-volcano Interaction on Earth and Mars*. Geological Society of London, Special Publication, **202**: 319-355.
- Guðmundsson, M. T. (Submitted 2001) Subglacial volcanic activity in Iceland. *Quaternary Science Reviews*, Special Publication, 1-19.
- Guðmundsson, M. T., Sigmundsson, F., Björnsson, H. (1997) Ice-volcano interaction of the 1996 Gjálp subglacial eruption, Vatnajökull, Iceland. *Nature*, **389**: 954-957.
- Guðmundsson, M. T., and Björnsson H. (1991) Eruptions in Grímsvötn, Vatnajökull, Iceland, 1934-1991. *Jökull*, **41**: 21-45.

- Helgason, J. (1999) Formation of Olympus Mons and the aureole-escarpment problem on Mars. *Geology*, **27**(3): 231-234.
- Hickson, C. J. (2000) Physical controls and resulting morphological forms of Quaternary ice-contact volcanoes in western Canada. *Geomorphology*, **32**: 239-261.
- Hollocher, K. (2004) Calculation of a norm from a bulk chemical analysis. Retrieved March 22, 2004, from <http://www.union.edu/public/geodept/courses/petrology/norms.htm>
- Jónsson, J. 1978. *Jarðfræðikort af Reykjanesskaga*. Orkustofnun Jarðhitadeild, OS JHD 7831: 71-72 and maps 16, 17, 19, 20.
- Jones, J. G. (1969) Pillow Lavas as depth indicators. *American Journal of Science*, **267**: 181-195.
- Jones, J. G., (1969) Intraglacial volcanoes of the Laugarvatn region, south-west Iceland, I. *Journal of the Geological Society of London*, **124**: 197-211.
- Jones, J. G., (1970) Intraglacial volcanoes of the Laugarvatn region, south-west Iceland, II. *Journal of Geology*, **78**: 127-140.
- Jones, J. G., and Nelson, P. H. H. (1970) The flow of basalt lava from air into water – its structural expression and stratigraphic significance. *Geological Magazine*, **107**: 13-21
- Kjartansson, G. (1943) *Árnesinga Saga*, Reykjavík: Árnesingafélagið í Reykjavík, 266 p.
- Kokelaar, B. P. (1983) The mechanism of Surtseyan volcanism. *Journal of the Geological Society of London*, **140**: 939-944.
- Kokelaar, P. (1986) Magma-water interactions in subaqueous and emergent basaltic volcanism. *Bulletin of Volcanology*, **48**: 275-289.
- Lajoie, J. and Stix J. (1992) Volcaniclastic rocks. In: Walker, R. G. and James, N. P. (eds.) *Facies Models: response to sea level change*. Stittsville: Geological Association of Canada, 101-118.
- Lanagan, P. D., McEwen, A. S., Keszthelyi, L. P., and Thordarson, T. (2001) Rootless cones on Mars indicating the presence of shallow equatorial ground ice in recent times. *Geophysical Research Letters*, **28**: 2365-2367.
- Lescinsky, D. T., and Fink, J. H. (2000) Lava and ice interaction at stratovolcanoes: Use of characteristic features to determine past glacial extends and future volcanic hazards. *Journal of Geophysical Research*, **105**(B10): 711-726.
- Lillesand, T. M. and Kiefer, R. W. (2000) *Remote sensing and image interpretation*, 4<sup>th</sup> ed. Toronto: John Wiley & Sons, 724 p.

- Mathews, W. H. (1947) "Tuyas", flat-topped volcanoes in northern British Columbia. *American Journal of Science*, **245**: 560-570.
- Morrissey, M., Zimanowski, B., Wohletz, K., and Buettner, R. (2000) Phreatomagmatic fragmentation. *In: Sigurdsson H. (ed.), Encyclopedia of Volcanoes*. Toronto: Academic Press, 431-445.
- Morse, S. A. (1980) *Basalts and phase diagrams: an introduction to quantitative use of phase diagrams in igneous petrology*. New York: Springer-Verlag, 493 p.
- Plint, A. G., Eyles, N., Eyles, C. H., and Walker, G. W. (1992) Control of sea level change. *In: Walker, R. G. and James, N. P. (eds.) Facies Models: response to sea level change*, Stittsville, Ontario: Geological Association of Canada, 15-25.
- Rinaldi, C. A. (1982) The Upper Cretaceous in the James Ross Island Group. *In: Craddock, C. (ed.) Antarctic Geoscience*. Madison, Wisconsin: The University of Wisconsin Press, 281-286.
- Sabins, F. F. (2000) *Remote sensing: principles and interpretation, 3<sup>rd</sup> ed.* New York: W. H. Freeman and Company, 494 p.
- Sheridan, M. F. and Wohletz, K. H. (1983) Hydrovolcanism: basic considerations and review. *In: Sheridan, M. F. and Barberi, F. (eds.), Explosive Volcanism. Journal of Volcanology and Geothermal Research*, **17**: 1-29.
- Sigvaldason, G. F. (1992) Recent hydrothermal explosion craters in an old hyaloclastite flow, central Iceland. *Journal of Volcanology and Geothermal Research*, **54**: 53-63.
- Skilling, I. P. (1994) Evolution of an englacial volcano: Brown Bluff, Antarctica. *Bulletin of Volcanology*, **56**: 573-591.
- Smellie, J. L., and Skilling, I. P. (1994). Products of subglacial volcanic eruptions under different ice thicknesses: two examples from Antarctica. *Sedimentary Geology*, **91**: 115-129.
- Smellie, J. L. (2000) Subglacial Eruptions. *In: Sigurdsson H. (ed.), Encyclopedia of Volcanoes*. Toronto: Academic Press, 403-418.
- Stötter, J., Wastl, M., Caseldine, C., and Häberle, T. (1999) Holocene paleoclimatic reconstruction in northern Iceland: approaches and results. *Quaternary Science Reviews* **18**: 457-474.
- Thordarson, T. and Hoskuldsson, A. (2002) *Iceland*. Hertfordshire: Terra, 200 pp.
- Van der Pluijijm, B. A., Marshak, S. (1997) *Earth structure: an introduction to structural geology and tectonics*. New York: McGraw-Hill, 495 pp.

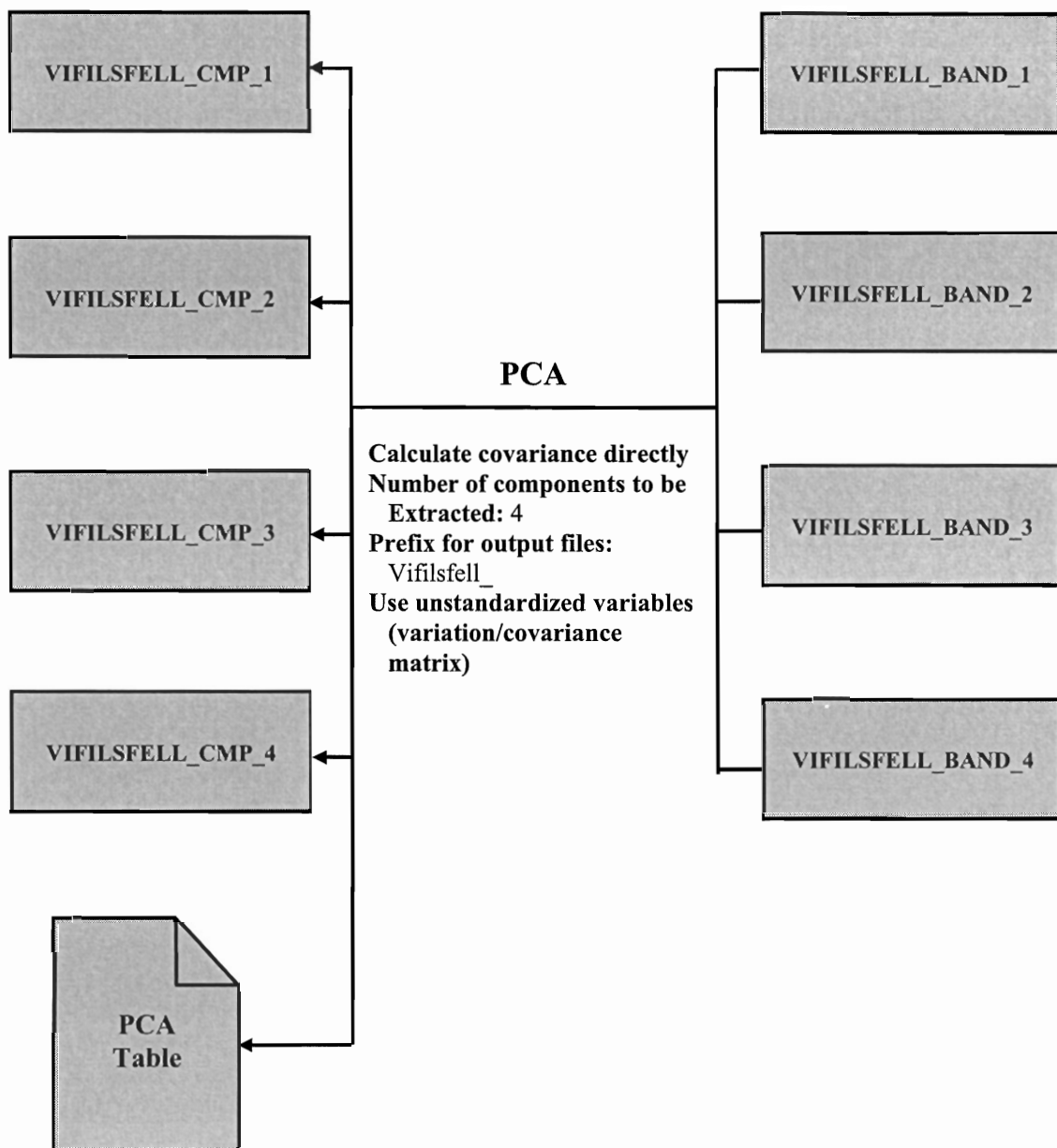
- Walker, G. P. L. and Blake, D. H. (1966) The formation of a palagonite breccia mass beneath a valley glacier in Iceland. *Quarterly Journal of the Geological Society of London*, **122**: 45-61.
- Walker, G. P. L. (1965) Some aspects of Quaternary volcanism in Iceland. *Transactions of the Leicester Literary and Philosophical Society*, **59**: 25-40.
- Walker, R. G. (1992) Turbidites and submarine fans. In: Walker, R. G. and James, N. P. (eds.) *Facies Models: response to sea level change*, Stittsville, Ontario: Geological Association of Canada, 239-263.
- Werner, R., Schmincke, H.-U., and Sigvaldason, G. (1996) A new model for the evolution of table mountains: volcanological and petrological evidence from Herdubreid and Herdubreidartögl volcanoes (Iceland). *Geologische Rundschau*, **85**: 390-397.
- Werner, R. and Schmincke, H.-U. (1999) Englacial vs lacustrine origin of volcanic table mountains: evidence from Iceland. *Bulletin of Volcanology*, **60**: 335-354.
- White, W. M. (2003) Geochemistry by William M. White, Cornell University, an on-line textbook, eventually to be published by: John-Hopkins University Press. Retrieved March 22, 2004, from <http://www.geo.cornell.edu/geology/classes/geo455/chapters.html>
- Wilson, M. (2001) *Igneous petrogenesis: a global tectonic approach*. Boston: Kluwer Academic Publishers, 466 p.
- Winter, J. D. (2001) *An introduction to igneous and metamorphic petrology*. Toronto: Prentice-Hall, 697 p.
- Wohletz, K. H. (1986) Explosive magma-water interactions: Thermodynamics, explosion mechanism, and field studies. *Bulletin of Volcanology*, **48**: 245-264.
- Wohletz, K. H. (1983) Mechanisms of hydrovolcanic pyroclast formation: grain-size, scanning electron microscopy, and experimental studies. *Journal of Volcanology and Geothermal Research*, **17**: 31-63.
- Zimanowski, B. (1998) Phreatomagmatic Explosions. In: *From magma to tephra*. Freundt, A. and Rosi, M. (eds.), Amsterdam: Elsevier, 25-54.

# **Appendix A**

## Remote Sensing

### A.1.1 Cartographic Model 1 (Principal Component Analysis)

The PCA module uses Principal Component Analysis to determine the variability within a set of bands and transform them into a series of new component images that are uncorrelated with each other. Successive components contain progressively less of the variance found in the original bands.



## A.1.2 Principal Components Analysis

### Variance/Covariance Matrix

	Vifilfell Band 1	Vifilfell Band 2	Vifilfell Band 3	Vifilfell Band 4
Vifilfell Band 1	37.39	12.63	14.44	43.87
Vifilfell Band 2	12.63	12.60	14.05	29.21
Vifilfell Band 3	14.44	14.05	16.42	31.66
Vifilfell Band 4	43.87	29.21	31.66	96.06

### Correlation Matrix

	Vifilfell Band 1	Vifilfell Band 2	Vifilfell Band 3	Vifilfell Band 4
Vifilfell Band 1	1.00	0.58	0.58	0.73
Vifilfell Band 2	0.58	1.00	0.98	0.84
Vifilfell Band 3	0.58	0.98	1.00	0.80
Vifilfell Band 4	0.73	0.84	0.80	1.00

### Component Analysis

	Component 1	Component 2	Component 3	Component 4
% Variance	85.85	9.47	4.51	0.17
Eigen Value	139.48	15.39	7.33	0.27

### Eigen Vectors

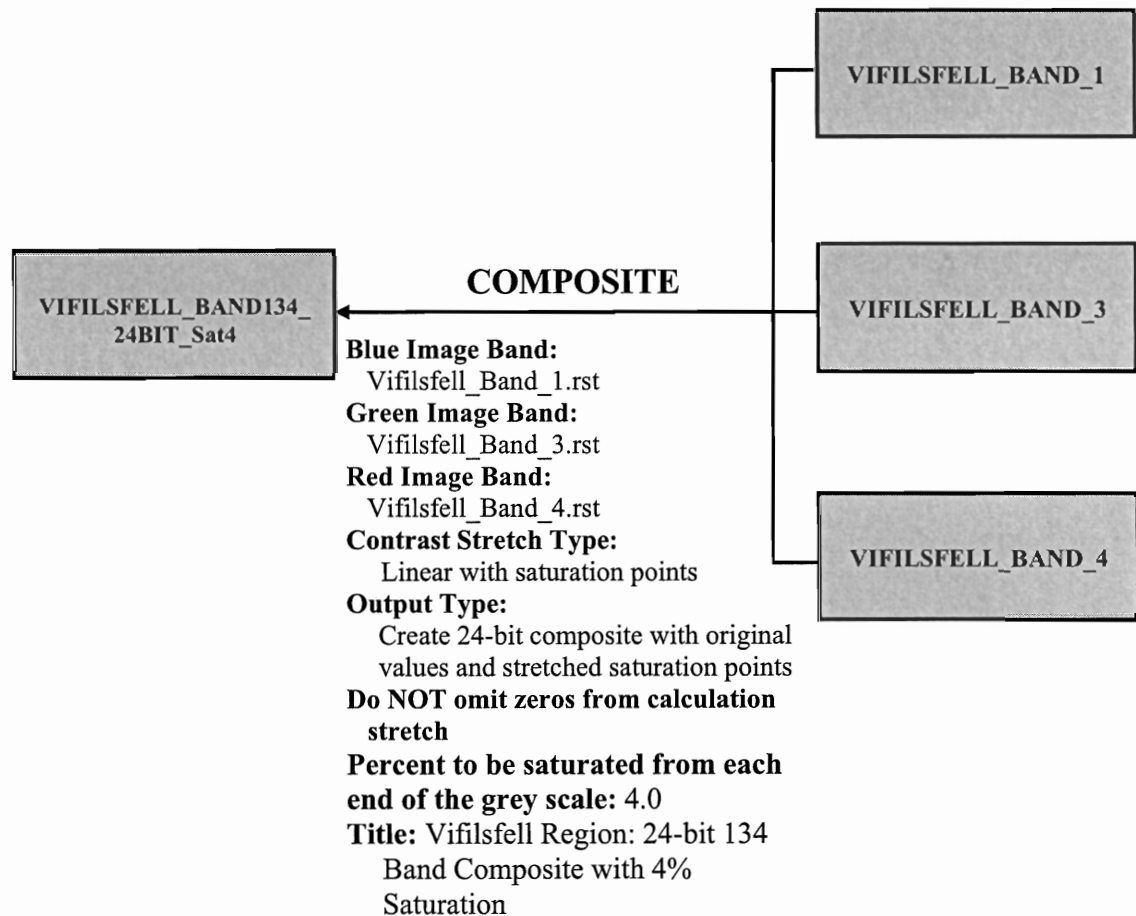
	Component 1	Component 2	Component 3	Component 4
Eigen Vector 1	0.42	-0.88	0.20	-0.03
Eigen Vector 2	0.26	0.27	0.49	-0.79
Eigen Vector 3	0.29	0.28	0.68	0.61
Eigen Vector 4	0.82	0.27	-0.50	0.05

### Loading

	Component 1	Component 2	Component 3	Component 4
Vifilfell Band 1	0.82	-0.57	0.09	0.00
Vifilfell Band 2	0.87	0.30	0.37	-0.12
Vifilfell Band 3	0.84	0.27	0.46	0.08
Vifilfell Band 4	0.98	0.11	-0.14	0.00

## A.2 Cartographic Model 2 (24-bit band composite)

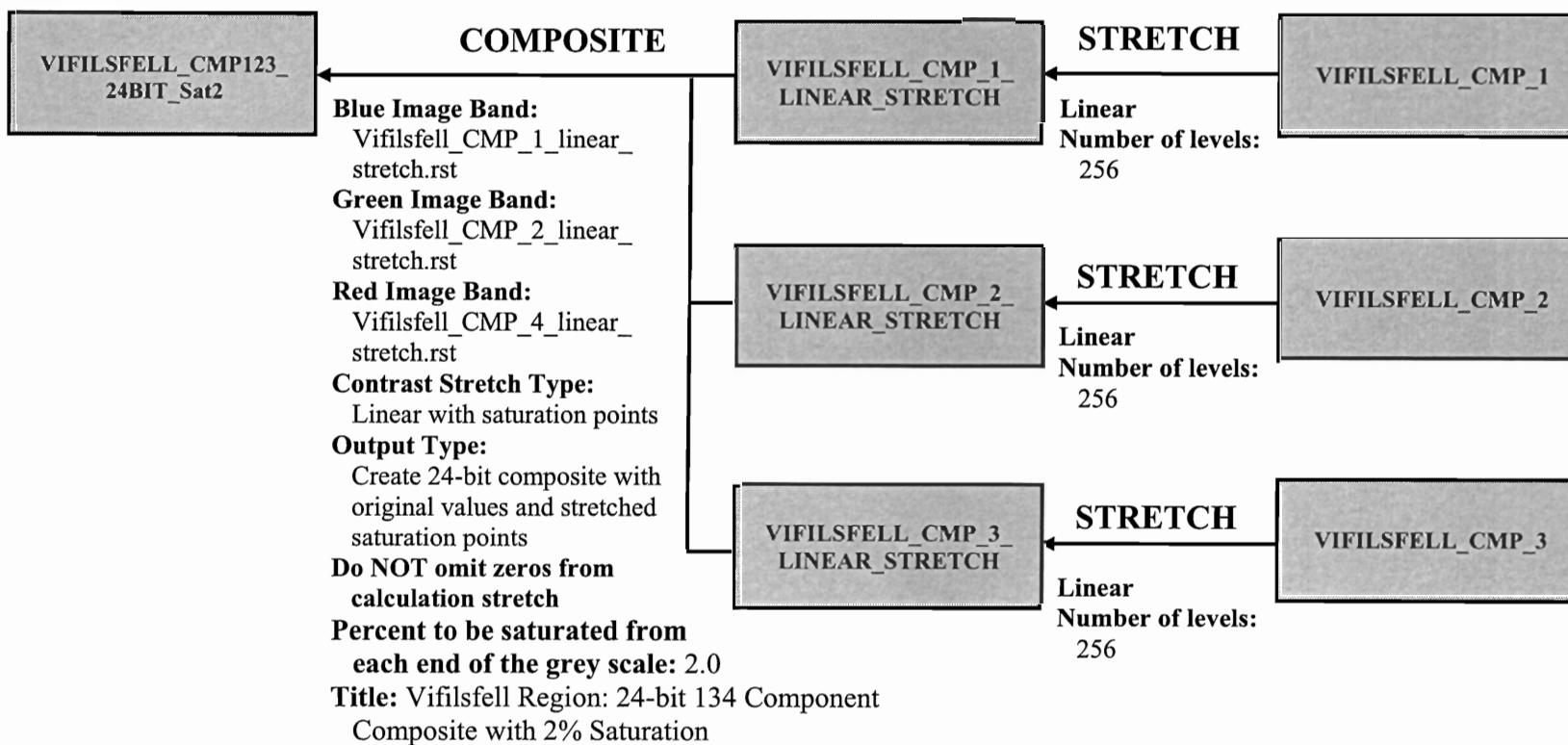
The purpose of this step is to produce 24-bit images for visualization and qualitative inspection. Colour composite images contain more information than single band images and can enhance features that may not be readily apparent in grey scale. In IDRISI32 version 2, colour bands are ordered in the sequence blue, green, and red. The COMPOSITE module can be used to create both 24-bit and 8-bit composite images. Principal Component Analysis reveals bands 1, 3, and 4 have the most variance and, therefore, combining these bands results in an image that conveys more information than any other possible combination of original bands.





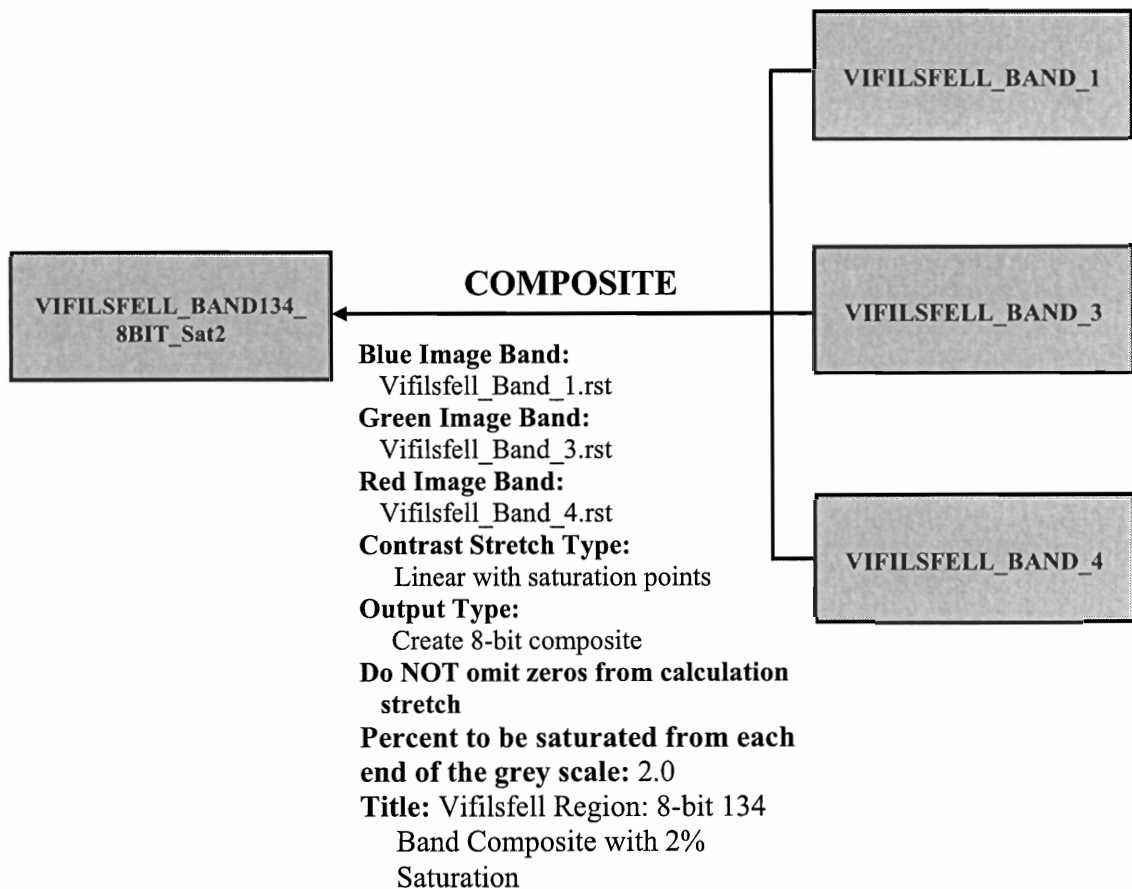
### A.3 Cartographic Model 3 (24-bit component composite)

Component images are combined into composite images in the same fashion as band images; however, components generated with unstandardized variables typically contain integer values outside the permissible byte range (i.e. negative values and values greater than 255). Component images must, therefore, be scaled from 0-255, prior to being imputed into the COMPOSITE module.



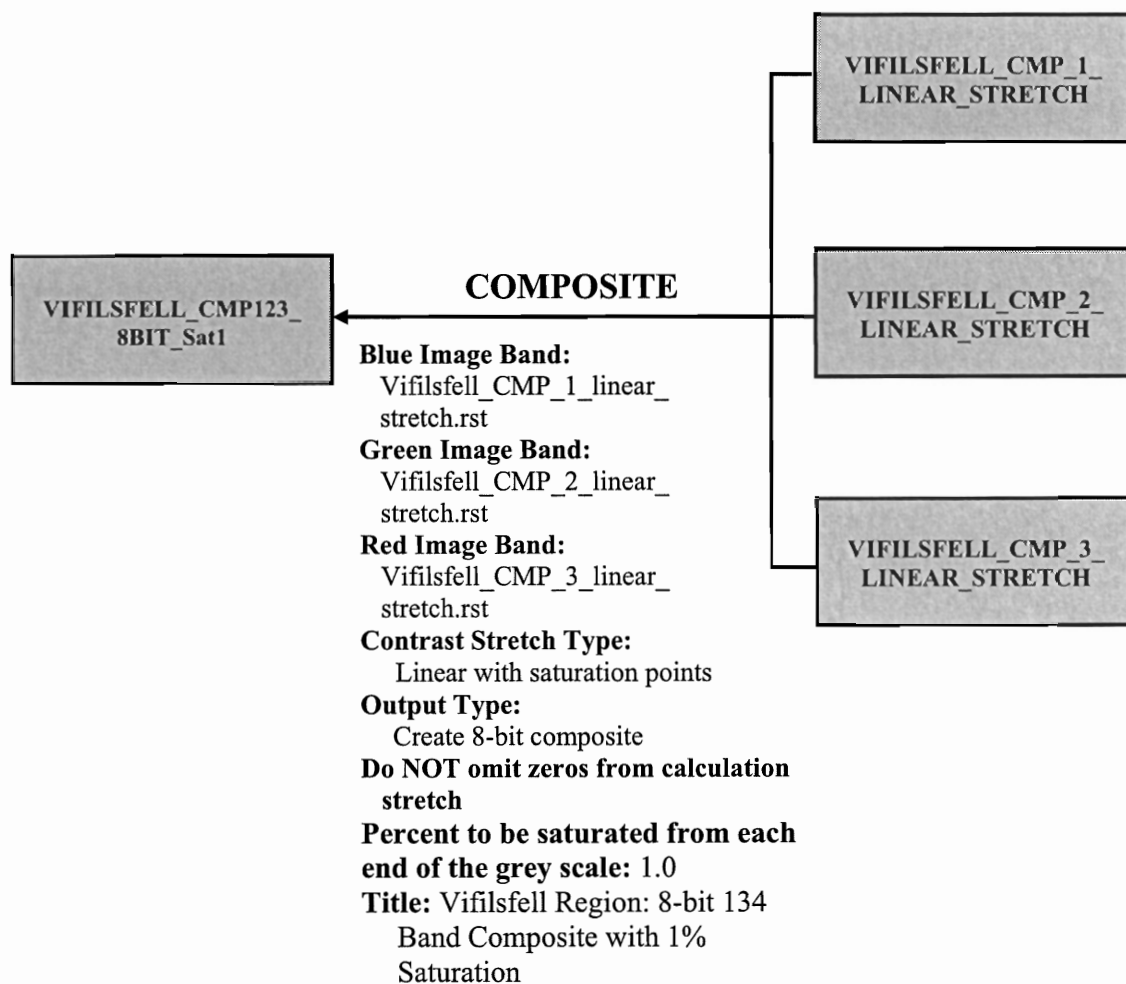
## A.4 Cartographic Model 4 (8-bit band composite)

The purpose of this step is to generate a composite image that can be used to develop unsupervised classifications. According to the results of PCA, bands 1, 3, and 4 contain the most information among the four original SPOT 5 bands. A composite image derived from bands 1, 3, and 4 is, therefore, the optimum band combination for use in subsequent unsupervised classifications.



## A.5 Cartographic Model 5 (8-bit component composite)

The first three component images contain 99.83% of the total variation in the original data set. Combination of components 1, 2 and 3 into an 8-bit composite produces an image with minimal information loss that is ideal for use during subsequent cluster classifications.



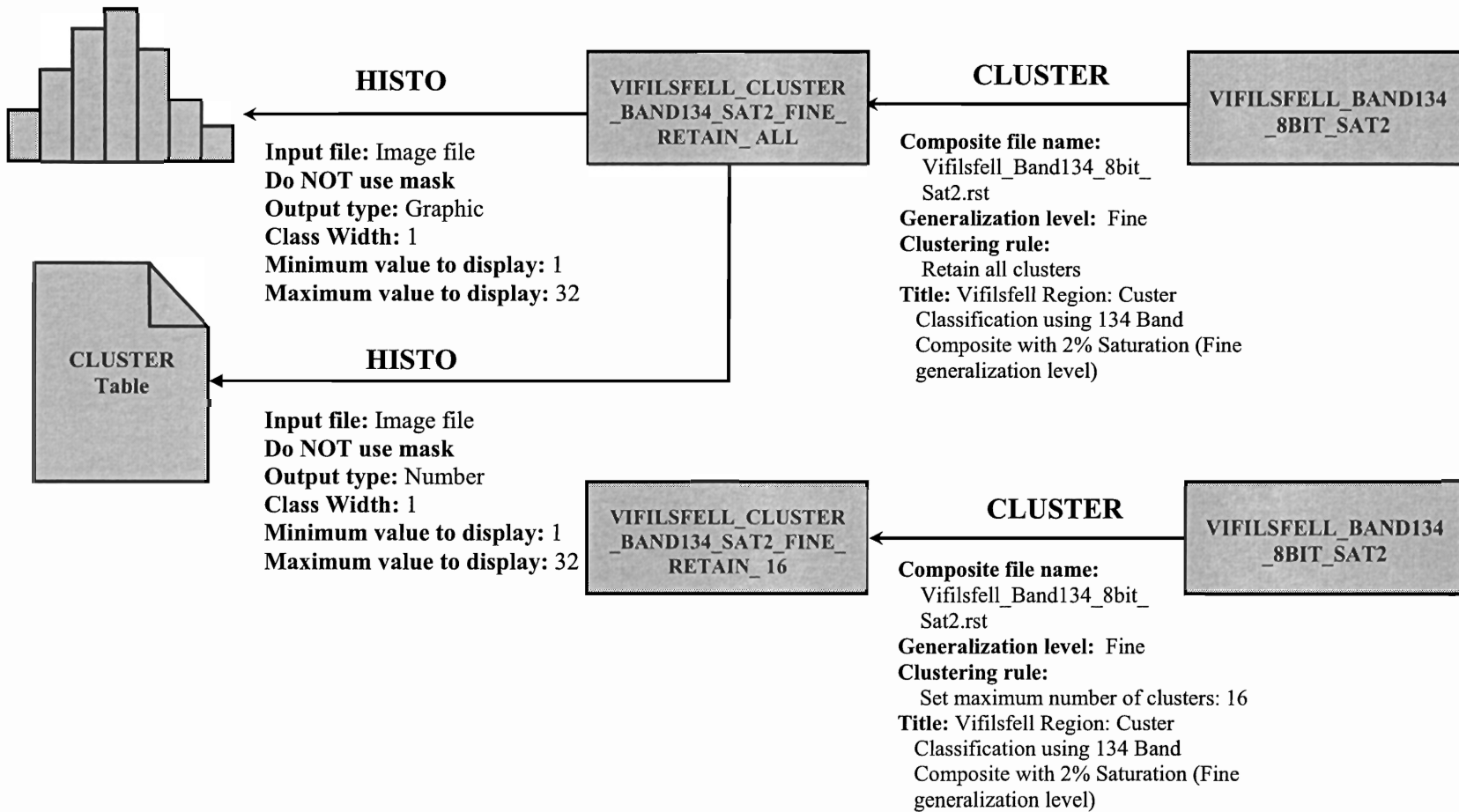
## **A.6 Cartographic Model 6 (band composite classification)**

The CLUSTER module utilizes 8-bit composite images to identify discrete spectral signatures (clusters) within the data. The CLUSTER module can only classify 8-bit composites composed of three constituent images; however, if the three bands are selected conscientiously, the composite image will contain nearly all of the unique information within the complete data set. The best results using CLUSTER are obtained using a fine generalization level with an analyst-defined maximum number of clusters. To determine the optimum number of clusters, the CLUSTER classification is performed with all clusters retained. The HISTO module is then used to identify natural breaks in the frequency distribution of the cluster classification. The cluster classification must also be evaluated qualitatively to search for patterns of spatial organization clusters. If the spatial distribution of clusters follows an identifiable trend, these clusters may correspond to rare ground-cover types within the image. If the spatial distribution of low frequency clusters is random the clusters are likely erroneous. Once the maximum number of significant clusters is determined, the CLUSTER module is run a second time with an operator-defined cluster threshold set to exclude insignificant clusters. Excluded clusters are forced into significant clusters with the most similar spectral signatures. Amalgamation of low frequency clusters into spectrally similar high frequency clusters helps to prevent division of spectrally variable information classes into large number subgroups that must subsequently be recombined.

To ensure that CLUSTER is best choice of unsupervised classifier for the data set, the CLUSTER classification results are compared with classification results from the ISOCLUST module. The ISOCLUST module is similar in its operation to CLUSTER;

however, ISOCLUST considers all spectral bands in the original data rather than just three. The ISOCLUST module nevertheless requires a three-band composite seed image to perform a classification and the choice of the seed composite image affects the classification result. The result from ISOCLUST is similar to the product of the CLUSTER classification and no significant improvements are observed. The results of the ISOCLUST classification are, therefore, abandoned in favor of the original results from CLUSTER. Cartographic Model 6 (Appendix A.6.1) summarizes the procedure for generating a unsupervised classification from the B1-B3-B4 8-bit composite image using CLUSTER.

### A.6.1 Cartographic Model 6: (band composite classification)



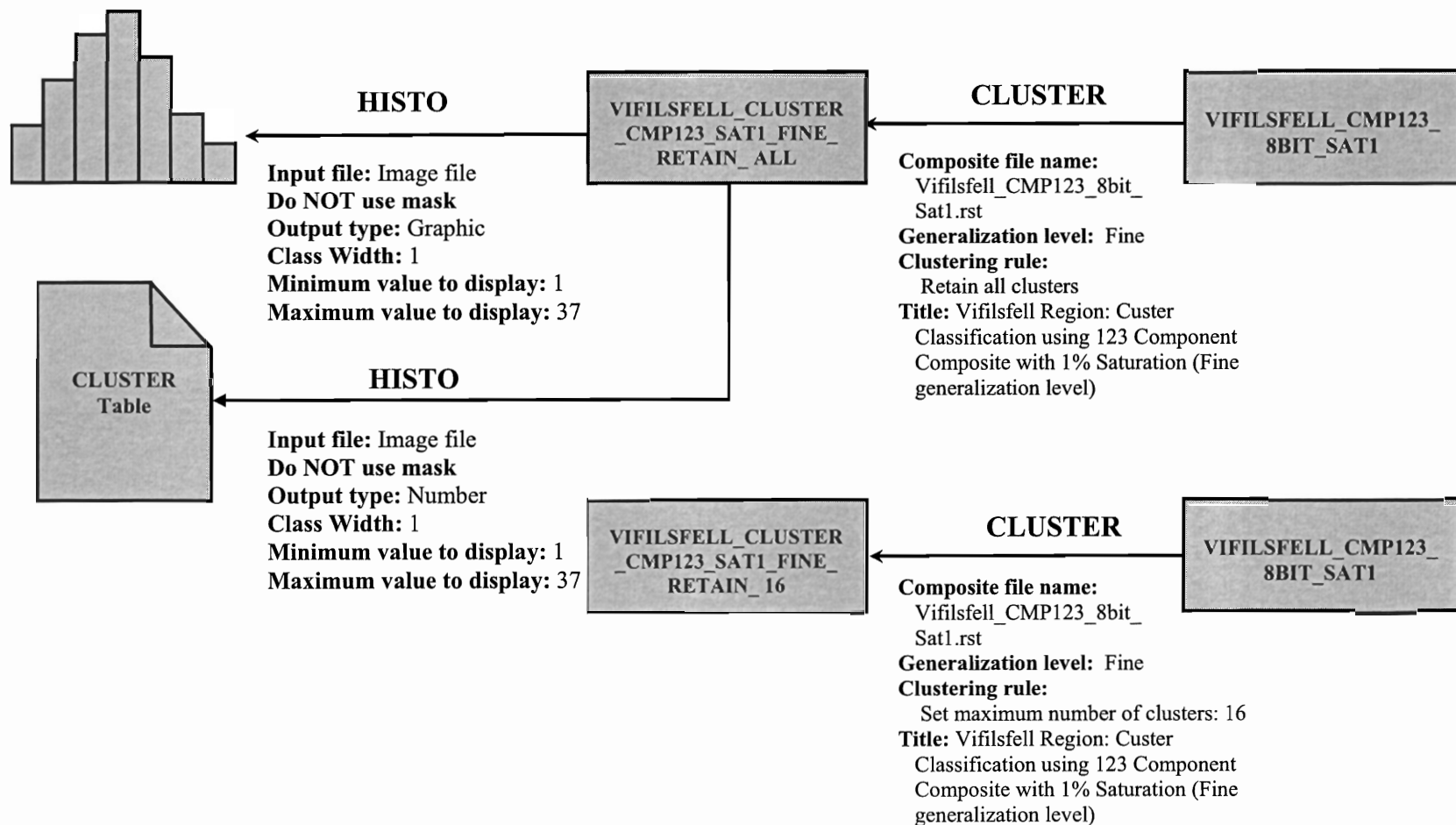
## A.6.2 Band Composite Classification: cluster frequency

Class	Lower Limit	Upper Limit	Frequency	Proportion	Cumulative Frequency	Cumulative Proportion
0	1.00	1.99	1564586	0.1324	1564586	0.1324
1	2.00	2.99	1461945	0.1238	3026531	0.2562
2	3.00	3.99	1228678	0.1040	4255209	0.3602
3	4.00	4.99	1056601	0.0894	5311810	0.4497
4	5.00	5.99	946655	0.0801	6258465	0.5298
5	6.00	6.99	836402	0.0708	7094867	0.6006
6	7.00	7.99	667412	0.0565	7762279	0.6571
7	8.00	8.99	575986	0.0488	8338265	0.7058
8	9.00	9.99	505797	0.0428	8844062	0.7487
9	10.00	10.99	445822	0.0377	9289884	0.7864
10	11.00	11.99	444305	0.0376	9734189	0.8240
11	12.00	12.99	399202	0.0338	10133391	0.8578
12	13.00	13.99	382212	0.0324	10515603	0.8902
13	14.00	14.99	281461	0.0238	10797064	0.9140
14	15.00	15.99	227142	0.0192	11024206	0.9332
15	16.00	16.99	208546	0.0177	11232752	0.9509
16	17.00	17.99	148173	0.0125	11380925	0.9634
17	18.00	18.99	101549	0.0086	11482474	0.9720
18	19.00	19.99	89937	0.0076	11572411	0.9796
19	20.00	20.99	74614	0.0063	11647025	0.9859
20	21.00	21.99	70821	0.0060	11717846	0.9919
21	22.00	22.99	30517	0.0026	11748363	0.9945
22	23.00	23.99	26766	0.0023	11775129	0.9968
23	24.00	24.99	23973	0.0020	11799102	0.9988
24	25.00	25.99	6718	0.0006	11805820	0.9994
25	26.00	26.99	4747	0.0004	11810567	0.9998
26	27.00	27.99	2088	0.0002	11812655	1.0000
27	28.00	28.99	199	0.0000	11812854	1.0000
28	29.00	29.99	154	0.0000	11813008	1.0000
29	30.00	30.99	40	0.0000	11813048	1.0000
30	31.00	31.99	28	0.0000	11813076	1.0000
31	32.00	32.99	24	0.0000	11813100	1.0000

File name: Vifilsfell\_cluster\_134\_8bit\_sat2\_fine\_retain\_all

### A.7.1 Cartographic Model 7 (component composite classification)

The procedure used for developing a cluster classification from the 8-bit composite image C1-C2-C3 is the same as the method used to classify B1-B2-B3 (Appendix A.6.1).





## A.7.2 Component Composite Classification: cluster frequency

Class	Lower Limit	Upper Limit	Frequency	Proportion	Cumulative Frequency	Cumulative Proportion
0	1.00	1.99	1686151	0.1427	1686151	0.1427
1	2.00	2.99	1552645	0.1314	3238796	0.2742
2	3.00	3.99	1133119	0.0959	4371915	0.3701
3	4.00	4.99	1040280	0.0881	5412195	0.4582
4	5.00	5.99	728499	0.0617	6140694	0.5198
5	6.00	6.99	675512	0.0572	6816206	0.5770
6	7.00	7.99	580250	0.0491	7396456	0.6261
7	8.00	8.99	571904	0.0484	7968360	0.6745
8	9.00	9.99	528058	0.0447	8496418	0.7192
9	10.00	10.99	485415	0.0411	8981833	0.7603
10	11.00	11.99	484654	0.0410	9466487	0.8014
11	12.00	12.99	400239	0.0339	9866726	0.8352
12	13.00	13.99	362827	0.0307	10229553	0.8659
13	14.00	14.99	319257	0.0270	10548810	0.8930
14	15.00	15.99	316970	0.0268	10865780	0.9198
15	16.00	16.99	294213	0.0249	11159993	0.9447
16	17.00	17.99	166946	0.0141	11326939	0.9588
17	18.00	18.99	113873	0.0096	11440812	0.9685
18	19.00	19.99	95194	0.0081	11536006	0.9765
19	20.00	20.99	76477	0.0065	11612483	0.9830
20	21.00	21.99	40790	0.0035	11653273	0.9865
21	22.00	22.99	26656	0.0023	11679929	0.9887
22	23.00	23.99	24264	0.0021	11704193	0.9908
23	24.00	24.99	24248	0.0021	11728441	0.9928
24	25.00	25.99	20970	0.0018	11749411	0.9946
25	26.00	26.99	16442	0.0014	11765853	0.9960
26	27.00	27.99	14557	0.0012	11780410	0.9972
27	28.00	28.99	12442	0.0011	11792852	0.9983
28	29.00	29.99	9850	0.0008	11802702	0.9991
29	30.00	30.99	3797	0.0003	11806499	0.9994
30	31.00	31.99	3418	0.0003	11809917	0.9997
31	32.00	32.99	1686	0.0001	11811603	0.9999
32	33.00	33.99	1015	0.0001	11812618	1.0000
33	34.00	34.99	85	0.0000	11813003	1.0000
34	35.00	35.99	66	0.0000	11813069	1.0000
35	36.00	36.99	18	0.0000	11813087	1.0000
36	37.00	37.99	13	0.0000	11813100	1.0000

File name: Vifilsfell\_cluster\_cmp123\_sat1\_fine\_retain\_all

# **Appendix B**

## **Field Observations**

## B.1 Field Observations

Zone	Region Name	Waypoint Number	UTM Zone 27 <sup>1</sup>		Elevation (m) <sup>2</sup>	Sample Name	Bedding Orientation	Outcrop Description
			Easting	Northing				
9	Arnarþúfur (proximal)	42	471636	7102202	155	V01	265/12	<p><i>General:</i> gulley exposure to the SE of the largest hyaloclastite mound near Northern Bláfjöll</p> <p><i>Matrix:</i> palagonitized hyaloclastite; light brown to rust coloured, well bedded; bed thickness range 1-7 cm, modal thickness 1-2 cm</p> <p><i>Clasts:</i> glassy clasts (black); diameter range &lt;1-4 mm, modal diameter 1 mm, dominantly subangular clasts with uncommon subrounded clasts</p> <p><i>Other:</i> exposed surfaces are light brown to rust coloured; fresh surfaces have dark brown ground mass; matrix supported beds; abundant armoured lapilli with glass clast cores in some beds; ungraded; aphyric</p>
9	Arnarþúfur (proximal)	43	471977	7101776	263	V02	262/16	<p><i>General:</i> gulley exposure to the E of Wpt043</p> <p><i>Matrix:</i> palagonitized hyaloclastite with light brown weathering surfaces</p> <p><i>Clasts:</i> &gt;50% glass clasts; black to dark grey; diameter range 1-5 mm, modal diameter 2 mm; dominantly angular clasts with uncommon subrounded clasts</p> <p><i>Other:</i> exposed surfaces are light brown to rust coloured; fresh surfaces have dark brown groundmass; matrix supported to clast supported beds; well bedded</p>
2	Northern Bláfjöll	44	472478	7101319	502			<p><i>General:</i> former water-air interface (passage zone); 499 m clinometer elevation</p> <p><i>Other:</i> the transition from mixed hyaloclastite and scoria/breccia to sheet lava occurs over a span of ~4 m; mixed hyaloclastite and scoria form a sharp contact with an overlying scoria unit, which is 0.5 m thick and contains 50% scoria and undulose beds; an intermediate lava unit 1 m thick overlies the undulating scoria unit and exhibits a sharp basal contact; a 40 cm thick lava unit directly overlies the intermediate lava unit; the 40 cm</p>

<sup>1</sup>Datum: WGS 84

<sup>2</sup>Elevations are derived from GPS measurements unless otherwise stated

Zone	Region Name	Waypoint Number	UTM Zone 27 <sup>1</sup>		Elevation (m) <sup>2</sup>	Sample Name	Bedding Orientation	Outcrop Discription
			Easting	Northing				
2	Northern Bláfjöll (continued)	44						thick lava unit has undulose contacts with the deposits above and below; the 40 cm thick lava unit is in turn overlain by a 1.7 m thick unit consisting of sheet lava; a 0.5 m thick scoria unit with an undulose basal contact overlies the 1.7 m thick sheet lava; a sharp planar contact separates the scoria from a 6 m thick sheet lava unit; the uppermost planar contact at 499 m corresponds to the passage zone and represents the highest lake level during the period of lava emplacement
2	Northern Bláfjöll / Vífilfell (contact)	45	472522	7101393	501			<i>General:</i> contact between the upper surface of Northern Bláfjöll and the base of Vífilfell; 526m clinometer elevation; a sharp planar contact separates Northern Bláfjöll lavas and Vífilfell hyaloclastite deposits <i>Glacial striations:</i> parallel lineations trending southeast-northwest are evident on the upper surface of the Northern Bláfjöll lava plateau <i>Other:</i> lowermost Vífilfell deposits consist exclusively of hyaloclastite (i.e. there are no basal pillow lavas)
8	Vífilfell (peak)	-	-	-	655*			<i>General:</i> peak of Vífilfell; palagonitized hyaloclastite
-	Outside study region	48	469055	7104289	199			<i>General:</i> No outcrops
13	Aeolean sediments (outside study region)	49	469168	7104223	157			<i>General:</i> 0.3-1 m thick accumulation of pale to rust brown aeolian sediments; very fine-grained (powdery); presumably derived from hyaloclastite
11	Arnarþúfur (distal)	50 51 52 53 54 55	469410 469397 469398 469393 469389 469388	7104011 7104020 7104030 7104038 7104038 7104031	204 204 204 204 205 204	V03	252/24	<i>General:</i> Wpt050-Wpt055 are a series of small 2-3 m <sup>2</sup> outcrops of palagonitized hyaloclastite; 0.5-1 m in height <i>Other:</i> of all of the collected samples, V03 is the most distant from Northern Bláfjöll; outcrops are typically massive with poorly-defined to nonexistent bedding

\* Geodetic survey marker elevation

Zone	Region Name	Waypoint Number	UTM Zone 27 <sup>1</sup>		Elevation (m) <sup>2</sup>	Sample Name	Bedding Orientation	Outcrop Discription
			Easting	Northing				
11	Arnarþúfur (distal)	56	469516	7103950	212	V04		<p><i>General:</i> 12 m by 20 m outcrop; 5 m in height</p> <p><i>Matrix:</i> palagonitized hyaloclastite</p> <p><i>Clasts:</i> 10-25% glass clasts; diameter range 0.5-5 mm; vesicle embayments</p> <p><i>Other:</i> poorly defined bedding; non-planar (deformed) beds; rythmic bedding alternating between fine grained dark beds and course-grained lighter coloured beds; ungraded; maxtrix supported</p> <p><i>Lineations:</i> occur perpendicular to bedding and form cross-cutting relationships with beds; positive relief features; lineations trend 62-242, 72-272-62-242, and 59-239; in one exposure a strike-dip measurement of 063/70 is obtained; lineations and the surrounding material appears homogeneous; the lineations are not glacial striations</p>
10	Arnarþúfur (central)	57	469595	7103904	218	V05	198/52 010/56	<p><i>General:</i> intensely weathered outcrop; 8 m in height</p> <p><i>Matrix:</i> palogonitized hyaloclastite</p> <p><i>Clasts:</i> 15-20% black glass clasts; diameter range 0.5-2 mm, modal diameter 1 mm, subrounded to subangular clasts, vesicle embayments</p> <p><i>Other:</i> well-defined bedding; beds thicknesses range from 0.5 cm to 9 cm, beds dip in opposite directions away from a central axis; ungraded; matrix supported; beds are coarse grained and contain abundant armoured lapilli with glass clast cores</p>
10	Arnarþúfur (central)	59	469753	7103773	226	V06 V07	198/52 010/56	<p><i>General:</i> 6 m by 10 m outcrop; sample V06 is from the bottom of the outcrop; sample V07 is from the top of the outcrop</p> <p><i>Matrix:</i> palagonitized hyaloclastite</p> <p><i>Clasts:</i> basal beds contain large glass clasts 2-2.5 cm in diameter and hyaloclastite cobbles up to 10-15 cm in diameter</p>

Zone	Region Name	Waypoint Number	UTM Zone 27 <sup>1</sup>		Elevation (m) <sup>2</sup>	Sample Name	Bedding Orientation	Outcrop Discription
			Easting	Northing				
10	Arnarþúfur (central)	60	470391	7103822	190	V08 V09	332/41 152/58	<p><i>General:</i> 15 m by 20 m outcrop; 10 m in height; sample V09 is from the bottom of the outcrop; sample V08 is from the top of the outcrop</p> <p><i>Matrix:</i> palagonitized hyaloclastite</p> <p><i>Other:</i> bedding is generally well defined except for near the outcrop margins where beds are deformed; beds are 3-4 cm thick; in the upper and lower regions of the outcrop beds dip in opposite directions</p>
10	Arnarþúfur (central)	61	470877	7103174	221	Wpt061	150/06 148/20 138/34 348/08	<p><i>General:</i> palagonitized hyaloclastite outcrop 13 m in height; outcrop divides into lower, middle, and upper zones</p> <p><i>Lower zone:</i> scree mantles most of the lower 9 m of the outcrop, which includes both lower and middle zones; in the lower zone, 2 m from the base of the outcrop, bedding is 348/08 and dips opposite to the direction of the beds above; beds in the lowermost 1-1.5 m contain less armoured lapilli than in other sections of the outcrop</p> <p><i>Middle zone:</i> planar beds contain abundant armoured lapilli with glass clast cores; unarmoured glass clasts are common and have diameters up to 15 mm; bedding orientations range from 150/06 to 138/34; upper sections of the middle zone become increasingly massive with poorly defined bedding and common lenses of coarse armoured lapilli; lenses appear to have random orientations; the massive unit is 1 m thick and contains less than 10% armoured lapilli by volume; a sample is collected from the massive unit that contains lens deposits</p> <p><i>Upper zone:</i> the massive unit grades upwards into very finely laminated beds and then into planar beds with fine-grained (&lt;1 mm) matrix that supports subrounded to subangular clasts and abundant (30-40%) armoured lapilli that are 2-4 mm in diameter and contain glass clast cores; the upper 3 m of the outcrop contains rythmically layered beds that steepen systematically from near horizontal to 34° to the N-NW</p>

Zone	Region Name	Waypoint Number	UTM Zone 27 <sup>1</sup>		Elevation (m) <sup>2</sup>	Sample Name	Bedding Orientation	Outcrop Discription
			Easting	Northing				
10	Arnarþúfur (central)	62	470923	7103206	213	Wpt062	295/19 270/20	<p><i>General:</i> palagonitized hyaloclastite outcrop near the middle of the cluster of mounds that forms the central Arnarþúfur deposit; outcrop is 10 m in height; Wpt062 includes lower and upper zones; scree mantles much of the lower sections of the outcrop</p> <p><i>Lower zone:</i> rhythmically bedded outcrop containing abundant armoured lapilli with glass clast cores; beds are typically 2 cm thick with mm scale internal laminations; thick beds contain a higher proportion of armoured lapilli than thin beds; lapilli are 4-10 mm in diameter and comprise approximately 20% of the volume of the beds</p> <p>beds contain approximately 70% glass clasts and are clast supported; glass clasts are up to 30 mm in diameter and are angular to subangular in shape; clasts are vesicle poor; armoured lapilli are rare to absent; beds are well indurated; no cross bedding</p>
10	Arnarþúfur (central)	63	471110	7103183	186		244/16	<p><i>General:</i> palagonitized hyaloclastite; rare armoured lapilli; clast diameters up to 10-15 mm, 4 mm average clast diameter</p>
10	Arnarþúfur (central)	64	471115	7103142	125		072/50	<p><i>General:</i> palagonitized hyaloclastite outcrop 5 m SSE of Wpt063; basal beds are curvplanar to planar with poorly defined internal structure; deposits within the middle of the outcrop contain well defined cm scale beds with dominantly curvplanar bedding; uppermost beds contain abundant glass clasts with curiplanar bedding; overall the bedding curvature increases upwards and the deposits appear to have slumped to towards the SE</p>
10	Arnarþúfur (central)	65	471128	7103103	187		140/79	<p><i>General:</i> palagonitized hayaloclastite; near vertical bedding; clast supported (~80% clasts); clast diameters range from 3-30 mm with a modal diameter of 4 mm; bedding planes are curivplanar and the inclination of beds decreases down dip, towards the SE</p>

Zone	Region Name	Waypoint Number	UTM Zone 27 <sup>1</sup>		Elevation (m) <sup>2</sup>	Sample Name	Bedding Orientation	Outcrop Discription
			Easting	Northing				
9	Arnarþúfur (proximal)	66	471517	7102533	232		200/21 131/21	<i>General:</i> palagonitized hayaloclastite; very large deposit (approximately 150 m by 60 m and 30 in height); primarily massive with rare bedding; where present bedding in poorly defined and indistinct; abundant and boulders with bedding; large boulders (2 m by 2 m by 2 m) appear to be collapsed blocks; abundant armoured lapilli; clasts range from 2 mm to 20 m in diameter; clasts are typically angular to subangular; glass clast proportion is within beds is up to 50%, however, beds are dominantly matrix supported
9	Arnarþúfur (proximal)	67	471307	7102846	198		188/30	<i>General:</i> palgonitized hayloclastite; parallel bedding; abundant armoured lapilli; up to 70% clasts; clast supported beds; clast diameters 2-6 mm
9	Arnarþúfur (proximal)	68	471828	7102163	234			<i>General:</i> palagonitized hayloclastite; curvilinear beds that thicken down dip; matrix supported; clast range 2-3 mm; the outcrop contains an anomalous 3-4 cm thick bed consisting almost exclusively of class clasts 4-12 mm in diameter with a modal diameter of 5 mm.
9	Arnarþúfur (proximal)	69	472089	7102244	238			<i>General:</i> palagonitized hyaloclastite; blocky with poorly defined bedding
9	Arnarþúfur (proximal)	70 71	472018 472024	7101944 7102013	275 264	Wpt070	310/15 251/12	<i>General:</i> palagonitized hayloclastite; well-defined planar bedding; subangular clasts 1-5 mm in diameter, modal diameter 2 mm; matrix supported beds; armoured lapilli is absent
9	Arnarþúfur (proximal)	72	472375	7101964	292			<i>General:</i> isolated palagonitized hayloclastite mound on the slopes of Northern Bláfjöll; folded hayloclastite beds; fold axis trends 029-209; conjugate fracture at the nose of the fold with 50° and 130° angles of intersection
9	Arnarþúfur (proximal)	73	471801	7102426	228			<i>General:</i> palagonitized hayloclastite, large antiform within the center of the deposit with a long axis trending 140-320



Zone	Region Name	Waypoint Number	UTM Zone 27 <sup>1</sup>		Elevation (m) <sup>2</sup>	Sample Name	Bedding Orientation	Outcrop Discription
			Easting	Northing				
10	Arnarþúfur (central)	75	470993	7103266	209		139/30 139/35	<p><i>General:</i> palagonitized hayloclastite; well-defined bedding; a series of fractures run parallel to bedding; faults run perpendicular to bedding</p> <p><i>Faults and fractures:</i> eight faults occur over a span of ~6 m; each fault has a similar orientation (139-35) with a series of associated fractures oriented perpendicular to the fault plane; fractures are offset by the faults and are therefore older; faults and fractures are typically infilled with fine-grained palagonite groundmass; faults are generally several meters in length; from NE to SW fault charactersits are as follows:</p> <p><i>Fault 1:</i> sinstral; 15 cm displacement  <i>Fault 2:</i> 100 cm SW of Fault 1; sinstral  <i>Fault 3:</i> 70 cm SW of Fault 2; sinstral  <i>Fault 4:</i> 90 cm SW of Fault 3; sinstral; 4 cm displacement  <i>Fault 5:</i> 80 cm SW of Fault 4; dextral; 10 cm displacement  <i>Fault 6:</i> 40 cm SW of Fault 5; dextral; 12 cm displacement  <i>Fault 7:</i> 155 cm SW of Fault 6; sinstral; 6 cm displacement  <i>Fault 8:</i> 80 cm SW of Fault 7; sinstral; 27 cm displacement</p>
9	Arnarþúfur (proximal)	76	471104	7103185	191			<p><i>General:</i> palagonitized hyaloclastite with rhythmic bedding and abundant flow structures (i.e. well-defined flutes)</p> <p><i>Flutes:</i> 154-334, 152-332</p> <p><i>Other:</i> bedding ranges from planar to irregular and convolute; coarse-grained groundmass; armoured lapilli with diameters up to 15 cm</p>
12	A'a flows beneath Arnarþúfur	-	-	-	-			<p><i>General:</i> a'a lava flows underling Arnarþúfur deposits and contain glacial strations; 10-20 m NE of Wpt076</p> <p><i>Glacial striations:</i> 149-329, 141-321, 145-325  Glacial striations are parallel to the long-axis of Arnarþúfur</p> <p><i>Tectonic faulting:</i> SW-NE (perpendicular to long-axis of Arnarþúfur)</p>
4	Vífilsfell (peripheral)	77	473272	7101315	496			<p><i>General:</i> palagonitized hyaloclastite; steeply inclined beds; ladder ripples; spindle bombs up to 30-40 cm in diameter; abundant wall-rock lithics</p>

Zone	Region Name	Waypoint Number	UTM Zone 27 <sup>1</sup>		Elevation (m) <sup>2</sup>	Sample Name	Bedding Orientation	Outcrop Discription
			Easting	Northing				
5	Vífilsfell (crater region)	78	473206	7101274	572	Wpt078	310/32	<i>General</i> : zeolitized hyaloclastite; pale grey colour
5	Vífilsfell (crater region)	79	473023	7101196	605			<i>General</i> : zeolitized hyaloclastite; pale grey colour unlaminated; massive (no evident bedding)
5	Vífilsfell (crater region)	80	472956	7101177	588			<i>General</i> : zone of intense zeolitization
5	Vífilsfell (crater region)	81	472916	7101096	569		358/11	<i>General</i> : palagonitized hyaloclastite below zeolitization zone; well-defined bedding
5	Vífilsfell (crater region)	82	472884	7101135	516			<i>General</i> : welded scoria unit with sharp basal contact; magnetic flux measurements reveal that the welded scoria unit has strong normal magnetization
5	Vífilsfell (crater region)	83	472821	7100997	554		222/44	<i>General</i> : welded scoria unit with a sharp basal contact; a 20 cm thick massive hyaloclastite unit grades upwards into a 3 m thick scoria unit and then forms a sharp contact with a 0.5 m thick agglutinated scoria unit that grades into a 1-3 m thick welded scoria deposit; the welded scoria unit has a superincumbent 0.5 m thick upper agglutinated scoria unit, which is in turn overlain by a deeply eroded hyaloclastite unit
5	Vífilsfell (crater region)	84	472866	7100984	580		152/30	<i>General</i> : palagonitized hyaloclastite
5	Vífilsfell (crater region)	85	472811	7100952	579		104/20	<i>General</i> : palagonitized hyaloclastite
5	Vífilsfell (crater region)	86	472839	7100953	585		228/44	<i>General</i> : palagonitized hyaloclastite
5	Vífilsfell (crater region)	87	472902	7100962	589		282/24	<i>General</i> : palagonitized hyaloclastite
5	Vífilsfell	88	472929	7100948	593		245/46	<i>General</i> : palagonitized hyaloclastite; ring fracture with slickensides; beds dip 245/46; slickensides are inclined 15° from the down dip direction with an orientation of 270-44
5	Vífilsfell	89	472931	7100940	590			<i>General</i> : palagonitized hyaloclastite; ring fracture with slickensides <i>Ring fracture</i> : 3 m long section of curved fault plane with slickensides; fault plane cross cuts bedding and has a displacement of many 10s of cm

Zone	Region Name	Waypoint Number	UTM Zone 27 <sup>1</sup>		Elevation (m) <sup>2</sup>	Sample Name	Bedding Orientation	Outcrop Discription
			Easting	Northing				
3	Northern Bláfjöll (possible contact with Vífilsfell)	90	473313	7100870	466			General: possible contact between Northern Bláfjöll and Vífilsfell on the SE side of Northern Bláfjöll; pillow breccia terminates abruptly against a fine-grained crystalline unit that is tan in colour and exhibits cooling fractures perpendicular to the surface of the deposit; the fine-grained crystalline unit is ~30 cm thick with a 2-20 cm thick mantle of sand-sized palagonite that grades into a clast rich breccia with palagonite matrix; a diapir originating from the fine-grained crystalline unit extends upwards through a thick deposit of overlying palagonite
4	Vífilsfell (peripheral)	-	-	-	-			General: dyke with pillowed surfaces within palagonitized hyaloclastite; located on the steep slopes on the north-northwest side of Vífilsfell
2	Vífilsfell	91	472510	7101345	511	Wpt091		General: palagonitized hyaloclastite; Vífilsfell sample obtained from above the contact between Northern Bláfjöll and Vífilsfell on NE side of Northern Bláfjöll
2	Northern Bláfjöll / Vífilsfell (contact)	92	472509	7101361	509	Wpt092		General: sharp planar contact between Northern Bláfjöll and Vífilsfell; below the contact vesicle-rich Northern Bláfjöll lavas with a well-preserved upper glassy surface that terminates abruptly against palagonitized hyaloclastite from Vífilsfell; sample Wpt092 spans the contact
2	Northern Bláfjöll / Vífilsfell (contact)	93	472525	7101412	492			General: sharp planar contact between Northern Bláfjöll and Vífilsfell; the upper surface of the Northern Bláfjöll lavas below the hyaloclastite does not exhibit a red oxidation zone; palagonitized hyaloclastite from Vífilsfell contains angular lithic fragments near contact
2	Northern Bláfjöll	94	472467	7101376	457	Wpt094		General: sample collected from Northern Bláfjöll is from the middle of a 3 m thick lava flow below the contact; within this section of the lava flow vesicles are rare to absent and flow banding is common; magnetic flux measurements of lava show that it has strong normal magnetization
1	Northern Bláfjöll	95	473763	7102346	158			General: gravel quarry (pillow lavas) on the northern side of Bláfjöll
4	Vífilsfell (peripheral)	97	473307	7101318	535			General: <i>in situ</i> volcanic bomb (crystalline) within palagonitized hyaloclastite; bomb is ~30 cm in diameter

Zone	Region Name	Waypoint Number	UTM Zone 27 <sup>1</sup>		Elevation (m) <sup>2</sup>	Sample Name	Bedding Orientation	Outcrop Discription
			Easting	Northing				
5	Vifilsfell (crater rim)	99	473200	7101192	592		280/30	<i>General:</i> outer margin of the crater; palagonitized hyaloclastite; well bedded
5	Vifilsfell (crater rim)	100	473160	7101118	626		078/30	<i>General:</i> inner margin of the crater; palagonitized hyaloclastite; well bedded
5	Vifilsfell (crater rim)	101	473205	7101109	618		178/18 456/18	<i>General:</i> crater rim with concave down beds of palagonitized hyaloclastite; beds dip towards the vent on one side of the crater rim and directly away from the vent on the other side
4	Vifilsfell	102	472855	7101061	548			<i>General:</i> massive deposits of palagonitized hyaloclastite; <i>Clasts:</i> abundant scoria clasts and volcanic bombs up to 20 cm in diameter; 3 cm average clast diameter
6	Vifilsfell (vent region)	103	472789	7101064	523		155/60	<i>General:</i> steeply dipping beds inclined towards the vent; palagonitized hyaloclastite; thin convolute to planar beds; ripple marks indicate down-dip flow direction
6	Vifilsfell (vent region)	104 105 106 107 108 110 111 112 113 114 115 116	472792 472785 472787 472781 472756 472750 472745 472745 472746 472757 472735 472763	7101054 7101062 7101070 7101082 7101079 7101096 7101084 7101084 7101119 7101091 7100992 7100998	529 - 537 532 521 530 518 515 476 520 539 547	Wpt107	132/52 148/55 140/50 150/62 162/68 120/60 059/61 034/54  102/54 220/39 232/50	<i>General:</i> Wpt103-Wpt116 are a series of observation points that define the location of the central vent of Vifilsfell; steeply dipping beds of palagonitized hyaloclastite form a horse-shoe shaped deposit around the vent that opens to the S-SW (195°); separation between observation points is less than GPS measurement uncertainty; the following samples are ordered in counter-clockwise series from the SE to the SW: Wpt103, Wpt104, Wpt106, Wpt105, Wpt107, Wpt108, Wpt110, Wpt113, Wpt114, Wpt111, and Wpt112; Wpt115 and Wpt116 are located along the inner slope of the crater wall, opposite to the opening in the horse-shoe vent proximal deposits; Wpt113 corresponds to the inferred center of the volcanic vent <i>Clasts:</i> abundant scoria clasts 2-7 mm in diameter; average clast diameter 4 mm; lenses of clasts within thin palagonite beds are common <i>Bedding:</i> beds dip towards the vent and have ripple marks that indicate an approximate down-dip flow direction; beds are planar to convolute with well-defined internal lamination

Zone	Region Name	Waypoint Number	UTM Zone 27 <sup>1</sup>		Elevation (m) <sup>2</sup>	Sample Name	Bedding Orientation	Outcrop Description
			Easting	Northing				
7	Vífilsfell (channel)	117	472592	7101032	488		200/32	<i>General:</i> channel extending from the S-SW opening in vent proximal deposits; channel curves NW with distance from the vent; palagonitized hyaloclastite with abundant flow structures (i.e. ripple marks and climbing ripples); some outcrops are massive with no visible bedding
		118	472611	7101057	448			
7	Vífilsfell (channel)	119	472461	7101073	491			<i>General:</i> channel abruptly terminates at the edge of the Northern Bláfjöll plateau where a cliff extends from the ledge to a scree slope several hundred meters below; channel deposits include beds of fine-grained palagonitized hyaloclastite and abundant metre-scale blocks of palagonite
5	Vífilsfell	120	472641	7101233	532		298/20	<i>General:</i> bedded palagonitized hyaloclastite
5	Vífilsfell	121	472689	7101348	597		261/32	<i>General:</i> bedded palagonitized hyaloclastite
5	Vífilsfell	122	472923	7101255	612			<i>General:</i> bedded palagonitized hyaloclastite containing volcanic bombs
5	Vífilsfell	123	473039	7101214	615			<i>General:</i> bedded palagonitized hyaloclastite containing volcanic bombs (visibility through fog <5 m)

# Appendix C

## Geochemistry

## C.1 Geochemical analysis of glass samples from the Vífilsfell Region, Southwest Iceland

### Electron Microprobe Data: original oxide weight percentages

#### Northern Bláfjöll

Sample	Probe #	SiO2	TiO2	Al2O3	Cr2O3	FeO	MnO	MgO	CaO	Na2O	K2O	P2O5	Total	Comments
Wpt094	98	48.71	1.77	14.66	0.01	11.73	0.13	8.57	11.72	2.38	0.04	0.17	99.89	Wpt094 clast 1 site1
Hyaloclastite	99	49.12	1.79	14.72	0.03	11.60	0.25	8.49	11.61	2.42	0.03	0.18	100.23	Wpt094 clast 1 site2
Sample from	100	49.19	1.75	14.75	0.02	11.48	0.15	8.50	11.53	2.42	0.04	0.16	99.98	Wpt094 clast 1 site3
Northern	101	49.19	1.73	14.71	0.01	11.56	0.13	8.52	11.60	2.39	0.03	0.12	99.98	Wpt094 clast 1 site4
Bláfjöll	102	48.82	1.72	14.83	0.03	11.90	0.24	8.50	11.61	2.39	0.05	0.11	100.19	Wpt094 clast 1 site5
Underlying	103	48.62	1.70	14.82	0.02	11.47	0.15	8.60	11.74	2.35	0.03	0.16	99.68	Wpt094 clast 2 site1
Vífilsfell	104	48.99	1.81	14.78	0.02	11.22	0.18	8.48	11.58	2.39	0.04	0.14	99.62	Wpt094 clast 2 site2
	105	48.78	1.71	14.77	0.03	11.83	0.10	8.55	11.81	2.42	0.05	0.15	100.21	Wpt094 clast 2 site3
	106	49.00	1.71	14.96	0.02	11.92	0.20	8.33	11.53	2.42	0.03	0.14	100.24	Wpt094 clast 3 site1
	107	48.61	1.89	14.80	0.02	11.76	0.13	8.33	11.60	2.44	0.05	0.17	99.79	Wpt094 clast 3 site2
	108	48.55	1.77	14.74	0.04	11.58	0.23	8.24	11.80	2.41	0.06	0.21	99.62	Wpt094 clast 5 site1
	109	48.84	1.81	14.71	0.07	11.15	0.11	8.37	11.71	2.37	0.04	0.17	99.35	Wpt094 clast 5 site2
	110	48.33	1.67	14.74	0.05	11.54	0.36	8.53	11.80	2.39	0.07	0.12	99.60	Wpt094 clast 6 site1
	111	48.28	1.71	14.82	0.08	11.54	0.24	8.51	11.89	2.38	0.06	0.15	99.65	Wpt094 clast 6 site2
	112	49.11	1.76	14.79	0.07	11.24	0.27	8.64	11.71	2.36	0.05	0.12	100.11	Wpt094 clast 6 site3
	113	49.06	1.74	14.98	0.08	11.92	0.21	8.27	11.88	2.42	0.05	0.16	100.77	Wpt094 clast 7 site1
	114	48.88	1.80	14.85	0.08	11.57	0.17	8.29	11.64	2.41	0.05	0.15	99.88	Wpt094 clast 7 site2

<b>Average</b>		48.83	1.75	14.79	0.04	11.59	0.19	8.45	11.69	2.40	0.04	0.15	99.93	
<b>Standard Deviation</b>		0.28	0.05	0.08	0.03	0.24	0.07	0.12	0.12	0.03	0.01	0.03	0.34	

Original oxide weight percentages (continued)

Vífilsfell

Sample	Probe #	SiO2	TiO2	Al2O3	Cr2O3	FeO	MnO	MgO	CaO	Na2O	K2O	P2O5	Total	Comments
Wpt091	115	49.25	1.79	14.86	0.05	11.53	0.19	8.21	11.77	2.43	0.04	0.13	100.25	Wpt091 clast 1 site1
Sample from Vífilsfell	116	49.12	1.75	14.82	0.10	11.71	0.26	8.20	11.86	2.46	0.06	0.15	100.49	Wpt091 clast 1 site2
	117	49.11	1.73	15.05	0.08	11.46	0.15	8.24	11.76	2.38	0.07	0.17	100.19	Wpt091 clast 2 site1
	118	49.08	1.76	14.78	0.05	11.85	0.16	8.21	11.86	2.46	0.04	0.12	100.38	Wpt091 clast 2 site2
	119	49.09	1.82	14.84	0.04	11.54	0.10	8.18	11.98	2.43	0.09	0.12	100.23	Wpt091 clast 3 site1
	120	49.13	1.81	14.97	0.02	11.61	0.15	8.25	11.70	2.40	0.08	0.14	100.26	Wpt091 clast 3 site2
	121	49.16	1.81	14.76	0.05	11.62	0.23	8.19	11.92	2.48	0.05	0.11	100.37	Wpt091 clast 4 site1
	122	48.98	1.76	14.65	0.03	11.42	0.11	8.28	11.79	2.53	0.05	0.13	99.74	Wpt091 clast 5 site1
	123	48.91	1.82	14.63	0.04	11.31	0.15	8.27	11.82	2.46	0.07	0.13	99.61	Wpt091 clast 5 site2
	124	49.22	1.78	14.68	0.03	11.47	0.15	8.22	11.87	2.51	0.06	0.18	100.17	Wpt091 clast 6 site1
	125	48.93	1.73	14.70	0.05	11.44	0.25	8.17	11.92	2.51	0.07	0.14	99.91	Wpt091 clast 6 site2
	126	49.13	1.71	14.86	0.03	11.93	0.09	8.23	11.88	2.53	0.05	0.17	100.60	Wpt091 clast 7 site1
	127	49.03	1.71	14.87	0.03	11.16	0.15	8.19	11.94	2.48	0.06	0.17	99.77	Wpt091 clast 7 site2
	128	48.80	1.75	14.99	0.02	11.68	0.09	8.28	11.76	2.48	0.07	0.15	100.08	Wpt091 clast 8 site1
	129	49.15	1.83	15.04	0.02	11.90	0.03	8.24	11.89	2.46	0.10	0.18	100.84	Wpt091 clast 8 site2
	130	48.61	1.78	14.80	0.02	11.38	0.15	8.24	11.76	2.46	0.09	0.18	99.45	Wpt091 clast 10 site1
	131	48.42	1.85	14.89	0.04	11.50	0.12	8.22	11.71	2.47	0.10	0.18	99.50	Wpt091 clast 10 site2
	132	48.46	1.85	14.94	0.03	11.51	0.27	8.24	11.78	2.46	0.07	0.16	99.76	Wpt091 clast 11 site1
	133	48.40	1.78	14.90	0.04	11.61	0.25	8.23	11.83	2.45	0.09	0.15	99.72	Wpt091 clast 11 site2
	134	49.25	1.87	14.88	0.01	11.81	0.22	8.35	11.79	2.48	0.08	0.14	100.89	Wpt091 clast 12 site1
	135	49.03	1.69	14.93	0.04	11.61	0.21	8.27	11.83	2.46	0.06	0.13	100.26	Wpt091 clast 12 site2
	136	48.25	1.74	14.97	0.05	11.02	0.14	8.41	11.73	2.45	0.08	0.12	98.95	Wpt091 clast 13 site1
	137	49.05	1.74	14.87	0.04	11.48	0.05	8.49	11.90	2.41	0.07	0.15	100.26	Wpt091 clast 13 site2

<b>Average</b>		48.94	1.78	14.86	0.04	11.55	0.16	8.25	11.83	2.46	0.07	0.15	100.07	
<b>Standard Deviation</b>		0.30	0.05	0.12	0.02	0.22	0.07	0.08	0.08	0.04	0.02	0.02	0.46	

Sample	Probe #	SiO2	TiO2	Al2O3	Cr2O3	FeO	MnO	MgO	CaO	Na2O	K2O	P2O5	Total	Comments
Wpt092	166	47.59	1.83	14.02	0.02	11.75	0.12	8.25	11.88	2.47	0.12	0.16	98.20	Wpt092 clast1 site1
Contact	167	47.56	1.85	14.00	0.02	11.26	0.26	8.19	11.60	2.45	0.12	0.17	97.48	Wpt092 clast1 site2
Between	169	47.91	1.81	13.98	0.01	11.31	0.15	8.14	11.79	2.41	0.13	0.13	97.76	Wpt092 clast2 site1
Northern	170	47.63	1.80	13.98	0.03	11.43	0.20	8.13	11.75	2.43	0.09	0.15	97.61	Wpt092 clast2 site2
Bláfjöll	171	47.60	1.88	14.03	0.02	10.50	0.26	8.07	11.56	2.44	0.12	0.13	96.62	Wpt092 clast3 site1
Vífilsfell	172	48.08	1.84	14.03	0.04	11.31	0.19	8.15	11.72	2.43	0.11	0.15	98.07	Wpt092 clast3 site2
(Sample clasts from Vífilsfell)	174	48.82	1.90	14.78	0.01	11.23	0.12	8.09	11.82	2.48	0.12	0.18	99.57	Wpt092 clast4 site1
	175	48.10	1.87	14.75	0.02	10.56	0.17	7.99	11.61	2.49	0.09	0.13	97.79	Wpt092 clast4 site2

<b>Average</b>		47.91	1.85	14.20	0.02	11.17	0.18	8.13	11.72	2.45	0.11	0.15	97.89	
<b>Standard Deviation</b>		0.44	0.04	0.37	0.01	0.38	0.05	0.07	0.10	0.03	0.01	0.02	0.89	



**Original oxide weight percentages (continued)**

Sample	Probe #	SiO2	TiO2	Al2O3	Cr2O3	FeO	MnO	MgO	CaO	Na2O	K2O	P2O5	Total	Comments
Wpt107 Sample from Vifilsfell	200	49.12	1.84	14.94	0.04	11.83	0.28	8.27	11.95	2.44	0.08	0.18	100.97	Wpt107 clast1 site1
	201	48.97	1.80	14.84	0.05	11.66	0.10	8.15	11.68	2.39	0.05	0.17	99.84	Wpt107 clast1 site2
	202	48.92	1.69	14.68	0.03	11.06	0.24	8.44	11.89	2.37	0.06	0.12	99.50	Wpt107 clast2 site1
	203	48.82	1.69	15.00	0.03	11.85	0.14	8.51	11.80	2.36	0.05	0.15	100.42	Wpt107 clast2 site2
	204	48.77	1.83	14.82	0.03	11.27	0.26	8.29	11.97	2.41	0.12	0.12	99.89	Wpt107 clast3 site1
	205	48.61	1.79	14.80	0.03	11.62	0.19	8.18	11.78	2.48	0.11	0.13	99.73	Wpt107 clast3 site2
	206	48.92	1.75	14.86	0.01	12.05	0.36	8.48	11.96	2.41	0.09	0.12	101.01	Wpt107 clast4 site1
	207	48.99	1.75	14.97	0.03	11.82	0.20	8.43	12.00	2.43	0.08	0.15	100.85	Wpt107 clast4 site2
	208	48.95	1.70	14.85	0.02	11.50	0.28	8.14	12.03	2.45	0.08	0.13	100.14	Wpt107 clast5 site1
	209	49.20	1.80	14.93	0.05	11.79	0.19	8.09	12.04	2.50	0.10	0.10	100.79	Wpt107 clast5 site2
	210	48.90	1.76	14.75	0.00	11.60	0.21	8.14	11.80	2.47	0.11	0.10	99.84	Wpt107 clast5 site3
	211	48.95	1.78	14.85	0.03	11.46	0.13	8.11	11.86	2.47	0.10	0.12	99.87	Wpt107 clast5 site4
	212	49.17	1.74	14.83	0.03	12.15	0.11	8.17	11.91	2.48	0.10	0.12	100.82	Wpt107 clast6 site1
	213	49.18	1.82	14.91	0.02	11.47	0.23	8.09	11.73	2.41	0.11	0.10	100.08	Wpt107 clast6 site2
	214	49.07	1.75	15.11	0.03	11.71	0.13	8.13	12.02	2.45	0.09	0.09	100.57	Wpt107 clast7 site1
	215	49.08	1.70	15.01	0.05	11.59	0.15	8.15	11.99	2.47	0.07	0.14	100.40	Wpt107 clast7 site2
	216	49.04	1.74	14.96	0.05	11.92	0.10	8.53	11.85	2.35	0.07	0.15	100.76	Wpt107 clast8 site1
	217	49.02	1.75	14.69	0.05	11.60	0.14	8.43	11.87	2.46	0.07	0.12	100.19	Wpt107 clast8 site2
	218	48.90	1.73	14.93	0.04	11.49	0.09	8.26	11.89	2.48	0.08	0.17	100.05	Wpt107 clast9 site1
	219	48.90	1.80	14.81	0.02	11.67	0.11	8.15	12.02	2.45	0.08	0.14	100.15	Wpt107 clast9 site2
	220	48.97	1.83	14.90	0.04	11.82	0.12	8.19	11.75	2.51	0.10	0.11	100.35	Wpt107 clast10 site1
	221	49.07	1.79	14.76	0.01	11.90	0.16	8.22	11.75	2.48	0.10	0.16	100.40	Wpt107 clast10 site2
	222	49.09	1.78	14.78	0.04	11.46	0.16	8.09	11.83	2.45	0.10	0.17	99.95	Wpt107 clast11 site1
	223	48.84	1.76	14.80	0.03	11.63	0.17	8.26	11.87	2.44	0.10	0.15	100.06	Wpt107 clast11 site2
	224	48.82	1.82	14.87	0.02	11.45	0.22	8.24	11.67	2.48	0.09	0.16	99.84	Wpt107 clast11 site3
	225	48.84	1.78	14.91	0.02	11.56	0.20	8.28	11.67	2.45	0.09	0.15	99.94	Wpt107 clast11 site4
	226	49.01	1.78	14.87	0.03	11.32	0.32	8.17	11.63	2.47	0.09	0.19	99.89	Wpt107 clast12 site1
227	48.62	1.83	14.73	0.03	11.31	0.24	8.14	11.58	2.46	0.10	0.17	99.21	Wpt107 clast12 site2	
<b>Average</b>		48.96	1.77	14.86	0.03	11.63	0.19	8.24	11.85	2.45	0.09	0.14	100.20	
<b>Standard Deviation</b>		0.15	0.04	0.10	0.01	0.25	0.07	0.14	0.13	0.04	0.02	0.03	0.45	

**Original oxide weight percentages (continued)**

**Arnarpfur**

Sample	Probe #	SiO2	TiO2	Al2O3	Cr2O3	FeO	MnO	MgO	CaO	Na2O	K2O	P2O5	Total	Comments
V02 (Wpt043)	12	48.75	1.74	14.99	0.04	11.82	0.21	8.58	11.93	2.43	0.08	0.14	100.71	V02 clast1 site1
Proximal	13	48.65	1.68	15.01	0.03	11.94	0.31	8.53	12.05	2.39	0.11	0.15	100.83	V02 clast1 site2
Hyaloclastite	14	48.90	1.74	14.88	0.03	11.87	0.21	8.53	11.94	2.37	0.10	0.18	100.74	V02 clast2 site1
Mound	15	48.83	1.77	14.96	0.04	12.29	0.22	8.51	12.12	2.35	0.09	0.15	101.34	V02 clast2 site2
(Arnarpfur)	16	48.79	1.80	15.05	0.04	12.04	0.17	8.63	12.03	2.39	0.10	0.22	101.24	V02 clast3 site1
	17	48.67	1.74	14.99	0.04	11.87	0.17	8.56	12.11	2.36	0.09	0.17	100.77	V02 clast3 site2
	18	48.25	1.70	14.95	0.03	11.74	0.24	8.55	12.14	2.36	0.12	0.11	100.18	V02 clast4 site1
	19	48.12	1.66	14.89	0.01	11.64	0.27	8.44	11.94	2.38	0.10	0.11	99.56	V02 clast4 site2
	20	48.98	1.75	15.00	0.01	11.85	0.19	8.60	12.12	2.43	0.09	0.19	101.23	V02 clast5 site1
	21	49.01	1.73	15.06	0.04	11.51	0.27	8.51	12.03	2.38	0.10	0.18	100.83	V02 clast5 site2
	22	49.14	1.75	14.99	0.06	12.18	0.32	8.54	12.03	2.39	0.13	0.20	101.72	V02 clast6 site1
	23	49.19	1.76	14.91	0.03	11.78	0.22	8.55	11.95	2.35	0.13	0.18	101.04	V02 clast6 site2
	24	48.54	1.80	15.14	0.04	11.47	0.31	8.52	11.88	2.38	0.11	0.13	100.33	V02 clast7 site1
	25	48.54	1.70	15.11	0.04	12.03	0.20	8.56	12.16	2.35	0.10	0.15	100.94	V02 clast8 site1
	26	48.65	1.78	14.92	0.05	11.48	0.21	8.51	11.98	2.38	0.11	0.15	100.22	V02 clast8 site2
	27	48.66	1.74	15.04	0.04	11.26	0.24	8.47	12.01	2.31	0.09	0.16	100.03	V02 clast10 site1
	28	47.28	1.74	14.63	0.03	11.31	0.19	8.33	11.99	2.33	0.10	0.17	98.10	V02 clast10 site2
	29	48.97	1.92	15.00	0.05	11.69	0.21	8.58	12.00	2.42	0.13	0.16	101.13	V02 clast12 site1
	30	48.77	1.76	14.98	0.05	11.67	0.25	8.56	11.99	2.39	0.14	0.21	100.77	V02 clast12 site2
	31	48.34	1.82	15.08	0.07	11.66	0.34	8.52	11.90	2.36	0.12	0.17	100.38	V02 clast14 site1
	32	48.33	1.71	14.96	0.04	11.88	0.14	8.58	12.04	2.37	0.10	0.18	100.33	V02 clast14 site2
	33	48.41	1.69	15.00	0.03	11.41	0.32	8.87	12.12	2.33	0.08	0.20	100.46	V02 clast15 site1
	34	48.61	1.69	14.97	0.04	11.93	0.20	8.86	12.16	2.26	0.09	0.14	100.94	V02 clast15 site2
<b>Average</b>		48.62	1.75	14.98	0.04	11.75	0.24	8.56	12.03	2.37	0.11	0.17	100.60	
<b>Standard Deviation</b>		0.40	0.06	0.10	0.01	0.27	0.05	0.11	0.08	0.04	0.02	0.03	0.73	

Original oxide weight percentages (continued)

Sample	Probe #	SiO2	TiO2	Al2O3	Cr2O3	FeO	MnO	MgO	CaO	Na2O	K2O	P2O5	Total	Comments
V03 (Wpt051) Distal Hyaloclastite Mound (Arnarpfur)	37	49.48	1.73	14.77	0.04	12.02	0.21	8.67	11.99	2.35	0.08	0.16	101.51	V03 clast1 site1
	38	49.48	1.83	14.81	0.04	11.88	0.28	8.63	11.93	2.38	0.06	0.17	101.51	V03 clast1 site2
	39	49.28	1.68	14.87	0.02	11.38	0.21	8.58	11.98	2.38	0.09	0.18	100.67	V03 clast2 site1
	40	49.32	1.71	14.61	0.05	11.91	0.19	8.61	11.98	2.32	0.08	0.13	100.92	V03 clast2 site2
	41	49.20	1.78	14.83	0.03	12.06	0.20	8.63	11.86	2.40	0.09	0.24	101.31	V03 clast4 site1
	42	49.32	1.76	14.94	0.03	11.89	0.26	8.61	12.06	2.38	0.06	0.17	101.47	V03 clast4 site2
	43	49.31	1.73	14.72	0.05	11.39	0.20	8.51	12.11	2.38	0.07	0.21	100.67	V03 clast5 site1
	44	49.22	1.77	14.65	0.04	11.61	0.23	8.69	11.85	2.32	0.11	0.18	100.67	V03 clast6 site1
	45	49.31	1.73	14.63	0.03	11.81	0.19	8.72	12.05	2.38	0.07	0.17	101.07	V03 clast6 site2
	46	48.93	1.72	14.67	0.06	11.64	0.19	8.65	12.07	2.37	0.09	0.14	100.51	V03 clast8 site1
	47	49.21	1.77	15.06	0.04	12.26	0.17	8.69	12.05	2.43	0.10	0.15	101.93	V03 clast8 site2
	48	49.39	1.75	14.84	0.04	11.59	0.27	8.67	11.97	2.35	0.09	0.17	101.12	V03 clast9 site1
	49	48.57	1.76	14.47	0.01	11.47	0.21	8.58	11.96	2.38	0.08	0.18	99.68	V03 clast10 site1
	50	48.75	1.69	14.63	0.02	11.56	0.31	8.54	11.93	2.34	0.09	0.13	99.99	V03 clast10 site2
	51	48.89	1.73	14.80	0.01	11.91	0.25	8.63	12.11	2.41	0.09	0.21	101.04	V03 clast11 site1
	52	49.29	1.73	14.80	0.02	11.81	0.29	8.54	11.94	2.38	0.08	0.23	101.10	V03 clast11 site2
	53	48.65	1.74	14.63	0.04	11.67	0.28	8.53	12.09	2.35	0.10	0.17	100.24	V03 clast12 site1
	54	48.71	1.77	14.51	0.03	11.42	0.24	8.56	12.06	2.34	0.10	0.18	99.93	V03 clast12 site2
55	49.10	1.69	14.80	0.03	11.79	0.19	8.60	11.87	2.34	0.07	0.17	100.66	V03 clast14 site1	
56	49.02	1.84	14.76	0.05	11.74	0.17	8.61	12.03	2.33	0.10	0.20	100.84	V03 clast14 site2	
57	49.25	1.74	14.92	0.05	11.48	0.19	8.59	12.07	2.42	0.12	0.21	101.03	V03 clast15 site1	
58	48.95	1.68	14.82	0.04	11.64	0.26	8.58	11.92	2.32	0.13	0.22	100.56	V03 clast15 site2	

<b>Average</b>		49.12	1.74	14.75	0.04	11.72	0.23	8.61	11.99	2.37	0.09	0.18	100.84	
<b>Standard Deviation</b>		0.27	0.04	0.14	0.01	0.23	0.04	0.06	0.08	0.03	0.02	0.03	0.56	

Sample	Probe #	SiO2	TiO2	Al2O3	Cr2O3	FeO	MnO	MgO	CaO	Na2O	K2O	P2O5	Total	Comments
V06 (Wpt059) Distal Hyaloclastite Mound Upper-Section (Arnarpfur)	59	47.95	1.85	14.85	0.03	12.39	0.15	8.56	11.87	2.39	0.11	0.17	100.32	V06 clast1 site1
	60	47.76	1.71	14.71	0.05	11.91	0.11	8.46	11.94	2.35	0.11	0.16	99.26	V06 clast1 site2
	61	48.97	1.78	15.23	0.04	11.92	0.22	8.36	12.10	2.36	0.12	0.18	101.27	V06 clast2 site1
	62	47.92	1.77	14.91	0.05	12.04	0.13	8.31	11.86	2.39	0.11	0.16	99.64	V06 clast2 site2
	63	48.74	1.70	15.02	0.04	11.39	0.22	8.97	12.07	2.29	0.08	0.20	100.74	V06 clast3 site1
	64	48.75	1.73	14.96	0.05	12.11	0.25	9.09	11.97	2.28	0.10	0.16	101.45	V06 clast3 site2
	65	49.05	1.72	14.78	0.05	11.62	0.18	8.55	11.84	2.41	0.13	0.20	100.52	V06 clast9 site1
	66	48.77	1.73	14.97	0.06	11.78	0.14	8.55	11.94	2.39	0.12	0.21	100.67	V06 clast9 site2
	67	48.94	1.67	14.91	0.08	12.06	0.19	8.92	11.88	2.26	0.05	0.18	101.15	V06 clast10 site1
	68	48.98	1.75	14.88	0.03	12.13	0.20	8.96	11.92	2.26	0.06	0.11	101.28	V06 clast10 site2

<b>Average</b>		48.58	1.74	14.92	0.05	11.94	0.18	8.67	11.94	2.34	0.10	0.17	100.63	
<b>Standard Deviation</b>		0.35	0.05	0.08	0.01	0.31	0.07	0.20	0.08	0.06	0.02	0.02	0.50	

**Original oxide weight percentages (continued)**

Sample	Probe #	SiO2	TiO2	Al2O3	Cr2O3	FeO	MnO	MgO	CaO	Na2O	K2O	P2O5	Total	Comments
V07 (Wpt059)	71	49.28	1.72	14.94	0.03	11.37	0.19	8.63	11.99	2.39	0.13	0.18	100.85	V07 clast1 site1
Distal	72	49.56	1.69	15.05	0.05	11.67	0.13	8.66	12.12	2.45	0.12	0.15	101.65	V07 clast1 site2
Hyaloclastite	73	49.71	1.80	15.13	0.03	11.24	0.18	8.55	12.05	2.31	0.09	0.19	101.27	V07 clast2 site1
Mound	74	49.94	1.66	15.04	0.03	12.13	0.15	8.61	12.00	2.41	0.10	0.15	102.25	V07 clast2 site2
Lower-Section (Arnarpfur)	75	49.49	1.66	15.11	0.02	11.69	0.19	8.92	11.96	2.31	0.07	0.21	101.64	V07 clast3 site1
	76	49.34	1.74	14.89	0.01	11.62	0.28	9.05	11.88	2.32	0.11	0.19	101.44	V07 clast3 site2
	77	49.20	1.74	15.02	0.04	11.25	0.12	9.08	11.92	2.30	0.10	0.15	100.92	V07 clast4 site1
	78	49.25	1.64	14.99	0.04	11.37	0.17	9.02	11.98	2.26	0.12	0.17	101.01	V07 clast4 site2
	79	48.85	1.70	14.90	0.04	11.63	0.20	8.75	11.90	2.32	0.11	0.16	100.56	V07 clast5 site1
	80	48.84	1.77	14.97	0.04	12.03	0.02	8.64	12.08	2.31	0.07	0.17	100.94	V07 clast5 site2

<b>Average</b>		49.35	1.71	15.00	0.03	11.60	0.16	8.79	11.99	2.34	0.10	0.17	101.25	
<b>Standard Deviation</b>		0.37	0.05	0.08	0.01	0.31	0.07	0.21	0.08	0.06	0.02	0.02	0.51	

Sample	Probe #	SiO2	TiO2	Al2O3	Cr2O3	FeO	MnO	MgO	CaO	Na2O	K2O	P2O5	Total	Comments
V08 (Wpt060)	81	48.54	1.73	15.12	0.05	11.94	0.05	8.68	12.12	2.26	0.09	0.15	100.73	V08 clast1 site1
Distal	82	48.79	1.73	15.06	0.05	11.58	0.09	8.71	12.06	2.26	0.07	0.13	100.52	V08 clast1 site2
Hyaloclastite	83	49.75	1.64	15.11	0.05	11.61	0.06	8.68	11.92	2.28	0.08	0.19	101.37	V08 clast2 site1
Mound	84	49.27	1.67	15.06	0.06	11.20	0.00	8.65	11.97	2.34	0.07	0.11	100.39	V08 clast2 site2
Upper-Section (Arnarpfur)	85	49.20	1.78	15.08	0.06	11.50	0.00	8.52	11.99	2.31	0.07	0.16	100.67	V08 clast3 site1
	86	49.77	1.78	14.98	0.05	11.30	0.05	8.55	11.92	2.33	0.08	0.16	100.97	V08 clast3 site2
	87	49.41	1.64	15.04	0.05	11.43	0.05	8.55	11.93	2.34	0.06	0.14	100.64	V08 clast4 site1
	88	49.12	1.72	15.15	0.05	11.20	0.09	8.55	11.92	2.27	0.04	0.13	100.24	V08 clast4 site2
	89	47.99	1.67	15.02	0.06	12.08	0.10	8.64	12.06	2.32	0.07	0.15	100.15	V08 clast5 site1
	90	49.49	1.70	15.13	0.03	11.82	0.15	8.49	12.01	2.39	0.09	0.16	101.47	V08 clast5 site2

<b>Average</b>		49.13	1.71	15.08	0.05	11.57	0.06	8.60	11.99	2.31	0.07	0.15	100.72	
<b>Standard Deviation</b>		0.56	0.05	0.05	0.01	0.30	0.05	0.08	0.07	0.04	0.02	0.02	0.44	

**Original oxide weight percentages (continued)**

Sample	Probe #	SiO2	TiO2	Al2O3	Cr2O3	FeO	MnO	MgO	CaO	Na2O	K2O	P2O5	Total	Comments
Wpt070	230	49.31	1.80	14.87	0.04	11.51	0.22	8.20	11.63	2.45	0.07	0.17	100.27	Wpt070 clast1 site1
Median	231	49.01	1.79	14.80	0.04	11.39	0.31	8.18	11.59	2.51	0.11	0.18	99.90	Wpt070 clast1 site2
Hyaloclastite	232	49.09	1.78	15.06	0.04	11.51	0.25	8.21	11.48	2.49	0.07	0.16	100.12	Wpt070 clast2 site1
Mound from	233	48.90	1.83	15.03	0.04	11.42	0.29	8.14	11.62	2.54	0.08	0.17	100.05	Wpt070 clast2 site2
Central	234	49.14	1.70	14.91	0.07	11.97	0.19	8.31	11.87	2.49	0.12	0.15	100.92	Wpt070 clast2 site3
Hyaloclastite	235	49.29	1.84	14.96	0.04	11.87	0.17	8.21	11.84	2.47	0.11	0.18	100.98	Wpt070 clast2 site4
Mound	236	49.13	1.81	14.86	0.02	11.47	0.27	8.27	11.91	2.46	0.10	0.16	100.46	Wpt070 clast3 site1
(Arnarpfur)	237	49.31	1.78	14.90	0.06	11.73	0.17	8.22	11.95	2.43	0.10	0.16	100.81	Wpt070 clast3 site2
	238	49.11	1.76	14.94	0.05	11.70	0.23	8.18	11.85	2.43	0.10	0.15	100.50	Wpt070 clast4 site1
	239	49.06	1.80	14.76	0.06	11.95	0.11	8.19	11.80	2.46	0.10	0.13	100.42	Wpt070 clast4 site2
	240	49.02	1.81	14.87	0.01	11.39	0.18	8.19	11.87	2.43	0.09	0.13	100.00	Wpt070 clast5 site1
	241	48.85	1.83	14.93	0.06	11.98	0.16	8.25	12.01	2.45	0.11	0.17	100.80	Wpt070 clast5 site2
	242	49.17	1.78	14.77	0.05	11.74	0.11	8.12	11.79	2.50	0.09	0.19	100.31	Wpt070 clast6 site1
	243	49.24	1.77	14.92	0.04	11.73	0.11	8.05	11.94	2.51	0.10	0.19	100.58	Wpt070 clast6 site2
<b>Average</b>		49.12	1.79	14.90	0.04	11.67	0.20	8.19	11.80	2.47	0.10	0.17	100.44	
<b>Standard Deviation</b>		0.14	0.04	0.09	0.02	0.22	0.07	0.06	0.16	0.03	0.02	0.02	0.35	

**Control Sample**

Sample	Probe #	SiO2	TiO2	Al2O3	Cr2O3	FeO	MnO	MgO	CaO	Na2O	K2O	P2O5	Total	Comments
BCR-1	3	56.17	2.51	13.43	0.00	11.14	0.13	3.97	7.51	2.73	1.43	0.28	99.29	BCR-1 control1
Control	35	53.33	2.32	13.52	0.02	11.71	0.20	3.82	7.42	3.03	1.57	0.33	97.30	BCR-1 control2
Sample	36	55.42	2.34	13.24	0.02	11.24	0.16	3.77	7.36	3.18	1.73	0.43	98.89	BCR-1 control3
	70	56.13	2.29	13.84	0.00	11.78	0.18	3.94	7.67	2.73	1.44	0.34	100.33	BCR-1 control4
	91	56.39	2.25	13.56	0.00	12.15	0.12	3.59	7.19	3.26	1.72	0.26	100.50	BCR-1 control5
	97	55.65	2.32	13.14	0.00	12.36	0.23	3.60	7.21	3.27	1.61	0.25	99.63	BCR-1 control6
	138	55.30	2.31	13.43	0.00	12.11	0.10	3.73	7.24	3.36	1.56	0.30	99.43	BCR-1 control7
	139	54.60	2.20	13.16	0.00	12.74	0.24	3.71	7.37	3.51	1.60	0.30	99.43	BCR-1 control8
	164	55.46	2.32	13.16	0.00	11.45	0.20	3.61	7.26	3.09	1.58	0.24	98.37	BCR-1 control9
	165	56.46	2.32	13.17	0.00	10.98	0.13	3.66	7.21	2.93	1.55	0.30	98.71	BCR-1 control10
	228	55.65	2.31	13.78	0.00	11.61	0.29	3.71	7.40	2.85	1.39	0.41	99.40	BCR-1 control11
	229	55.91	2.24	13.39	0.00	12.37	0.23	3.54	6.93	2.65	1.64	0.34	99.24	BCR-1 control12
	364	55.46	2.37	13.41	0.00	10.86	0.22	3.39	7.05	2.80	1.35	0.28	97.20	BCR-1 control13
	365	56.47	2.08	13.22	0.00	11.17	0.11	3.19	6.70	3.31	1.74	0.36	98.36	BCR-1 control14
<b>Average</b>		55.60	2.30	13.39	0.00	11.69	0.18	3.66	7.25	3.05	1.57	0.32	99.00	
<b>Standard Deviation</b>		0.84	0.10	0.23	0.01	0.58	0.06	0.20	0.24	0.27	0.12	0.06	0.97	

## C.2 Geochemical analysis of glass samples from the Vífilfell Region, Southwest Iceland

### Electron Microprobe Data: Oxide weight percentages normalized to 100%

#### Northern Bláfjöll

Sample	Probe #	Norm. SiO <sub>2</sub>	Norm. TiO <sub>2</sub>	Norm. Al <sub>2</sub> O <sub>3</sub>	Norm. Cr <sub>2</sub> O <sub>3</sub>	Norm. FeO	Norm. MnO	Norm. MgO	Norm. CaO	Norm. Na <sub>2</sub> O	Norm. K <sub>2</sub> O	Norm. P <sub>2</sub> O <sub>5</sub>	Norm. Total	Comments
Wpt094	98	48.76	1.77	14.67	0.01	11.75	0.13	8.58	11.74	2.38	0.04	0.18	100.00	Wpt094 clast 1 site1
Hyaloclastite	99	49.01	1.78	14.69	0.03	11.57	0.25	8.47	11.58	2.41	0.03	0.18	100.00	Wpt094 clast 1 site2
Sample from	100	49.20	1.75	14.75	0.02	11.49	0.15	8.50	11.54	2.42	0.04	0.16	100.00	Wpt094 clast 1 site3
Northern	101	49.20	1.73	14.71	0.01	11.57	0.13	8.52	11.60	2.39	0.03	0.12	100.00	Wpt094 clast 1 site4
Bláfjöll	102	48.73	1.72	14.80	0.03	11.88	0.24	8.49	11.59	2.38	0.05	0.11	100.00	Wpt094 clast 1 site5
Underlying	103	48.78	1.71	14.87	0.02	11.51	0.15	8.63	11.78	2.36	0.03	0.16	100.00	Wpt094 clast 2 site1
Vífilfell	104	49.18	1.82	14.83	0.02	11.26	0.18	8.51	11.62	2.40	0.04	0.14	100.00	Wpt094 clast 2 site2
	105	48.68	1.71	14.74	0.03	11.81	0.10	8.53	11.79	2.41	0.05	0.15	100.00	Wpt094 clast 2 site3
	106	48.88	1.70	14.92	0.02	11.89	0.20	8.31	11.50	2.42	0.03	0.14	100.00	Wpt094 clast 3 site1
	107	48.71	1.89	14.83	0.02	11.78	0.13	8.35	11.62	2.45	0.05	0.17	100.00	Wpt094 clast 3 site2
	108	48.73	1.77	14.80	0.04	11.62	0.23	8.27	11.85	2.42	0.06	0.21	100.00	Wpt094 clast 5 site1
	109	49.16	1.82	14.81	0.07	11.22	0.11	8.43	11.79	2.38	0.04	0.17	100.00	Wpt094 clast 5 site2
	110	48.53	1.68	14.80	0.05	11.59	0.36	8.57	11.85	2.40	0.07	0.12	100.00	Wpt094 clast 6 site1
	111	48.45	1.71	14.87	0.08	11.58	0.24	8.54	11.93	2.39	0.06	0.15	100.00	Wpt094 clast 6 site2
	112	49.06	1.76	14.77	0.07	11.22	0.27	8.63	11.69	2.36	0.05	0.12	100.00	Wpt094 clast 6 site3
	113	48.68	1.73	14.87	0.08	11.83	0.21	8.20	11.79	2.40	0.05	0.16	100.00	Wpt094 clast 7 site1
	114	48.94	1.80	14.86	0.08	11.58	0.17	8.30	11.66	2.41	0.05	0.15	100.00	Wpt094 clast 7 site2

<b>Average</b>		48.86	1.76	14.80	0.04	11.60	0.19	8.46	11.70	2.40	0.04	0.15	100.00	
<b>Standard Deviation</b>		0.24	0.06	0.07	0.03	0.21	0.07	0.13	0.12	0.02	0.01	0.03	0.00	

**Normalized oxide weight percentages (continued)**

**Vífilsfell**

Sample	Probe #	Norm. SiO2	Norm. TiO2	Norm. Al2O3	Norm. Cr2O3	Norm. FeO	Norm. MnO	Norm. MgO	Norm. CaO	Norm. Na2O	Norm. K2O	Norm. P2O5	Norm. Total	Comments
Wpt091	115	49.13	1.79	14.82	0.05	11.50	0.19	8.19	11.74	2.43	0.04	0.13	100.00	Wpt091 clast 1 site1
Sample from	116	48.88	1.74	14.75	0.10	11.65	0.26	8.16	11.81	2.45	0.06	0.15	100.00	Wpt091 clast 1 site2
Vífilsfell	117	49.02	1.73	15.02	0.08	11.44	0.15	8.22	11.74	2.37	0.07	0.17	100.00	Wpt091 clast 2 site1
	118	48.90	1.76	14.73	0.05	11.80	0.16	8.18	11.81	2.45	0.04	0.12	100.00	Wpt091 clast 2 site2
	119	48.98	1.82	14.80	0.04	11.51	0.10	8.16	11.95	2.42	0.09	0.12	100.00	Wpt091 clast 3 site1
	120	49.00	1.80	14.93	0.02	11.58	0.15	8.23	11.67	2.40	0.08	0.14	100.00	Wpt091 clast 3 site2
	121	48.98	1.80	14.71	0.05	11.58	0.23	8.16	11.88	2.47	0.05	0.11	100.00	Wpt091 clast 4 site1
	122	49.11	1.76	14.69	0.03	11.45	0.11	8.30	11.82	2.54	0.05	0.13	100.00	Wpt091 clast 5 site1
	123	49.10	1.83	14.68	0.04	11.36	0.15	8.31	11.87	2.47	0.07	0.14	100.00	Wpt091 clast 5 site2
	124	49.13	1.78	14.66	0.03	11.45	0.15	8.21	11.85	2.51	0.06	0.18	100.00	Wpt091 clast 6 site1
	125	48.97	1.73	14.72	0.05	11.45	0.25	8.18	11.93	2.52	0.07	0.14	100.00	Wpt091 clast 6 site2
	126	48.83	1.70	14.77	0.03	11.85	0.09	8.18	11.81	2.52	0.05	0.16	100.00	Wpt091 clast 7 site1
	127	49.15	1.72	14.90	0.03	11.18	0.15	8.21	11.96	2.48	0.06	0.17	100.00	Wpt091 clast 7 site2
	128	48.76	1.75	14.98	0.02	11.67	0.09	8.27	11.75	2.48	0.07	0.15	100.00	Wpt091 clast 8 site1
	129	48.74	1.81	14.92	0.02	11.80	0.03	8.17	11.79	2.44	0.10	0.18	100.00	Wpt091 clast 8 site2
	130	48.88	1.79	14.88	0.02	11.44	0.15	8.28	11.82	2.47	0.09	0.18	100.00	Wpt091 clast 10 site1
	131	48.67	1.86	14.97	0.04	11.55	0.12	8.26	11.77	2.48	0.10	0.18	100.00	Wpt091 clast 10 site2
	132	48.57	1.85	14.97	0.03	11.54	0.27	8.26	11.81	2.47	0.07	0.16	100.00	Wpt091 clast 11 site1
	133	48.53	1.78	14.94	0.04	11.64	0.25	8.25	11.86	2.46	0.09	0.15	100.00	Wpt091 clast 11 site2
	134	48.82	1.85	14.75	0.01	11.71	0.22	8.28	11.69	2.46	0.08	0.14	100.00	Wpt091 clast 12 site1
	135	48.90	1.68	14.89	0.04	11.58	0.21	8.25	11.80	2.45	0.06	0.13	100.00	Wpt091 clast 12 site2
	136	48.76	1.76	15.13	0.05	11.14	0.14	8.50	11.85	2.48	0.08	0.12	100.00	Wpt091 clast 13 site1
	137	48.92	1.73	14.84	0.04	11.45	0.05	8.47	11.87	2.40	0.07	0.15	100.00	Wpt091 clast 13 site2

<b>Average</b>	48.90	1.77	14.84	0.04	11.54	0.16	8.25	11.82	2.46	0.07	0.15	100.00
<b>Standard Deviation</b>	0.17	0.05	0.13	0.02	0.18	0.07	0.09	0.08	0.04	0.02	0.02	0.00

Sample	Probe #	Norm. SiO2	Norm. TiO2	Norm. Al2O3	Norm. Cr2O3	Norm. FeO	Norm. MnO	Norm. MgO	Norm. CaO	Norm. Na2O	Norm. K2O	Norm. P2O5	Norm. Total	Comments
Wpt092	166	48.46	1.86	14.27	0.02	11.96	0.12	8.40	12.10	2.52	0.12	0.17	100.00	Wpt092 clast1 site1
Contact	167	48.79	1.90	14.36	0.02	11.55	0.26	8.40	11.90	2.52	0.13	0.17	100.00	Wpt092 clast1 site2
Between	169	49.00	1.85	14.30	0.01	11.57	0.16	8.32	12.06	2.47	0.13	0.13	100.00	Wpt092 clast2 site1
Northern	170	48.79	1.85	14.32	0.03	11.71	0.20	8.32	12.04	2.49	0.10	0.15	100.00	Wpt092 clast2 site2
Bláfjöll	171	49.26	1.94	14.52	0.02	10.87	0.27	8.36	11.97	2.52	0.12	0.14	100.00	Wpt092 clast3 site1
Vífilsfell	172	49.02	1.88	14.31	0.04	11.53	0.20	8.31	11.95	2.48	0.11	0.16	100.00	Wpt092 clast3 site2
(Sample clasts	174	49.03	1.91	14.85	0.01	11.28	0.12	8.13	11.87	2.49	0.12	0.19	100.00	Wpt092 clast4 site1
from Vífilsfell)	175	49.19	1.91	15.09	0.03	10.80	0.17	8.17	11.87	2.55	0.10	0.13	100.00	Wpt092 clast4 site2

<b>Average</b>	48.94	1.89	14.50	0.02	11.41	0.19	8.30	11.97	2.50	0.12	0.16	100.00
<b>Standard Deviation</b>	0.18	0.03	0.31	0.01	0.36	0.05	0.10	0.08	0.03	0.01	0.02	0.00

**Normalized oxide weight percentages (continued)**

Sample	Probe #	Norm. SiO2	Norm. TiO2	Norm. Al2O3	Norm. Cr2O3	Norm. FeO	Norm. MnO	Norm. MgO	Norm. CaO	Norm. Na2O	Norm. K2O	Norm. P2O5	Norm. Total	Comments
Wpt107	200	48.65	1.82	14.80	0.04	11.72	0.28	8.19	11.83	2.42	0.08	0.18	100.00	Wpt107 clast1 site1
Sample from	201	49.05	1.80	14.86	0.05	11.68	0.10	8.16	11.69	2.39	0.05	0.17	100.00	Wpt107 clast1 site2
Vifilsfell	202	49.16	1.70	14.75	0.03	11.12	0.25	8.48	11.95	2.38	0.06	0.12	100.00	Wpt107 clast2 site1
	203	48.62	1.69	14.94	0.03	11.80	0.14	8.48	11.75	2.35	0.05	0.15	100.00	Wpt107 clast2 site2
	204	48.83	1.83	14.84	0.03	11.29	0.26	8.30	11.98	2.41	0.12	0.12	100.00	Wpt107 clast3 site1
	205	48.75	1.80	14.84	0.03	11.65	0.19	8.20	11.81	2.49	0.11	0.13	100.00	Wpt107 clast3 site2
	206	48.43	1.74	14.71	0.01	11.93	0.35	8.39	11.84	2.39	0.09	0.12	100.00	Wpt107 clast4 site1
	207	48.58	1.74	14.85	0.03	11.72	0.20	8.36	11.90	2.41	0.08	0.15	100.00	Wpt107 clast4 site2
	208	48.88	1.69	14.83	0.02	11.48	0.28	8.13	12.01	2.44	0.08	0.13	100.00	Wpt107 clast5 site1
	209	48.81	1.78	14.81	0.05	11.70	0.19	8.02	11.95	2.48	0.10	0.10	100.00	Wpt107 clast5 site2
	210	48.98	1.77	14.77	0.00	11.62	0.21	8.15	11.81	2.48	0.11	0.10	100.00	Wpt107 clast5 site3
	211	49.02	1.78	14.87	0.03	11.48	0.13	8.12	11.88	2.47	0.10	0.12	100.00	Wpt107 clast5 site4
	212	48.77	1.73	14.71	0.03	12.05	0.11	8.11	11.81	2.46	0.10	0.12	100.00	Wpt107 clast6 site1
	213	49.14	1.82	14.90	0.02	11.46	0.23	8.08	11.72	2.41	0.11	0.10	100.00	Wpt107 clast6 site2
	214	48.79	1.74	15.02	0.03	11.65	0.13	8.09	11.96	2.43	0.09	0.09	100.00	Wpt107 clast7 site1
	215	48.88	1.69	14.95	0.05	11.54	0.15	8.11	11.94	2.46	0.07	0.13	100.00	Wpt107 clast7 site2
	216	48.66	1.73	14.85	0.05	11.83	0.10	8.46	11.76	2.34	0.07	0.15	100.00	Wpt107 clast8 site1
	217	48.93	1.75	14.67	0.05	11.58	0.14	8.41	11.84	2.45	0.07	0.12	100.00	Wpt107 clast8 site2
	218	48.87	1.73	14.92	0.04	11.48	0.09	8.26	11.89	2.48	0.08	0.17	100.00	Wpt107 clast9 site1
	219	48.83	1.80	14.78	0.02	11.66	0.11	8.14	12.01	2.44	0.08	0.14	100.00	Wpt107 clast9 site2
	220	48.80	1.83	14.85	0.04	11.78	0.12	8.16	11.71	2.51	0.10	0.11	100.00	Wpt107 clast10 site1
	221	48.87	1.78	14.70	0.01	11.85	0.16	8.19	11.71	2.47	0.10	0.16	100.00	Wpt107 clast10 site2
	222	49.11	1.78	14.79	0.04	11.46	0.16	8.09	11.84	2.45	0.10	0.17	100.00	Wpt107 clast11 site1
	223	48.81	1.76	14.79	0.03	11.63	0.17	8.25	11.86	2.44	0.10	0.15	100.00	Wpt107 clast11 site2
	224	48.90	1.82	14.89	0.02	11.46	0.22	8.25	11.69	2.48	0.09	0.16	100.00	Wpt107 clast11 site3
	225	48.86	1.78	14.91	0.02	11.57	0.20	8.29	11.68	2.45	0.09	0.15	100.00	Wpt107 clast11 site4
	226	49.07	1.79	14.88	0.03	11.33	0.32	8.18	11.65	2.48	0.09	0.19	100.00	Wpt107 clast12 site1
	227	49.01	1.84	14.85	0.03	11.40	0.25	8.21	11.67	2.48	0.10	0.17	100.00	Wpt107 clast12 site2
<b>Average</b>		48.86	1.77	14.83	0.03	11.60	0.19	8.22	11.83	2.44	0.09	0.14	100.00	
<b>Standard Deviation</b>		0.17	0.04	0.08	0.01	0.20	0.07	0.13	0.11	0.04	0.02	0.03	0.00	



Normalized oxide weight percentages (continued)

Arnarpfur

Sample	Probe #	Norm. SiO2	Norm. TiO2	Norm. Al2O3	Norm. Cr2O3	Norm. FeO	Norm. MnO	Norm. MgO	Norm. CaO	Norm. Na2O	Norm. K2O	Norm. P2O5	Norm. Total	Comments
V02 (Wpt043)	12	48.41	1.73	14.89	0.04	11.74	0.21	8.52	11.85	2.41	0.08	0.13	100.00	V02 clast1 site1
Proximal	13	48.25	1.66	14.89	0.03	11.84	0.30	8.46	11.95	2.37	0.11	0.15	100.00	V02 clast1 site2
Hyaloclastite	14	48.54	1.73	14.77	0.03	11.79	0.21	8.47	11.86	2.35	0.10	0.18	100.00	V02 clast2 site1
Mound	15	48.18	1.75	14.76	0.04	12.13	0.22	8.40	11.96	2.32	0.09	0.15	100.00	V02 clast2 site2
(Arnarpfur)	16	48.19	1.78	14.86	0.04	11.89	0.16	8.52	11.88	2.36	0.10	0.21	100.00	V02 clast3 site1
	17	48.30	1.73	14.87	0.04	11.78	0.16	8.50	12.02	2.34	0.09	0.17	100.00	V02 clast3 site2
	18	48.16	1.70	14.92	0.03	11.72	0.24	8.53	12.12	2.35	0.12	0.11	100.00	V02 clast4 site1
	19	48.33	1.67	14.96	0.01	11.69	0.27	8.47	11.99	2.39	0.10	0.11	100.00	V02 clast4 site2
	20	48.39	1.73	14.82	0.01	11.70	0.19	8.50	11.97	2.40	0.09	0.19	100.00	V02 clast5 site1
	21	48.60	1.72	14.94	0.04	11.41	0.27	8.44	11.93	2.36	0.10	0.18	100.00	V02 clast5 site2
	22	48.31	1.72	14.74	0.05	11.97	0.31	8.40	11.82	2.35	0.13	0.20	100.00	V02 clast6 site1
	23	48.69	1.74	14.76	0.03	11.66	0.22	8.46	11.83	2.32	0.13	0.17	100.00	V02 clast6 site2
	24	48.39	1.79	15.09	0.04	11.43	0.30	8.50	11.84	2.38	0.11	0.13	100.00	V02 clast7 site1
	25	48.09	1.68	14.97	0.04	11.92	0.20	8.48	12.05	2.33	0.10	0.15	100.00	V02 clast8 site1
	26	48.54	1.77	14.89	0.05	11.46	0.21	8.49	11.95	2.38	0.11	0.15	100.00	V02 clast8 site2
	27	48.64	1.74	15.04	0.04	11.25	0.24	8.47	12.00	2.31	0.09	0.16	100.00	V02 clast10 site1
	28	48.19	1.77	14.91	0.04	11.52	0.20	8.49	12.22	2.37	0.11	0.17	100.00	V02 clast10 site2
	29	48.42	1.90	14.84	0.05	11.56	0.21	8.49	11.87	2.39	0.13	0.16	100.00	V02 clast12 site1
	30	48.40	1.74	14.87	0.05	11.58	0.24	8.49	11.90	2.37	0.14	0.21	100.00	V02 clast12 site2
	31	48.16	1.82	15.03	0.07	11.61	0.34	8.48	11.85	2.35	0.12	0.17	100.00	V02 clast14 site1
	32	48.17	1.71	14.91	0.04	11.84	0.14	8.55	12.00	2.37	0.10	0.18	100.00	V02 clast14 site2
	33	48.19	1.68	14.94	0.03	11.36	0.31	8.83	12.06	2.32	0.08	0.20	100.00	V02 clast15 site1
	34	48.15	1.67	14.83	0.04	11.82	0.20	8.78	12.04	2.24	0.09	0.14	100.00	V02 clast15 site2
<b>Average</b>		48.33	1.74	14.89	0.04	11.68	0.23	8.51	11.96	2.35	0.10	0.16	100.00	
<b>Standard Deviation</b>		0.18	0.05	0.09	0.01	0.21	0.05	0.10	0.10	0.04	0.02	0.03	0.00	

**Normalized oxide weight percentages (continued)**

Sample	Probe #	Norm. SiO2	Norm. TiO2	Norm. Al2O3	Norm. Cr2O3	Norm. FeO	Norm. MnO	Norm. MgO	Norm. CaO	Norm. Na2O	Norm. K2O	Norm. P2O5	Norm. Total	Comments
V03 (Wpt051)	37	48.75	1.70	14.56	0.04	11.85	0.21	8.54	11.81	2.32	0.08	0.16	100.00	V03 clast1 site1
Distal	38	48.75	1.80	14.59	0.04	11.71	0.28	8.51	11.76	2.34	0.06	0.17	100.00	V03 clast1 site2
Hyaloclastite	39	48.96	1.67	14.77	0.02	11.30	0.21	8.52	11.90	2.37	0.09	0.18	100.00	V03 clast2 site1
Mound	40	48.87	1.69	14.48	0.05	11.80	0.19	8.54	11.87	2.30	0.08	0.13	100.00	V03 clast2 site2
(Amarpfur)	41	48.56	1.76	14.63	0.03	11.90	0.20	8.52	11.70	2.37	0.09	0.24	100.00	V03 clast4 site1
	42	48.61	1.73	14.72	0.03	11.72	0.26	8.48	11.89	2.34	0.06	0.17	100.00	V03 clast4 site2
	43	48.98	1.72	14.62	0.05	11.31	0.20	8.45	12.03	2.36	0.06	0.21	100.00	V03 clast5 site1
	44	48.89	1.76	14.55	0.04	11.54	0.23	8.63	11.77	2.31	0.11	0.18	100.00	V03 clast6 site1
	45	48.78	1.71	14.47	0.03	11.68	0.19	8.63	11.92	2.35	0.07	0.17	100.00	V03 clast6 site2
	46	48.68	1.72	14.59	0.06	11.58	0.19	8.61	12.01	2.36	0.09	0.14	100.00	V03 clast8 site1
	47	48.27	1.74	14.77	0.04	12.03	0.17	8.53	11.82	2.39	0.10	0.14	100.00	V03 clast8 site2
	48	48.84	1.73	14.67	0.04	11.46	0.26	8.57	11.84	2.33	0.09	0.17	100.00	V03 clast9 site1
	49	48.73	1.77	14.52	0.01	11.50	0.21	8.61	12.00	2.39	0.08	0.18	100.00	V03 clast10 site1
	50	48.75	1.69	14.63	0.02	11.56	0.31	8.54	11.93	2.34	0.09	0.13	100.00	V03 clast10 site2
	51	48.39	1.71	14.64	0.01	11.79	0.25	8.54	11.98	2.39	0.09	0.21	100.00	V03 clast11 site1
	52	48.75	1.71	14.64	0.02	11.68	0.28	8.44	11.81	2.35	0.08	0.23	100.00	V03 clast11 site2
	53	48.53	1.73	14.59	0.04	11.64	0.28	8.51	12.06	2.34	0.10	0.17	100.00	V03 clast12 site1
	54	48.75	1.77	14.52	0.03	11.42	0.24	8.57	12.07	2.34	0.10	0.18	100.00	V03 clast12 site2
	55	48.78	1.68	14.70	0.03	11.72	0.18	8.55	11.79	2.33	0.06	0.16	100.00	V03 clast14 site1
	56	48.61	1.83	14.64	0.05	11.64	0.17	8.53	11.93	2.31	0.10	0.20	100.00	V03 clast14 site2
	57	48.74	1.73	14.76	0.05	11.36	0.18	8.50	11.95	2.39	0.12	0.21	100.00	V03 clast15 site1
	58	48.68	1.67	14.73	0.04	11.57	0.26	8.54	11.85	2.31	0.13	0.22	100.00	V03 clast15 site2

Average		48.71	1.73	14.63	0.03	11.63	0.23	8.54	11.90	2.35	0.09	0.18	100.00	
Standard Deviation		0.17	0.04	0.09	0.01	0.19	0.04	0.05	0.10	0.03	0.02	0.03	0.00	

Sample	Probe #	Norm. SiO2	Norm. TiO2	Norm. Al2O3	Norm. Cr2O3	Norm. FeO	Norm. MnO	Norm. MgO	Norm. CaO	Norm. Na2O	Norm. K2O	Norm. P2O5	Norm. Total	Comments
V06 (Wpt059)	59	47.80	1.84	14.80	0.03	12.35	0.15	8.53	11.83	2.38	0.11	0.17	100.00	V06 clast1 site1
Distal	60	48.11	1.72	14.82	0.05	12.00	0.11	8.52	12.03	2.36	0.11	0.16	100.00	V06 clast1 site2
Hyaloclastite	61	48.36	1.76	15.04	0.04	11.77	0.22	8.25	11.95	2.33	0.12	0.18	100.00	V06 clast2 site1
Mound	62	48.09	1.77	14.96	0.05	12.09	0.13	8.34	11.90	2.39	0.11	0.16	100.00	V06 clast2 site2
Upper-Section	63	48.39	1.69	14.91	0.04	11.31	0.22	8.90	11.98	2.27	0.08	0.20	100.00	V06 clast3 site1
(Amarpfur)	64	48.05	1.71	14.75	0.05	11.93	0.25	8.96	11.80	2.25	0.09	0.16	100.00	V06 clast3 site2
	65	48.80	1.71	14.70	0.05	11.56	0.17	8.51	11.78	2.40	0.13	0.20	100.00	V06 clast9 site1
	66	48.45	1.72	14.87	0.06	11.70	0.14	8.49	11.87	2.37	0.12	0.21	100.00	V06 clast9 site2
	67	48.38	1.66	14.74	0.08	11.92	0.19	8.82	11.75	2.24	0.05	0.18	100.00	V06 clast10 site1
	68	48.36	1.73	14.69	0.03	11.98	0.20	8.85	11.76	2.23	0.06	0.11	100.00	V06 clast10 site2

Average		48.28	1.73	14.83	0.05	11.86	0.18	8.62	11.86	2.32	0.10	0.17	100.00	
Standard Deviation		0.19	0.05	0.08	0.01	0.28	0.07	0.21	0.08	0.05	0.02	0.02	0.00	

**Normalized oxide weight percentages (continued)**

Sample	Probe #	Norm. SiO2	Norm. TiO2	Norm. Al2O3	Norm. Cr2O3	Norm. FeO	Norm. MnO	Norm. MgO	Norm. CaO	Norm. Na2O	Norm. K2O	Norm. P2O5	Norm. Total	Comments
V07 (Wpt059)	71	48.86	1.71	14.81	0.03	11.28	0.19	8.56	11.89	2.37	0.13	0.18	100.00	V07 clast1 site1
Distal	72	48.76	1.66	14.81	0.05	11.48	0.13	8.52	11.92	2.41	0.12	0.15	100.00	V07 clast1 site2
Hyaloclastite	73	49.09	1.78	14.94	0.03	11.10	0.18	8.45	11.89	2.28	0.09	0.19	100.00	V07 clast2 site1
Mound	74	48.84	1.62	14.71	0.03	11.87	0.15	8.42	11.74	2.36	0.10	0.15	100.00	V07 clast2 site2
Lower-Section (Arnarpfur)	75	48.70	1.63	14.87	0.02	11.50	0.19	8.78	11.77	2.27	0.07	0.21	100.00	V07 clast3 site1
	76	48.64	1.72	14.68	0.01	11.46	0.27	8.93	11.72	2.29	0.10	0.19	100.00	V07 clast3 site2
	77	48.76	1.73	14.88	0.04	11.15	0.12	8.99	11.81	2.28	0.09	0.15	100.00	V07 clast4 site1
	78	48.76	1.63	14.84	0.04	11.26	0.17	8.93	11.86	2.24	0.12	0.17	100.00	V07 clast4 site2
	79	48.58	1.69	14.82	0.04	11.57	0.20	8.70	11.83	2.31	0.10	0.16	100.00	V07 clast5 site1
	80	48.39	1.75	14.83	0.04	11.92	0.02	8.56	11.97	2.28	0.07	0.16	100.00	V07 clast5 site2

<b>Average</b>		48.74	1.69	14.82	0.03	11.46	0.16	8.68	11.84	2.31	0.10	0.17	100.00	
<b>Standard Deviation</b>		0.19	0.06	0.08	0.01	0.29	0.07	0.22	0.08	0.05	0.02	0.02	0.00	

Sample	Probe #	Norm. SiO2	Norm. TiO2	Norm. Al2O3	Norm. Cr2O3	Norm. FeO	Norm. MnO	Norm. MgO	Norm. CaO	Norm. Na2O	Norm. K2O	Norm. P2O5	Norm. Total	Comments
V08 (Wpt060)	81	48.19	1.72	15.01	0.05	11.86	0.05	8.62	12.04	2.24	0.09	0.15	100.00	V08 clast1 site1
Distal	82	48.53	1.72	14.98	0.05	11.52	0.09	8.66	12.00	2.25	0.07	0.13	100.00	V08 clast1 site2
Hyaloclastite	83	49.08	1.62	14.91	0.05	11.45	0.06	8.56	11.75	2.25	0.08	0.19	100.00	V08 clast2 site1
Mound	84	49.08	1.67	15.00	0.06	11.15	0.00	8.62	11.92	2.33	0.07	0.11	100.00	V08 clast2 site2
Upper-Section (Arnarpfur)	85	48.87	1.76	14.98	0.06	11.42	0.00	8.46	11.91	2.30	0.07	0.16	100.00	V08 clast3 site1
	86	49.29	1.76	14.84	0.05	11.19	0.05	8.47	11.80	2.31	0.08	0.16	100.00	V08 clast3 site2
	87	49.09	1.63	14.95	0.05	11.36	0.05	8.49	11.85	2.33	0.06	0.14	100.00	V08 clast4 site1
	88	49.01	1.71	15.12	0.05	11.17	0.09	8.53	11.89	2.27	0.04	0.13	100.00	V08 clast4 site2
	89	47.92	1.67	15.00	0.06	12.06	0.10	8.63	12.04	2.31	0.07	0.15	100.00	V08 clast5 site1
	90	48.78	1.68	14.91	0.03	11.65	0.15	8.37	11.84	2.35	0.09	0.16	100.00	V08 clast5 site2

<b>Average</b>		48.78	1.69	14.97	0.05	11.48	0.06	8.54	11.90	2.29	0.07	0.15	100.00	
<b>Standard Deviation</b>		0.44	0.05	0.07	0.01	0.30	0.05	0.09	0.10	0.04	0.02	0.02	0.00	

**Normalized oxide weight percentages (continued)**

Sample	Probe #	Norm. SiO2	Norm. TiO2	Norm. Al2O3	Norm. Cr2O3	Norm. FeO	Norm. MnO	Norm. MgO	Norm. CaO	Norm. Na2O	Norm. K2O	Norm. P2O5	Norm. Total	Comments
Wpt070	230	49.18	1.80	14.83	0.04	11.48	0.22	8.18	11.59	2.45	0.07	0.17	100.00	Wpt070 clast1 site1
Median	231	49.06	1.79	14.81	0.04	11.40	0.31	8.19	11.60	2.51	0.11	0.18	100.00	Wpt070 clast1 site2
Hyaloclastite	232	49.03	1.78	15.04	0.04	11.49	0.25	8.20	11.47	2.48	0.07	0.16	100.00	Wpt070 clast2 site1
Mound from	233	48.88	1.83	15.03	0.04	11.41	0.29	8.13	11.62	2.54	0.08	0.17	100.00	Wpt070 clast2 site2
Central	234	48.69	1.69	14.77	0.07	11.86	0.18	8.23	11.76	2.47	0.12	0.15	100.00	Wpt070 clast2 site3
Hyaloclastite	235	48.81	1.83	14.82	0.04	11.75	0.17	8.13	11.72	2.45	0.11	0.18	100.00	Wpt070 clast2 site4
Mound	236	48.90	1.80	14.79	0.02	11.42	0.26	8.24	11.86	2.44	0.10	0.16	100.00	Wpt070 clast3 site1
(Arnarofur)	237	48.92	1.77	14.78	0.06	11.64	0.17	8.15	11.85	2.41	0.10	0.16	100.00	Wpt070 clast3 site2
	238	48.87	1.75	14.86	0.05	11.64	0.23	8.14	11.79	2.42	0.10	0.15	100.00	Wpt070 clast4 site1
	239	48.85	1.79	14.70	0.06	11.90	0.11	8.16	11.75	2.45	0.10	0.13	100.00	Wpt070 clast4 site2
	240	49.02	1.81	14.87	0.01	11.39	0.18	8.19	11.87	2.43	0.09	0.13	100.00	Wpt070 clast5 site1
	241	48.46	1.81	14.81	0.05	11.89	0.16	8.18	11.91	2.43	0.11	0.17	100.00	Wpt070 clast5 site2
	242	49.01	1.77	14.73	0.05	11.70	0.11	8.09	11.75	2.49	0.09	0.19	100.00	Wpt070 clast6 site1
	243	48.95	1.76	14.83	0.04	11.66	0.11	8.01	11.87	2.49	0.10	0.19	100.00	Wpt070 clast6 site2

<b>Average</b>		48.90	1.78	14.83	0.04	11.62	0.20	8.16	11.74	2.46	0.10	0.16	100.00	
<b>Standard Deviation</b>		0.17	0.04	0.10	0.02	0.19	0.07	0.06	0.13	0.04	0.01	0.02	0.00	

**Control Sample**

Sample	Probe #	Norm. SiO2	Norm. TiO2	Norm. Al2O3	Norm. Cr2O3	Norm. FeO	Norm. MnO	Norm. MgO	Norm. CaO	Norm. Na2O	Norm. K2O	Norm. P2O5	Norm. Total	Comments
BCR-1	3	56.57	2.53	13.53	0.00	11.22	0.13	4.00	7.56	2.75	1.44	0.28	100.00	BCR-1 control1
Control	35	54.81	2.39	13.90	0.02	12.04	0.20	3.93	7.62	3.12	1.62	0.34	100.00	BCR-1 control2
Sample	36	56.04	2.37	13.39	0.02	11.37	0.16	3.81	7.44	3.22	1.75	0.43	100.00	BCR-1 control3
	70	55.94	2.28	13.80	0.00	11.74	0.18	3.93	7.65	2.72	1.44	0.34	100.00	BCR-1 control4
	91	56.11	2.24	13.49	0.00	12.09	0.12	3.58	7.16	3.25	1.71	0.26	100.00	BCR-1 control5
	97	55.85	2.33	13.18	0.00	12.41	0.23	3.61	7.23	3.28	1.62	0.26	100.00	BCR-1 control6
	138	55.62	2.32	13.51	0.00	12.18	0.10	3.75	7.28	3.37	1.56	0.30	100.00	BCR-1 control7
	139	54.92	2.21	13.23	0.00	12.81	0.24	3.73	7.42	3.53	1.61	0.30	100.00	BCR-1 control8
	164	56.37	2.36	13.38	0.00	11.64	0.20	3.67	7.38	3.14	1.61	0.25	100.00	BCR-1 control9
	165	57.20	2.35	13.34	0.00	11.13	0.13	3.71	7.30	2.96	1.57	0.31	100.00	BCR-1 control10
	228	55.98	2.32	13.87	0.00	11.68	0.29	3.73	7.44	2.87	1.40	0.41	100.00	BCR-1 control11
	229	56.34	2.26	13.50	0.00	12.47	0.23	3.57	6.98	2.67	1.66	0.34	100.00	BCR-1 control12
	364	57.06	2.44	13.79	0.00	11.18	0.23	3.49	7.25	2.89	1.39	0.29	100.00	BCR-1 control13
	365	57.41	2.12	13.44	0.00	11.35	0.11	3.24	6.81	3.37	1.77	0.37	100.00	BCR-1 control14

<b>Average</b>		56.16	2.32	13.53	0.00	11.81	0.18	3.70	7.32	3.08	1.58	0.32	100.00	
<b>Standard Deviation</b>		0.76	0.10	0.23	0.01	0.54	0.06	0.20	0.23	0.27	0.12	0.06	0.00	

### C.3 CIPW Norm Calculation Program

Sample Number: Wpt094 Northern Bláfjöll (hyaloclastite)

Rock Analysis		Correction Factors		Corrected Analysis	Normative Minerals	Weight % Norm	Volume % Norm
SiO2	48.86 %	Total=100%? Y/N	N	48.80	Quartz		
TiO2	1.76 %	Fe3+/(Total Iron)	0.1	1.75	Plagioclase	49.75	56.49
Al2O3	14.80 %			14.78	Orthoclase	0.24	0.28
Fe2O3	%	Total Fe as FeO	11.60	1.29	Nepheline		
FeO	11.60 %	Desired Fe2O3	1.29	10.42	Leucite		
MnO	0.19 %	Desired FeO	10.44	0.19	Kalsilite		
MgO	8.46 %	Weight corr. factor	0.999	8.45	Corundum		
CaO	11.70 %			11.69	Diopside	22.59	20.73
Na2O	2.40 %			2.40	Hypersthene	11.95	10.54
K2O	0.04 %			0.04	Wollastonite		
P2O5	0.15 %	Zero values not shown		0.15	Olivine	9.87	8.32
CO2	%				Larnite		
SO3	%				Acmite		
S	%				K2SiO3		
F	%				Na2SiO3		
Cl	%				Rutile		
Sr	ppm	Norm calculation checks: Norm seems OK			Ilmenite	3.32	2.15
Ba	ppm				Magnetite	1.87	1.10
Ni	ppm				Hematite		
Cr	386 ppm			0.06	Apatite	0.35	0.33
Zr	ppm				Zircon		
Total	99.96			100.02	Perovskite		
					Chromite	0.09	0.05
					Sphene		
					Pyrite		
					Halite		
					Fluorite		
					Anhydrite		
					Na2SO4		
					Calcite		
					Na2CO3		
					Total	100.03	99.99
					Fe3+/(Total Fe) in rock	10.0	10.0
					Mg/(Mg+Total Fe) in rock	56.5	56.5
					Mg/(Mg+Fe2+) in rock	59.1	59.1
					Mg/(Mg+Fe2+) in silicates	64.1	64.1
					Ca/(Ca+Na) in rock	72.9	72.9
					Ca/(Ca+Na) in plagioclase	57.7	57.7
					Differentiation Index	50.0	56.8
					Calculated density, g/cc	3.07	3.07
					Calculated liquid density	2.73	2.73
					Calculated viscosity, dry	2.0	2.0
					Calculated viscosity, wet	1.9	1.9
					Estimated liquidus temp.	1236	1236
					Estimated H2O content	0.31	0.31

This program was written by Kurt Hollocher, Geology Department, Union College, Schenectady, NY, 12308, hollochk@union.edu

# Norm Calculation Program

Sample Number: **Wpt091 Vifilsfell**

Rock Analysis		Correction Factors		Corrected Analysis		Normative Minerals		Weight % Norm	Volume % Norm
SiO2	48.90 %	Total=100%? Y/N	N	48.84	Quartz				
TiO2	1.77 %	Fe3+/(Total Iron)	0.1	1.77	Plagioclase	50.03	56.76		
Al2O3	14.84 %			14.83	Orthoclase	0.41	0.49		
Fe2O3	%	Total Fe as FeO	11.54	1.28	Nepheline				
FeO	11.54 %	Desired Fe2O3	1.28	10.37	Leucite				
MnO	0.16 %	Desired FeO	10.38	0.16	Kalsilite				
MgO	8.25 %	Weight corr. factor	0.999	8.24	Corundum				
CaO	11.82 %			11.80	Diopside	23.23	21.28		
Na2O	2.46 %			2.46	Hypersthene	10.55	9.28		
K2O	0.07 %			0.07	Wollastonite				
P2O5	0.15 %			0.15	Olivine	10.16	8.54		
CO2	%				Larnite				
SO3	%				Acmite				
S	%				K2SiO3				
F	%				Na2SiO3				
Cl	%				Rutile				
Sr	ppm				Ilmenite	3.36	2.17		
Ba	ppm				Magnetite	1.86	1.09		
Ni	ppm				Hematite				
Cr	390 ppm			0.06	Apatite	0.35	0.33		
Zr	ppm				Zircon				
Total	99.96			100.03	Perovskite				
					Chromite	0.09	0.05		
					Sphene				
					Pyrite				
					Halite				
					Fluorite				
					Anhydrite				
					Na2SO4				
					Calcite				
					Na2CO3				
					Total	100.04	99.99		
					Fe3+/(Total Fe) in rock	10.0	10.0		
					Mg/(Mg+Total Fe) in rock	56.0	56.0		
					Mg/(Mg+Fe2+) in rock	58.6	58.6		
					Mg/(Mg+Fe2+) in silicates	63.8	63.8		
					Ca/(Ca+Na) in rock	72.6	72.6		
					Ca/(Ca+Na) in plagioclase	57.0	57.0		
					Differentiation Index	50.4	57.3		
					Calculated density, g/cc	3.06	3.06		
					Calculated liquid density	2.73	2.73		
					Calculated viscosity, dry	2.0	2.0		
					Calculated viscosity, wet	1.9	1.9		
					Estimated liquidus temp.	1235	1235		
					Estimated H2O content	0.31	0.31		

This program was written by Kurt Hollocher, Geology Department, Union College, Schenectady, NY, 12308, hollochk@union.edu

### Norm Calculation Program

Sample Number: **Wpt092 Vífilsfell (above Northern Bláfjöll-Vífilsfell contact)**

Rock Analysis		Correction Factors		Corrected Analysis	Normative Minerals	Weight % Norm	Volume % Norm
SiO2	48.94 %	Total=100%? Y/N	N	48.88	Quartz		
TiO2	1.89 %	Fe3+/(Total Iron)	0.1	1.89	Plagioclase	49.09	55.77
Al2O3	14.50 %			14.48	Orthoclase	0.71	0.85
Fe2O3	%	Total Fe as FeO	11.41	1.27	Nepheline		
FeO	11.41 %	Desired Fe2O3	1.27	10.25	Leucite		
MnO	0.19 %	Desired FeO	10.27	0.19	Kalsilite		
MgO	8.30 %	Weight corr. factor	0.999	8.29	Corundum		
CaO	11.97 %			11.96	Diopside	24.85	22.80
Na2O	2.50 %			2.50	Hypersthene	8.88	7.83
K2O	0.12 %			0.12	Wollastonite		
P2O5	0.16 %			0.16	Olivine	10.65	8.98
CO2	%				Larnite		
SO3	%				Acmite		
S	%				K2SiO3		
F	%				Na2SiO3		
Cl	%				Rutile		
Sr	ppm				Ilmenite	3.59	2.32
Ba	ppm				Magnetite	1.84	1.09
Ni	ppm				Hematite		
Cr	230 ppm			0.03	Apatite	0.37	0.36
Zr	ppm				Zircon		
Total	99.98			100.02	Perovskite		
					Chromite	0.04	0.03
					Sphene		
					Pyrite		
					Halite		
					Fluorite		
					Anhydrite		
					Na2SO4		
					Calcite		
					Na2CO3		
					Total	100.02	100.03
					Fe3+/(Total Fe) in rock	10.0	10.0
					Mg/(Mg+Total Fe) in rock	56.5	56.5
					Mg/(Mg+Fe2+) in rock	59.0	59.0
					Mg/(Mg+Fe2+) in silicates	64.4	64.4
					Ca/(Ca+Na) in rock	72.6	72.6
					Ca/(Ca+Na) in plagioclase	55.4	55.4
					Differentiation Index	49.8	56.6
					Calculated density, g/cc	3.07	3.07
					Calculated liquid density	2.73	2.73
					Calculated viscosity, dry	2.0	2.0
					Calculated viscosity, wet	1.9	1.9
					Estimated liquidus temp.	1234	1234
					Estimated H2O content	0.31	0.31

This program was written by Kurt Hollocher, Geology Department, Union College, Schenectady, NY, 12308, hollochk@union.edu

# Norm Calculation Program

Sample Number: Wpt107 Vífilfell

Rock Analysis		Correction Factors		Corrected Analysis	Normative Minerals	Weight % Norm	Volume % Norm
SiO2	48.86 %	Total=100%? Y/N	N	48.80	Quartz		
TiO2	1.77 %	Fe3+/(Total Iron)	0.1	1.77	Plagioclase	49.84	56.57
Al2O3	14.83 %			14.81	Orthoclase	0.53	0.64
Fe2O3	%	Total Fe as FeO	11.60	1.29	Nepheline		
FeO	11.60 %	Desired Fe2O3	1.29	10.43	Leucite		
MnO	0.19 %	Desired FeO	10.44	0.19	Kalsilite		
MgO	8.22 %	Weight corr. factor	0.999	8.21	Corundum		
CaO	11.83 %			11.81	Diopside	23.35	21.40
Na2O	2.44 %			2.44	Hypersthene	10.35	9.10
K2O	0.09 %			0.09	Wollastonite		
P2O5	0.14 %	Zero values not shown		0.14	Olivine	10.35	8.69
CO2	%				Larnite		
SO3	%				Acmite		
S	%				K2SiO3		
F	%	Norm calculation checks:			Na2SiO3		
Cl	%	Norm seems OK			Rutile		
Sr	ppm				Ilmenite	3.36	2.17
Ba	ppm				Magnetite	1.87	1.10
Ni	ppm				Hematite		
Cr	123 ppm			0.02	Apatite	0.32	0.31
Zr	ppm				Zircon		
<b>Total</b>	<b>99.96</b>			<b>100.00</b>	Perovskite		
					Chromite	0.03	0.02
					Sphene		
					Pyrite		
					Halite		
					Fluorite		
					Anhydrite		
					Na2SO4		
					Calcite		
					Na2CO3		
					<b>Total</b>	<b>100.00</b>	<b>100.00</b>
					Fe3+/(Total Fe) in rock	10.0	10.0
					Mg/(Mg+Total Fe) in rock	55.8	55.8
					Mg/(Mg+Fe2+) in rock	58.4	58.4
					Mg/(Mg+Fe2+) in silicates	63.4	63.4
					Ca/(Ca+Na) in rock	72.8	72.8
					Ca/(Ca+Na) in plagioclase	57.1	57.1
					Differentiation Index	50.4	57.2
					Calculated density, g/cc	3.06	3.06
					Calculated liquid density	2.73	2.73
					Calculated viscosity, dry	2.0	2.0
					Calculated viscosity, wet	1.9	1.9
					Estimated liquidus temp.	1235	1235
					Estimated H2O content	0.31	0.31

This program was written by Kurt Hollocher, Geology Department, Union College, Schenectady, NY, 12308, hollochk@union.edu



### Norm Calculation Program

Sample Number: **V02 (Wpt043) Arnarpúfur (proximal hyaloclasite mound)**

Rock Analysis		Correction Factors		Corrected Analysis	Normative Minerals	Weight % Norm	Volume % Norm
SiO2	48.33 %	Total=100%? Y/N	N	48.27	Quartz		
TiO2	1.74 %	Fe3+/(Total Iron)	0.1	1.73	Plagioclase	49.61	56.35
Al2O3	14.89 %			14.87	Orthoclase	0.59	0.71
Fe2O3	%	Total Fe as FeO	11.68	1.30	Nepheline		
FeO	11.68 %	Desired Fe2O3	1.30	10.50	Leucite		
MnO	0.23 %	Desired FeO	10.51	0.23	Kalsilite		
MgO	8.51 %	Weight corr. factor	0.999	8.50	Corundum		
CaO	11.96 %			11.94	Diopside	23.32	21.41
Na2O	2.35 %			2.35	Hypersthene	8.33	7.34
K2O	0.10 %			0.10	Wollastonite		
P2O5	0.16 %	Zero values not shown		0.16	Olivine	12.53	10.56
CO2	%				Larnite		
SO3	%				Acmite		
S	%				K2SiO3		
F	%	Norm calculation checks: Norm seems OK			Na2SiO3		
Cl	%				Rutile		
Sr	ppm				Ilmenite	3.29	2.12
Ba	ppm				Magnetite	1.88	1.11
Ni	ppm				Hematite		
Cr	339 ppm			0.05	Apatite	0.37	0.36
Zr	ppm				Zircon		
Total	99.96			100.00	Perovskite		
					Chromite	0.07	0.04
					Sphene		
					Pyrite		
					Halite		
					Fluorite		
					Anhydrite		
					Na2SO4		
					Calcite		
					Na2CO3		
					<b>Total</b>	<b>99.99</b>	<b>100.00</b>
					Fe3+/(Total Fe) in rock	10.0	10.0
					Mg/(Mg+Total Fe) in rock	56.5	56.5
					Mg/(Mg+Fe2+) in rock	59.1	59.1
					Mg/(Mg+Fe2+) in silicates	63.9	63.9
					Ca/(Ca+Na) in rock	73.7	73.7
					Ca/(Ca+Na) in plagioclase	58.5	58.5
					Differentiation Index	50.2	57.1
					Calculated density, g/cc	3.07	3.07
					Calculated liquid density	2.74	2.74
					Calculated viscosity, dry	1.9	1.9
					Calculated viscosity, wet	1.8	1.8
					Estimated liquidus temp.	1245	1245
					Estimated H2O content	0.28	0.28

This program was written by Kurt Hollocher, Geology Department, Union College, Schenectady, NY, 12308, hollochk@union.edu

### Norm Calculation Program

Sample Number: V03 (Wpt051) Arnarpúfur (distal hyaloclasite mound)

Rock Analysis		Correction Factors		Corrected Analysis	Normative Minerals	Weight % Norm	Volume % Norm
SiO2	48.71 %	Total=100%? Y/N	N	48.65	Quartz		
TiO2	1.73 %	Fe3+/(Total Iron)	0.1	1.73	Plagioclase	48.90	55.58
Al2O3	14.63 %			14.61	Orthoclase	0.53	0.64
Fe2O3	%	Total Fe as FeO	11.63	1.29	Nepheline		
FeO	11.63 %	Desired Fe2O3	1.29	10.45	Leucite		
MnO	0.23 %	Desired FeO	10.46	0.23	Kalsilite		
MgO	8.54 %	Weight corr. factor	0.999	8.53	Corundum		
CaO	11.90 %			11.88	Diopside	23.48	21.57
Na2O	2.35 %			2.34	Hypersthene	10.86	9.58
K2O	0.09 %			0.09	Wollastonite		
P2O5	0.18 %	Zero values not shown		0.18	Olivine	10.62	8.96
CO2	%				Larnite		
SO3	%				Acmite		
S	%				K2SiO3		
F	%				Na2SiO3		
Cl	%	Norm calculation checks: Norm seems OK			Rutile		
Sr	ppm				Ilmenite	3.29	2.12
Ba	ppm				Magnetite	1.87	1.10
Ni	ppm				Hematite		
Cr	348 ppm			0.05	Apatite	0.42	0.40
Zr	ppm				Zircon		
Total	99.97			100.03	Perovskite		
					Chromite	0.07	0.04
					Sphene		
					Pyrite		
					Halite		
					Fluorite		
					Anhydrite		
					Na2SO4		
					Calcite		
					Na2CO3		
					Total	100.04	99.99
					Fe3+/(Total Fe) in rock	10.0	10.0
					Mg/(Mg+Total Fe) in rock	56.7	56.7
					Mg/(Mg+Fe2+) in rock	59.3	59.3
					Mg/(Mg+Fe2+) in silicates	64.1	64.1
					Ca/(Ca+Na) in rock	73.7	73.7
					Ca/(Ca+Na) in plagioclase	58.1	58.1
					Differentiation Index	49.4	56.2
					Calculated density, g/cc	3.07	3.07
					Calculated liquid density	2.73	2.73
					Calculated viscosity, dry	1.9	1.9
					Calculated viscosity, wet	1.9	1.9
					Estimated liquidus temp.	1239	1239
					Estimated H2O content	0.30	0.30

This program was written by Kurt Hollocher, Geology Department, Union College, Schenectady, NY, 12308, hollochk@union.edu

### Norm Calculation Program

Sample Number: V06 (Wpt059) Arnarpúfur (distal mound, upper-section)

Rock Analysis		Correction Factors		Corrected Analysis	Normative Minerals	Weight % Norm	Volume % Norm
SiO2	48.28 %	Total=100%? Y/N	N	48.22	Quartz		
TiO2	1.73 %	Fe3+/(Total Iron)	0.1	1.73	Plagioclase	49.33	55.96
Al2O3	14.83 %			14.81	Orthoclase	0.59	0.71
Fe2O3	%	Total Fe as FeO	11.86	1.32	Nepheline		
FeO	11.86 %	Desired Fe2O3	1.32	10.66	Leucite		
MnO	0.18 %	Desired FeO	10.67	0.18	Kalsilite		
MgO	8.82 %	Weight corr. factor	0.999	8.81	Corundum		
CaO	11.86 %			11.85	Diopside	22.90	21.02
Na2O	2.32 %			2.32	Hypersthene	8.39	7.40
K2O	0.10 %			0.10	Wollastonite		
P2O5	0.17 %			0.17	Olivine	13.34	11.24
CO2	%				Larnite		
SO3	%				Acmite		
S	%				K2SiO3		
F	%				Na2SiO3		
Cl	%				Rutile		
Sr	ppm				Ilmenite	3.29	2.12
Ba	ppm				Magnetite	1.91	1.13
Ni	ppm				Hematite		
Cr	314 ppm			0.05	Apatite	0.39	0.38
Zr	ppm				Zircon		
Total	100.15			100.22	Perovskite		
					Chromite	0.07	0.04
					Sphene		
					Pyrite		
					Halite		
					Fluorite		
					Anhydrite		
					Na2SO4		
					Calcite		
					Na2CO3		
					Total	100.21	100.00
					Fe3+/(Total Fe) in rock	10.0	10.0
					Mg/(Mg+Total Fe) in rock	57.0	57.0
					Mg/(Mg+Fe2+) in rock	59.6	59.6
					Mg/(Mg+Fe2+) in silicates	64.4	64.4
					Ca/(Ca+Na) in rock	73.8	73.8
					Ca/(Ca+Na) in plagioclase	58.8	58.8
					Differentiation Index	49.9	56.7
					Calculated density, g/cc	3.07	3.07
					Calculated liquid density	2.74	2.74
					Calculated viscosity, dry	1.8	1.8
					Calculated viscosity, wet	1.8	1.8
					Estimated liquidus temp.	1248	1248
					Estimated H2O content	0.27	0.27

This program was written by Kurt Hollocher, Geology Department, Union College, Schenectady, NY, 12308, hollochk@union.edu

### Norm Calculation Program

Sample Number: V07 (Wpt059) Arnarþúfur (distal mound, lower-section)

Rock Analysis		Correction Factors		Corrected Analysis	Normative Minerals	Weight % Norm	Volume % Norm
SiO2	48.74 %	Total=100%? Y/N	N	48.68	Quartz		
TiO2	1.69 %	Fe3+/(Total Iron)	0.1	1.69	Plagioclase	49.27	55.89
Al2O3	14.82 %			14.80	Orthoclase	0.59	0.71
Fe2O3	%	Total Fe as FeO	11.46	1.27	Nepheline		
FeO	11.46 %	Desired Fe2O3	1.27	10.30	Leucite		
MnO	0.16 %	Desired FeO	10.31	0.16	Kalsilite		
MgO	8.68 %	Weight corr. factor	0.999	8.67	Corundum		
CaO	11.84 %			11.82	Diopside	22.75	20.89
Na2O	2.31 %			2.31	Hypersthene	11.36	10.03
K2O	0.10 %			0.10	Wollastonite		
P2O5	0.17 %	Zero values not shown		0.17	Olivine	10.53	8.90
CO2	%				Larnite		
SO3	%				Acmite		
S	%				K2SiO3		
F	%				Na2SiO3		
Cl	%	Norm calculation checks:			Rutile		
Sr	ppm	Norm seems OK			Ilmenite	3.21	2.07
Ba	ppm				Magnetite	1.84	1.09
Ni	ppm				Hematite		
Cr	314 ppm			0.05	Apatite	0.39	0.38
Zr	ppm				Zircon		
Total	99.97			100.02	Perovskite		
					Chromite	0.07	0.04
					Sphene		
					Pyrite		
					Halite		
					Fluorite		
					Anhydrite		
					Na2SO4		
					Calcite		
					Na2CO3		
					Total	100.01	100.00
					Fe3+/(Total Fe) in rock	10.0	10.0
					Mg/(Mg+Total Fe) in rock	57.5	57.5
					Mg/(Mg+Fe2+) in rock	60.0	60.0
					Mg/(Mg+Fe2+) in silicates	64.9	64.9
					Ca/(Ca+Na) in rock	73.9	73.9
					Ca/(Ca+Na) in plagioclase	58.9	58.9
					Differentiation Index	49.9	56.6
					Calculated density, g/cc	3.07	3.07
					Calculated liquid density	2.73	2.73
					Calculated viscosity, dry	1.9	1.9
					Calculated viscosity, wet	1.9	1.9
					Estimated liquidus temp.	1238	1238
					Estimated H2O content	0.30	0.30

This program was written by Kurt Hollocher, Geology Department, Union College, Schenectady, NY, 12308, hollochk@union.edu

### Norm Calculation Program

Sample Number: V08 (Wpt060) Arnarþúfur (distal mound, upper-section)

Rock Analysis		Correction Factors		Corrected Analysis	Normative Minerals	Weight % Norm	Volume % Norm
SiO2	48.78 %	Total=100%? Y/N	N	48.72	Quartz		
TiO2	1.69 %	Fe3+/(Total Iron)	0.1	1.69	Plagioclase	49.68	56.33
Al2O3	14.97 %			14.95	Orthoclase	0.41	0.50
Fe2O3	%	Total Fe as FeO	11.48	1.27	Nepheline		
FeO	11.48 %	Desired Fe2O3	1.28	10.32	Leucite		
MnO	0.06 %	Desired FeO	10.33	0.06	Kalsilite		
MgO	8.54 %	Weight corr. factor	0.999	8.53	Corundum		
CaO	11.90 %			11.89	Diopside	22.67	20.80
Na2O	2.29 %			2.29	Hypersthene	12.10	10.67
K2O	0.07 %			0.07	Wollastonite		
P2O5	0.15 %	Zero values not shown		0.15	Olivine	9.64	8.14
CO2	%				Larnite		
SO3	%				Acmite		
S	%				K2SiO3		
F	%				Na2SiO3		
Cl	%	Norm calculation checks: Norm seems OK			Rutile		
Sr	ppm				Ilmenite	3.21	2.07
Ba	ppm				Magnetite	1.84	1.09
Ni	ppm				Hematite		
Cr	515 ppm			0.08	Apatite	0.35	0.33
Zr	ppm				Zircon		
Total	99.95			100.02	Perovskite		
					Chromite	0.12	0.07
					Sphene		
					Pyrite		
					Halite		
					Fluorite		
					Anhydrite		
					Na2SO4		
					Calcite		
					Na2CO3		
					Total	100.02	100.00
					Fe3+/(Total Fe) in rock	10.0	10.0
					Mg/(Mg+Total Fe) in rock	57.0	57.0
					Mg/(Mg+Fe2+) in rock	59.6	59.6
					Mg/(Mg+Fe2+) in silicates	64.8	64.8
					Ca/(Ca+Na) in rock	74.2	74.2
					Ca/(Ca+Na) in plagioclase	59.6	59.6
					Differentiation Index	50.1	56.8
					Calculated density, g/cc	3.07	3.07
					Calculated liquid density	2.73	2.73
					Calculated viscosity, dry	2.0	2.0
					Calculated viscosity, wet	1.9	1.9
					Estimated liquidus temp.	1237	1237
					Estimated H2O content	0.31	0.31

This program was written by Kurt Hollocher, Geology Department, Union College, Schenectady, NY, 12308, hollochk@union.edu

### Norm Calculation Program

Sample Number: **Wpt070 Arnarpúfur (central hyaloclastite mound)**

Rock Analysis		Correction Factors		Corrected Analysis	Normative Minerals	Weight % Norm	Volume % Norm
SiO2	48.90 %	Total=100%? Y/N	N	48.84	Quartz		
TiO2	1.78 %	Fe3+/(Total Iron)	0.1	1.78	Plagioclase	49.89	56.62
Al2O3	14.83 %			14.81	Orthoclase	0.59	0.71
Fe2O3	%	Total Fe as FeO	11.62	1.29	Nepheline		
FeO	11.62 %	Desired Fe2O3	1.29	10.44	Leucite		
MnO	0.20 %	Desired FeO	10.45	0.20	Kalsilite		
MgO	8.16 %	Weight corr. factor	0.999	8.15	Corundum		
CaO	11.74 %			11.73	Diopside	23.02	21.09
Na2O	2.46 %			2.46	Hypersthene	10.79	9.49
K2O	0.10 %			0.10	Wollastonite		
P2O5	0.16 %			0.16	Olivine	10.02	8.41
CO2	%				Larnite		
SO3	%				Acmite		
S	%				K2SiO3		
F	%				Na2SiO3		
Cl	%				Rutile		
Sr	ppm				Ilmenite	3.38	2.18
Ba	ppm				Magnetite	1.87	1.10
Ni	ppm				Hematite		
Cr	430 ppm			0.06	Apatite	0.37	0.35
Zr	ppm				Zircon		
Total	99.96			100.02	Perovskite		
					Chromite	0.09	0.05
					Sphene		
					Pyrite		
					Halite		
					Fluorite		
					Anhydrite		
					Na2SO4		
					Calcite		
					Na2CO3		
					Total	100.02	100.00
					Fe3+/(Total Fe) in rock	10.0	10.0
					Mg/(Mg+Total Fe) in rock	55.6	55.6
					Mg/(Mg+Fe2+) in rock	58.2	58.2
					Mg/(Mg+Fe2+) in silicates	63.3	63.3
					Ca/(Ca+Na) in rock	72.5	72.5
					Ca/(Ca+Na) in plagioclase	56.8	56.8
					Differentiation Index	50.5	57.3
					Calculated density, g/cc	3.06	3.06
					Calculated liquid density	2.73	2.73
					Calculated viscosity, dry	2.0	2.0
					Calculated viscosity, wet	1.9	1.9
					Estimated liquidus temp.	1235	1235
					Estimated H2O content	0.31	0.31

This program was written by Kurt Hollocher, Geology Department, Union College, Schenectady, NY, 12308, hollochk@union.edu

# Norm Calculation Program

Sample Number: **BCR-1 (control sample)**

Rock Analysis		Correction Factors		Corrected Analysis	Normative Minerals	Weight % Norm	Volume % Norm
SiO2	56.16 %	Total=100%? Y/N	N	56.09	Quartz	8.57	9.61
TiO2	2.32 %	Fe3+/(Total Iron)	0.1	2.32	Plagioclase	44.43	49.32
Al2O3	13.53 %			13.51	Orthoclase	9.34	10.83
Fe2O3	%	Total Fe as FeO	11.81	1.31	Nepheline		
FeO	11.81 %	Desired Fe2O3	1.31	10.61	Leucite		
MnO	0.18 %	Desired FeO	10.63	0.18	Kalsilite		
MgO	3.70 %	Weight corr. factor	0.999	3.69	Corundum		
CaO	7.25 %			7.24	Diopside	13.00	11.33
Na2O	3.08 %			3.08	Hypersthene	17.54	14.38
K2O	1.58 %			1.58	Wollastonite		
P2O5	0.32 %			0.32	Olivine		
CO2	%				Larnite		
SO3	%				Acmite		
S	%				K2SiO3		
F	%				Na2SiO3		
Cl	%				Rutile		
Sr	ppm				Ilmenite	4.41	2.76
Ba	ppm				Magnetite	1.90	1.08
Ni	ppm				Hematite		
Cr	36 ppm			0.01	Apatite	0.74	0.69
Zr	ppm				Zircon		
Total	99.92			99.94	Perovskite		
					Chromite	0.01	0.01
					Sphene		
					Pyrite		
					Halite		
					Fluorite		
					Anhydrite		
					Na2SO4		
					Calcite		
					Na2CO3		
					Total	99.94	100.01
					Fe3+/(Total Fe) in rock	10.0	10.0
					Mg/(Mg+Total Fe) in rock	35.8	35.8
					Mg/(Mg+Fe2+) in rock	38.3	38.3
					Mg/(Mg+Fe2+) in silicates	44.8	44.8
					Ca/(Ca+Na) in rock	56.5	56.5
					Ca/(Ca+Na) in plagioclase	39.9	39.9
					Differentiation Index	62.3	69.8
					Calculated density, g/cc	2.97	2.97
					Calculated liquid density	2.65	2.65
					Calculated viscosity, dry	3.6	3.6
					Calculated viscosity, wet	3.3	3.3
					Estimated liquidus temp.	1101	1101
					Estimated H2O content	0.96	0.96

This program was written by Kurt Hollocher, Geology Department, Union College, Schenectady, NY, 12308, hollochk@union.edu

## C.4 Hypersthene Conversion

### Northern Bláfjöll

#### Wpt094

##### Hypersthene conversion (Weight % Norm)

Qz'	Quartz derived from hypersthene	6.43
Ol'	Olivine derived from hypersthene	5.52

##### Final Quartz and Olivine (Weight % Norm)

Qz''	Total Quartz	6.43
Ol''	Total Olivine	15.39

##### Coordinates of the Quartz-Olivine-Plagioclase Triangle

Qz'''	Total normalized Quartz	8.98
Ol'''	Total normalized Olivine	21.51
Plag'''	Total normalized Plagioclase	69.51

### Vífilsfell

#### Wpt091

##### Hypersthene conversion (Weight % Norm)

Qz'	Quartz derived from hypersthene	5.67
Ol'	Olivine derived from hypersthene	4.88

##### Final Quartz and Olivine (Weight % Norm)

Qz''	Total Quartz	5.67
Ol''	Total Olivine	15.04

##### Coordinates of the Quartz-Olivine-Plagioclase Triangle

Qz'''	Total normalized Quartz	8.01
Ol'''	Total normalized Olivine	21.26
Plag'''	Total normalized Plagioclase	70.73

#### Wpt092

##### Hypersthene conversion (Weight % Norm)

Qz'	Quartz derived from hypersthene	4.78
Ol'	Olivine derived from hypersthene	4.10

##### Final Quartz and Olivine (Weight % Norm)

Qz''	Total Quartz	4.78
Ol''	Total Olivine	14.75

##### Coordinates of the Quartz-Olivine-Plagioclase Triangle

Qz'''	Total normalized Quartz	6.97
Ol'''	Total normalized Olivine	21.49
Plag'''	Total normalized Plagioclase	71.54



## Hypersthene Conversion (continued)

### Wpt107

#### Hypersthene conversion (Weight % Norm)

Qz'	Quartz derived from hypersthene	5.56
Ol'	Olivine derived from hypersthene	4.79

#### Final Quartz and Olivine (Weight % Norm)

Qz''	Total Quartz	5.56
Ol''	Total Olivine	15.14

#### Coordinates of the Quartz-Olivine-Plagioclase Triangle

Qz'''	Total normalized Quartz	7.88
Ol'''	Total normalized Olivine	21.47
Plag'''	Total normalized Plagioclase	70.66

### Arnarpúfur

#### V02 (Wpt043)

#### Hypersthene conversion (Weight % Norm)

Qz'	Quartz derived from hypersthene	4.48
Ol'	Olivine derived from hypersthene	3.85

#### Final Quartz and Olivine (Weight % Norm)

Qz''	Total Quartz	4.48
Ol''	Total Olivine	16.38

#### Coordinates of the Quartz-Olivine-Plagioclase Triangle

Qz'''	Total normalized Quartz	6.35
Ol'''	Total normalized Olivine	23.25
Plag'''	Total normalized Plagioclase	70.40

#### V03 (Wpt051)

#### Hypersthene conversion (Weight % Norm)

Qz'	Quartz derived from hypersthene	5.84
Ol'	Olivine derived from hypersthene	5.02

#### Final Quartz and Olivine (Weight % Norm)

Qz''	Total Quartz	5.84
Ol''	Total Olivine	15.64

#### Coordinates of the Quartz-Olivine-Plagioclase Triangle

Qz'''	Total normalized Quartz	8.30
Ol'''	Total normalized Olivine	22.22
Plag'''	Total normalized Plagioclase	69.48

## Hypersthene Conversion (continued)

### V06 (Wpt059)

#### Hypersthene conversion (Weight % Norm)

Qz'	Quartz derived from hypersthene	4.52
OI'	Olivine derived from hypersthene	3.87

#### Final Quartz and Olivine (Weight % Norm)

Qz''	Total Quartz	4.52
OI''	Total Olivine	17.21

#### Coordinates of the Quartz-Olivine-Plagioclase Triangle

Qz'''	Total normalized Quartz	6.36
OI'''	Total normalized Olivine	24.22
Plag'''	Total normalized Plagioclase	69.42

### V07 (Wpt059)

#### Hypersthene conversion (Weight % Norm)

Qz'	Quartz derived from hypersthene	6.13
OI'	Olivine derived from hypersthene	5.24

#### Final Quartz and Olivine (Weight % Norm)

Qz''	Total Quartz	6.13
OI''	Total Olivine	15.77

#### Coordinates of the Quartz-Olivine-Plagioclase Triangle

Qz'''	Total normalized Quartz	8.61
OI'''	Total normalized Olivine	22.15
Plag'''	Total normalized Plagioclase	69.24

### V08 (Wpt060)

#### Hypersthene conversion (Weight % Norm)

Qz'	Quartz derived from hypersthene	6.52
OI'	Olivine derived from hypersthene	5.58

#### Final Quartz and Olivine (Weight % Norm)

Qz''	Total Quartz	6.52
OI''	Total Olivine	15.22

#### Coordinates of the Quartz-Olivine-Plagioclase Triangle

Qz'''	Total normalized Quartz	9.13
OI'''	Total normalized Olivine	21.31
Plag'''	Total normalized Plagioclase	69.56
Qz'''	Total normalized Quartz	8.19
OI'''	Total normalized Olivine	21.24
Plag'''	Total normalized Plagioclase	70.57

## Hypersthene Conversion (continued)

### Control Sample

#### BCR-1

##### Hypersthene conversion (Weight % Norm)

Qz'	Quartz derived from hypersthene	8.95
Ol'	Olivine derived from hypersthene	8.59

##### Final Quartz and Olivine (Weight % Norm)

Qz''	Total Quartz	17.52
Ol''	Total Olivine	8.59

##### Coordinates of the Quartz-Olivine-Plagioclase Triangle

Qz'''	Total normalized Quartz	24.83
Ol'''	Total normalized Olivine	12.18
Plag'''	Total normalized Plagioclase	62.98